On Dynamics of Fluidic Jet Switching and Shear Layer Instabilities

Michael Mair

St Catherine's College

University of Oxford

A thesis submitted for the degree of

Doctor of Philosophy

Hilary 2019

This thesis is dedicated to all those who are denied the path to adequate schooling due to social injustice, political ignorance and the lack of state support

Acknowledgements

I would like to greatly thank Dr Marko Bacic for giving me the opportunity of pursuing a DPhil under his supervision. His passion for engineering science as well as his encouragement and support have turned this project into a great, successful and also fun endeavour. I would also like to thank him for not only being a supervisor but also a mentor.

I would also like to thank Chris Nicholls for all the fruitful discussions about fluidics throughout the years. I wish him all the best for his DPhil.

Thanks as well to Amir Ibrahim, Alex Bucknell, Nathan Donaldson and all my friends in the lab for making my time in Oxford an unforgettable memory.

Special thanks to my partner Sibylle and daughter Emma whom I cannot imagine to live without.

Last but not least, many thanks to my parents who made all this possible.

"As in most fast-evolving endeavours of research, controversy is not lacking becasue of human ability to extrapolate and synthesize limited information based on scant data and to reshape it into model or theory. We do not claim to be superhuman; therefore, this manuscript is bound to be biased and incomplete."[1]

[1]Israel J. Wygnanski, 1986

Abstract

Active flow control systems pave the way for increased cycle efficiency and reduced operational costs of next-generation jet engines. An active fluidic switching device is here proposed as the technological building block required for such a system. A novel switching mechanism based on acoustic excitation of natural flow instabilities is developed for that purpose and, what's more, investigated experimentally, numerically and analytically. The novel actuation mechanism outperforms the current state of the art and thus offers great potential to be used in future aerospace applications. Unlike conventional actuators, acoustic excitation is shown to achieve the balancing act between high bandwidth, sufficient control authority and cost effectiveness.

A proof of concept study using low-frequency excitation and low subsonic flow velocities reveals that the excitation and amplification of the natural shear layer instability results in detachment, switching and reattachment of the flow in a Coandă based fluidic device. The switching mechanism is explained by an enhanced roll-up of vortical structures on the unattached side of the jet causing an asymmetry in entrainment that ultimately leads to a pressure drop sufficient to counteract the attachment force. The detailed analysis of the switching mechanism then allows the development of a second device that operates up to sonic conditions using ultrasound. However, the switching mechanism of the second device is found to rely on the excitation of a different flow instability; namely, the jet preferred

mode as well as the first subharmonic of the natural shear layer instability. This can be attributed to a change in the shear layer characteristics as the Reynolds number increases.

In addition, ambiguous data obtained from both Large-Eddy Simulation and Particle Image Velocimetry suggest a fundamental different relationship between the natural shear layer instability and the jet preferred mode with respect to the currently accepted point of view. This is investigated separately by means of the downstream development of the shear layer characteristics of an excited round jet subject to different initial conditions.

Contents

Nomenclature

Acronyms

AC Alternating current

DNS Direct Numerical Simulation

JCL Jet centre line

$LAFPA$ Localised arc-filament plasma actuator

LES Large Eddy Simulation

PSP Pressure sensitive paint

$RANS$ Reynolds Averaged Navier-Stokes

$SDBD$ Single dielectric barrier discharge

SPL Sound pressure level

$WALE$ Wall-adapting eddy-viscosity model

$ZNMF$ Zero-net mass flux

AFC Active Flow Control

BVT Breakthrough Vehicle Technology

CFD Computational Fluid Dynamics

FSD Fluidic Switching Device

NASA National Aeronautics and Space Administration

PIV Particle Imaging Velocimetry

TCAT 21st Century Aircraft Technology

UEET Ultra-high Efficiency Engine Technology

Greek Symbols

β	Wall attachment angle	$\circ$
Δ	Difference, displacement	$-, \mathrm{m}$
ϵ	Turbulence dissipation rate, rate of entrainment	$\mathrm{m}^2/\mathrm{s}^3, -$
η	Efficiency	$-$
γ	Heat capacity ratio	$-$
λ	Wavelength, thermal conductivity, eigenvalue of H_{ij}	$\mathrm{m}, \mathrm{W/m/K}, -$
μ	Viscosity	$\mathrm{Pa} \cdot \mathrm{s}$
ω	Angular frequency, vorticity	$1/\mathrm{s}$
Ω_{ij}	Antisymmetric part of A_{ij}	m^2/s
∂	Change in value of a variable, Kronecker delta function	$-$
Φ	Flow variable	$-$
ρ	Fluid density	$\mathrm{kg/m}^3$
σ	Jet spread rate	$-$
τ	Vortex turn-over time, time period, stress tensor	$\mathrm{s}, \mathrm{s}, -$
θ	Momentum thickness, angle formed by JCL and attachment wall	$\mathrm{m}, \circ$

Roman Symbols

$\dot{m}$	Mass flow rate	ks
$\hat{p}$	Pressure amplitude	Pa
A	Area	m^2
A_{ij}	Velocity gradient tensor	m^2/s
Am	Amplitude flow factor	$-$
AR	Aspect ratio	$-$
b	Setback distance	m
c	Speed of sound	m/s
c_p	Heat capacity at constant pressure	$-$
C_w	WALE constant	$-$
C_μ	Momentum coefficient	$-$

CFL	Courant-Friedrichs-Lewy number	–
D	Diameter	m
d_s	Distance splitter to nozzle	m
d_v	Distance vent to nozzle	m
E	Energy	J
f	Frequency	1/s
F^+	Non-dimensional frequency	m
$g(x)$	Function of x	–
h	Nozzle height	m
H_{ij}	Pressure Hessian	Pa
i	Complex number	–
k_{1-4}	Constants	–
L	Length scale	m
M	Outer membrane radius, Molar mass	m, kg/mol
m	Mode number	–
Mn	Mach number	–
N	Number of cycles	–
P	Power	W
p	Pressure	Pa
p_p	Phase angle	–
Pr	Pressure ratio	–
Q	Volume flow rate	m^3/s
Q_m, q_d	Monopole and dipole source terms	–
R	Radius, gas constant	m, J/K/mol
r	Membrane radius	m
Re	Reynolds number number	–
s	Entropy	J/K

S_{ij}	Symmetric part of A_{ij}	m^2/s
St	Strouhal number	–
T	Temperature	K
t	Time	s
T_s	Non-dimensional switching time	–
u	Fluid velocity	m/s
V	Volume	m^3
w	Nozzle width, work	m, J
x	Variable	–
x_a	Attachment length	m
y	Variable	–
y^+	Non-dimensional wall distance	–
z	Variable	–

Superscripts

$'$	Fluctuating component
$\bar{}$	Time average of variable x

Subscripts

0	Centreline
∞	Free stream
ave	Average
e	Nozzle exit
eq	Equivalent
ex	Excitation
exp	Experimental
i	Component in all directions
in	Inlet
j	Jet, component in all directions

max	Maximum
min	Minimum
n	Natural mode
out	Outlet
p	Preferred mode
pc	Potential core
R	Response
ref	Reference
rms	Root-mean-square
s	Switching, sampling
T	Transducer
t	Total

List of Figures

List of Tables

Chapter 1

Introduction

1.1 Background and Motivation

The aerospace industry is at the forefront of innovation - always pushing the boundaries for new and better technologies. This is not only spurred by competition among aircraft and jet engine manufacturers but also due to the current debate on climate change and the finite amount of fossil fuels. Increasing thermodynamic efficiency while decreasing operational costs is therefore the primary objective to be reached by future aircraft. What's more is that the global appetite for efficient and low-cost transportation is also increased by a growing number of passengers each year. In order to meet that demand the number of jets added to the global aircraft fleet shows an average annual increase of 5% [4]. Another equally important factor for the future development of air transport is noise emission during take-off and landing. Airport expansion projects are often impeded by the objections of local communities around the airport [5].

Potential routes to meet the requirements of future aircraft are easily identified and a vast amount of different concepts have been proposed in the past. For aircraft manufacturers, for example, one of the most attractive concepts is the control of flow

separation over an airfoil. An effective technology that avoids or suppresses flow separation could lead to substantial improvements such as, increase of the lift-to-drag ratio [6], weight reduction due to a smaller wing [7] as well as shorter runways due to a lower stall speed [8, 9]. Apart from passive flow control methods, such as winglets and ribbles, active flow control devices have not achieved commercial readiness.

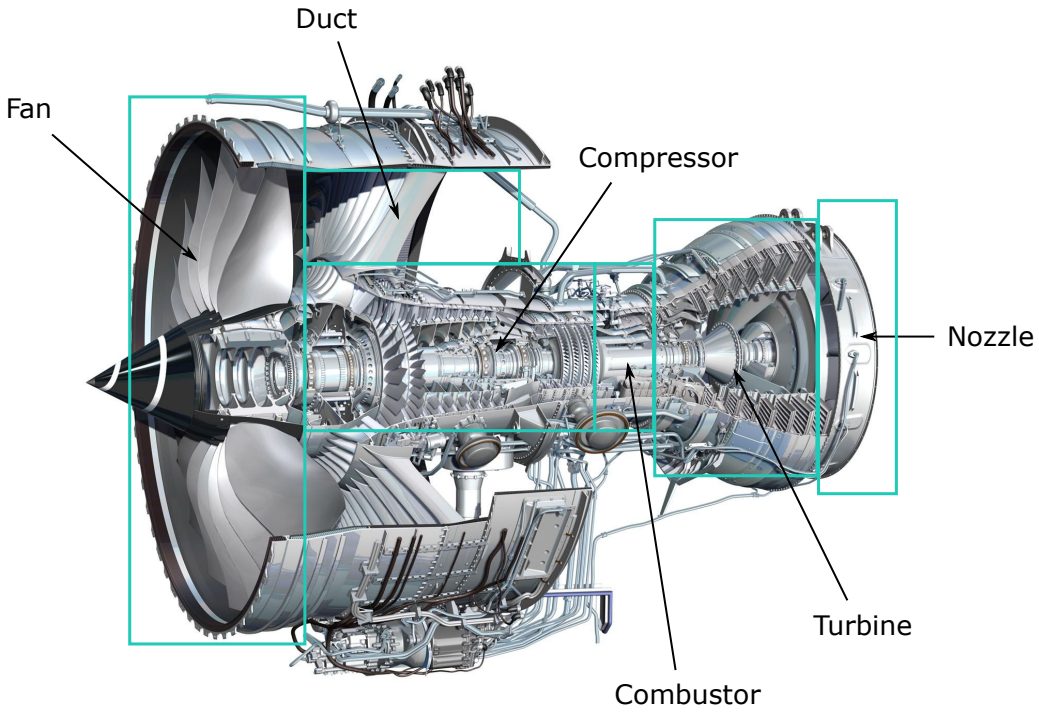

Figure 1.1: Schematic of a Rolls Royce Trent 500 engine

With respect to a modern jet engine there are even more opportunities for technological improvements that would increase thermodynamic efficiency, reduce fuel burn, decrease weight and enhance performance. The major components of a modern jet engine are shown in Fig.1.1. Air enters the fan intake, is being compressed, with the majority leaving through the bypass duct and cold nozzle to generate thrust. Some of the air (1/6th to 1/10th) enters the core to drive the first compressor stage. The compressor increases the pressure and simultaneously causes the gas temperature to rise as well. The combustion process converts the chemically bound energy of the

fuel into kinetic energy of the flow. The turbine then converts the enthalpy of the combustor exit air into useful work required to drive the compressor. Since the flow loses the same amount of energy its pressure and temperature have to decrease. The remaining energy of the flow is sufficient to generate thrust that's required to propel the aircraft.

The working principle of such an engine is described in Fig.1.2 by the idealized Brayton cycle with numbers 1,2,3,4 being the thermodynamic states of the fluid. The processes involved in between those states are:

$1 \rightarrow 2$ Air enters the compressor and undergoes isentropic (adiabatic) compression

$2 \rightarrow 3$ Fuel is injected under isobaric conditions and combustion takes place

$3 \rightarrow 4$ Exhaust gases in the turbine expand isentropically (adiabatically) and work is extracted to drive the compressor

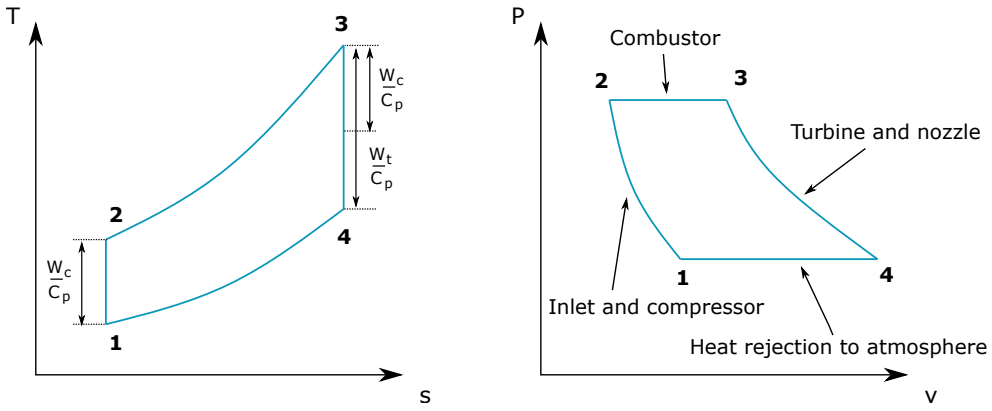

Figure 1.2: Idealized Brayton cycle

The efficiency η of the above cycle can be expressed in terms of the pressure ratio across the compressor so that

$$\eta = 1 - \frac{1}{(p_2/p_1)^{(\gamma-1)/\gamma}} \tag{1.1}$$

Increasing the efficiency can therefore be achieved by increasing the total pressure p_2 at the inlet of the combustion chamber through, for instance, a higher loading per stage. Increasing the loading, however, increases the risk of flow separation on the compressor blades and hence might facilitate compressor stall. Modern compressors therefore use complex 3D-optimised compressor blades to ensure that a sufficient stall margin is maintained [10].

Due to the steady improvements in engine performance, annual increments of efficiency gains are measured in points of a percent. This stresses that engineers are approaching the point at which the full potential of increasing efficiency through shape optimisation has been exploited. In other words, step changes in engine performance cannot be achieved by pure passive mechanical designs and optimisations. Therefore, concepts that involve the use of computer controlled systems to affect aerothermodynamic phenomena such as flow separation, heat transfer and alike are gaining attraction in scientific and industrial communities.

This is evident when looked at turbines as well. Both engine efficiency and power are increased at higher turbine entry temperatures (T_3 in Fig.1.2). However, the increase of the turbine entry temperature of commercial jet engines over the last decades began to plateau around the time of the new millennium [11]. This suggests, inter alia, that improved turbine thermal management with ever more optimised locations and shapes of cooling holes has diminishing returns. Here as well, new concepts using flow manipulation and control need to be developed. With respect to turbine thermal management, such new concepts might include, for instance, unsteady injection of the cooling flow or its modulation based on different requirements during take-off, cruise and landing.

The ability to actively control internal and external flows and its great potential for revolutionary advances in aerodynamic performance is further highlighted by the fact that three of NASA's major research projects, namely Breakthrough Vehicle Tech-

nology (BVT), Ultra-high Efficiency Engine Technology (UEET) and 21st Century Aircraft Technology (TCAT) highlight the importance of active flow control (AFC) for next generationn aircraft [12]. However, despite its great potential there are hardly any active flow control devices used in real-world aerospace applications. This underlines the difficulties associated with the design of active flow control systems [2]. The present thesis takes on that precise challenge and aims to tackle the flow control actuation challenge by investigating sound based fluidic actuators.

1.2 The Need for Unsteady Control - Thesis Objectives

The need for unsteady, rather than steady, control is based on the inherent characteristics of most flows. Many flow phenomena and flow-related losses, especially in aerospace applications, are unsteady in nature and hence emerge with a characteristic frequency or feature a time-dependent component. Generally speaking, this calls for an equally unsteady control strategy. Even flow phenomena that, considered globally, appear to be quasi-steady, e.g. flow separation over an aerofoil, are only steady in a time-averaged sense and hence can potentially be controlled more effectively if unsteady actuation is used [13, 14]. Although the time-dependent coherence of most flow phenomena, such as separation control, has long been known and acknowledged, it has never been exploited. The underlying problem here is the design philosophy itself: the assumption of steady-state flow [15]. This is mainly due to the Reynolds-averaged equations that have prevented the designer from taking the unsteadiness of the flow into account. This then implies that the use of unsteady control techniques could also lead to complete new design rules. It is hence not foreseeable what consequences active flow control systems might have on future aircraft.

Despite the obvious advantage of an unsteady control strategy for unsteady flow

phenomena, active control is also required when the location of the control input is fixed (e.g. engine frame) but the flow to be controlled is caused by moving or rotating entities (fan flutter control, tip leakage control or rotating stall control, just to name a few).

Knowing now that a potential route to unlock fuel burn improvements and efficiency gains lies in an unsteady control technique, the question arises how to achieve such an unsteady momentum addition into the flow? Finding a suitable technique

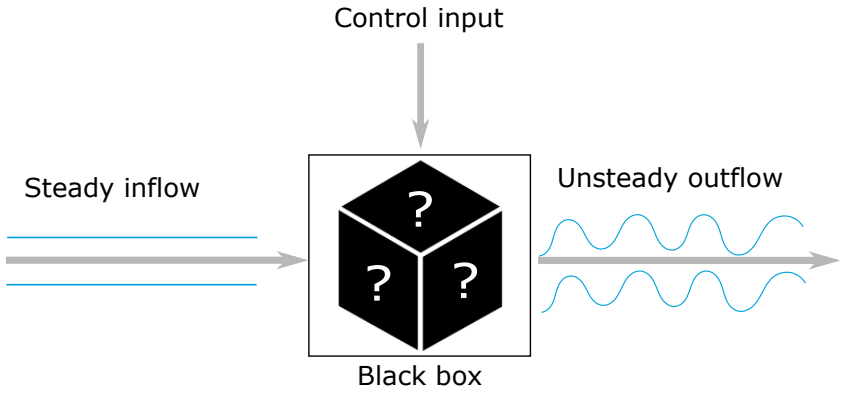

Figure 1.3: The main question: How to turn a steady inflow into an unsteady outflow?

that replaces the black box in Fig.1.3 is the main focus in active flow control research. A so-called fluidic device[1] with an active control input is here proposed as the main building block of an unsteady flow control system. Such devices were originally referred to as fluid amplifiers and introduced by the U.S. Army Harry Diamond Laboratories in the late 50s [16]. The working principle of a typical fluidic device is based on the Coandă effect, the tendency of a jet of fluid to be attached to an adjacent wall. If two walls are placed opposite to each other with the jet centerline as the symmetry line of the device geometry, the jet randomly attaches to one of the two walls. With an either passive or active control input the jet can then be switched to the opposing wall and back causing an oscillatory movement at the device outlet. Such devices

[1]Fluidic devices and their design as well as their working principle will be discussed in detail in the succeeding chapters

have experienced an upsurge in the last decade as laboratory-scale experiments have shown in abundance that both active and passive flow control techniques have the potential to unlock significant efficiency gains and fuel burn improvements. Passive oscillators have here received most of the attention because of their relatively simple and robust design. For a comprehensive review of such oscillators the reader is referred to Gregory et al [17]. Substantial contribution in terms of flow visualisation of the internal flow in passive oscillators was further done by Paschereit et al [18, 19, 20, 21] or Tesař et al [22]. With respect to an active driving mechanism the open literature has only little to offer. This will be highlighted in chapter 3. However, despite any advantages the drawbacks and limitations of most actuator technologies have hampered the implementation of flow control strategies into real-world applications. But instead of finding new alternative solutions, it seems that the scientific community has only focused on optimizing or redesigning passive fluidic oscillators. And although they have now been studied experimentally, numerically and analytically to a large extent and are hence very well understood, they are still rarely seen to have achieved commercial readiness. It is therefore of utmost importance to find a novel actuation mechanism that outperforms the current state of the art.

This thesis is inspired and spurred by both the challenges in actuator development and the potential efficiency gains for next generation aircraft. An active bistable fluidic device was believed to satisfy the strict requirements for aerospace applications and hence was chosen to be the subject of this research endeavour. The main objective of this thesis is therefore the development and detailed investigation of a novel actuation mechanism based on low-cost and low-power piezo buzzers. This is despite the fact that Gregory et al [23] abandoned Piezo buzzers as suitable actuators for fluidic devices due to their insufficient control authority. This conclusion will be shown to be not necessarily correct.

A second objective arises within this thesis which aims to shed some light onto the

characteristics of vortex development in a free shear layer. To be more specific, the dependency of the jet preferred mode on the shear layer mode and the huge variation regarding the preferred mode Strouhal number reported in the literature, both topics that have vexed scientists for decades, will be investigated in more detail.

1.3 Thesis Outline

Chapter 2 of this thesis is an extended chapter reviewing the state of the art of fluidic devices, flow control actuators and the basics in fundamental fluid mechanics with respect to shear layer instabilities. Chapter 3 goes on to outline the experimental and numerical procedures used in this study. Chapter 4 presents experimental results of an excited circular jet issuing into ambient air subject to different initial conditions. Although this is not directly linked to the fluidic device to be developed in this thesis, this study was performed to investiagte the fundamentals of the excitation of shear layer instabilities. It further tries to shed some light onto the duality of the two most important jet instabilities; The shear layer mode and the jet preferred mode. This is followed by a proof-of-concept study of an acoustically driven and actively controlled fluidic diverter in Chapter 5. Results are shown for low-frequency excitation and relatively low flow velocities. The device performance as well as the flow physics that govern the flow control mechanism are described by a combination of experiments and high-fidelity numerical simulations. The knowledge gained in Chapter 5 is then used to redesign, optimise and adapt both the device geometry and the input signal so that the new AFC device fulfills the requirements to be used in aerospace applications (Chapter 5). Finally, Chapter 7 concludes the thesis.

Published Articles (As of Dec. 2019)

- Mair, M., Bacic, M., & Ireland, P. (2019). On Dynamics of Acoustically Driven Bistable Fluidic Valves. Journal of Fluids Engineering, 141(6).

- Mair, M., & Bacic, M. (2019). Active Fluidic Switching at High Mach Numbers. In AIAA Aviation 2019 Forum (p. 3683).

- Mair, M., Turner, J., Bacic, M.,& Ireland, P. (2017). Switching Dynamics of a Fluid Diverter Valve Using Ultrasonic Excitation for Active Flow Control. In 47th AIAA Fluid Dynamics Conference (p. 4309).

- Mair, M., Chen, L. W., Turner, J., Bacic, M.,& Ireland, P. (2016). Experimental and Numerical Analysis of a Piezo Driven Fluidic Device for Active Flow Control. In 52nd AIAA/SAE/ASEE Joint Propulsion Conference (p. 4860).

Chapter 2

Literature Review

2.1 Introduction

A literature review on the topic of flow control is bound to be incomplete as it is pursued at present by more scientists and engineers than any other topic in fluid mechanic [24]. It is nonetheless believed that all relevant studies that are crucial to put this thesis into context and understand the grounds for this endeavour are presented in the following.

This chapter consists of four major parts. Fundamental aspects of coherent structures in free shear layers, flow instabilities and their control are discussed first. Specific terminology that is relevant for this thesis is explained where appropriate. This part shall be considered an overview and unavoidable introduction to shear layer instabilities as their understanding are a prerequisite to this thesis. Critical notes are made where appropriate but it shall be stressed at this point that the discussion of the numerical and experimental results presented through out this thesis will review the literature not only in more detail but also more critical. The first part is then followed by a brief survey of flow control actuators and their inherent limitations. The state of the art of fluidic devices, both passive and active, and their potential

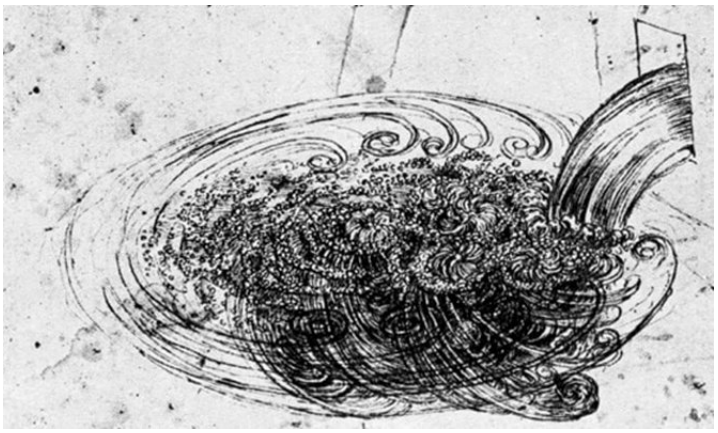

Figure 2.1: Schematic of a plane two-dimensional shear layer formed downstream of a splitter plate

use in aerospace applications is presented thereafter. This will highlight the gaps and shortcomings in previous research that this thesis intends to fill. The first three parts are not directly linked to each other and could therefore be discussed independently. However, this thesis combines all three topics in one since a fluidic device with a novel actuation methodology is developed which will further be shown to rely on flow instabilities. Finally, the last part outlines the structure of this thesis and summarizes again its objective.

2.2 Instability Waves and Fundamental Flow Control

2.2.1 Development of Coherent Structures

Fig.2.1 shows Leonardo da Vinci's sketch of water exiting from a square hole into a pool. The mixing region appears to be fairly chaotic but is dominated by large- and small-scale vortical structures. The structures maintain roughly the same size and further appear to be periodic in time. This is one of the oldest representations of what shall be called *coherent structures*. Here, the definition of a coherent structure is

adopted form Robinson [25] - a quasi-periodic repeating pattern of coherent motion in the flow. In this section only one particular type of coherent structure is considered, namely that which is formed within a free shear layer.

A free shear layer, also called mixing layer, is formed when two streams with different velocities merge together [26]. This is undoubtedly a fundamental component in basically all fluid engineering applications as well as in nature. Two types of shear layers are considered here that are relevant to this thesis. The first is a plane two-dimensional shear layer of the kind that is formed downstream of a splitter plate or trailing edge (Fig.2.2). This is a very generic shear layer with its characteristics being representative of most other shear layers as well. The second type of shear layer is that which is formed by a free jet exiting into an ambient and stationary fluid. For all other types of shear layers, such as those formed by complex three-dimensional atmospheric layer interaction, separated flows, cavity flows or wake flows the reader is referred to the open literature.

2.2.1.1 Free Shear Layers

The velocity distribution across a free shear layer can, in general, be described by a hyperbolic tangent velocity profile with a peak vorticity at its inflection point ($y = 0$ in Eq.2.1).

$$u(y) = 0.5 \cdot [1 + tanh(y)] \tag{2.1}$$

Such flows are unstable to disturbances of certain wavelengths [27, 28]. This means that the flow may be stable to disturbances below some threshold, while disturbances above that threshold grow [29]. The amplification of such disturbances is due to the Kelvin-Helmholtz instability [26] which can be found in all flows with a Reynolds number above a critical value that is close to zero [27]. Fig.2.2 shows a schematic of such a free shear layer formed downstream of a splitter plate.

With respect to the downstream development of a plane two-dimensional shear

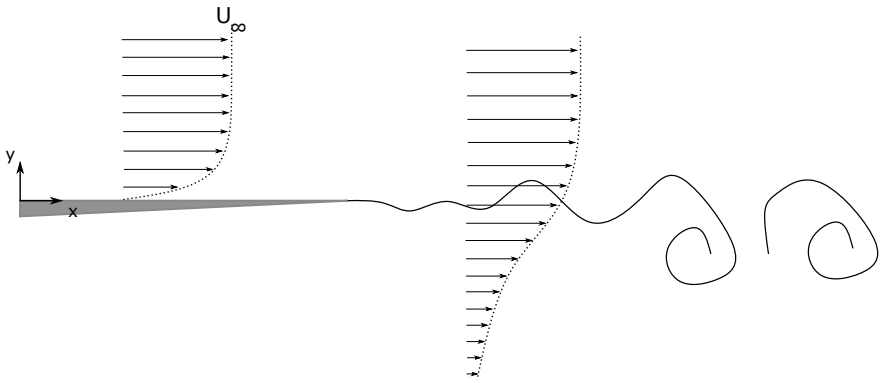

Figure 2.2: Schematic of a plane two-dimensional shear layer formed downstream of a splitter plate

layer one may distinguish four different regions. Immediately downstream of the trailing edge the perturbation level is very low and the mean shear layer characteristics, i.e. the velocity profile, change only little along x but more along the y coordinate [30]. This is also the region where the power spectral density exhibits a dominant frequency, the natural frequency f_n, whose amplitude grows exponentially with downstream distance. Deviation from exponential growth first occurs when the root-mean-square amplitude reaches $\approx 5\%$ of the free stream velocity [31, 32]. The velocity fluctuations eventually roll up into vortical structures when the maximum amplitude, e.g. 10% of u_∞, is reached [26, 29, 31]. The second region is then characterised by coherent structures that are formed at a frequency equal to the natural shear layer frequency f_n and convected downstream with the flow. The non-linear saturation of the primary instability is further accompanied by the emergence of subharmonic components. The third region starts where the subharmonic frequency has reached its saturation amplitude leading to the merging of neighbouring vortices. This leads to half the passage frequency and twice the spacing between two adjacent structures [26, 29, 33, 34]. Pairing events were first demonstrated in the 1960s by Wille [35] and Freymuth [33, 36]. Pairing was later found to be the major reason for the shear layer spreading [37]. Ho & Huang [30] further found in the early 80s that

the excitation of the *nth* subharmonic frequency leads to the merging of n vortices indicating that the generation of the subharmonic is the main driver of vortex merging . The last region is determined by the break down of the larger eddies into smaller eddies until they reach scales at which the dissipation of energy takes place [38].

Turbulent flows were long time considered to be random without any coherent structures[1] [41]. This is because the seemingly chaotic nature made it difficult for the scientists of the last century to find a proper description of turbulent motion that is not based on stochastic approaches [26]. This is despite the fact that large- and small-scale structures have already been observed to be coherent both in space and time by Leonardo da Vinci in the 1500s (Fig.2.1). The concept of orderly structures arose in the 1960s with the work of Liepmann [42] and Townsend [43] with the latter showing that coherent structures can also be inferred from statistical analysis [29]. This concept further attained increasing popularity with the pioneering work of Crow & Champagne [3] and Brown & Roshko [44] who found large-scale coherent structures even at high Reynolds numbers. The importance of coherent structures for the understanding of turbulence, entrainment and aerodynamic noise production became so profound that *"virtually every turbulence researcher [was] pursuing them in one form or another"* [45]. This brought forth a *new* concept that describes and analyses coherent motion in free shear layers in Fourier space rather than physical space as was done before. This is simply because instability waves, the primary source of coherent structures, are best described in the frequency domain.

Due to the then newly introduced description in Fourier space the quest to find an universal non-dimensional value for the natural shear frequency f_n had begun. The governing parameters that dictate the frequency of the shear layer roll-up were found

[1]One might infer from the name *coherent structure* that the formation of large-scale structures is spatially and temporarily fixed. However, each naturally occurring structure is, to some degree, subject to jitter in its formation, shape, size, orientation, convection velocity, mutual interaction and breakdown [39]. This jitter can be physically, and quantitatively, related to the intermittency of the outer region [40].

to be the momentum thickness θ as well as the average speed $u_{ave} = \frac{u_\infty}{2}$ [26, 30, 46, 47]. Hence, the non-dimensional shear layer roll-up frequency is defined as

$$St_\theta = \frac{f\theta}{u_{ave}} \tag{2.2}$$

with St being the Strouhal number. The first who tried to quantify the roll-up frequency was Michalke in the 1960s [48]. He assumed that the natural shear layer mode is also the most unstable mode. On the basis of this assumption, he used linear stability analysis to determine which superimposed perturbation on a hyperbolic-tangent velocity profile yields the maximum growth rate. The value he found was $St_\theta = 0.032$ [26, 28, 33, 49]. This value was later confirmed experimentally by Freymuth [36], Miksad [50] as well as Ho & Huang [30]. The problem here is that the wave with maximum growth rate is not necessarily the frequency of the natural shear layer roll-up.

2.2.1.2 Free Jets

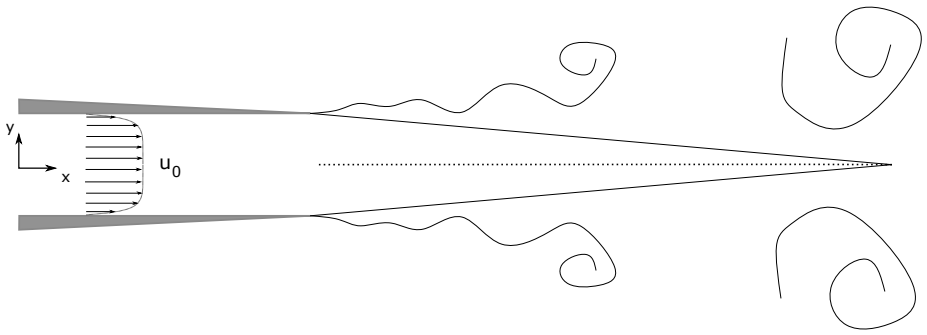

Figure 2.3: Schematic of a free jet with centreline velocity u_0. Cone represents the potential core region

For reasons of clarity Fig.2.4 shows the basic flow regimes of a free jet exiting from a circular nozzle. The initial, axisymmetric region is defined by a core of uniform velocity, the jet potential core. Its end x_{pc} is defined as the point where the jet

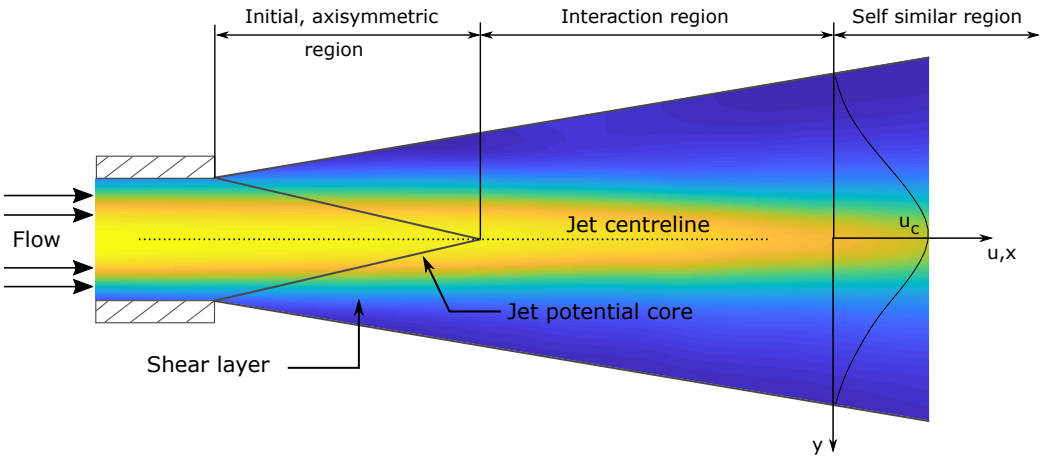

Figure 2.4: Schematic flow field and basic flow regimes of a circular jet

centreline velocity starts to decay. Hence, this is the point where the shear layers merge. Downstream of that the jet transitions through interactions of large and small scale vortical structures until it becomes fully developed in the self similar region [51]. The shear layer roll-up of a free jet[2] is similar, if not the same, to the roll-up of a two-dimensional free shear layer of the kind described above [26, 33, 46]. Hence, shear layer characteristics such as the Strouhal number of the natural shear layer frequency f_n obtained from experiments with free jets are valid for plane two-dimensional free shear layers as well and vice versa. Albeit unspoken, this is done, for instance, in the most recent review article about shear layer instabilities by Samimy et al [26]. The velocity used to make the frequency non-dimensional is then the centreline velocity u_0 [32, 39, 45]. The frequency of the most unstable mode, the frequency with maximum growth rate, thus becomes $St_\theta = 0.016$.

However, the natural shear layer roll-up frequency of a free jet was found to be at $St_\theta = 0.012$ in several independent studies by Zaman et al [39, 45, 52] and Rajagopalan & Ko [53]. Pfizenmaier [54] also reported that the natural roll-up frequency is in fact lower than the most unstable mode [39]. Hussain [45] further found

[2]Only circular jets are here considerd. The shear layer dynamics of non-circular jets are discussed separately.

that $St_\theta = 0.012$ corresponds to the frequency of maximum amplification whereas $St_\theta = 0.016$ to the frequency of maximum amplification rate. Hence, as was already indicated above, the most unstable mode does not correspond to the natural shear layer mode. It is rather the wave that attains the largest amplitude that causes the shear layer to roll up. Although Samimy et al [26] make references to those findings, they do not make the conclusion that the most unstable mode and the natural shear layer frequency are not the same. The dominant characteristics of the shear layer mode can be summarized as:

- The power spectrum of a natural free shear layer contains a most amplified frequency f_n causing the initial roll-up of vortical structures [26, 55, 37, 44]
- The location of the shear layer roll-up coincides with the non-linear saturation of f_n [26, 56, 30, 57]
- Subharmonic components of f_n which are generated during the growth of f_n provoke the downstream pairing of neighbouring vortices before the end of the potential core [26, 39, 50]

The shear layer of a circular jet, as sketched in Fig.2.3, spreads with downstream distance and eventually leads to a decrease in the centreline velocity u_0. This occurs when the mixing layer closes on itself at the jet centreline [26]. This location (the tip of the cone in Fig.2.3) is called the end of the potential core [29] and constitutes the main difference between the free shear layer of a plane two-dimensional flow and a free jet. The end of the potential core as well as the jet diameter D are important length scales that are related to another dominant instability in the flow [26, 58]. The associated frequency scales with D so that $St_D^p = \frac{f_p D}{u_0} \approx const$ and is called the *jet preferred mode*, the passage frequency of vortices at the end of the potential core [26, 33, 58, 59, 60, 61].The jet preferred mode Strouhal number is usually 0.3 but values reported in the open literature vary between 0.2 and 0.7 [33, 45, 61]. This

variation is often said to be due to random disturbances in different facilities and differences in initial conditions[3] [26, 33, 58, 59, 60, 61, 62] . The name *jet preferred mode* stems from the pioneering work of Crow & Champagne in the early 1970s [3]. They found that the jet response to acoustic excitation is maximum - in terms of fluctuation intensity - if $St_D = 0.3$. How it became the general accepted view that the jet preferred mode also corresponds to the frequency of passing vortices at the end of the potential core is not at all apparent for the present author. This, however, requires a more in depth discussion and so comes that an entire chapter of this thesis is dedicated to that topic alone. For the time being, though, we shall adopt the common point of view. Hence, the jet preferred mode and the initial shear layer instability are coupled by successive pairing events since the jet preferred mode is up to an order of magnitude smaller than the shear layer mode. In case no pairing takes place the momentum thickness has to increase sufficiently fast for $f_n\theta$ to approach f_pD [26].

For most of the last century the discussion of jet instabilities was mainly confined to axisymmetric modes, the jet preferred mode f_p and the shear layer mode f_n. The last two decades, however, brought forth a vast amount of experimental [58, 62, 63], theoretical [41, 64] and numerical studies [65, 66] as well as a combination of the three [67] that focus equally on helical modes. The existence and growth of such modes depends on the ratio of the jet diameter to the momentum thickness at the nozzle exit $\frac{D}{\theta}$ [26]. It further appears that the number of unstable helical modes increases as the shear layer thickness gets thinner [68]. It has also been shown through a modal decomposition of an experimental dataset that the axisymmetric mode dominates the dynamics only up to $x = 3D$ [69]. The helical mode $m = 2$ is further found to contain the most energy at the end of the potential core [70, 71]. The modal decomposition of

[3]If the passage frequency of vortices at the end of the potential core changes with initial conditions it seems somewhat odd to the present author that the jet preferred mode is determined by D. This topic will be discussed in more detail at a later stage of this thesis.

an experimental or numerical dataset in order to obtain physically important features of the flow field is gaining increasing popularity [72]. By doing so one hopes to obtain reduced order models that help in the understanding of basic turbulence, chemical mixing, noise generation and momentum transfer [64, 69]. A detailed review of helical modes and modal analysis can be found in [26] and [72], respectively. The topic surrounding different modes, especially the jet preferred mode, will be resumed and discussed in much more detail several times through out this thesis.

2.2.2 Excitation of Jet Instabilities

The excitation of intrinsic instabilities in jets is a substantial tool to not only deepen our basic understanding of shear-layer dynamics, but also to alter significantly the downstream development of the flow [33]. Crow & Champagne [3] were the first to show that an excitation frequency at the jet preferred mode ($St_D = 0.3$ and $\frac{u'}{u_0} = 2\%$) leads to the highest possible amplitude under non-linear saturation forming large coherent structures that do not undergo pairing. They further showed that the volume of entrained fluid at $x = 4D$ has increased by over 30% with respect to the unforced case. However, the Strouhal number preference was lost at sufficiently low amplitudes of forcing. The same Strouhal number value of 0.3 has also been confirmed by Hussain & Zaman [39, 73] in several jets with a variety of initial conditions, although they found a slight dependency on Re. More recently, Samimy et al [59, 74, 75, 76] developed a localized arc filament plasma actuator and demonstrated experimentally as well as numerically that also high Reynolds number super sonic jets show a Strouhal number preference around $St_D = 0.3$. They also found that the breakdown and interaction of coherent structures are the dominant source of noise. However, using linear frequency response analysis Garnaud et al [65] found that the jet preferred mode amounts to $St_D = 0.45$ for $Re = 1000$. This is somewhat consistent with the findings of Hussain and Zaman [73] who showed that the preferred

mode Strouhal number increases at lower Re. Nonetheless, in contrast to the study of Garnaud et al [65], Gohil et al [77] found that the jet preferred mode is indeed at ≈ 0.3 for the same Re using Direct Numerical Simulation (DNS). This highlights that the value of the preferred mode Strouhal number as well as its universality and dependency on the flow conditions is highly disputed in the literature [61]. Petersen & Samet [78], for instance, show that the preferred mode is a natural shear layer instability that scales with θ whereas Zaman & Hussain [39, 79] conclude that the jet preferred mode remains the same irrespective of the boundary layer being laminar or turbulent . In general, however, the two dominant characteristics of the jet preferred mode were identified in numerous studies and can be summarized as:

- Roll-up of large coherent structures and the absence of any downstream pairing event [3, 59, 62, 73, 80]
- Maximum increase in entrainment causing the end of the jet potential core to move upstream [3, 59, 62, 73, 80]

The pioneering work of Crow & Champagne in the early 1970ies triggered an avalanche of studies that investigated the spatio-temporal evolution of vortical structures in circular and non-circular as well as forced and unforced jets. In the vast majority of these studies the jet preferred mode is considered to be the passage frequency of vortices at the end of the potential core. For the present author it is not apparent how, why and when this became the common point of view. Indeed, the frequency of the jet preferred mode, first determined by Crow & Champagne [3] to be at $St_D = 0.3$, is below the shear layer mode and therefore might approach one of its subharmonics at the end of the potential core. It is, however, still inconclusive to equate those two frequencies. This is also because the passage frequency of vortices at the end of the potential core in the experiments of Crow & Champagne amounts to $St_D = 0.44$ [3, 78], a rarely cited finding. Moreover, the initial definition

of the preferred mode required artificial forcing of the jet. This makes it somewhat arbitrary that many studies claim to have identified the jet preferred mode by, for example, simply placing a hotwire inside an unforced jet. The huge scatter regarding the value of the jet preferred mode Strouhal number might therefore rather be a huge scatter of the subharmonic shear layer mode being based on the wrong length-scale. A convincing argument supporting that statement is seen in Fig.2.5. Studies that have identified the jet preferred mode by the jet response to some sort of artificial forcing correspond to references A ([3, 81, 59, 82, 75, 83]). The value of the preferred mode Strouhal number ranges from 0.28 to 0.35. Studies that have identified the jet preferred mode without any means of forcing correspond to references B ([84, 85, 86, 87, 88, 89, 90, 91]). The value of the preferred mode Strouhal number ranges here from 0.24 to 0.64. The graph contains all references from Gutmark & Ho [61] who try to explain the variation of the reported preferred mode Strouhal numbers by spatially coherent disturbances in individual facilities. The graph also contains additional studies of the last two decades to reinforce the present hypothesis. Note that the studies from Kibens [34] and Bechert & Pfitzenmaier [92] presented in the study of Gutmark & Ho [61] are not considered since they only measure the radiated noise spectrum. Spectral peaks in the acoustic field do not necessarily indicate the jet preferred mode since pairing of neighbouring vortices is the main source of sound production in a jet and there is no subharmonic component for the excitaion of the jet preferred mode [93, 94, 34].

Moreover, it is more plausible that natural disturbances in individual facilities affect the shear layer mode and hence its subharmonics rather than the jet preferred mode. This ought to say that random disturbances as well as turbulence intensity - or rather the interaction of both - might as well feature a spectral peak at f^* which is in the vicinity of the shear layer mode. If the amplitude of f^* is similar to the initial instability under *'clean'* conditions it is reasonable to assume that the shear

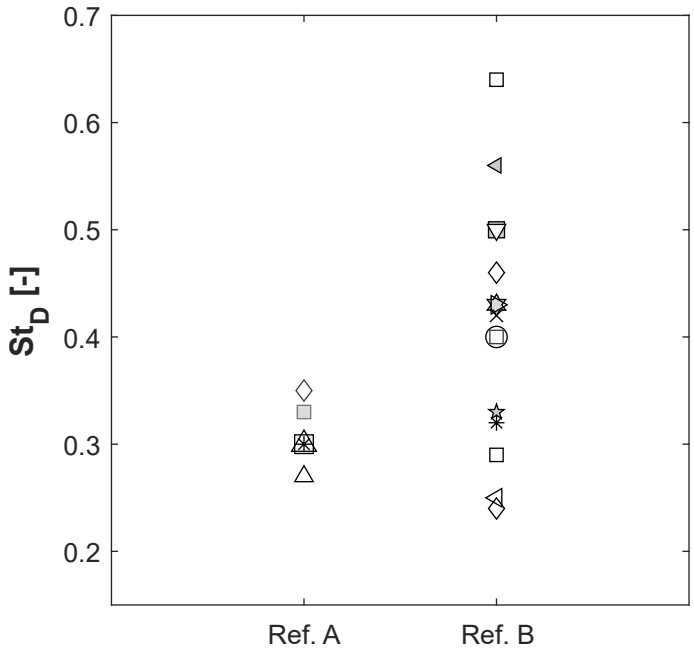

Figure 2.5: Reported values for the jet preferred mode. References A correspond to studies that use artificial forcing. References B correspond to studies that determine the jet preferred mode by means of the unforced jet characteristics

layer mode locks on to f^* despite no change in the initial conditions. Note that the turbulent intensity is often around $1-3\%$ and therefore in the same order of magnitude as the forcing level.

One can also argue that, in case the jet preferred mode was the subharmonic at the end of the potential core, the excitation at that frequency should provoke pairing rather then discourage it completely. The open literature, however, does not provide any explanation why the excitation of the jet preferred mode causes large coherent vortical structures that do not undergo pairing. Having said that, the author of this thesis assumes that the required forcing amplitude to identify the jet preferred mode has to exceed the amplitude of the initial shear layer instability before it saturates. The natural roll-up as well as its possible downstream pairing events would therefore be suppressed. The fact that the jet preferred mode requires higher forcing amplitudes is also confirmed by Samimy et al [59] and Crow & Champagne [3].

Apart from mixing enhancements using the excitation of inherent flow instabilities, it was demonstrated by Zaman [52, 95] that turbulence and broadband noise can also be suppressed if excited at $St_\theta = 0.017$. The frequency corresponds to the wave with maximum growth rate which, when amplified, causes an early roll-up of coherent structures. The excitation of the initial shear layer instability, in contrast, leads to organized large-scale structures that undergo successive pairing. The acoustic spectra in the far field exhibits peaks at frequencies that corresponds to the subharmonics of the excitation frequency indicating that the merging of neighbouring vortices are the prime source of noise production [34]. Zaman and Hussain [39, 79] also concluded that an excitation frequency equal to the roll-up frequency promotes pairing and, what's more, results in a centreline fluctuation intensity much higher than that at the jet preferred mode. This was not observed by Crow & Champagne [3] since their experimental set-up did not allow excitation frequencies that high ($f_n > f_p$).

However, the most striking effect of excitation is produced by an appropriate combination of controlled axial and circumferential excitation [96]. Reynolds et al [97] demonstrated experimentally that dual-mode excitation results in bifurcating (splitting of the jet into two or more jets) and blooming (spreading) of the jet. For irrational values of the frequency ratio an *amazing shower of vortex rings* can be obtained (Fig.2.6). This was also demonstrated numerically by Gohil et al [98] who showed that the spreading angle can get as high as 180°.

On a personal note: It appears to me that it somehow became best practice to use the diameter D to make any measured peak in the power spectral density of a jet non-dimensional and thereby neglect the effect of the momentum thickness on the evolution of vortical structures especially in the near field of a jet. Wu & Huerre [99], for instance, quantify the frequencies of radiated sound waves of a subsonic circular jet and report numbers up to $St_D = 4$ near the nozzle. Davitian et al [100] state that St_D is based on the frequency of the initial fundamental instability and show an

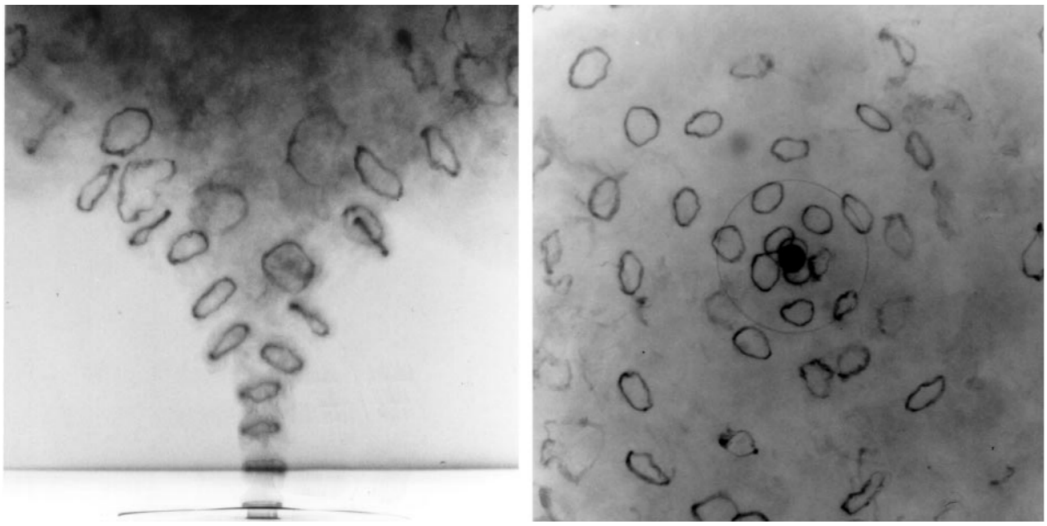

Figure 2.6: Side and axial views of a blooming water jet at $Re = 4300$

upstream shear layer velocity spectra with a peak at $St_D = 0.8$. *Gudmundsson and Colonius [41] use a microphone array to find shear layer instabilities close to the nozzle exit at* $x/D = 0.5$ *but nonetheless use* D *to make the measured frequency non-dimensional. Jung et al [69] also use the diameter* D *to find the dominant Strouhal number of a turbulent axisymmetric jet along* $x/D = 2-6$ *using a 138 hot-wire probe. Han & Goldstein [101] also specify the frequency of dominant fluctuation along the downstream distance using* D. *Using acoustic excitation they further observe strong vortex pairing at* $St_D = 0.9$ *which, to me, might as well indicate an excitation of the shear layer roll-up frequency at* $St_\theta = 0.012$ *[39]. More over, for a jet in cross flow with a velocity ratio of* $R = 6$ *Narayanan et al [102] determine the dominant vortical structures not only based on* D *but also on the jet exit velocity* u_0 *despite the fact that Michalke [28, 49] as well as Ho & Huang [30] found that the most probable passage frequency scales with the initial momentum thickness of the jet boundary layer and the average velocity* u_{ave} *between two streams. The values for* St_D *obtained by Narayanan et al [102] are therefore disproportionately low (*$St_D = 0.004$ *to* 0.22*). They further found that excitation at* $St_D = 0.2$*, which is twice the frequency of what they call 'the preferred mode', causes the maximum enhancement in mixing between*

the two fluids. Similar to what was said about the study of Han & Goldstein [101], the Strouhal number value that obtains the maximum response in terms of mixing could also rather indicate the excitation of the shear layer mode ($St_\theta = 0.012$) [30]. It thus seems that many studies do not take the momentum thickness into account when the frequency of passing vortices is considered. If the non-dimensional parameter is based on the wrong length scale it becomes impractical, if not impossible, to compare the results of different independent studies. Furthermore, it appears that the name preferred mode has been used quite inflationary over the past few years. This ought to say that the original definition by Crow & Champagne is often neglected and that some researchers, such as Gohil et al [103], designate any mode that dominates somewhere in the flow field as the preferred mode. Note here that the original definition is that the jet preferred mode corresponds to the excitation frequency f_p of the axial perturbation that produces the largest total amplification [3, 104].

2.2.3 Circular and Non-circular Jets

The nozzle shape plays a major role in the downstream development of a jet [105, 106, 107]. A change in the curvature radius along the perimeter of the nozzle orifice (corners and major axis sections of elliptic jets) leads to a variation in the momentum thickness which, in turn, causes significant differences in the evolution of vortical structures [108, 109]. Vortex rings with different size and convection speed then interact strongly with each other and result in self-deformation [110]. As a consequence, the departure of nozzle-axisymmetry leads to a faster decay of the centreline velocity and a higher fluctuation intensity indicating an increased overall entrainment rate for non-circular jets [108]. This is, inter alia, the reason why non-circular jets have a higher significance for practical applications. Those include improved large- and small-scale mixing in low- and high-speed flows, and enhanced combustor performance, by improving combustion efficiency, reducing combustion instabilities and

undesired emissions. Additional applications include noise suppression, heat transfer, and thrust vector control [107, 111]. Tam [112] further observed that the interaction of vortex rings rounds off the corners of the jet and hence assists the jet flow to evolve into a more circular cross-section. The change in the cross-sectional shape of the jet eventually leads to a phenomenon called *axis-switching*[4] [113].

Although the departure from two-dimensional behaviour is inversely proportional to the aspect ratio AR [105], the instability characteristics of a jet with $AR = 4$ do not show significant variations along most of its span and even downstream up to $14h$ [114]. Hence, the shear layer roll-up along the long side of a rectangular jet can be considered effectively two-dimensional. Therefore, qualitative and also quantitative results gained from circular jets are, in general, applicable to rectangular jets as well. This is supported by the results of Shih et al [114] who found that the non-dimensional shear layer roll-up frequency of the long side of a rectangular jet with $AR = 4$ remains constant at $St_\theta = 0.012$ within the entire velocity range tested ($10-100\frac{m}{s}$). Moreover, Hussain and Husain [115] studied incompressible elliptic jets of different aspect ratios and initial conditions and found that $St_\theta = 0.012$ is also valid for the shear layer roll-up of elliptical jets.

With respect to the *preferred mode* of a circular jet it shall, for now, only be said that there exists an equal counterpart for rectangular jets. Further discussions regarding the length scale with which the preferred mode frequency is made non-dimensional (St_h or $St_{D_{eq}}$) and what flow characteristics it evokes are made in Chapter 4.

[4]Spreading in the minor-axis plane (the plane containing the minor axis of the nozzle) is much greater than that in the major-axis plane. Therefore, some distance downstream from the nozzle the cross-section of the jet eventually switches its orientation [109].

2.2.4 Effect of Secondary Nozzle Flows

Apart from the downstream shape of the jet itself, the nozzle shape and associated upstream duct shape also excercises a secondary effect on the flow. These secondary flow phenomena can be divided into stress-induced and skew-induced flows. A lateral deflection or skewing of a boundary layer as is the case for a 3D shaped duct, e.g. turbomachine blade passage, causes an embedded-vortex flow [116]. The generation of such vortices is an inviscid process and can be attenuated by viscous or turbulent stresses, though rather slowly [117]. Since the nozzle shape in this study has no curvature skew-induced vortex flows are not further considered. The curvature of the upstream nozzle inlet is considered to be neglibile as the nozzle orifice is located up to 15 nozzle heights downstream of it.

Stress-induced counter-rotating pairs of vortices can be found in each corners of a rectangular turbulent nozzle flow. These vortices rotate about a streamwise axis, are generated by Reynolds stresses and are generally much weaker than skew-induced vortices [116]. These vortices are further responsible for the axis switching of rectangular jets far downstream of the nozzle orifice. Given that their effect is only marginal in the near field of a jet, stress-induced vorticity inside a rectangular nozzle is not considered either in this study.

2.3 Flow Control Actuators

Active flow control implies energy addition and interaction with the flow by means of an actuator. Depending on the flow condition and the desired flow manipulation such actuators can vary between moving object, fluidic or plasma actuation mechanisms. In the following a brief overview of existing actuator technologies is presented.

2.3.1 Actuator Types

2.3.1.1 Moving Object

Moving object actuators can take various forms, although the vast majority consists of piezoelectric flaps and electro active dimples [2]. A piezoelectric flap is a flat beam that is fixed at one end and cantilevered on the other (see Fig.2.7). The piezoelectric effect causes a displacement of the free end if AC voltage is applied [23]. The oscillatory motion of the flap can interact directly with the flow so to introduce spanwise or streamwise vortical disturbances into the flow [118]. The displacement of the free-tip is typically in the order of $1\,mm$ and depends mainly on the flap size, excitation frequency an power input. Seifert et al [119], for instance, were able to achieve a peak-to-peak displacement of $13\,mm$ using a $35\,mm$ by $60\,mm$ plate, an excitation frequency of $170\,Hz$ and $0.65\,W$ per actuator. They further successfully demonstrated the effectiveness of piezoelectric flaps for flow separation control. Other applications include the control of turbulent boundary layer streaks [120], free shear flows [121], and a fluidic oscillator [23]. In all cases, the piezoelectric transducer creates a geometrical or fluid dynamic asymmetry in a receptive location in the flowfield [17].

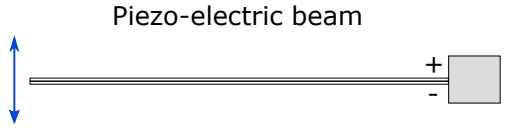

Figure 2.7: Schematic of a Piezo-electric beam

Active dimples produce unsteady surface depressions that interact with the flow and modify the near-wall vorticity [2, 122]. They consist of an elastomer sandwiched between compliant electrodes and operate upon application of an electric field (Fig.2.8) [123]. The electric field produces a mechanical pressure in the electro-active

polymer since oppositely charged electrodes cause a mechanical compression in the thickness direction whilst the repulsion of like charges on the same electrode causes the surface to expand [1]. Since lateral strain is constrained due to the fixed electrodes, the elastomer buckles in the vertical direction and hence produces out-of-plane motion. According to Dearing et al [1] the ultimate goal is to integrate such dimples, along with shear-stress and pressure sensors as well as a distributed control system, into a flexible 'smart skin' which could be incorporated into an airframe structure. A summary of the requirements to effectively reduce drag including concepts of open- and closed-loop control are given by Morrison [124].

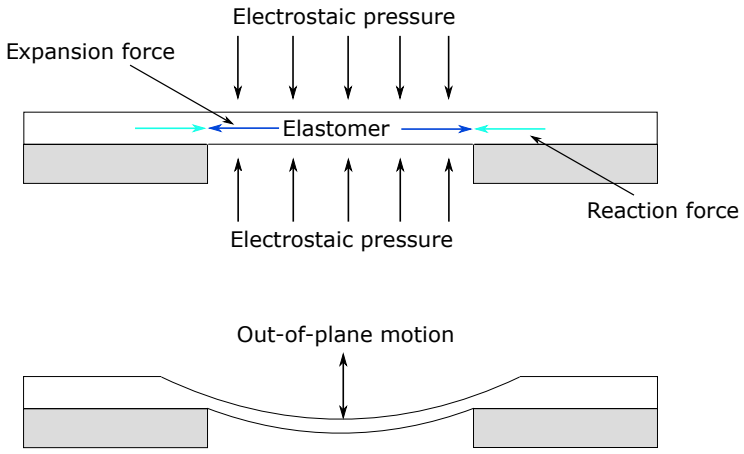

Figure 2.8: Schematic of a Electro-active polymer (EAP) 'dimple' [1]

2.3.1.2 Fluidic

Purely fluidic actuators can be further divided into zero-net mass flux (ZNMF) or synthetic jet actuators and those with a non-zero net mass flux that require an external fluid source.

A synthetic jet uses a vibrating diaphragm to drive oscillatory flow through a small orifice or slot [125]. The piezoelectric diaphragm is located inside a cavity and fixed at its perimeter. When a voltage is applied, the diaphragm bends due to the reverse

piezoelectric effect and displaces a fluid volume [2]. As the membrane moves down, the outside fluid is ingested into the cavity. When the membrane moves up, the fluid is discharged through the slot. The ejected fluid separates at the sharp edges of the orifice and forms a shear layer that rolls up to form a vortex ring. This vortex ring travells away from the orifice by its own self-induced velocity and therefore contains net momentum [126]. By the time the membrane moves down again, the vortex ring is sufficiently far away from the orifice and hence unaffected by the entrained fluid. When operated periodically a vortical column is generated and a momentum flux is induced. Although synthetic jets have zero net mass flux in nature, they do impart net momentum to the ambient fluid and thus can be used to modify a given flow field [127]. A schematic of such an actuator is shown in Fig.2.9. An extensive review of synthetic jet actuators including alternative designs with, for instance, electromagnetically driven pistons was done by Glezer & Amitay [126]. The properties of synthetic jet actuators have been investigated theoretically [125], experimentally [128, 129, 130] and numerically [131, 132, 133]. More recent developments are summarized in [134]. Potential applications for a synthetic jet include jet vectoring and enhanced entrainment [135], heat transfer enhancement [136], modification of aerodynamic lift and drag [137, 138] or flow separation control [6, 139, 140]. The size of ZNMF devices can vary substantially depending on the application and the desired resonant frequency of the cavity. Sawant et al [141], for instance, have recently developed a synthetic jet actuator with a cavity height of only $1.1\,mm$. Potential benefits of such micro-actuators include lower weight, lower power consumption, and arrays of devices with individual addressability [141]. However, the fabrication of such micro-actuators poses a challenge itself. Silicon micromachining can here be used for batch-fabricating the top and bottom dies of the chip-scale ZNMF actuator as was done by Sawant et al [141].

Other actuators that expel periodic momentum from one or more orifices with a non-zero mass flux are pulsed jets, powered resonance tubes, combustion actuators

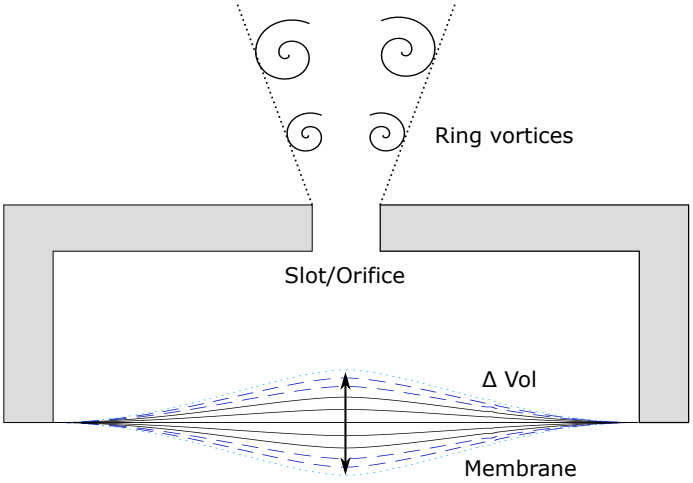

Figure 2.9: Schematic of a piezoelectric synthetic jet actuator (ZNMF) [2]

and fluidic amplifiers. However, unlike their ZNMF counterparts, they do require an external fluid source [2].

Pulsed jets can be generated via a fast acting solenoid valve or a high-speed rotating siren [142, 143]. A solenoid valve simply opens or closes a fluid path and can therefore not only adjust the pulsing frequency but also the duty cycle. If a siren is used, only the frequency can be adjusted via its rotational speed. Pulsed jets have a substantial advantage in comparison to steady jets [2]. This is mainly due to the fact the basically all primary and secondary flow phenomena, such as flow separation, are time dependent in nature [15]. An effective control strategy thus requires some degree of unsteadiness. Hence, many studies include a spectral analysis of the underlying control mechanism so to find the point of best performance. Pulsed jets have been used successfully for various flow control applications. Garnier [144], for instance, achieved reattachment of separated flow in an S-shaped inlet duct. He also showed that pulsed jets can achieve equivalent performance at half the mass flow rate compared to continuous jets if the pulsing frequency is higher than the natural frequency present in the separated zone of the uncontrolled flow. Furthermore, Bons et al [142] showed that pulsed jets are highly effective in controlling laminar boundary

layer separation on a low pressure turbine blade.

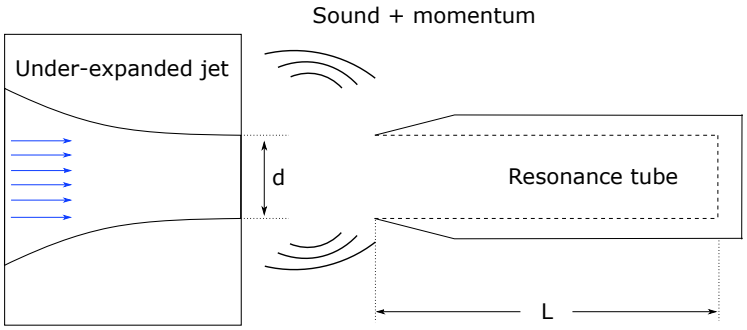

Figure 2.10: Schematic of a powered resonance tube [2]

Powered resonance tubes, or Hartmann tubes, consist of an underexpanded jet aimed at a cylindrical resonator tube open at one end and closed at the other. The periodic flow in and out of the resonator tube, and its interaction with the oncoming jet produces acoustic tones up to a frequency of $12\,kHz$ and amplitudes as high as $150\,dB$ [145]. A very detailed description of the working principle of powered resonance tubes including potential applications is given by Kastner & Samimy [146] and Raman & Srinivasan [147]. They are especially interesting for supersonic shear flow applications due to their very high perturbation levels. However, it appears that their high level of complexity has hampered the implementation in real world applications, even on a laboratory scale. Most studies regarding powered resonance tubes have so far only been confined to their own development such as those by Raman et al [148], Khanafseh & Raman [149] or Kastner & Samimy [146].

Combustion actuators exploit the chemical energy of a fuel/oxidizer mixture which is ignited within a miniature combustion chamber. A high-pressure pulse is created and a momentary high-momentum jet of exhaust products is expelled through an orifice [150]. The entire combustion process is complete within several milliseconds

and the cycle starts anew with fresh fuel/oxidizer mixture entering the chamber while displacing the remaining combustion products [151]. Combustion actuators are capable of reaching supersonic velocities at the jet orifice and have thus a high potential for high speed flow applications. Brzozowksi et al [150] investigated the effect of combustion actuators for transient separation control on an airfoil at high Reynolds numbers but achieved only limited success.

2.3.1.3 Plasma

There are two major types of plasma actuators: namely, single dielectric barrier discharge (SDBD) actuators and spark actuators. The former have gained increasing popularity within the last two decades, probably because of their relative simplicity and ease of assembly. They consist of an asymmetric pair of electrodes separated by a dielectric material [2]. An example configuration is shown in Fig.2.11. Upon the application of a high enough voltage the air over the covered electrode starts to weakly ionize [152]. The ionized air generates a body-force vector field that acts

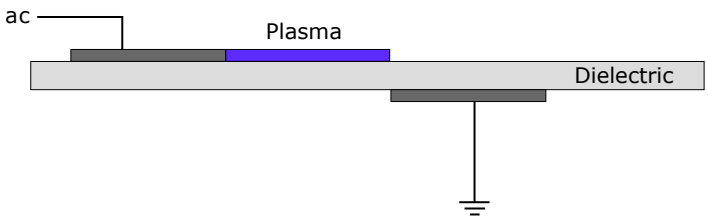

Figure 2.11: Schematic of a free jet with centreline velocity u_0. Cone represents the potential core region

on the momentum of the external flow [153]. The maximum velocities that have been obtained experimentally for optimised designs amount to approximately $12\frac{m}{s}$

[154]. The theoretical maximum induced velocity was calculated by Likhanskii et al [155] to be around $35\frac{m}{s}$ which reflects well upon their inherent limitations. However, despite those obvious limitations there is a wealth of studies regarding the potential use of SDBD actuators in aerospace applications. Although many of them report some degree of success with respect to an improved performance, the external flow conditions hardly reflect the conditions in the real world. Thomas et al [156] obtained remarkable results for flow control around a bluff body but mean free stream velocities were on the order of $\approx 4\,\frac{m}{s}$. Corke et al [157] used SDBD actautors for controlling flow separation over an airfoil and achieved an increase in the maximum angle of attack by 7°. The free stream velocity was here also relatively low and did not exceed $21\,\frac{m}{s}$. Goeksel et al [158] also achieved dramatic separation delays over an airfoil but free stream velocities did not even exceed $11\,\frac{m}{s}$. Wall et al [159] also obtained good results for controlling flow separation over a low-pressure turbine blade. However, the free stream velocity was here kept at a very low level as well ($u_\infty = 1.8\,\frac{m}{s}$).

An alternative to SDBD are the so called localized arc-filament plasma actuators (LAFPA) introduced by Samimy et al [74]. A rapid discharge between two electrodes promotes a sudden gas heating producing significant local pressure perturbations with independent control of the frequency and phase. Samimy et al [59, 160] have demonstrated the capability to excite strongly amplified instabilities in a $\mathrm{Mn} = 1.3$ jet with such arc-filament actuators. Kleinman et al [161] then implemented a numerical plasma model to investigate the coupling between the plasma sparks and the vortical jet shear layer turbulence downstream of the nozzle. The results were shown to match the temperature and near-field pressure measured in the experiments by Samimy et al [59]. Furthermore it was highlighted that the shear layer response to excitation is mainly due to the pressure perturbations by the plasma. If the plasma is discharged inside a cavity with one or more orifices the heat and pressure rise can cause a pulsed-plasma synthetic or spark jet [162, 163]. The principle is similar to combustion-driven

synthetic jet actuators but do not require additional oxidizer and fuel supply. A single cycle of spark jet operation consists of three different stages: energy deposition, discharge and recovery [164]. During the recovery process the cavity gets filled with surrounding fluid so that enough mass is available for the next discharge. The time needed for each refilling process clearly depends on both the cavity size and the amount of energy deposited and therefore limits the actuator bandwidth. The device designed by Narayanaswamy et al. [162] generates peak velocities of 250 m/s at frequencies up to 5 kHz.

2.3.2 Requirements, Drawbacks and Limitations

The desired characteristics of an ideal flow control actuator include low power consumption, fast time response, reliability, low cost, low mass and ease of manufacturing. The actuator should preferably be fully electronic with no moving parts and, what's more, be capable of introducing a significant disturbance into the flow [165]. It should also withstand harsh environments, e.g. high temperatures and pressures, offer sufficient control authority over a wide range of flow conditions (high bandwidth) and offer the possibility to be controlled in closed-loop. Finding an actuator that fulfils all of the above requirements is an elusive goal, though, not impossible. Nevertheless, the difficulties that actuators have to overcome to be used in aerospace applications is also emphasised by the small number of instances in which active flow control has successfully transitioned from a laboratory prototype to commercial readiness [2].

Moving object actuators, by definition, feature at least one moving part and hence are more prone to mechanical damage than their no-moving counterparts. In addition, most control mechanism require that the actuator is driven at its natural frequency, which again increases the probability of mechanical failure [165]. With respect to active dimples it is further important to note that a smart 'skin' (as proposed by Dearing et al [1]) requires a number of dimples in the thousands or more since they

are $10 - 1000\,\mu m$ in size. With the advancement of actuator technology such electro-active polymer dimples have nonetheless the potential to revolutionize the design of next-generation aircraft.

ZNMF actuators have the main disadvantage of not achieving the required perturbation level to be used for high speed flow control. They typically achieve a maximum velocity below approximately $100\,\frac{m}{s}$ [2]. Furthermore, they must be operated at or near their resonance frequency which, as already mentioned, can lead to mechanical failure [2, 166].

Pulsed jets, as opposed to ZNMF actuators, require an external fluid source [167]. And although there is no moving part interacting directly with the flow there are moving parts involved to generate the pulsed jet itself. Hence, mechanical failure constitutes a major disadvantage once again. It is further not possible to phase lock a pulsed jet (if driven by a siren or rotating valve) to the flow phenomena in question. This prevents pulsed jets to be used for the control of, for instance, turbine tip leakage or compressor stall.

Combustion actuators have the obvious drawback of requiring both fuel and oxidizer [168]. Requirements on power consumption and cost might therefore not be met. The time it takes to reinitiate the combustion cycle further limits the bandwidth in the frequency domain. If operated in a resonant mode (as proposed by Crittenden et al [151]) mechanical failure might pose a problem, too.

There are numerous types of fluidic devices with different geometries, actuation methodology or working principle. Hence it is not possible to specify any advantages or disadvantages that apply equally for all devices. Drawbacks and limitations will thus be considered separately in Sec.2.4.

SDBD actuators fulfil basically all requirements that were especified at the beginning; apart from sufficient control authority, as they are heavily limited by their relatively low maximum induced velocity ($\approx 35\frac{m}{s}$)[155]. They might be a good can-

didate for flow control applications at low main flow velocities but otherwise feature insuperable limitations.

LAFPA and spark jet actuators have a high control authority but, at the same time, require a supply power in the order of $\approx 50\,W$ with break down voltages of several kV [74]. What's more is that it becomes more difficult to spark the plasma as the ambient pressure increases [169]. This might lower the required power in low pressure environments but, conversely, limits the use of plasma spark actuators in, for instance, a high-pressure compressor or turbine stage.

2.4 Fluidic Devices

The name *fluidics* combines the two words *fluid* and *logic* indicating that the original idea was to develop a fluid element that performs logic output states similiar to those of a digital computer [170]. Those states are either 'on' or 'off', '1' or '0'. This mentality can be traced back to the fact that the time in which fluidic devices experienced their first upsurge falls within the era of the development of early personal computers. Much work was therfore done that aimed to develop logic control circuits consisting of possible fluid elements [171]. Fluidic devices became so popular that there was a tendency *to use fluidics in anything and everything, without giving adequate attention to whether it offered any true advantages over existing technologies* [172]. After they have been heavily overemphasized in their infancy, they have experienced a renaissance in the last decade or so. This becomes apparent by the vast amount of studies regarding fluidic oscillators published in recent years.

2.4.1 Coandă Effect

The Coandă effect, named after Henri Coandă, is the tendency of a jet of fluid to be attached to an adjacent wall [173]. If a jet flows freely out of a nozzle, the shear

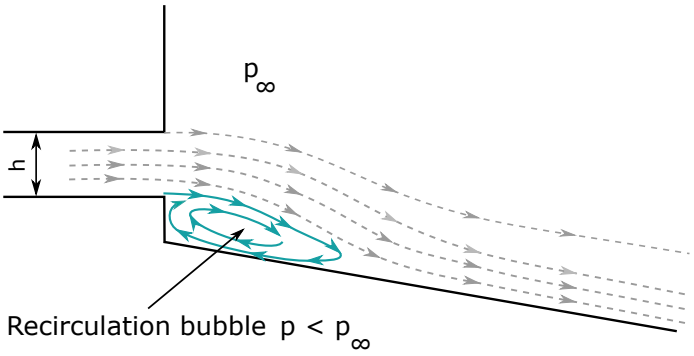

Figure 2.12: Schematic of the Coandă effect

layer entrains surrounding fluid into the spreading jet. If a wall is placed on one side, the entrainment is restricted and hence results in an one-sided decrease in pressure. The resulting pressure gradient across the jet causes it to bend towards the adjacent wall. This restricts the entrainment even further and bends the jet until it is fully attached. Ultimately, a recirculation bubble is formed which maintains the attachment (Fig.2.12) [174, 172]. If a second wall is placed on the other side of the jet, the attachment occurs in a purely random manner, though, remains stable. The randomness is due to small imbalances in the flow and hence the entrainment on either side of the jet.

2.4.2 Characteristics and Basic Geometric Parameters

Throughout the thesis, fluidic devices are divided into two kinds. Those that are bistable and require an active control mechanism to generate an oscillating outflow and those which do so without any external interference (passive). The former are called fluidic switching devices whereas the latter are usually referred to as oscillators or fluidic amplifiers.

A schematic of a generic bistable fluidic device is shown in Fig.2.13. It consists of an inlet plenum followed by a nozzle, an interaction region, at least two control ports

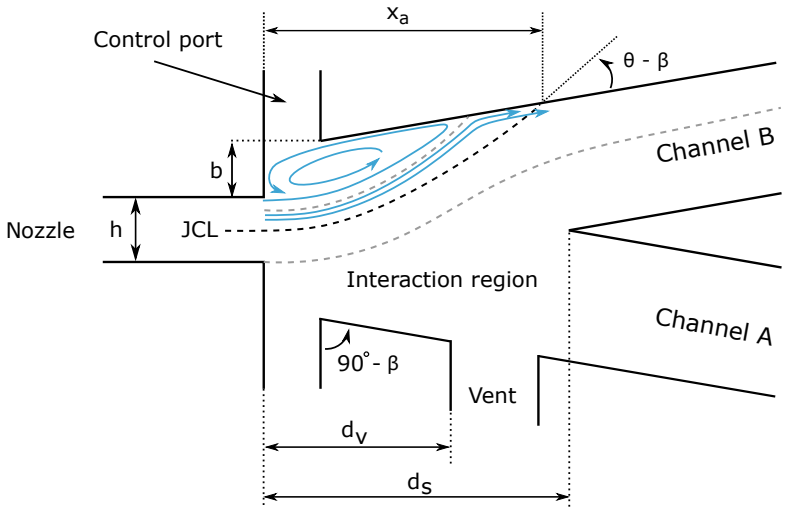

Figure 2.13: Basic geometric parameters of a bistable fluidic device. Vent is only shown on one side.

as well as two outlet channels separated by a splitter.[5] The flow enters the interaction region through the nozzle and adheres to one of the two attachment walls A or B by means of the Coandă effect. The pressure in the separation bubble, also called recirculation bubble, is constant and the centreline of the jet can be aproximated as a circular arc up to the point of reattachment with radius R [175, 176]. If no control is applied, the attachment remains stable and the flow follows the surface of the wall. If a small amount of force/momentum is exerted at the right location, the flow detaches and switches to the opposite wall. The means of forcing the jet to switch to the opposite wall is an active research field. Different actuation types that have been used in the past are presented in Sec.2.4.3.2. However, the governing geometric parameters shown in Fig.2.13 are:

- Setback distance b
- Wall attachment angle β

[5]Outlet channels do not need to be separated by a splitter. A sweeping motion of the jet is obtained if a single outlet downstream of the interaction region is used.

- Nozzle width w
- Nozzle height h
- Splitter distance d_s
- Presence and location of vents d_v

General statements regarding the device performance with respect to a change in the device geometry cannot be given since the control mechanism plays here the decisive role. The influence of different setbacks on the switching dynamics using a conventional control mass flow as means of forcing is studied by, for instance, Ozgu & Stenning [177] or Savkar [176]. Setback distance d_s, wall attachment angle β as well as the nozzle width w have no effect on the pressure gradient across the jet in steady state and only affect the dynamics of switching. This becomes apparent considering the jet curvature equation which determines not only the steady state characteristics of a reattached jet but also the time dependent dynamics due to a change in the attachment force [178]. The equation reads as

$$\dot{m}\sqrt{\frac{3}{\sigma h w^2}}\frac{1}{\sqrt{\Theta}}\frac{1}{\sqrt{R}}\frac{dR}{dt} - (\frac{\dot{m}^2}{\rho h w^2})\frac{1}{R} = \Delta p \tag{2.3}$$

where $\dot{m}$ is the mass flow rate through the nozzle, σ the spreading rate of the jet, Δp the attachment force and Θ the angle formed by the jet centreline and the attachment wall. In steady state ($\frac{dR}{dt} = 0$) the above equation reduces to

$$\frac{u_e^2 h}{R} = \Delta p \tag{2.4}$$

and thus indicates that the nozzle height is the only geometric feature that affects the pressure across the jet. Nozzle width, attachment angle and setback only affect the time dependent characteristics. The left hand side of Eq.2.3 governs the dynamic response of a jet to change in pressure.

The jet curvature equation was first introduced by Ries [178] in the early 1970s who aimed at modelling the dynamic changes in a fluidic amplifier during switching. The equation was here derived based on the behaviour of ideal gas, geometric relations, continuity of mass being transferred between recirculation bubble and the main jet as well as the momentum equation. The original purpose of Eq.2.3 was to find an analytical description of the jet curvature as a function of a control mass flow $\dot{m}_c$ and time t. Here $\dot{m}_c$ determines the rate of inflation of the recirculaiton bubble and the resulting change in Δp across the jet. For the present study, however, no control mass flow is used and a change in pressure is obtained by an assymetry in entrainment. Eq.2.3 will be used several times through out this thesis for both the steady state and dynamic response of the jet curvature to a pressure difference across both sides of the jet.

Vents are typically placed upstream of the splitter leading edge and are used as an additional reservoir of high pressure fluid that helps to inflate the recirculation bubble and hence the switching process once the reattachment length exceeds d_v [179].

The splitter distance d_s is crucial to the performance of the device. For an upstream location of the splitter leading edge close to the nozzle orifice, for instance, the jet attachment will eventually become unstable as soon as the splitter leading edge interacts with the jet potential core. This is because an increased spillage of the main jet towards the unattached channel favours another recirculation bubble on the unattached side leading to an unstable flapping of the jet around the splitter leading edge. Furthermore, the splitter distance also determines where the reverse mass flow, if present, is fed into the main jet and therefore might strengthen the attachment. Depending on the actuation mechanism as well as on the shape of the splitter [180], values for $\frac{d_s}{h}$ are typically between 5 and 12 [166, 181]. Further work regarding wall design, venting, pressure recovery and switching mechanisms was done mainly in the 60s by, for instance, Sarpkaya and Kirshner [182], Harada et al [183],

and Lush [184, 185].

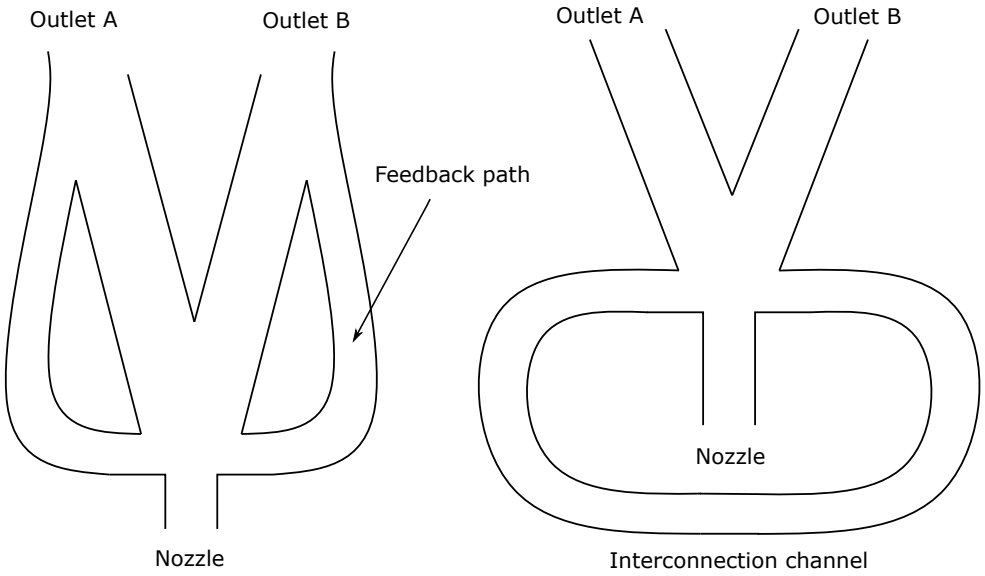

Figure 2.14: Schematic of a passive fluidic oscillator; Left: Feedback oscillator, right: sonic oscillator

2.4.3 Device Types

2.4.3.1 Passive Oscillators

There are two primary types of fluidic oscillators: wall attachment and jet interaction [17]. A wall attachment oscillator consists of either a feedback path or an interconnection channel between both control ports (Fig.2.14). In the former configuration, a part of the attached main flow enters the feedback path and is thus fed back and applied as a negative signal at the amplifier's control port to switch the jet [186]. The output oscillation frequency f_{out} is set by the transport time of the flow in the feedback path and by the filling time of the feedback capacitance. The operating frequency is therefore coupled to the mass flow rate through the device and a function of volume and length of the feedback path [187]. Gokoglu et al used Reynolds-Averaged-Navier-Stokes (RANS) simulations to study both a single oscillator [188] and an array of oscillators [189] and achieved output oscillation frequencies

up to $2.5\,kHz$ at $Mn = 1$. In another study Gokoglu et al [190] extended the velocity range studied to supersonic conditions ($Mn = 2.6$) and obtained oscillation frequencies of $3\,kHz$ for air and $7\,kHz$ for helium. Bettrich & Niehuis [191] developed a miniature oscillator of the order of a few mm to be used in turbomachinery applications (total device length $< 10\,mm$ and $h = 0.5\,mm$). They achieved output oscillation frequencies of up to $14\,kHz$. Wang et al [192] performed a combined numerical and experimental study and found that the oscillation frequency has nearly linear relationship with the length of its feedback loops. Tomac & Gregory [193] have further used a pair of fluidic oscillators with a shared feedback channel. As a result they obtained a phase-synchronized output oscillation. Much work regarding the visualisation of the internal flow structures has recently been done by Paschereit et al. [18, 19, 20, 21]. They found, for instance, that a growing recirculation bubble between the main flow and the attachment wall is the underlying mechanism that causes the main flow to oscillate. They further observed that geometrical features, in particular at the inlet and outlet of the mixing chamber, have a crucial impact on the oscillation frequency.

Fluidic oscillators that rely on an interconnection channel between both control ports were first introduced by Spyropoulos [194] and Viets [195] and further investigated and improved by, for instance, Arwatz et al [196], Kim et al [197] or Tesař et al [22]. The working mechanism is based on the propagation of compression and expansion waves at acoustic speed through the feedback tube that connects the two control nozzles [17]. Thus, they are often referred to as sonic oscillators. They achieve output oscillation frequencies in the range of several hundred Hz depending on flow rate and tube length [17, 196].

Jet interaction oscillators (Fig.2.15) are relatively new and consist of two jets impinging at each other [198]. With a proper cavity design the impingement becomes unstable and an oscillatory jet flow is generated at the output [199]. Gregory et al [200]

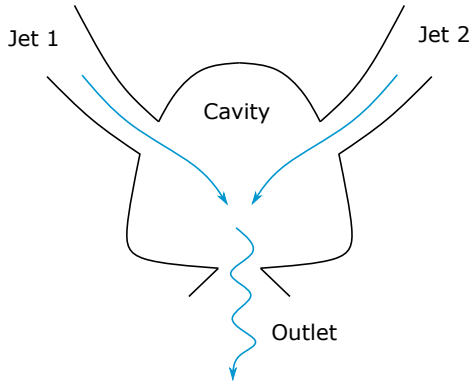

Figure 2.15: Schematic of a jet interaction oscillator

visualized the internal jet interactions of the feedback-free fluidic oscillator by using pressure-sensitive paint (PSP) and found that two counter-rotating vortices within the mixing chamber drive the output oscillation. The output oscillation frequency depends mainly on the size of the cavity. Nano-scale devices, for instance, achieve frequencies in the MHz range [201] while devices in the order of several mm are restricted to maximum oscillation frequencies that do not exceed $1\,kHz$ [202, 203].

Key advantages of fluidic oscillators are their high reliability and long lifetime since no moving parts are involved. Depending on the oscillator type and size they also achieve output oscillations over a wide range of frequencies. However, they have several severe drawbacks. First, they cannot be actively controlled and thus are limited to applications in which the output does not need to be phase locked or controlled in closed loop. Second, the output oscillation frequency is directly dependent on the prevalent mass flow rate which somewhat limits the utility of the device, as it is highly desireable to decouple these two parameters in most applications [2]. This can be done by removing the feedback tubes and replacing them with an active actuation mechanism. Such devices are discussed in the following.

2.4.3.2 Active Switches

In contrast to the thousands of papers that have been published in recent years regarding the development and application of passive oscillators, there are only a handful of studies that are concerned with devices having an active switching mechanism. Culley [204], for example, uses a conventional control mass flow operated by high-speed solenoid valves to switch the jet from one attachment wall to the other. Experimental results are shown for operator valves that are referenced to atmosphere as well as to the same source as the main flow. The maximum output oscillation frequency did not exceed $312\,Hz$ which was found to be caused by the jet dynamics (switching time) rather than the time response of the operating valves. A bistable fluidic device that uses a conventional control mass flow was also investigated numerically by Sun et al [205]. The minimum control flow necessary to switch jet was found to be below 10% of the main flow. It was also noted that the diverter performance can change significantly when integrated into a complex flow system.

Another interesting concept was explored by Gregory et al. [23] who used a cantilever piezoelectric beam located on the jet centreline with its free end oscillating up and down at the nozzle orifice ($h = 0.5\,mm$). The upstream pointing bender thus directly deflects the flow from one attachment wall to the other. The device was capable of switching high-speed jets ($Mn = 1$) up to a frequency of $5\,Hz$. The maximum oscillation frequency was shown to increase at lower flow rates although it was suggested that at higher frequencies the jet was most likely modulated in some other manner by the piezo bender, rather than by attachment to the adjacent walls. The concept successfully decoupled the frequency from the prevalent flow rate and is able to operate at engine realistic pressure ratios. However, the direct interaction of a thin piezoelectric bender interacting with a high-speed flow at relatively high frequencies presents implementation challenges. Furthermore, the device allows steady or full oscillatory motion only.

Both Gregory et al [206] and Tesař et al [207] used Single Dielectric Barrier Discharge (SDBD) actuators inside the control port channels and the interaction region, respectively, but only achieved switching at low flow velocities ($u_e < 10\frac{m}{s}$). Due to the inherent limitations of SDBD actuators, as discussed in Sec.2.3.1, it is questionable if surface-plasma based devices are suitable for aerospace applications.

Martin et al [208] used a piezoelectric driven synthetic jet actuator to switch a bistable fluid diverter. Although the synthetic jet produced peak velocities of up to $35\,\frac{m}{s}$ the main jet velocities did not exceed $10\,\frac{m}{s}$. What's more is that the synthetic jet was driven at two distinct resonance frequencies that produced nearly the same peak velocities. However, switching was only achieved at one of the two resonance frequencies. This somehow indicates that the mechanism behind switching is not only due to the imparted momentum of the synthetic jet actuator. In dynamic operation an output oscillation frequency of $25\,Hz$ was achieved.

More recently, Chen et al. [209] used a spark discharge inside the recirculation bubble to switch the flow. The device was successfully operated at pressure ratios up to 1.1 ($u_e = 50\,\frac{m}{s}$ and $Re = 1 \cdot 10^4$) and the minimum switching time was $20\,ms$. It has been found that the plasma spark discharges result in low density spots leading to thermal blocking effects. The recirculation bubble is then elongated causing the jet to strongly interact with the splitter which ultimately leads to switching.

According to Raghu [210], further development of actively controlled fluidic devices is needed to meet the requirements of high control authority and large frequency bandwidth actuators for flow control applications. However, to the author's best knowledge, no other active control concepts have been developed nor proposed in the past.

2.4.4 Aerospace Applications

Over the last two decades, fluidic devices have been used in basically all relevant parts of an aircraft so to achieve fuel-burn improvements, higher overall efficiency, less drag, higher manoeuvrability, and so forth. This includes not only the control of external flow around the wing [14, 211, 212] but also the control of internal flow in all major components of the engine including intake [213], compressor [214], combustor [215], turbine [216] and nozzle [217].

Most studies regarding flow control applications focus on the control of flow separation on an airfoil, probably because of the high potential gain [218, 219]. Seifert et al [14] found that stall is delayed and poststall characteristics are improved when oscillatory blowing is applied from the leading-edge region of the airfoil. Amitay et al [220] studied the effect of actuation frequency of a synthetic jet on the reattachment over a stalled airfoil. They observed that an actuation frequency of $F^+ = \frac{f_{act}L}{u_\infty} \sim \mathcal{O}(1)$, where L is a characteristic length of the separated region, leads to an unsteady attachment and vortical structures at the driving frequency that persist well beyond the trailing edge of the airfoil. Frequencies of $\mathcal{O}(10)$, in contrast, achieved a complete flow reattachment without organized vortical structures along the airfoil. Similar results were obtained for flow separation control on a vertical tail by Rathay et al [7]. They observed that synthetic jets can successfully delay flow separation and enable a significant size reduction of the tail if the non-dimensional actuation frequency is $\mathcal{O}(10)$. Using a fluidic oscillator Seele et al [221] also found that sweeping jets at the trailing edge of a vertical tail with $C_\mu = 2\%$ can increase the side force in excess of 50%, also enabling a significant size reduction of the tail. Here C_μ denotes the momentum coefficient which relates the momentum of the induced velocity to the free stream velocity according to $2\frac{A_{jet}}{A_{ref}}(\frac{u_j}{u_\infty})^2$.

An active control method to counteract the separation in an inlet duct of an engine was studied analytically by MacMartin et al [222]. It was found that unsteady fluid

injection at the separation point with 1.2% of the core flow imparts enough momentum into the boundary layer to substantially reduce separation. Although the actuator itself is not part of their investigation, they recommend a fluidic approach since synthetic jets do not provide sufficient control authority at high free stream velocities. They also claim that the pulsed injection is beneficial to suppress flow disturbances which otherwise might result in rotating stall further downstream. In contrast to that, Garnier [144] experimentally tested unsteady high-speed jets for separation control in a curved S-duct and recommended not to use pulsed jets since they increased the unsteady flow distortion. In a further experimental study by Kumar et al [223] flow separation along with reverse flow in a diffuser was also successfully eliminated using supersonic microjets, although no results were presented for unsteady actuation.

Apart from flow separation at the engine's inlet, many studies are dedicated to the control of flow separation at the suction side of stator vanes. If separation is delayed or even eliminated, the maximum load per compressor stage could be increased and thus offers the potential to build jet engines more compact. Culley et al [214] experimentally tested the effectiveness of steady and unsteady fluid injection from the suction surface in a low speed axial compressor. An embedded bistable fluidic actuator inside the vane using 1% of the core flow reduced separation effectively and led to a reduction of area-averaged pressure losses of 25%. Furthermore it was shown that the addition of oscillations to steady injection can reduce the level of injection required to obtain a given loss reduction. A similar study using synthetic jet actuators but the same experimental facility and stator vane model was performed by Braunscheidel et al [224]. But due to the low momentum output of the synthetic jet actuators the loss reduction for the entire passage was only around 5%. Another interesting application of fluidic devices is the active control of rotating stall and surge [225]. Delaying the onset of both events would allow operation closer to the current stall line and therefore enable the compressor to operate at higher pressure

ratios. Rafaello et al [226] used static pressure sensors to detect stall and were able to extend the stall point by air injection actuators equally spaced around the compressor circumference, upstream of the rotor. The pulsed jet injection was obtained by a solenoid valve and effectively counteracted the blockage of rotor cells. More recently, Staats et al [227] were able to control corner separation of a stator vane using an array of fluidic oscillators and achieved a static pressure rise of up to 2.5%.

Regarding the improvement of combustion performance Saiki et al [228] manipulated large-scale vortical structures using miniature jet actuators installed on the inner surface of the annular nozzle and achieved enhanced mixing of the fuel/oxidizer mixture. Meier et al [229] used an array of feedback free fluidic oscillators in a rocket combustion chamber and achieved a reduction in the instability pressure oscillation magnitude.

Imparting momentum into the boundary layer of the suction side of turbine blades also offers a great opportunity to avoid or suppress separation. Especially during high-altitude cruise the Reynolds number in low pressure turbines can drop below $2.5 \cdot 10^4$ (laminar boundary layer), despite high freestream turbulences [230]. This can cause flow separation and thus a substantial increase in losses through the turbine stage. Kurz et al [231] studied the effectiveness of boundary layer control and showed that fluidic oscillators are an appropriate way to suppress massive open separation bubbles in the low Reynolds number regime. Bettrich et al [232] obtained a 40% reduction in overall pressure losses using fluidic oscillators and carried out a more fundamental investigation focusing on the interaction of the boundary layer flow with high frequency actuation. Huang et al [216] used SDBD plasma actuators mounted upstream of the separation line. Experiments showed that reattachment occurs in all cases but there is a threshold amplitude above which the reattachment point is not changed appreciable, depending on the position of the plasma actuator. In a study by Rizzetta & Visbal [233] the plasma actuator effectiveness was determined using

the wake total pressure loss coefficient. Pulsed force application was more effective than continuous actuation and higher frequencies also revealed better results than low frequency actuation. The wake total pressure loss coefficient could be reduced by more than 50%. The effect of pulsed vortex generator jets to suppress separation was experimentally examined by Bons et al [142]. Even at very low frequencies the pulsed fluid injection was highly effective in controlling laminar boundary layer separation. This was explained by the relatively long relaxation time of the boundary layer to resume its separated state. At higher pulsing frequencies the boundary layer never recovered its fully uncontrolled state and remained attached at any point. Volino & Ibrahim [234] also used vortex generator jets and successfully delayed separation. Although the separation was still present, the separation bubble remained closed at all times. The results indicated a 20% increase in lift and up to 60% reduction in total pressure losses. They also observed that pulsed jets were more effective than steady injection and that at high frequencies the jet velocity could be decreased and the effect remained the same. Similar results were obtained by Sondergaard et al [235] and Rizzetta et al [236]. The latter one used numerical simulations and investigated both steady and unsteady injection. Both configurations achieved the desired result (delay of separation and reduction of wake total pressure losses by 56%), but the pulsed injection required less mass flow to attain the same level of improvement in efficiency.

Burns [237] numerically investigated a novel method to reduce tip leakage flow by sealing the tip clearance of turbine blades with oscillating jets injected from the surface of the rotor tip [238]. Furthermore, Stone et al [239] showed that trailing edge pulsed ejection using fluidic oscillators fills the momentum deficit in the wake more uniformly than other actuators tested, with expected benefits for tonal noise in engine fans. Furthermore, pulsed ejection was found to reduce broadband noise from the turbine.

With respect to the nozzle, there is a strong demand to improve the capability of fluidic thrust vector control [240]. This could avoid the conventional mechanical vectoring which works by turning the entire jet exit area. Raman et al [217] showed that miniature fluidic oscillators, mounted on one side of a rectangular nozzle, provide sufficient oscillatory and distributed mass addition to achieve a deflection of 15% using 1.6% of the main flow. The interested reader is referd to a review of thrust vectoring techniques by Kowal [241], Deree [242] or Pascoa et al [240].

Chapter 3

Methodology

This thesis consists of both experimental and numerical studies including several different set-ups and procedures. It was therefore chosen to include a methodology chapter which presents all of the experimental set-ups and numerical techniques separately. This ought to provide a framework to which the reader can refer to throughout the reading. Experimental set-ups are presented first. Numerical procedures including CFD and acoustic simulations are presented thereafter.

3.1 Experimental Set-up

Two major experimental set-ups are used in this thesis. The first concerns the functioning and performance evaluation of the fluidic devices under investigation and utilises classical measurements of the key properties $(p, t_s, \dot{m})$. The second is a non-intrusive optical diagnostic set-up that uses Particle Image Velocimetry (PIV) to visualise the flow. The latter is used to visualise a single switching event in a fluidic device as well as the shear layer dynamics of an acoustically excited round jet.

Within this thesis two major fluidic device configurations will be investigated. The first one can be considered a proof of concept device that uses low frequency excitation. Hence the device is subsequently called *low frequency device*. The second

major device configuration uses excitation frequencies in the ultrasonic range and hence is referred to as the *ultrasonic device*.

3.1.1 Fluidic Performance Bench Test

Each device is 3D printed using the stereolithography (SL) fabrication process. The SL apparatus used here (Objet30 Stratasys) jets microscopic layers of liquid photopolymer onto a build tray and instantly cures them with UV light. The accuracy is better than $\pm 0.1\,mm$. A schematic of both device configurations used in this study is shown in Fig.3.1. Each device features an inlet, a nozzle, an interaction region, two outlets and two control ports on either attachment side in which the respective sound sources are situated. The design of the low frequency device was adapted from a previous device that uses conventional control jets and studied by Tippets & Royle [243]. The ultrasonic device was designed based on the experimental and numerical results obtained from the low frequency device. Each device further features a perspex cover plate so to allow an independent measurement of the nozzle geometry, i.e. nozzle height h.

The remaining set-up is now described from a Lagrangian point of view.
On the upstream end of the experimental set-up, a $100\,psi$ line feeds a stagnation chamber that is located just upstream of the device inlet. The flow rate through the system is controlled by an Omega FMA-2609A/5520A flow controller. A pressure tapping inside the stagnation chamber determines the total inlet to static outlet pressure ratio $\mathrm{Pr} = \frac{p_{t,in}}{p_{out}}$. The flow then enters the device through the inlet and eventually reaches the nozzle orifice. Here, at the nozzle exit, another static pressure tapping is used to determine the local jet speed u_e and Mach number Mn.[1] Upon jetting into the interaction region the flow adheres to one of the two attachment walls

[1]This, however, is only the case for the ultrasonic device since the low frequency device operates only in the incompressible regime which allows the jet exit velocity to be determined by the flow rate.

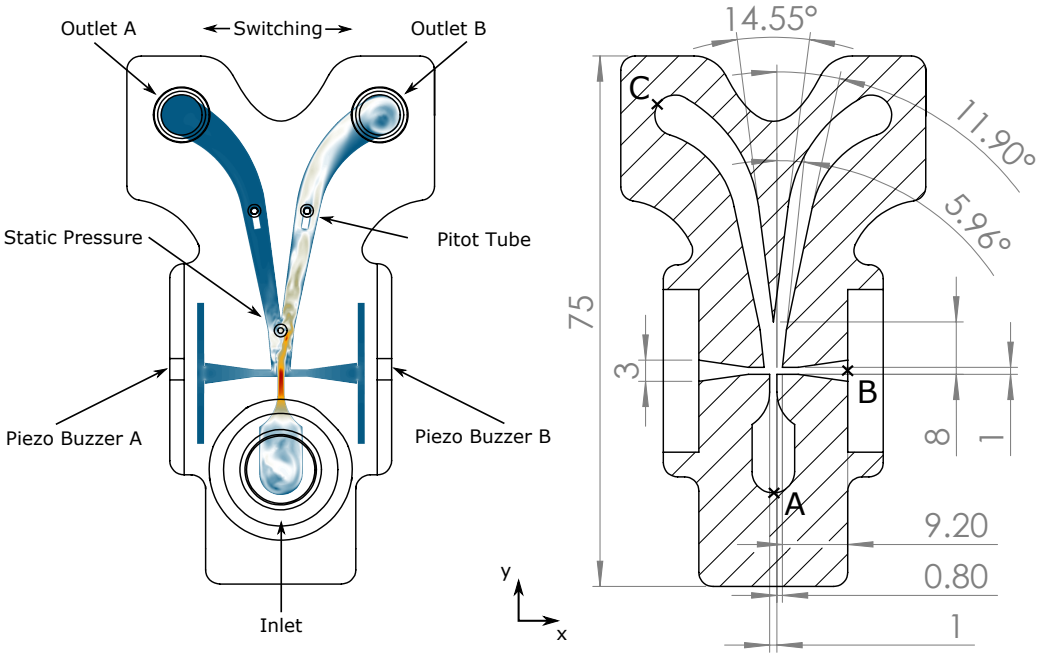

(a) Low-frequency device

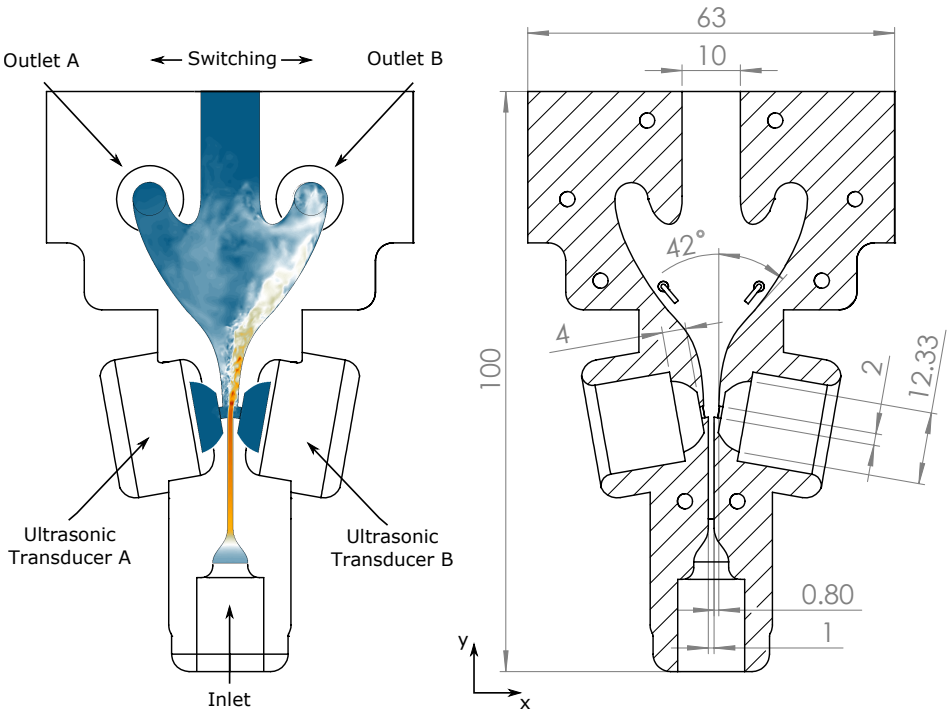

(b) Ultrasonic splitter-less device

Figure 3.1: Schematic and governing dimensions of two fluidic device designs used in this study

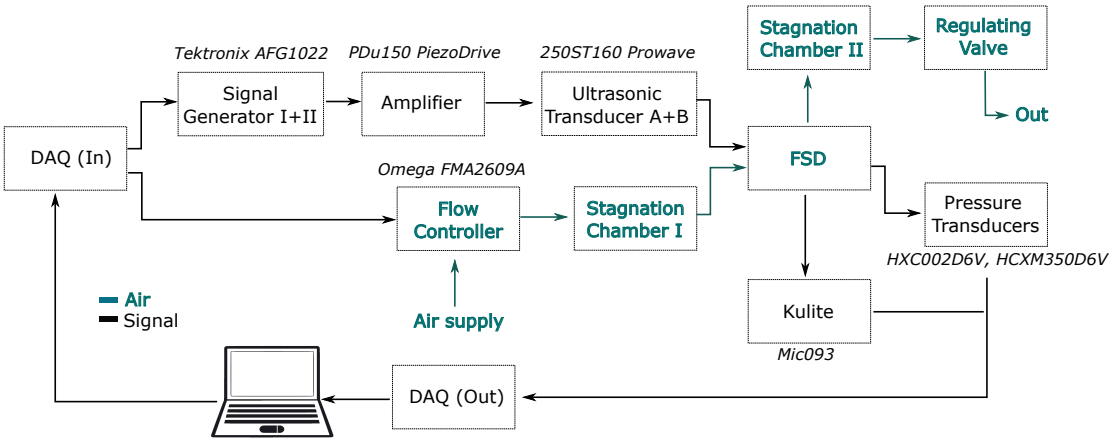

Figure 3.2: Schematic of the experimental set-up

Table 3.1: Pressure sensors used for the low frequency device

	Type	Range	Accuracy
$\mathbf{p_{t,in}}$ **stag. chamber**	HCXM010D6V	$0-10\,mbar$	$\pm 0.5\%$
$\mathbf{p_s}$ **nozzle orifice**	-	-	-
$\hat{\mathbf{p}}$ **interaction region**	LDES100UF6S	$0-100\,Pa$	$\pm 0.5\%$
$\mathbf{p_t}$ **channel A+B**	HCXM010D6V	$0-10\,mbar$	$\pm 0.5\%$

which both feature identical control port chambers. Each control port chamber hosts a respective sound source. The sound source of the low frequency device is a panel mount continuous external Piezo buzzer (Kingstate PKD-7246) with a $SPL = 108\,dB$ ($1\,V_{rms}$ at $10\,cm$). The sound source of the ultrasonic device is a ultrasonic transducer with a resonance frequency at $25\,kHz$ (Prowave 250ST150) and a $SPL = 112\,dB$ ($10\,V_{rms}$ at $30\,cm$). The signal for the sound source is a sine wave generated by a signal generator (Tektronix AFG1022) and further amplified using a 40W power amplifier (Kemo Electronic M034N) for the low frequency device and an ultra-low noise amplifier (PiezoDrive PDu150) for the ultrasonic device. The signal for each control port is triggered automatically and is 180° out of phase. Frequency, amplitude as well as the number of cycles are controlled independently.

After the jet has attached to one of the two sides, another pressure tapping lo-

Table 3.2: Pressure sensors used for the ultrasonic device

	Type	**Range**	**Accuracy**
$\mathbf{p_{t,in}}$ **stag. chamber**	HCX002D6V	$0 - 2\,bar$	$\pm 1\%$
$\mathbf{p_s}$ **nozzle orifice**	HCXM350D6V	$0 - 350\,mbar$	$\pm 0.5\%$
$\hat{\mathbf{p}}$ **interaction region**	Kulite Mic093	$95 - 185\,dB$	$\pm 0.25\%$
$\mathbf{p_t}$ **channel A+B**	HCXM350D6V	$0 - 350\,mbar$	$\pm 0.5\%$

cated in the middle of the device and inside the interaction region is used to measure the sound pressure level $\hat{p}$. For the low frequency device a pressure transducer with an operating range of $0 - 100\,Pa$ is used. The tube length between pressure tapping an pressure transducer is kept below $50\,mm$ and so its influence is assumed negligible ($\frac{50\,mm}{330\,m/s} < \frac{1}{3000\,Hz}s$). All measurements are further corrected by their frequency response obtained from the data sheet. For the ultrasonic device the sound pressure is measured using a high intensity microphone with a dynamic operating range of up to $\approx 1\,bar$. All amplitude measurements are further conducted in quiescent air only.

The flow then follows the attachment wall towards one of the two outlets of the device. $20\,h$ downstream of the nozzle orifice a Pitot probe on either side is used to record the total gauge pressure at $f_s = 30\,kHz$. This is used to indicate the attachment side as well as the switching time t_s. The data is further filtered using a first order analog low pass Butterworth filter with a cut off frequency at $1.5\,kHz$. The switching time is defined as the time between the onset of excitation and the point where the signal of the initially unattached side Pitot probe exceeds 90% of the final mean value. Pressure readings shown subsequently are referenced to atmosphere unless otherwise stated.

In contrast to the low frequency device, the ultrasonic device features a second stagnation chamber downstream of the device outlet. A regulating valve through which the air leaves the second stagnation chamber can be controlled manually so to block the flow and increase the overall pressure inside the device. This allows testing

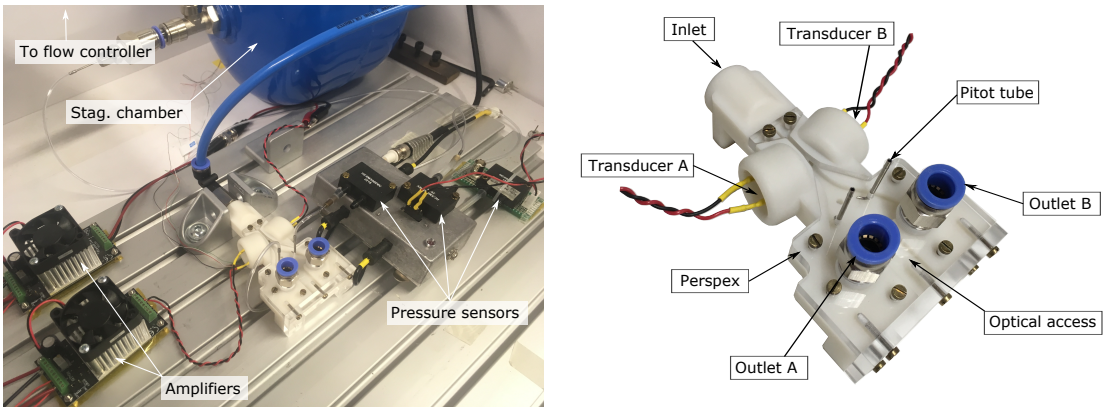

(a) Performance bench test (b) Splitter-less device

Figure 3.3: Experimental set-up

the device performance at higher densities. A schematic of the experimental set-up is shown in Fig.5.1. A table containing the characteristics of all types of pressure sensors used in this study is further shown in Tab.3.1 and 3.2. The devices are further fixed to a metal plate with additional lateral support so to avoid any vibration. The experimental set-up as well as a close-up view of the ultrasonic device is displayed in Fig.3.3 a.) and b.), respectively. For the experiments conducted with the low frequency device the Reynolds number Re_h based on the nozzle height h takes on values between $500 - 2500$. For the ultrasonic device the Reynolds number goes up to $2.7 \cdot 10^4$.

Experimental uncertainties for the performance testing of the ultrasonic device are as follows: Pressure measurements of the Pitot probes, which are used to determine the switching time t_s, feature an uncertainty that is more than two orders of magnitude lower than the average variation in switching time and therefore negligible. The pressure ratio Pr measured via the total inlet pressure inside the stagnation chamber as well as the set mass flow rate exhibit an uncertainty of $\pm 1\%$. The dimensions of the 3D printed device is within a tolerance of $0.1\,mm$. The maximum uncertainty of the calculated jet speed u_e is thus $\pm 3\%$. The sound pressure level measured inside the interaction region is accurate to within $\pm 0.3\%$.

Experimental uncertainties for the performance testing of the low-frequency device are as follows: The mass flow rate provided by the flow controller features an uncertainty of $\pm 1.5\%$ that amounts to less than $\pm 0.08\,LPM$ for the flow rates used in this study. The dimensions of the 3D printed FSD are, similar to the ultrasonic device, within a tolerance of $0.1\,mm$ given by the printer resolution. The uncertainty of the calculated average jet speed at the nozzle orifice due to geometric discrepancies and the accuracy of the flow controller then amounts to $\pm 3\%$. The maximum uncertainty at the highest SPL caused by the accuracy of the pressure sensor is $\pm 0.065\,dB$ ($\pm 0.5\%$). The variation in switching time at constant frequency, amplitude and mass flow rate is more than two orders of magnitude bigger than the uncertainty of the measurement. This will be shown in Chapter 4.

3.1.2 Flow Visualisation Set-up

Particle Image Velocimetry (PIV) is a laser-based optical diagnostic technique that measures the velocity vector field of a flow. Particles small enough to have no slip relative to the flow are introduced into the flow and illuminated by a laser. A high-speed camera captures the scattered light from the particles and thus generates images of particle distribution in the flow. This is exemplarily shown for an axisymmetric jet exiting from a nozzle in Fig.3.4.

In order to reconstruct the flow field, two images need to be taken shortly one after another. The interrogation window is then subdivided into smaller window sizes typically in the order of tens of pixels. Each window contains a specific pattern of particles which can be cross-correlated with the second image. A peak in the cross-correlation function then yields information about the magnitude and direction of the particles within that window. Therefore, a velocity vector field can be reproduced.

Here a dual-head Nd:YAG laser that produces a beam at $532\,nm$ with $600\,mJ$ per pulse is used. The PIV data rate is $15\,Hz$. The laser is passed through cylindrical

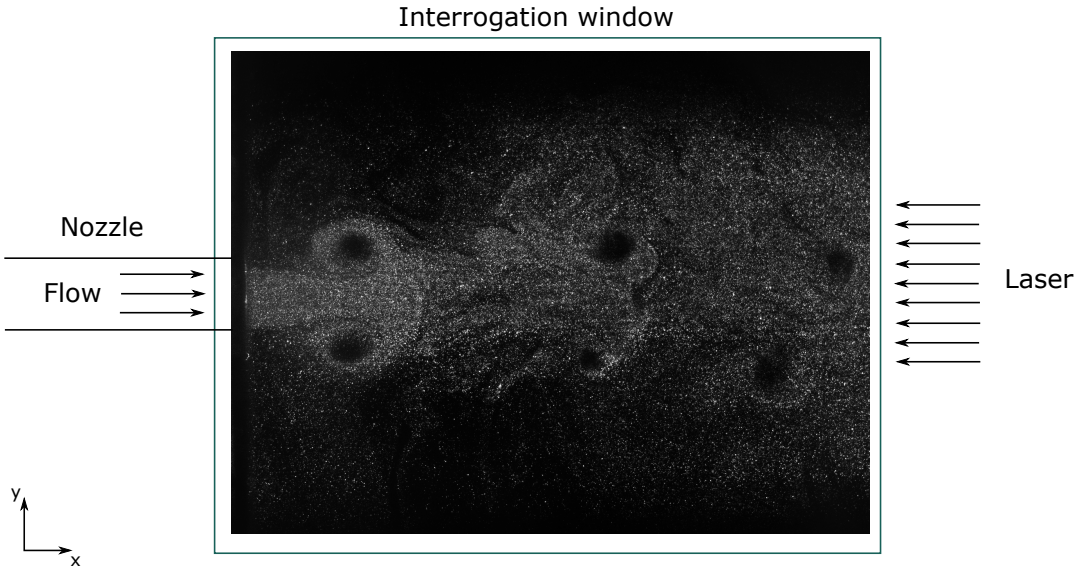

Figure 3.4: Raw image taken of a seeded flow with laser illuminated particles indicating shear layer roll-up of a circular jet flow

and spherical lenses to form it into a thin sheet with a thickness of approximately $0.5\,mm$. The flow is seeded with Di-Ethyl-Hexyl-Sebacate (DEHS) using a LaVision aerosol generator. The droplet size ranges between 0.3 and $1\,\mu m$. The particle density is controlled by two mass flow controllers (Omega FMA2609A & FMA5520A) and a bypass route as shown in Fig.3.5. Image pairs are acquired using a high-speed charge-coupled device (CCD) camera (Bobcat B1621) with a fixed inter-frame time of $200\,ns$. A calibration grid is used to set the focus, correct for optical distortion and scale the vector units to $\frac{m}{s}$. Dark images of a laser illuminated test section are further obtained and subtracted from all acquired images so to remove background light and impurities of the perspex sheet. The laser inter-pulse time is set so that an average particle displacement of approximately 8 pixels per frame is achieved. A standard decreasing window size multipass processing is further used to calculate the velocity vector field. The initial, second and third pass uses a 128x128, 64x64 and 32x32 pixel interrogation window, respectively. A 50% overlap is used for all passes

to improve spatial resolution. Processed images use a vector-validation filter that removes individual vectors that exceed a predetermined range and reinserts them based on an interpolation scheme. The spatial resolution of the final velocity vector field amounts to $< 0.1\,mm$. The stokes number based on the average particle size and the average nozzle exit velocity never exceeds 0.1. Errors associated with tracing accuracy are therefore around 1%. The mass flow controllers have an accumulated uncertainty of 2.5%.

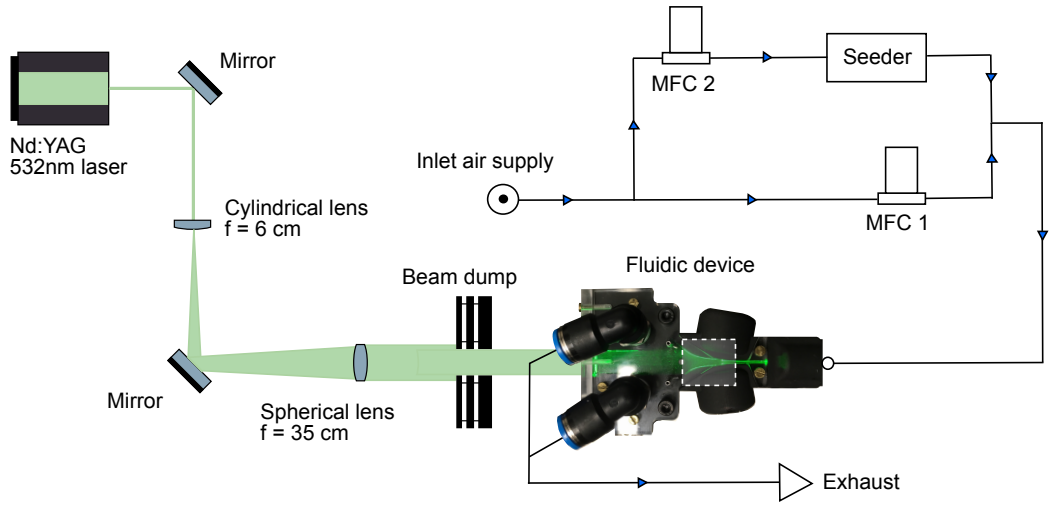

Figure 3.5: Schematic of the PIV set-up

3.1.2.1 Fluidic device

The ultrasonic device was designed without splitter so to have optical access for an incoming laser, making PIV feasible. The device was coated black so to minimize the scattered light from the device. The camera views a square field of $7x7\,mm$ centred on the jet axis and starting just downstream of the nozzle orifice. Set-back and attachment walls of the fluidic device are optically screened so to minimize any interference of a reflecting light. The device geometry, especially the wall attachment angle, as seen by subsequent PIV contour plots thus appears to differ from LES contour plots. Both the camera and the ultrasonic transducers are triggered by a

signal generator and synchronized with the laser pulse. Images of the steady state reattached jet are taken randomly. Images that are taken during the switching are phase-locked to the laser pulse. Different stages of a switching process are then acquired by changing the delay between laser pulse and the onset of excitation. Given that the laser can only be fired at $15\,Hz$ or less, only one image pair per switching event can be taken. The coated and illuminated FSD is shown in Fig.3.6.

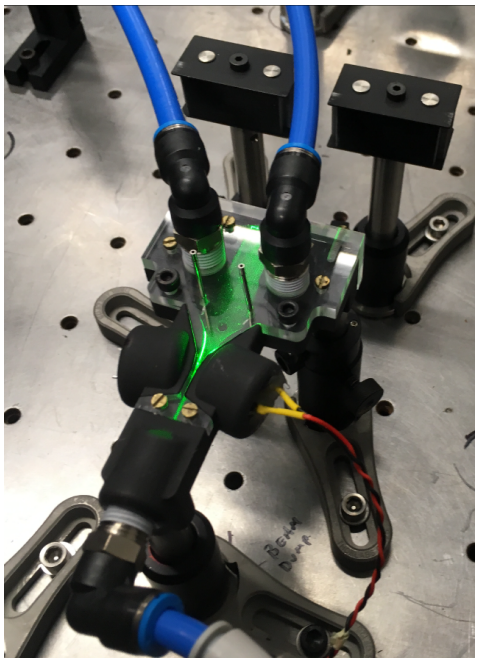

Figure 3.6: Painted fluidic device (ultrasonic splitter-less configuration) showing laser sheet entering between the two outlets

3.1.2.2 Excited Round Jet

A separate investigation of an excited circular jet exiting into ambient air is presented in Chapter 6. The experimental set-up is identical to the one presented above. The test section is a perspex box with a 3D printed cover plate, as shown in Fig.3.7. The cover plate consists of an opening with $D = 7.5\,mm$ and an additional circumferential slot through which low speed seeded air ($< 0.5\,\frac{m}{s}$) is introduced. Tubes with various lengths are further inserted through the opening centred in the middle. Sound

is introduced in an upstream 3D printed box in which seeded and non-seeded air are mixed. The sound source is a $50\,Watt$ Visaton round cabinet speaker (FRS 8 4 OHM) connected to a Tektronix signal generator (AFG1022) and a $40\,W$ power amplifier (Kemo Electronic M034N). Acoustic liner is used in both the upstream mixing box as well as the perspex box so to keep resonances and acoustic reflections to a minimum. An omnidirectional condenser microphone (Kingstate MKD-7690) is inserted through a side opening (see Fig.3.7) and measures the sound pressure level at $x = 1\,D$ downstream of the nozzle orifice. A schematic side view is shown in Fig 3.8.

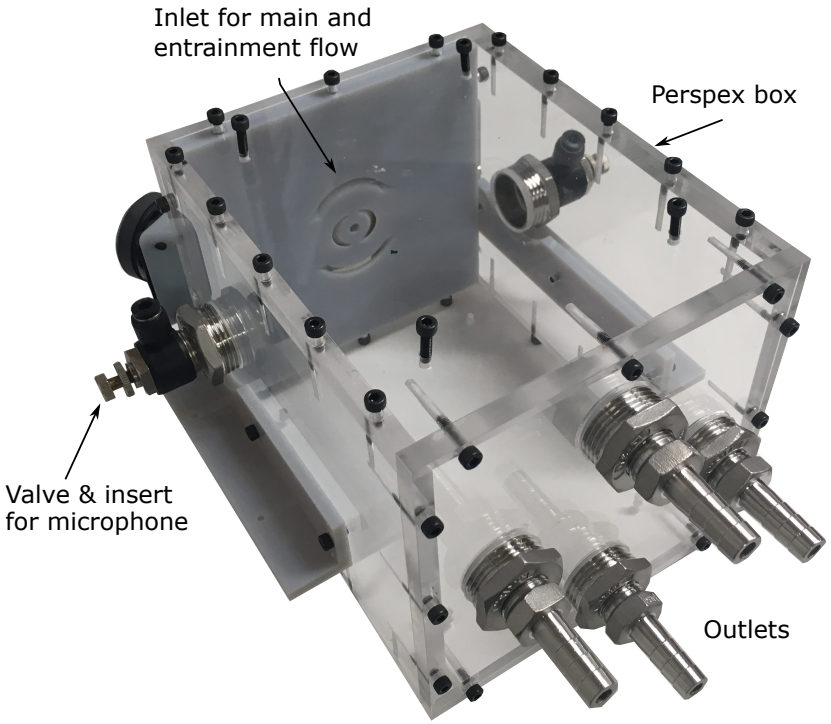

Figure 3.7: Test section of the circular jet excitation PIV experiments

The laser is fired at either $10\,Hz$ or $7.6\,Hz$. The former is used so to take advantage of aliasing noting that the excitation frequency is always a multiple of $10\,Hz$. The latter is chosen arbitrarily. Experimental parameters, such as the range of excitation frequencies or flow velocities, are discussed in more detail in Chapter 6.

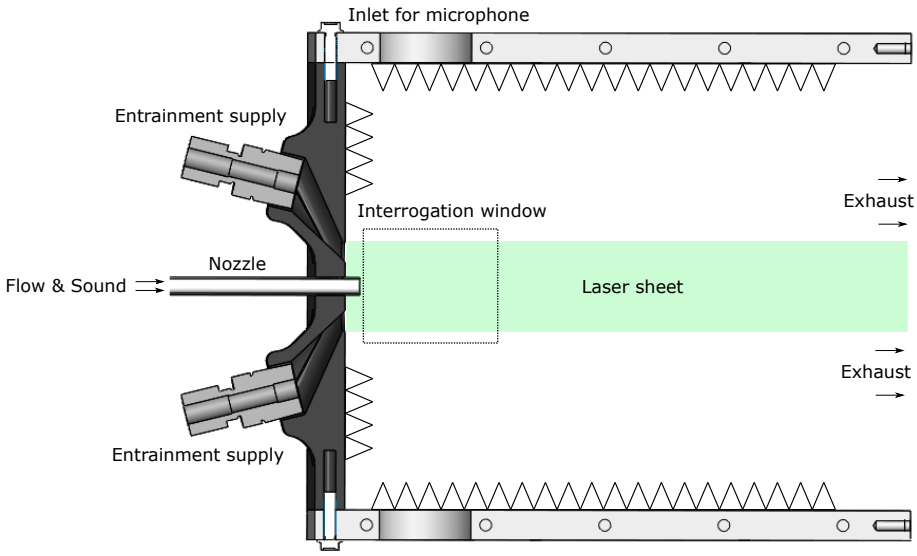

Figure 3.8: Schematic side view of the test section

3.2 Numerical Procedure

3.2.1 Computational Fluid Dynamics

3.2.1.1 Basic Concept

The governing equations of fluid flow are based on the conservation laws of physics. These fundamental equations are the continuity, momentum and energy equation. The continuity equation assures that the mass of a fluid is conserved. For an unsteady, three-dimensional and compressible fluid the continuity equation reads as

$$\frac{\partial \rho}{\partial t} + \frac{\partial (\rho u_i)}{\partial x_i} = 0 \tag{3.1}$$

where ρ is the fluid density, and u_i the velocity component in all directions x_i. Under the assumption of incompressibility Eq.3.1 becomes

$$\frac{\partial (u_i)}{\partial x_i} = 0 \tag{3.2}$$

The momentum equation states that the rate of change of momentum equals the sum of the forces on a fluid particle (Newton's second law). This is the Navier-Stokes (NS) equation which is written as

$$\frac{\partial(\rho u_i)}{\partial t} + \frac{\partial(\rho u_i u_j)}{\partial x_j} = -\frac{\partial p}{\partial x_i} + \frac{\partial \tau_{ij}}{\partial x_j} + S_i \tag{3.3}$$

where p is the static pressure, S_i a source term or body force and τ_{ij} a stress tensor. The stress tensor is further given by

$$\tau_{ij} = \mu\Big[\Big(\frac{\partial u_i}{\partial x_j} + \frac{\partial u_j}{\partial x_i}\Big) - \frac{2}{3}\partial_{ij}\frac{\partial u_i}{\partial x_i}\Big] \tag{3.4}$$

where μ is the viscosity of the fluid and ∂_{ij} the Kronecker delta function. The left hand side of Eq.3.3 represents the total acceleration of a fluid particle. The sum of forces that lead to this acceleration is consequently represented by the right hand side of Eq.3.3. The first term on the right, $\frac{\partial p}{\partial x_i}$, is the internal pressure gradient experienced by the fluid. The second term, the chief cause of complexity of solving the NS equation, is the diffusion term. This term represents the internal stress forces on a fluid particle taking into account viscous effects. The last term represents an external force such as gravity. Neglecting this term and assuming again that the flow is incompressible, the NS equation reduces to

$$\frac{\partial u_i}{\partial t} + \frac{\partial u_i u_j}{\partial x_j} = \frac{1}{\rho}\frac{\partial p}{\partial x_i} + \mu\frac{\partial^2 u_i}{\partial x_j^2} \tag{3.5}$$

The energy equation states that the rate of change of energy of a fluid particle is equal to the rate of heat addition to the fluid particle plus the rate of work done on the particle (first law of thermodynamics) [244]. The equation reads as

$$\rho c_p\frac{\partial T}{\partial t} + \rho c_p u_i\frac{\partial T}{\partial x_i} = -p\frac{\partial u_i}{\partial x_i} + \lambda\frac{\partial^2 T}{\partial x_i^2} - \tau_{ij}\frac{\partial u_i}{\partial x_j} \tag{3.6}$$

where c_p is the specific heat, T the total temperature and λ the thermal conductivity of the fluid. The left hand side of Eq.3.6 represents the change in energy due to the work done by pressure ($-p\frac{\partial u_i}{\partial x_i}$), the heat flux (diffusion) in or out of the system ($\lambda\frac{\partial^2 T}{\partial x_i^2}$) and the irreversible transfer of mechanical energy into heat ($\tau_{ij}\frac{\partial u_i}{\partial x_j}$).

The motion of a fluid in three dimensions is then described by a system of five partial differential equations: continuity equation (Eq.3.1), NS equation (Eq.3.3) in all three directions and energy equation (Eq.3.6). Together they form the basis of computational fluid mechanics. However, in case the flow is isothermal and incompressible, the energy equation can be dropped and only the continuity and momentum equations are solved to obtain the velocity and pressure fields.

Now, the essential idea behind CFD, and more specifically the finite volume method[2], is to divide the domain into smaller control volumes, integrate the equations over each control volume, discretize and converse the resulting integral equations into a system of algebraic equations and finally solve them by an iterative method [244].

The Navier–Stokes equations are non-linear, so many variables in these equations vary with respect to each other by powers of two or greater. The effects of non-linearity further increase with Re, leading to small instabilities in the flow. These instabilities result in flow fluctuations known as turbulence. Finding an exact solution for high Reynolds number flows is therefore a challenging task and currently only feasible for simple flow problems, such as steady, incompressible, laminar fully developed flow in a pipe [245, 246].

Depending on the desired degree of detail of the numerical solution one can either resolve the flow fluctuations or approximate them using a time averaging process. The former technique is computationally more expensive and is called Large Eddy Simulation (LES).[3] The latter is called Reynolds-Averaged-Navier-Stokes (RANS)

[2]There are several different numerical solution techniques such as finite difference, finite element and spectral methods. However, the well established CFD-code *CFX* which uses the finite volume method is used in this thesis.

[3]CFD simulations that resolve all scales of turbulent motions are called Direct Numerical Simu-

simulation and requires far less computational and temporal resources. In this thesis the focus is clearly set on LES since flow instabilities are the key parameter to understand the flow physics of the FSD to be developed. However, RANS simulations are performed as well since a time averaged result serves as a good initialisation for LES. Both techniques are thus briefly outlined in the following.

3.2.1.2 RANS Models

The principal idea behind RANS is that each flow variable Φ can be expressed as the sum of mean and fluctuating components (Reynolds decomposition), so that

$$\Phi = \bar{\Phi} + \Phi' \tag{3.7}$$

where $\bar{\Phi}$ is the time averaged quantity and Φ' the fluctuating component of the flow. Decomposing the flow velocity ($u = \bar{u} + u'$) and taking the time average ($\overline{u'} = 0$) then leads to the following form of the momentum equation, also called the Reynolds-Averaged-Navier-Stokes equation[4]

$$\frac{\partial \overline{u_i}}{\partial t} + \frac{\partial \overline{u_i u_j}}{\partial x_j} = \frac{1}{\rho}\frac{\partial}{\partial x_j}\Big[-\overline{p}\delta_{ij} + \mu\Big(\frac{\partial \overline{u_i}}{\partial x_j} + \frac{\partial \overline{u_j}}{\partial x_i}\Big) - \overline{u_i' u_j'}\Big] \tag{3.8}$$

Comparing the above equation with Eq.3.3 it becomes apparent that apart from the viscous part an additional term, the average of the product of the velocity fluctuations $\overline{u_i' u_j'}$, has been added to the total shear stress. Since the term only appears due to the Reynolds average, it is commonly referred to as Reynolds stress term. This term is further not resolvable and hence requires modelling in order to close the RANS equations for solving. What's more is that the Reynolds stresses are, in general, the

lation (DNS). LES, however, does only resolve the most energetic length scales while modelling the smaller length scales. This will be discussed in more detail later in this thesis. DNS will not be discussed.

[4]Here shown for incompressible flow

dominant part of the total shear stress and hence the key parameter to accurately model turbulence [247]. The RANS turbulence model used in this thesis will be discussed in Sec.3.2.1.4.

3.2.1.3 LES Models

In LES, the turbulent fields are separated into large-scale resolved and small-scale unresolved structures [248]. The length scale at which the small-scale structures remain unresolved is set by the grid spacing Δx. Given that the smaller and less energetic structures are at the upper end of the frequency spectra, LES can essentially be considered a low-pass filter of turbulent structures in both physical and Fourier space. However, turbulent scales smaller than the filter width Δx can still have a significant contribution to the flow field and hence need to be modelled [249]. When the NS equations are (spatially) filtered, one obtains a set of equations that is similar in the form to the RANS equations (Eq.3.8) [250]. They read as

$$\frac{\partial \overline{u_i}}{\partial t} + \frac{\partial \overline{u_i u_j}}{\partial x_j} = -\frac{1}{\rho}\frac{\partial \overline{p}}{\partial x_i} + \frac{\partial^2 \overline{u_i}}{\partial x_j^2} - \frac{\partial}{\partial x_j}(\overline{u_i u_j} - \overline{u_i}\,\overline{u_j}) \tag{3.9}$$

Note that the definition for $\overline{u}$ differs from the RANS equation. Here $\overline{u}$ represents a spatially filtered velocity rather than a time averaged as is the case in Eq.3.8. The last term $\overline{u_i u_j} - \overline{u_i}\,\overline{u_j}$ is called the subgrid-scale (SGS) Reynolds stress and, analogous to the Reynolds stress for the RANS equations, is not solvable and hence requires modelling.

Given that the RANS equations are based on the time-average of the Reynolds decomposed velocity field, only steady state results of the flow can be obtained. LES, in contrast, is based on a spatial filtering operation and hence is a transient simulation only. There is, of course, also the possibility to use unsteady RANS (URANS) simulations to obtain transient flow results. However, the freqency of

fluctuating components of, for instance, streamwise velocity across the Kolmogorov energy cascade cannot be captured by URANS as it is still a statistically steady flow simulation. And since the acoustic forcing frequencies used in this study lie within the freqeuncy band of turbulent fluctuation, LES is here the only appropriate approach.

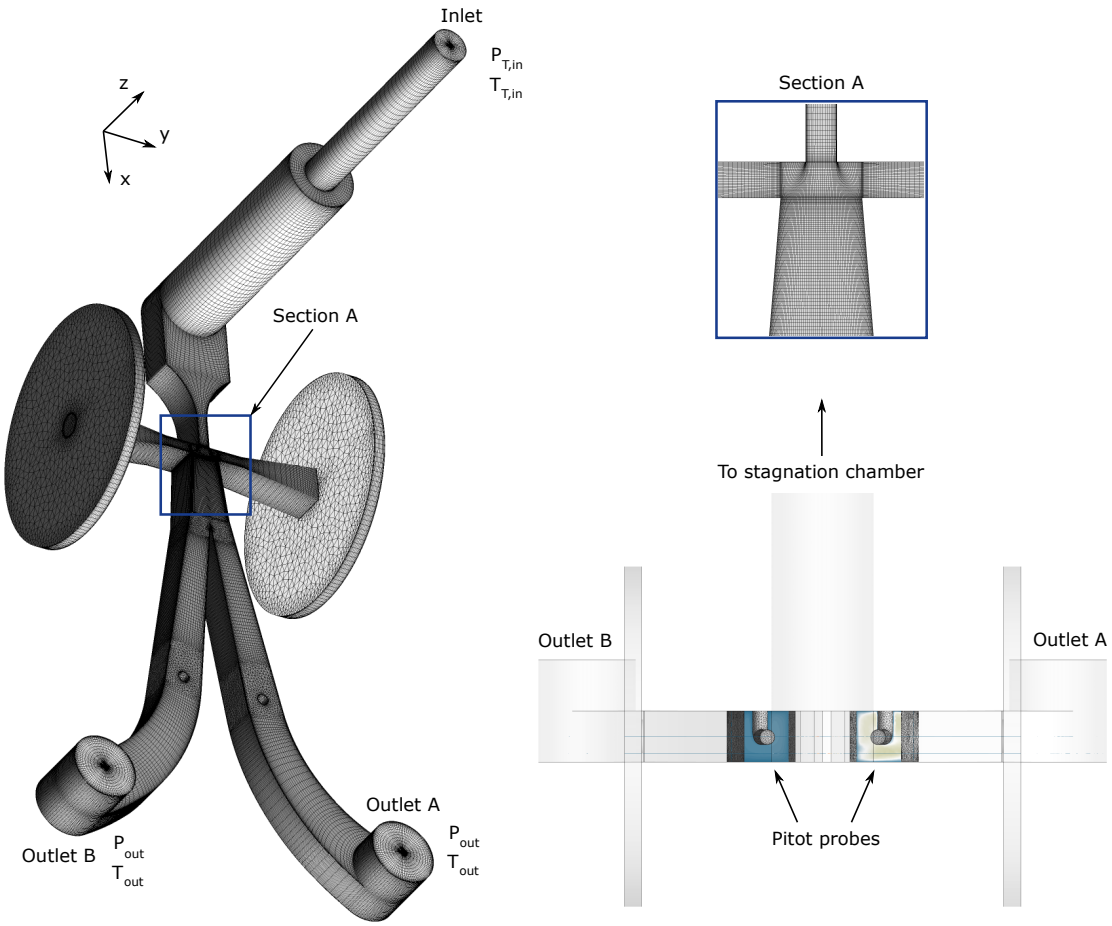

Figure 3.9: Grid topology of grid A1

3.2.1.4 Mesh and Computational Details

All CFD simulations carried out in this study use the element-based finite-volume method code ANSYS CFX. All LES are further initialized using fully converged steady state results (RANS). The turbulence model for the RANS simulations is Menter's SST (Shear Stress Transport) model since the present fluid domain contains

both a wall bounded flow and free shear layer.[5] The spatially filtered Navier-Stokes equations are advanced using a second-order accurate implicit method in time and are discretized by the second-order central difference scheme in space. The subgrid-scale stresses are modelled using the wall-adapting local eddy-viscosity model [252] since it returns a zero turbulent viscosity for laminar shear layers ($C_w = 0.325$).[6] The fluid obeys the equation of state for an ideal gas. The boundary conditions at the inlet are total pressure and temperature as measured experimentally inside the stagnation chamber. Atmospheric conditions are employed at both outlets A and B with the ability of flow entering through them. This allows the accurate modelling of a potential reverse mass flow.

Two device configurations will be studied numerically; The low-frequency device and the splitter-less ultrasonic device. For each device a truncated as well as a full-scale model will be used. The mesh for the low-frequency device is referred to as grid A1 (A2), for the full-scale and truncated model respectively. The mesh for the ultrasonic device is consequently referred to as grid B1 (B2). The truncated models consist of the nozzle and the interaction region only. They are used to investigate the natural (unexcited) dynamics of the free shear layer. The grid topology of the full-scale models is hybrid. The mesh of the truncated models is fully structured.

The hybrid grid topology of the full-scale model (grid A1 - low frequency device) is shown in Fig.3.9 and consists of 1.2 million cells (40 mesh points spanwise resolution) with $y^+ < 1$ for all walls apart from the nozzle side walls in z-direction. Given that the result for Large Eddy simulations are grid-dependent by definition, the computational domain requires thorough meshing with respect to the governing flow features. The spatial and temporal accuracy of the solution can be validated by means of the Courant-Friedrichs-Lewy (CFL) number [253] which relates flow velocity u, time step

[5]The SST mode switches between the $k-\omega$ and $k-\epsilon$ model such that $k-\omega$ is used for an accurate near wall treatment and $k-\epsilon$ for free shear flows [251].

[6]Recall that the range of Reynolds numbers used for the low-frequency device lies within $250-2500$

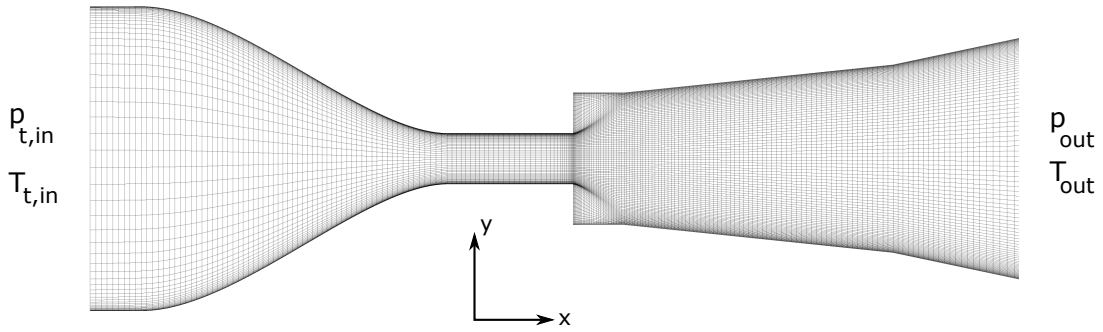

Figure 3.10: Grid topology of grid A2

Δt and grid spacing Δx so that

$$CFL = \frac{u\Delta t}{\Delta x} \tag{3.10}$$

The time step Δt of all LES regarding the low-frequency device is set to $1 \cdot 10^{-5}\, s$ so to obtain a maximum CFL number close to unity. This means that a fluctuating sequence of the energy containing features of the flow (around $3\, kHz$[7]) are represented by 30 time steps. Apart from the CFL number the mesh quality can also be examined by means of Kolmogorov's hypothesis which states that the energy cascade of turbulent eddies follows a power law ($-5/3$ slope) until turbulent kinetic energy is dissipated into heat [254]. In this regard, the power spectral density (Fig.3.11) shows that the grid resolves scales in the inertial sub-range of up to $10\, kHz$ and therefore captures the transfer of energy well beyond the integral scale. To further verify the quality of the mesh used herein Fig.3.11 also shows the resolved energy spectrum of a second grid with twice as many cells (grid A1+). The energy cascade of both grids is in good agreement with Kolmogorov's hypothesis and thus shows grid-convergence. The numerical error associated with grid resolution is therefore

[7]This belongs to the excitation frequency of the reference case that will be considered in this study

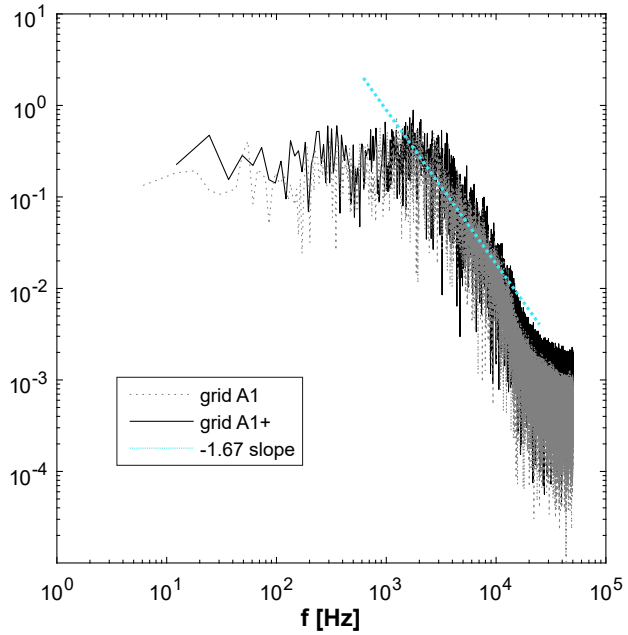

Figure 3.11: Resolved energy spectrum measured at $\frac{x}{h} = 7$ inside the unattached shear layer for grid A1 and A1+. The $-5/3$ slope indicates the theoretical energy cascade as depicted by Kolmogorov's hypothesis.

assumed to be insignificant. A further quality check of the computational model is performed by comparing the numerically obtained mass flow rates (determined by $p_{T,in}$) with the mass flow rates set experimentally. The time-averaged LES results are shown in Fig.3.12 For the given pressure ratios the mean difference in mass flow rate amounts to less than 1.6%.

With respect to the grid topology of the ultrasonic device (grid B1 and grid B2), it was chosen to predetermine the required grid spacing Δx based on the smallest expected length scales. This is done by calculating the Kolmogorov length scale $\eta = (\frac{\nu^3}{\epsilon})^{0.25}$, the scale at which viscosity dominates the flow and kinetic energy is dissipated into heat. The turbulence dissipation rate ϵ is further estimated using RANS simulations of the truncated model. The grid for the RANS simulation (grid B-R) consists of $0.7 \cdot 10^6$ cells with a maximum mesh expansion factor of 2 and a dimensionless wall distance in y-direction smaller then unity. Since a truncated model is used there is no reason to use the experimentally measured pressure ratios

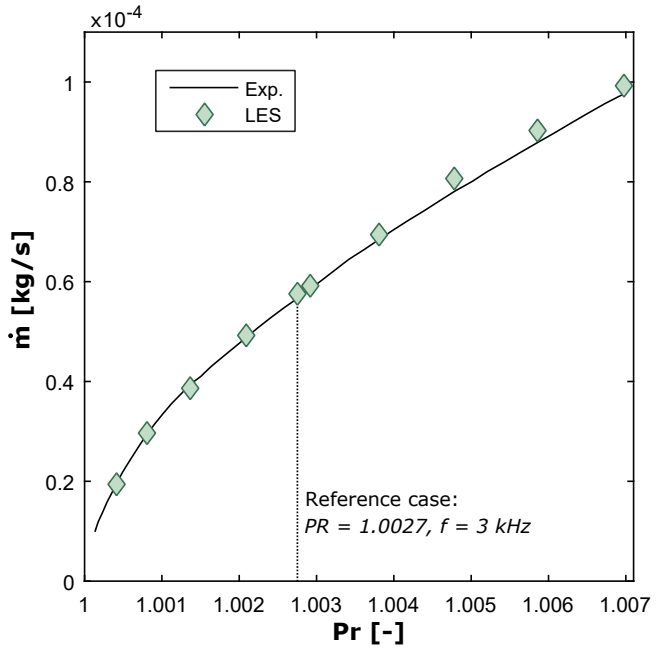

Figure 3.12: Steady state characteristic - comparison of mass flow rates between experiments and time averaged LES results

(across the full device) as boundary conditions for the numerical model. Inlet total pressures were thus chosen rather arbitrarily but, at the same time, adjusted so as to match the mass flow rates $\dot{m}_{Exp.}$ to within 4%. All mass flow rates $\dot{m}_{1-10}$ obtained from both LES and experiments are summarized in Tab.6.1.

Table 3.3: Mass flow rates through the truncated model ($\dot{m}\,(LES)$) and the full-scale device ($\dot{m}\,(Exp.)$) as set during the experiments in Sec.6

	1	**2**	**3**	**4**	**5**	**6**	**7**	**8**	**9**	**10**
$\mathbf{Pr}\,(\mathbf{Exp.})[-]$	1.041	1.048	1.055	1.061	1.068	1.076	1.084	1.093	1.103	1.112
$\dot{\mathbf{m}}\,(\mathbf{Exp.})[\mathbf{g/s}]$	0.298	0.319	0.340	0.361	0.383	0.404	0.425	0.446	0.468	0.489
$\dot{\mathbf{m}}\,(\mathbf{LES})[\mathbf{g/s}]$	0.303	0.326	0.350	0.374	0.395	0.418	0.440	0.460	0.487	0.508
$\mathbf{\Delta\dot{m}}\,[\%]$	1.89	2.10	2.83	3.26	3.12	3.42	3.32	2.99	3.93	3.85

A conservative guess of the Kolmogorov length scale is then obtained by computing ϵ_{max} for each flow rate $\dot{m}_1 - \dot{m}_{10}$. A grid-spacing to Kolmogorov length ratio of 30 is then used to assure that the average filter width Δ_x is at the lower end of the inertial sub-range [255]. For the flow rates used in the ultrasonic splitter-less device this amounts to an absolute grid-spacing ranging from $0.12\,mm$ to $0.08\,mm$. The

grid topology for the LES mesh is therefore set to have an average grid-spacing in x-direction of $0.1\,mm$. The simulation is advanced in time with $\Delta t = 2 \cdot 10^{-6}$ which yields a CFL number of less than unity inside the interaction region and an average across the domain of 1.4 and 2 for the lowest and highest flow rates, respectively. The LES mesh of the truncated model (grid B2) is then extended by the two outlets and the control port chambers. The hybrid grid topology of the full-scale device (grid B1) is shown in Fig.3.13. Information of all three grids is further summarized in Tab.3.4.

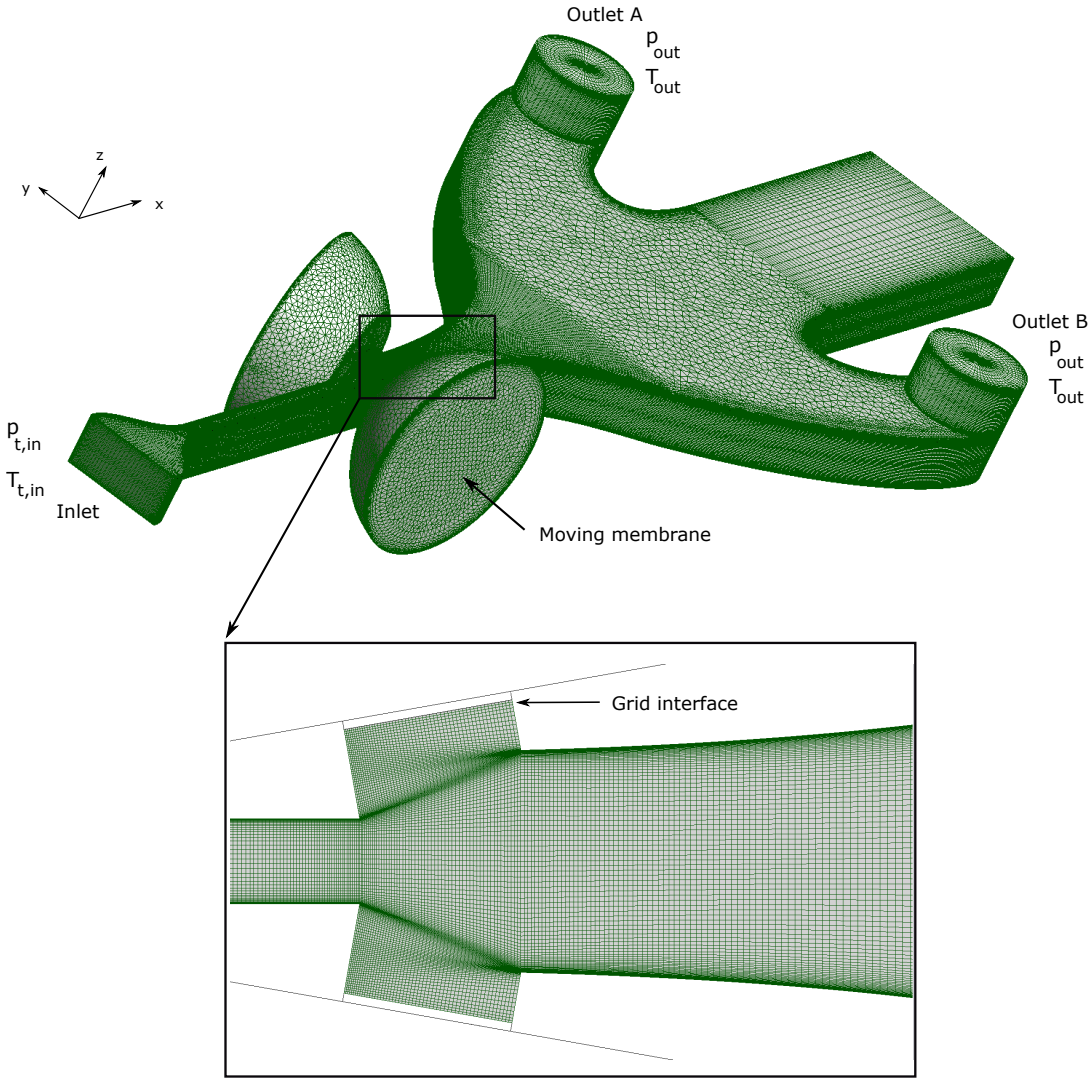

Figure 3.13: Grid topology of grid B1 and B2

The quality of the mesh (grid B1) is additionally examined by means of Kol-

Table 3.4: Additional mesh information

Grid	**Model**	**Cell count**	$\mathbf{\Delta_x}$ [**mm**]	$\mathbf{y^+}$ [$-$]	$\mathbf{z^+}$ [$-$]	$\mathbf{\Delta t}$ [μ**s**]
B-R	SST	$0.7 \cdot 10^6$	0.2	< 1	< 20	-
B1	WALE	$1.4 \cdot 10^6$	0.1	< 1	< 15	2
B2	WALE	$3.4 \cdot 10^6$	0.1	< 1	< 15	2

mogorov's hypothesis, as it was done for grid A1 and A2. In this regard, the power spectral density shown in Fig.3.14 shows that the LES grid resolves scales in the inertial sub-range of up to $80\,kHz$ and hence length scales that are multiple times smaller than the integral scale. Numerical errors associated with grid resolution are therefore assumed to be insignificant. The initial guess for the maximum dissipation rate obtained by RANS simulations (grid B-R) is retrospectively validated by LES results. The difference in ϵ_{max} between LES and RANS amounts to less than 1.9% for all flow rates.

The Piezo transducer generating acoustic excitation is directly modelled using a moving membrane fixed at its perimeter. The time and radius depending mesh displacement is expressed by [256]

$$\delta(r,t) = \frac{\Delta}{2} \cdot \left[1 - \frac{r^2}{r_M^2} + \frac{2r^2}{r_M^2} \cdot ln\Big(\frac{r}{r_M}\Big)\right] \cdot sin(2 \cdot \pi \cdot f \cdot t) \tag{3.11}$$

Here Δ states the maximum displacement and r_M the outer radius of the membrane. The maximum displacement is further set so that the experimentally measured value of $\hat{p}$ is matched. This is done at ambient conditions without any flow through the device ($Pr = 1$). The membrane displacement δ is exemplarily shown for different values of t in Fig.3.15.

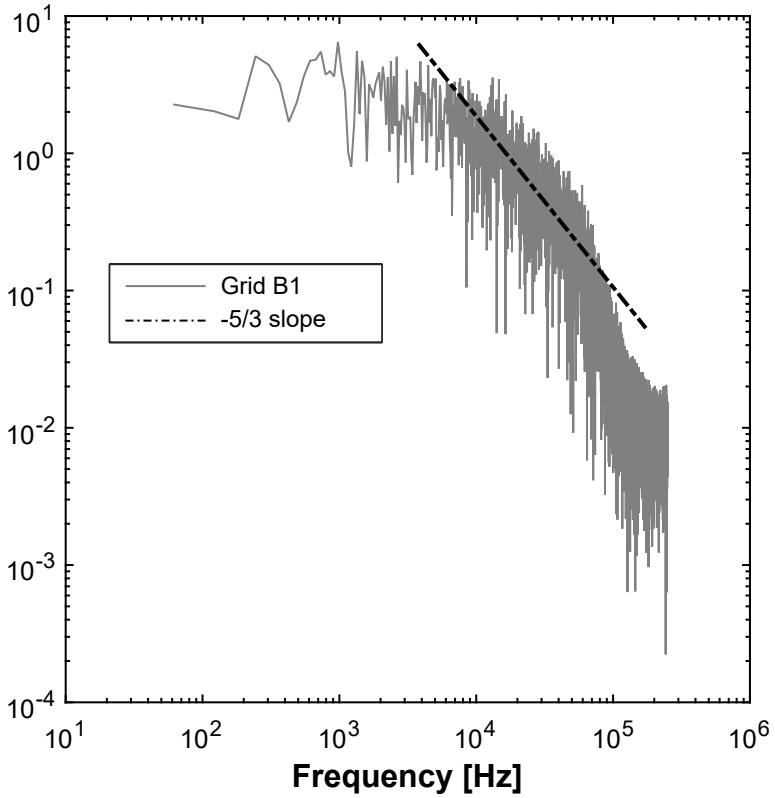

Figure 3.14: Resolved energy spectrum measured at $x = 7h$ inside the unattached shear layer for Grid B1. The -5/3 slope indicates the theoretical energy cascade as depicted by Kolmogoro's hypothesis

3.2.2 Acoustic Simulation

3.2.2.1 Governing Equations

Acoustic simulations will be performed to examine the eigenfrequencies of the control port chambers of the ultrasonic device. This is done by solving the time-independent form of the wave equation. The time-independent wave equation, also referred to as Helmholtz equation, can be derived by the the wave equation for sound waves in a lossless medium which reads as

$$\frac{1}{\rho c^2}\frac{\partial^2 p}{\partial t^2} + \frac{\partial}{\partial x_i} \cdot \big[-\frac{1}{\rho}(\frac{\partial}{\partial x_i} p - q_d)\big] = Q_m \tag{3.12}$$

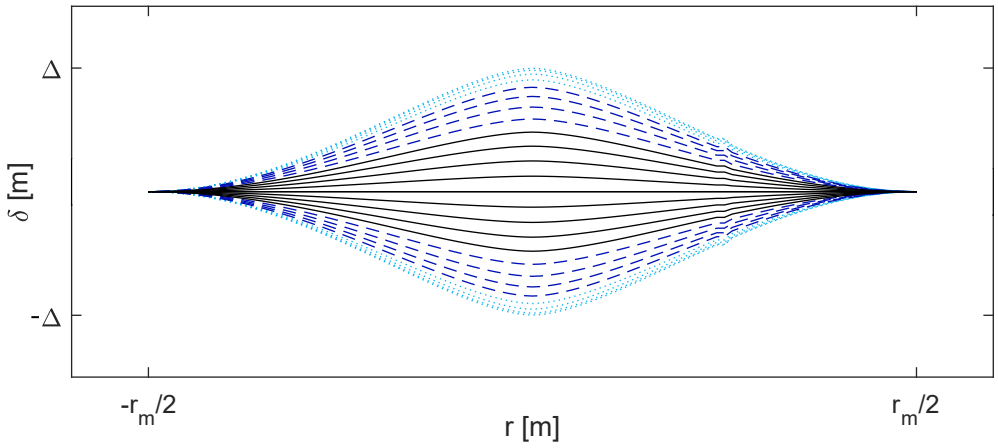

Figure 3.15: Membrane displacement according to Eq.3.11

where q_d and Q_m are optional dipole and monopole source terms, respectively. For a time-harmonic wave the wave equation is in fact separable meaning that

$$p(x_i, t) = p(x_i) \cdot e^{i\omega t} \tag{3.13}$$

where $i^2 = -1$ and $\omega = 2\pi f$. Neglecting a dipole source and assuming that the monopole source term has the same harmonic time-dependence, Eq.3.12 reduces to

$$-\frac{1}{\rho}\frac{\partial p^2}{\partial x_i^2} - \frac{\omega^2 p}{\rho c^2} = Q_m \tag{3.14}$$

This is called the time independent wave equation. In order to model an acoustic membrane, the monopole source term can be defined as a pressure boundary condition. The result of a frequency domain analysis at any point in time is then a complex time dependent pressure field

$$p = \hat{p}\, cos(2\pi f \cdot t + p_p) \tag{3.15}$$

where p_p represents the phase angle and $\hat{p}$ the pressure amplitude [257].

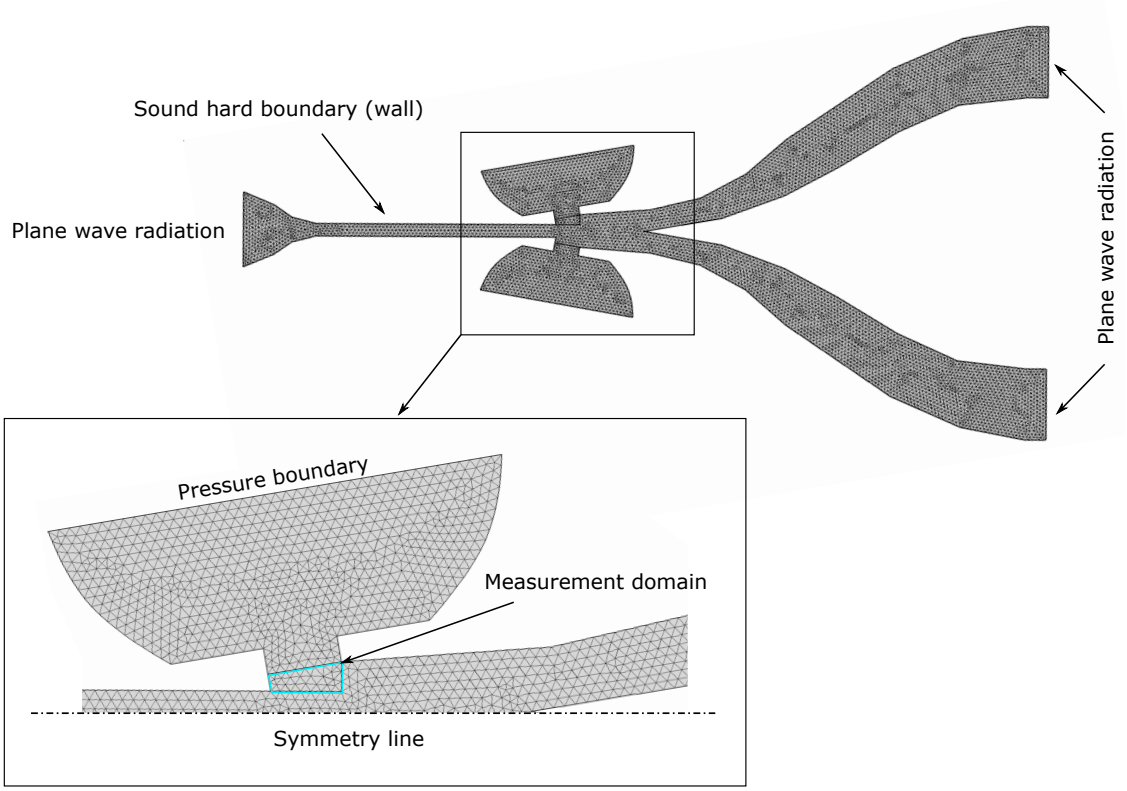

Figure 3.16: Grid topology of the acoustic model

3.2.2.2 Mesh and Computational Details

Modelling an acoustic wave requires a mesh density with at least 2 cells per wavelength (Nyquist criterion). However, given that the size of the FSD is relatively small, a considerably finer mesh using ≈ 45 cells per wave length (for $f = 25\,kHz$) can be used without scarifying on computing time. This corresponds to a maximum cell size of $0.3\,mm$. The unstructured grid topology is exemplarily shown for the full-scale device (splitter configuration) in Fig.3.16. Simulations are carried out at frequencies ranging from $18-40\,kHz$ with steps of $50\,Hz$. All simulations are further performed in $2D$ only. The membrane is modelled as a pressure boundary condition with $p = 1\,Pa$. Walls are modelled as reflecting sound hard boundaries. Inlet and outlets are modelled as plane wave radiation boundaries. A separate measurement domain at the location at which the sound wave interacts with the shear layer is used to compute the mean

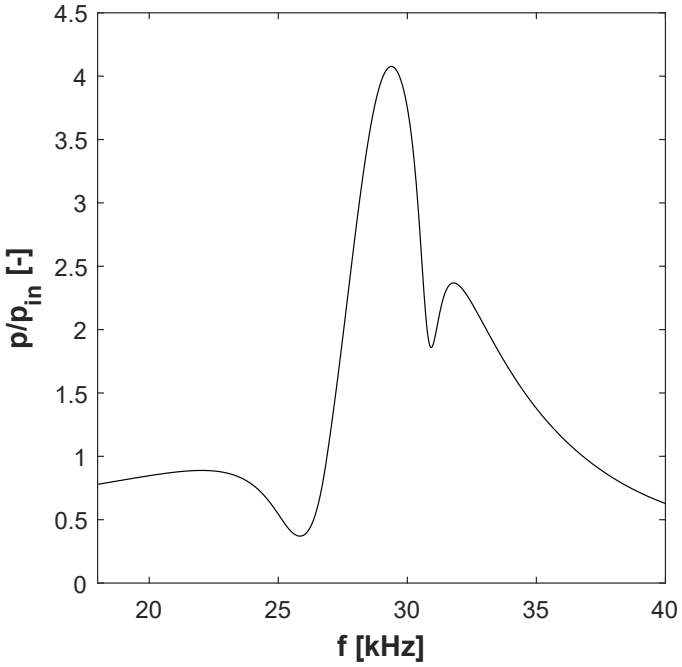

Figure 3.17: Frequency response of an input pressure $p_{in} = 1\,Pa$ inside the measurement domain

pressure amplitude, the absolute value of Eq.3.15, as a function of f. An example for the input pressure amplification is shown in Fig.3.17. Various control port chamber designs and there impact on the pressure amplification in the frequency domain will be investigated in Chapter 5.

Chapter 4

Thoughts on Jet Instability Modes

4.1 Introduction

As discussed in Chapter 2, jet instability modes have been the subject of numerous fundamental flow control studies since the discovery of coherent motion in turbulent flow more than half a century ago. This is hardly surprising given that they play a major role in entrainment, transition to turbulence or the development of small- and large-scale structures. The two non-dimensional frequencies found to be inherent in all Reynolds number jets, the jet preferred mode and the shear layer mode, have here caused quite some confusion with respect to their non-dimensional value, dpenendency on each other as well as their general existence. The duality of those instability modes is the subject of this chapter. Although this topic is not directly linked to fluidic devices, the main subject of this thesis, it was decided to conduct a more fundamental study in order to shed some light onto the uncertainties surrounding the jet preferred mode.

Here, the approach taken is to identify the jet preferred mode based on the jet response to acoustic excitation for different initial conditions but constant Re using Particle Imaging Velocimetry. To the author's best knowledge this is the first study

of its kind. However, it is important to note that this study is bound to be incomplete given the large scope and significance of initial conditions themselves. Drubka [88], for instance, dedicated his entire thesis to instabilities in the near field of turbulent jets and their dependence on initial conditions. Nonetheless, this chapter tries to unravel the link between the shear layer mode and the jet preferred mode.

4.2 New Hypotheses of Instability Interaction

Based on the dicussions made in Chapter 2 the three hypotheses proposed here can be summarized as follows:

1.) The jet preferred mode is not a local shear layer instability and hence not related or dependent on the most unstable mode of a jet

2.) The jet preferred mode can only be identified by some kind of artificial forcing

3.) The huge scatter of the jet preferred mode Strouhal number reported in the literature is in fact the variation of a subharmonic of the shear layer roll-up frequency due to differences in initial conditions

On the basis of those hypotheses it was decided to conduct an experiment in which the response of an acoustically excited free circular jet is investigated with respect to different initial conditions. Different initial conditions, i.e. different nozzle exit velocity profiles at constant Re, affect the shear layer roll-up frequency and hence the frequency of paired vortices [258]. The effect of different velocity profiles on the shear layer development was also investigated by Xu & Antonia [259], though, without forcing. They showed that a larger initial shear layer thickness produces a dimensionally lower frequency instability that results in vortical structures that develop and pair further downstream. It would then be an indication that the jet preferred mode is independent of the shear layer mode if the response of the jet to

acoustic excitation shows a preference at the same Strouhal number (St_D) despite changes in the initial conditions. However, irrespective of all plausible arguments supporting that hypothesis one might also argue that the power spectrum at the end of the potential core still shows the same spectral peaks despite different initial roll-up frequencies. A constant preferred mode Strouhal number would therefore not necessarily indicate that the jet preferred mode is independent of the shear layer mode. This again is further complicated by the fact that the end of the potential core shifts upstream as the initial momentum thickness decreases. Thus the question arises at which downstream location the spectral peaks should be compared to each other. Nonetheless, it will be shown later that the results of this study do not support this argument. Besides all that, there is also no lack in controversy in the open literature regarding the effect of initial conditions themselves. While Xu & Antonia [259] found no effect of initial conditions on the self similar region of a jet ($x > 30D$) but clear differences in the near field, Hussain & Zedan [260, 261] as well as George [262] found substantial differences in all regions of the jet.

The manner of changing the initial conditions as well as the choice of the experimental parameters will be highlighted in the following. Results will be presented thereafter.

4.3 Choice of Experimental Parameters

The experimental facility used in this study limits the choice of the experimental parameters such as Re, f_{ex} or D. This is because the laser sheet used for PIV has a finite width of $\approx 30\,mm$. Given that at least one nozzle diameter on either side of the jet ought to be within the interrogation window the maximum orifice size should not exceed $10\,mm$. It was opted for a nozzle diameter of $7.5\,mm$ in order to capture spreading angles that lead to a jet width of more than $3D$ within the region of interest. The centreline velocity u_c was chosen so that a root-mean-square sinusoidal surging

of up to 2% of the exit speed could be achieved [3]. This is further based on the maximum amplitude $\hat{p}$ that can be achieved for all frequencies within the bandwidth of the acoustic speaker. With $\hat{p} = 133\,dB$ this leads to

$$u_c = \frac{u'}{0.02 \cdot \sqrt{2}} = \frac{\hat{p}}{\rho c \cdot 0.02 \cdot \sqrt{2}} \approx 8\frac{m}{s} \tag{4.1}$$

This in turn leads to a hypothetical preferred excitation frequency of $320\,Hz$ ($St_D = 0.3$) and a Reynolds number of 4000. To cover a sufficient range of frequencies below and above the jet preferred mode the excitation frequency f_{ex} will be varied from 80 to $640\,Hz$ in steps of $20\,Hz$. Different initial conditions at the nozzle orifice are then obtained by simply changing the nozzle length. The four nozzle lengths l_N considered in this study are 7, 11, 38 and $80D$. The velocity profile for the smallest nozzle is nearly irrotational and features a relatively small momentum thickness θ. The longest nozzle, in contrast, has a more fully developed velocity profile with a larger momentum thickness at the orifice. This will be shown later. The jet velocity is kept constant for all l_N and the non dimensional excitation frequency is varied from $St_D = 0.1$ to 0.6. The preferred mode Strouhal number is then identified by means of the jet response as a function of St_D. The upstream shift of the end of the potential core as well as the widening of the shear layer serve here as a quantitative measure of the jet response. A microphone $2D$ downstream of the nozzle exit ensures a constant sound pressure level of $133\,dB$.

4.4 Flow Visualisation Studies

4.4.1 Unforced Jet Dynamics

The jet dynamics of the baseline cases, i.e. no excitation, are presented first. This demonstrates the effect of initial conditions on the near field of a jet.

Fig.4.1 a.) and b.) show the centreline velocity decay at constant flow rate $\dot{m}$ and constant exit velocity u_0, respectively. At constant $\dot{m}$ it becomes apparent that the different nozzle lengths represent different stages during the development of a fully developed velocity profile. The centreline velocity for the shortest nozzle ($7D$) is 25% below the centreline velocity of the longest nozzle ($80D$). Given the conservation of mass this indicates a more uniform (top-hat) velocity profile for the nozzle with $l_N = 7D$. The velocity profile of the longest nozzle, in contrast, is fully developed (boundary layers have merged) since there is essentially no difference between the exit velocity u_0 for $l_N = 38D$ and $80D$. In order to maintain the same Reynolds number based on the centreline velocity at the nozzle orifice $Re = \frac{u_0 D}{\nu}$ the flow rate $\dot{m}$ has to increase as the nozzle length l_N decreases. As can be seen in Fig.4.1 b.) the flow rate $\dot{m} = f(l_N)$ is set so to keep the centreline velocity within 3% of $u_{0,ref} = 8\frac{m}{s}$.
The end of the potential core x_{pc} varies between $\approx 3D$ and $\approx 3.5D$ in both figures a.) and b.) (when based on $u_{x_{pc}} = 0.95u_0$ as done in [263]). This is in perfect agreement with the results from Grandchamp & Hirtum [263] who investigated two different nozzle lengths $l_N = 1.2D$ and $53.2D$ and obtained a normalized potential core extent of $\frac{x_{pc}}{D} = 2.9$ and 3.3 for the same Reynolds number $Re = 4000$, respectively.
Note that the dashed lines in Fig.4.1 represent the smoothed centreline velocity decay which will be used for all future calculations regarding the length of the potential core.

The effect of the different nozzle lengths on the downstream development of the jet becomes even more apparent if the velocity profiles normal to the flow direction are considered. This can be seen in Fig.4.2 which shows the radial velocity distribution for different axial positions $\frac{x}{D}$ and different nozzle lengths l_N. There is no noticeable difference between the relative decay of the jet centreline velocity for both nozzle lengths upstream of $\frac{x}{D} = 2.5$. However, it is evident that the centreline velocity of the shorter nozzle ($l_N = 7D$) decays faster downstream of that. This is shown by a

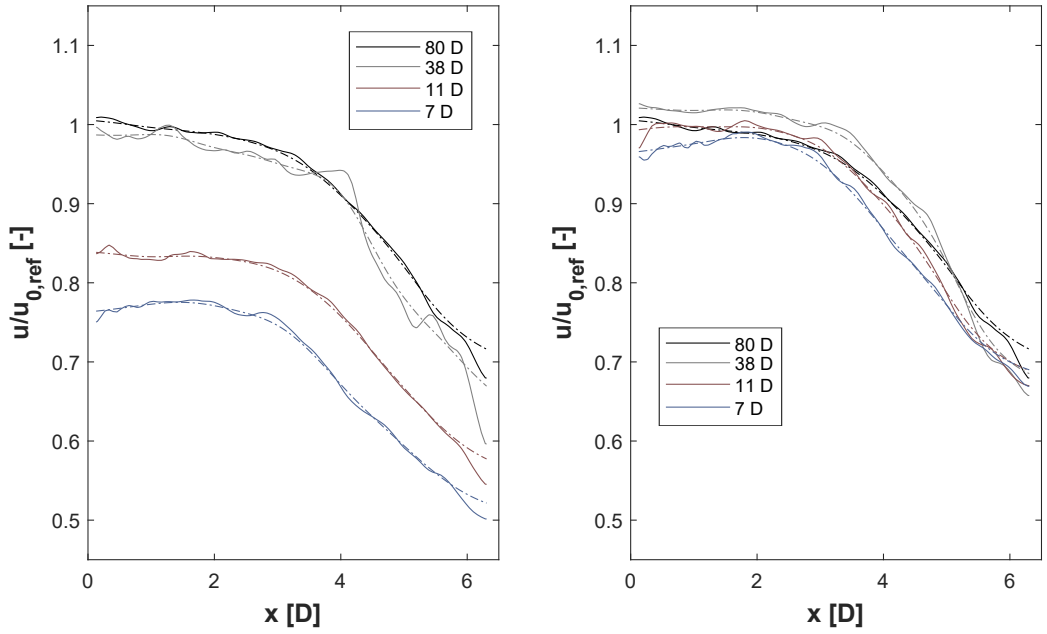

(a) constant $\dot{m}$ (b) constant $u_{0,ref}$

Figure 4.1: Centreline velocity decay for different nozzle lengths

slight difference at $y = 0$ and $x > 2.5D$. However, even more obvious are the different shapes of the velocity profile especially at $\frac{x}{D} = 1$. The shorter nozzle exhibits a more uniform velocity distribution around $y = 0$ resulting in greater shear. This again leads to higher vorticity and hence an earlier roll-up of the shear layer. In addition, the frequency of the shear layer roll-up also increases with respect to a longer nozzle since the momentum thickness at the nozzle orifice is smaller. An earlier roll-up as well as a higher frequency ultimately leads to more entrainment and hence to a wider shear layer and a faster decay of u_0. The spreading of the shear layer for all four nozzle lengths as a function of x is shown in Fig.4.3. It can be seen that a shorter nozzle length causes a larger shear layer for $\frac{x}{D} > 3.5$ indicating that $\frac{d\theta}{dx}$ increases as the nozzle length decreases. This is again a measure for the entrainment rate as well as the spreading angle. One can conclude that a shorter nozzle increases the shear layer roll-up frequency, shifts the roll-up location further upstream and causes a faster decay of u_0 which is synonymous to a wider shear layer, higher $\frac{d\theta}{dx}$ or enhanced entrainment. This is again in perfect agreement with previous results obtained by,

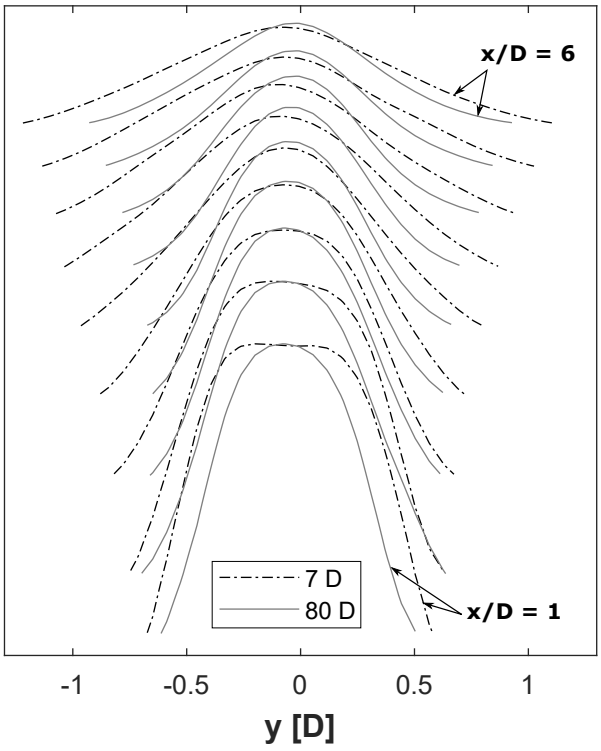

Figure 4.2: Radial velocity profile at different downstream locations

for instance, Russ & Strykowski [258], Xu & Antonia [259] or Kim & Choi [89] who showed that an increase in the initial boundary layer thickness leads to an increase in the streamwise location where vortices start to roll up and undergo pairing as well as a decrease in the instability frequency.[1]

It was also mentioned previously that the possibility exists that the frequency at the end of the potential core remains the same despite a change of the initial conditions. This assumption is indeed not completely unjustified since a lower momentum thickness at the nozzle orifice (shorter nozzle) is shown to cause a higher $\frac{d\theta}{dx}$ which in turn leads to the fact that at some downstream location x_x the momentum thickness of each shorter nozzle will coincide with momentum thickness of the longest nozzle. Now, if the ratio $\frac{u_{0,x_i}}{\theta_{x_i}}$ at x_x is constant and x_x further corresponds to the end of the

[1]This, on a side note, confirms what was said in the previous chapter about the link between $\frac{D}{\theta}$ and the location of the shear layer roll-up. As the Reynolds number goes up, the roll-up location moves upstream and approaches the nozzle orifice until $\frac{D}{\theta}$ reaches an asymptotic value.

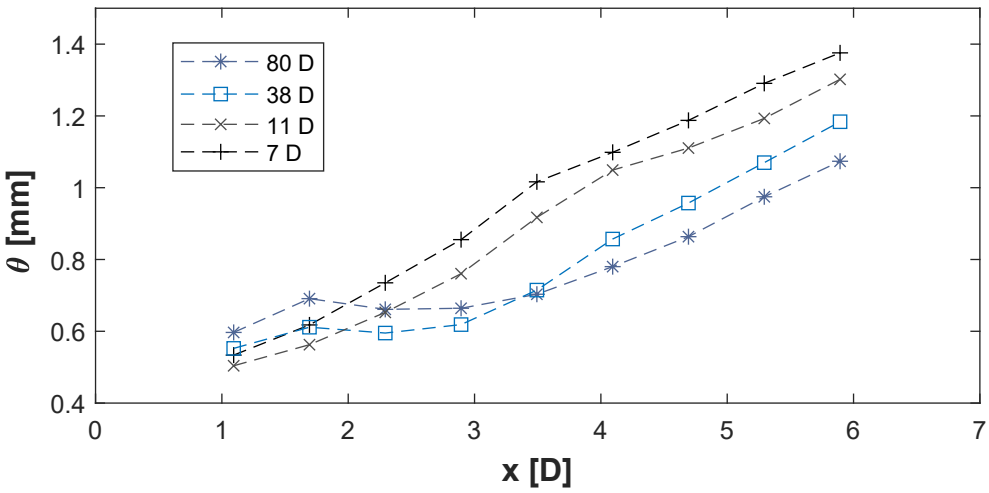

Figure 4.3: Boundary layer momentum thickness at different downstream locations

potential core - *assuming that the non-dimensional vortex passage frequency based on the local momentum thickness θ is constant along x* - the frequency at the end of the potential core would be the same for each nozzle length and different initial conditions. A constant jet preferred mode Strouhal number ($St_D = 0.3$) would therefore not indicate whether the preferred mode is independent of the shear layer mode or not. However, the results obtained from the present experiments do not show such a behaviour. This is shown in Fig.4.4. The initial roll-up frequency is shown to be higher for all shorter nozzle lengths with respect to $l_N = 80D$. The bigger gradient of $\frac{d\theta}{dx}$ for shorter nozzles causes the ratio $\frac{u_{0,x_i}}{\theta_{x_i}}$ and hence the vortex passage frequency to decrease faster. The location $\frac{x_x}{D}$ at which the passage frequency of $l_N = 7, 11$ and $38D$ matches the frequency of $l_N = 80D$ varies from 2 to 3.7 and therefore doesn't coincide with the respective ends of the potential cores ($\frac{x_{pc}}{D} = 3 - 3.5$). The difference in $\frac{u_{0,x_i}}{\theta_{x_i}}$ at x_{pc} between $l_N = 7D$ and $l_N = 80D$ is not huge and one might hesitate to draw a definite conclusion. However, Antonia & Zhao [264] also conclude that there is a difference in the vortex passage frequency at x_{pc} for different initial conditions, albeit not huge. Most striking for the present author is that the frequency of passing vortices at the end of the potential core decreases as the nozzle lengths decreases.

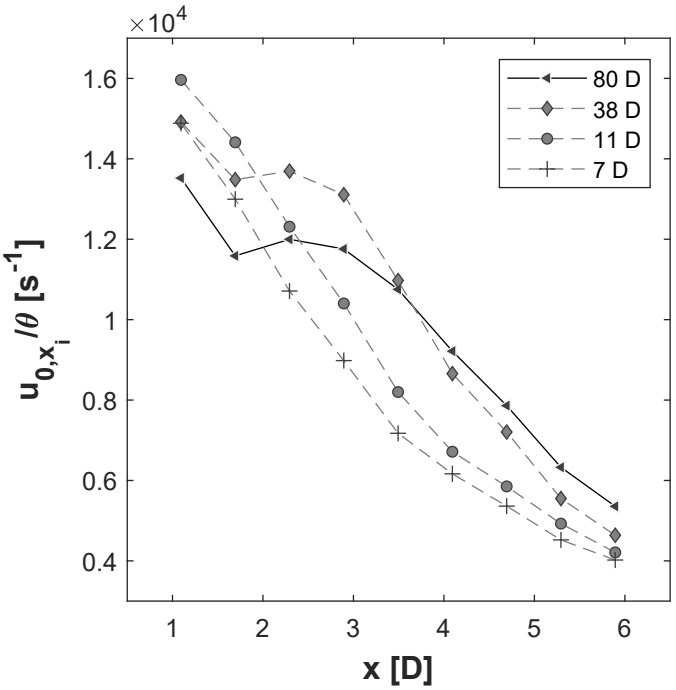

Figure 4.4: $\frac{u_{0,x_i}}{\theta_{x_i}}$ as a measure for the vortex passage frequency along x assuming a constant non-dimensional frequency St_θ

This can only mean that the more uniform velocity profiles with greater shear lead to more pairing events. Here, Fig.4.4 reveals that there are no pairing events for $l_N = 80D$ but at least one pairing event for, for example, $l_N = 11D$. This is seen by the halving of $\frac{u_{0,x_i}}{\theta_{x_i}}$ from x_0 to x_{pc}.

Having examined the effect of initial conditions on the natural jet dynamics the following highlights the dynamics under the combined effects of different initial conditions and acoustic excitation.

4.4.2 Excitation at Constant Jet Velocity

The effect of excitation on the flow field of the jet is exemplarily shown in Fig.4.5 and 4.6. The first two velocity vector fields correspond to the baseline case, i.e. no excitation, and $St_D = 0.3$, respectively. It is clearly evident that the excited jet features a shorter potential core and an increased spreading of the shear layer. Note that both

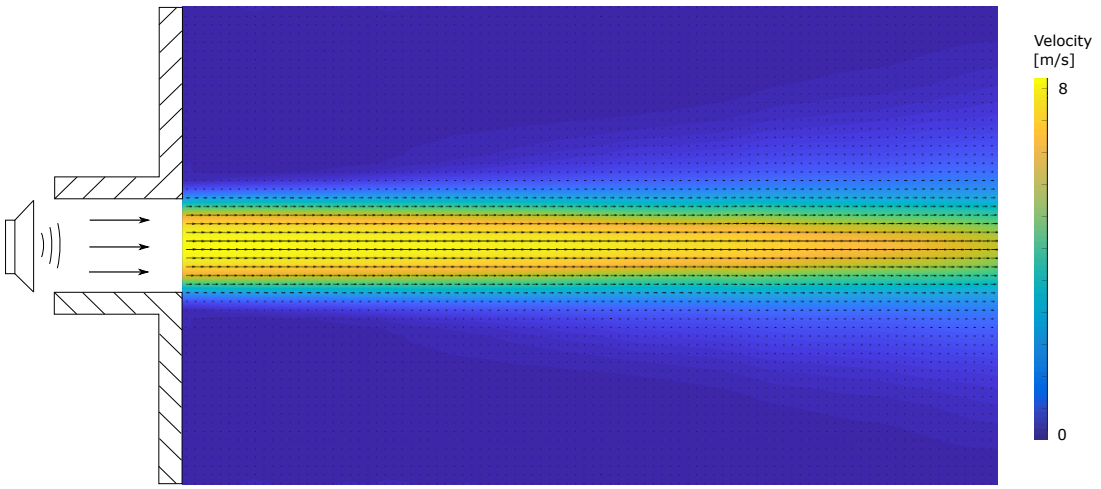

(a) Baseline

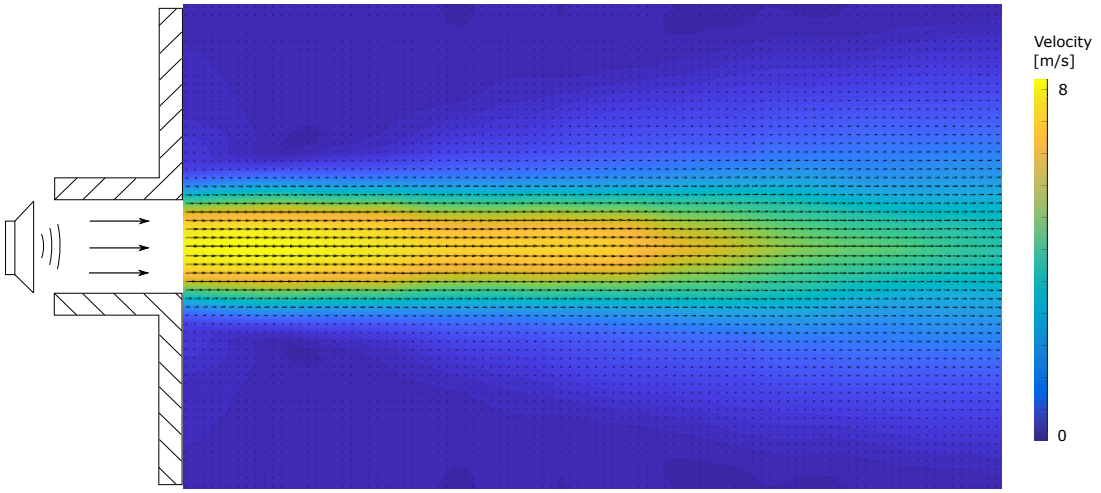

(b) $St_D = 0.3$ and $\frac{u'}{u_0} = 2\%$

Figure 4.5: Mean velocity vector field for $l_N = 80D$ and $u_0 = 8\frac{m}{s}$ using 200 image pairs

figures represent the average flow field using 200 image pairs taken at $f_s \approx 15\,Hz$.

Generally speaking, the roll-up of a natural shear layer is subject to natural disturbances in the flow and hence neither spatially nor temporally fixed. Acoustic excitation, however, causes the roll-up to be more coherent both in time and space. This becomes evident if one takes advantage of the effect of aliasing. This means that if the sampling frequency at which image pairs are recorded is set so that the excitation frequency is an integer multiple of it, one can spatially fix the dynamics of

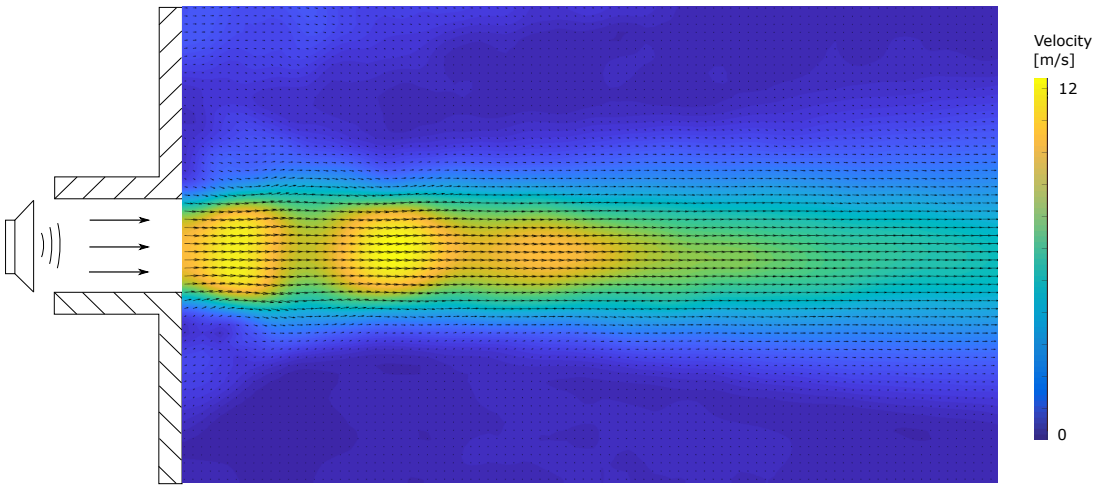

(a) Mean velocity field with $\frac{u'}{u_0} = 2\%$ and $St_D = 0.5$ (aliased sampling frequency)

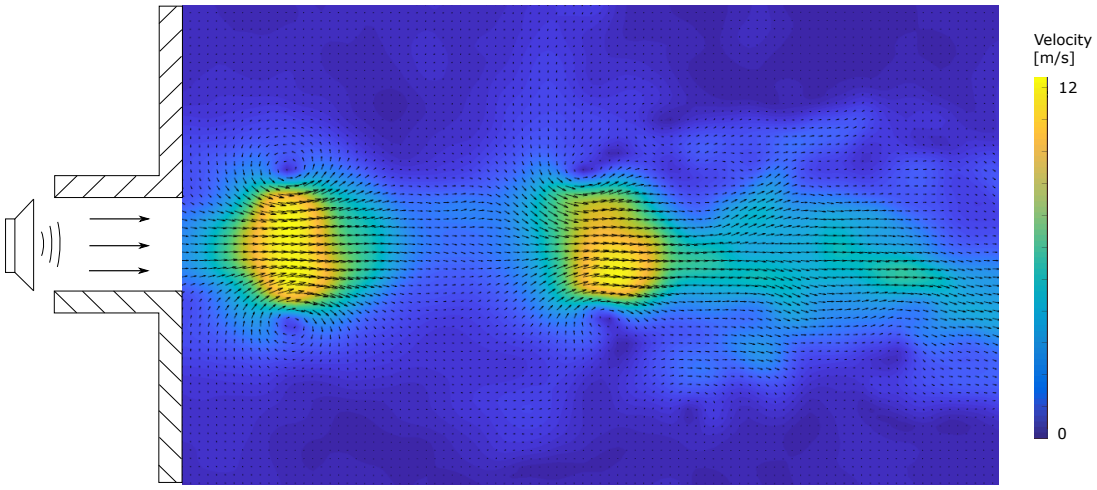

(b) Single snapshot with $\frac{u'}{u_0} = 12\%$ and $St_D = 0.3$

Figure 4.6: Velocity vector field for $l_N = 80D$, $u_0 = 8\frac{m}{s}$ and different excitation conditions

the shear layer for each image pair taken. This is exemplarily shown in Fig.4.6 a.). One can then, for instance, not only determine the number of vortices per unit time but also if vortices merge together. In the case of Fig.4.6 a.) it can be seen that three vortices (three velocity peaks along the centreline) are present at any time which also do not undergo pairing (distance Δx between the peaks is constant) and no coherent motion can be observed downstream of the last vortex. Furthermore, for all cases with excitation no pairing events were observed.

Although not relevant to the current investigation it was observed that the continuous inflow turns into a pulsating outflow with a flow response of $\frac{u'_r}{u_0} \approx 1$ at a sound pressure level of $146\,dB$. This corresponds to a forcing level of 12% and is seen in Fig.4.6 b.). The flow field resembles that of a synthetic jet with a superposition of net momentum. The nozzle orifice appears to expel axisymetric vortex rings with a momentum concentration in its centre. Furthermore, the vortex rings were observed to persist even beyond $\frac{x}{D} = 6$. The resulting flow field represents a pulsating flow at $320\,Hz$ which is a sensational finding that calls for further investigations and a possible application in fluidics.[2]

Quantitative data of the jet response to acoustic excitation with a forcing level of 2% is displayed in Fig.4.7 for $l_N = 80D$. The jet responds to nearly all excitation frequencies with enhanced mixing. This can be seen by a faster decay of the centreline velocity u_0 and an increase in the momentum thickness θ. At $St_D = 0.3$ the centreline velocity starts to decay almost immediately downstream of the nozzle orifice. The shear layer increase is marginal upstream of $\frac{x}{D} = 2.5$ but becomes more apparent downstream of that. At $\frac{x}{D} = 6$ and $St_D = 0.3$ the shear layer momentum thickness has grown by approximately 60% compared to the baseline case.

In order to plot the jet response as function of St_D based on the spreading of the shear layer, Fig.4.8 shows the difference in θ between each excited case and the baseline case. The values for $\Delta\theta$ are given in absolute numbers and correspond to the entire momentum thickness integrated from $-\infty$ to ∞. Each line in Fig.4.8 represents a different streamwise location x. It is obvious that the spreading of the shear layer is highest around an excitation frequency of $St_D = 0.3$. This is undoubtedly the preferred mode of the jet.

[2] A momentum-superimposed synthetic jet can either be used stand-alone or as the control method of a fluidic oscillator. Two control ports with acoustic speakers can be connected to the same pressure source as the oscillator and be driven 180 degree out of phase. The momentum bursts issuing from both control ports can alternately push the jet from one attachment wall to the other. This could result in a fluidic oscillator with arbitrary output frequency.

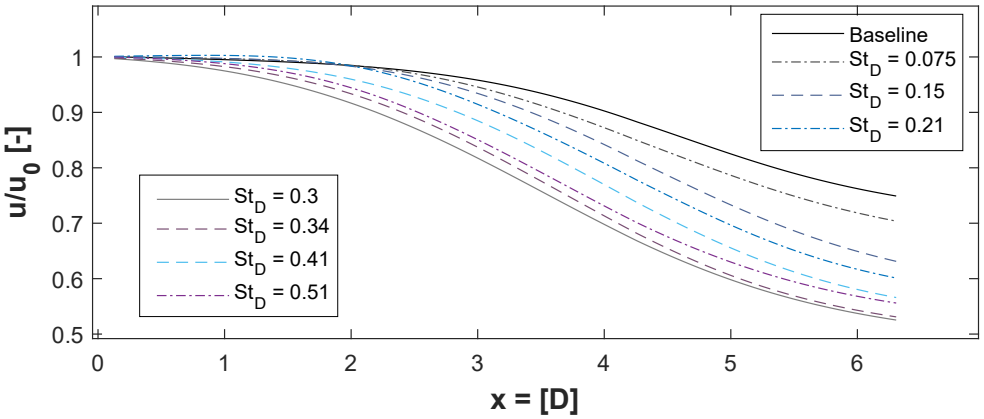

(a) Centreline velocity decay

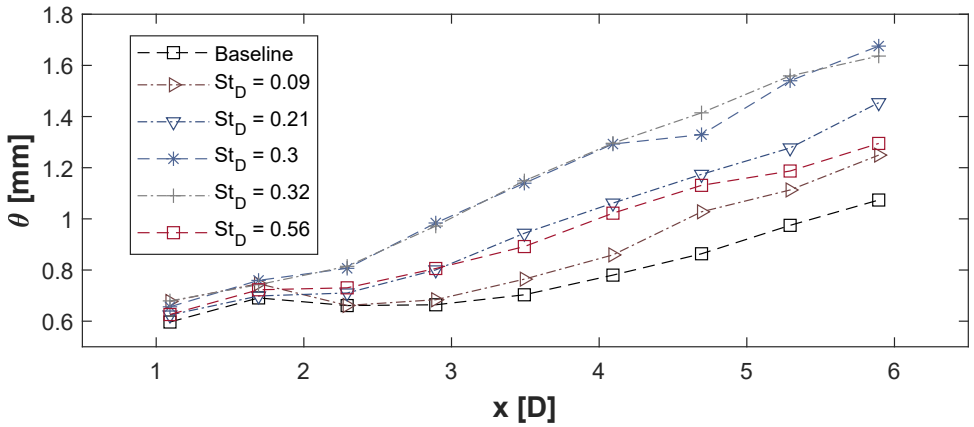

(b) Spreading of the shear layer

Figure 4.7: Flow response to acoustic excitation along x

The same conclusion can be drawn from Fig.4.9 a.) which shows the end of the potential core x_{pc} as a function of St_D. It is again obvious that the jet exhibits a maximum response at $St_D = 0.3$. Note that x_{pc} is here arbitrarily defined as the point where 90% of the initial centreline velocity u_0 is reached. Fig.4.9 b.) further shows the average difference in θ along x, i.e. the mean of Fig.4.8. It is clearly evident that both graphs serve as a good means to identify the jet preferred mode.

In order to examine the effect of initial conditions on the preferred mode Strouhal number the same set of experiments is repeated for each nozzle length l_N. Hence, the decay of the centreline velocity as well as the radial velocity profile at x_{1-9} is determined for each excitation frequency and different l_N. Unfortunately, no useful

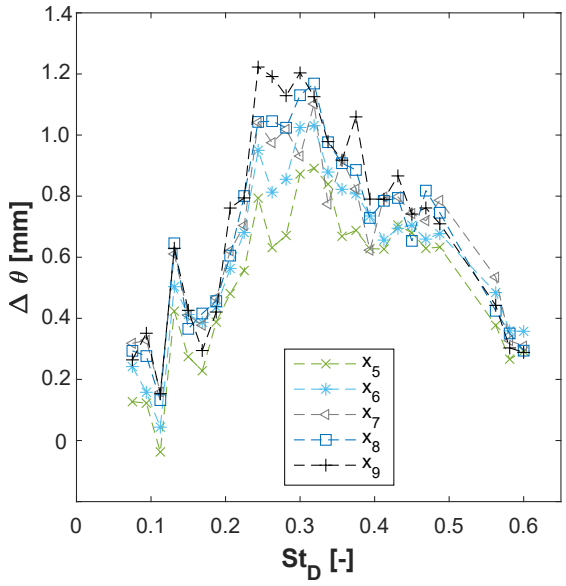

Figure 4.8: Increase in θ with respect to the baseline case as a function of Strouhal number. Different lines correspond to different downstream locations x_i

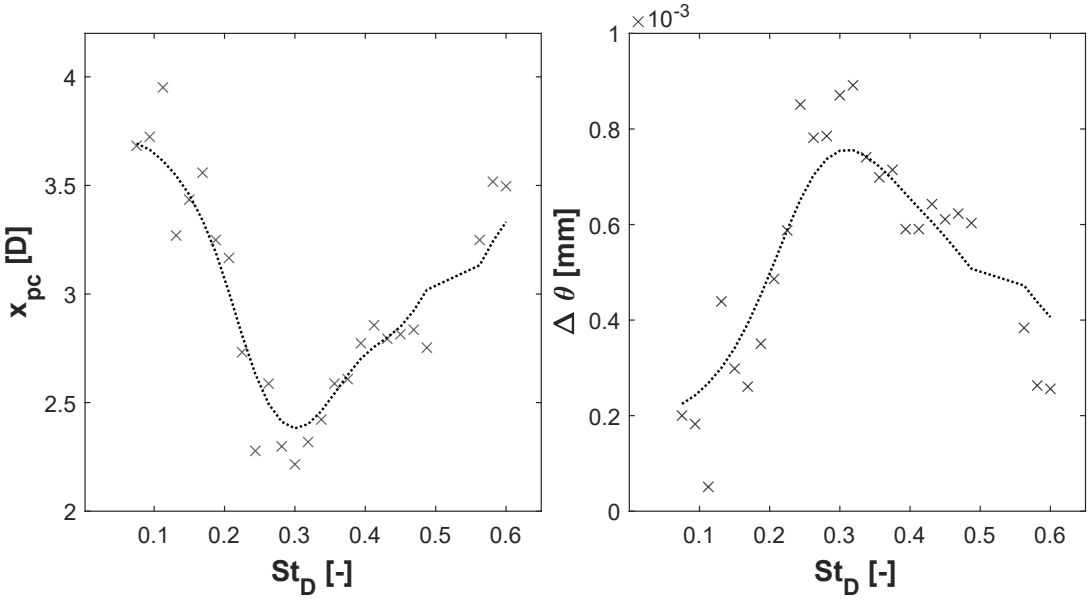

(a) Potential core length

(b) Average increase in θ

Figure 4.9: Jet response to acoustic excitation as a function of excitation frequency for $l_N = 80D$

data was obtained for $l_N = 7D$. The results for the remaining three nozzle lengths are summarized in Fig.4.10. The jet response for $l_N = 11D$ shows a strong preference at $St_D = 0.3$. Furthermore, the preference is stronger and much more pronounced

compared to $l_N = 80D$. The length of the jet potential core decreases from $x_{pc} = 3.5D$ at $St_D = 0.1$ to $x_{pc} = 1.5D$ at $St_D = 0.3$. There is no apparent effect of excitation around $St_D = 0.1$ and 0.6. The preference at $St_D = 0.3$ for $l_N = 11D$ is less obvious when the increase in θ along x is considered. The maximum spreading of the shear layer is seen to be around $St_D = 0.3$ but features a rather flat plateau up to $St_D = 0.5$. The overall difference to the baseline case is smaller compared to $l_N = 80D$. This is because the baseline case for the shorter nozzle already features a significant larger shear layer as it was seen in Sec.4.4.1. Apart from that, the response is seen to be almost the same between $St_D = 0.25$ and 0.35 which shows that the jet preferred mode can only be identified properly if a broad range of excitation frequencies is used. This is rarely the case for other studies done in the past. No distinction in the jet response could be made if the jet was only excited at frequencies between $St_D = 0.25$ and $St_D = 0.35$. This is even more pronounced when looked at the spreading of the shear layer displayed in Fig.4.10 b.).

The jet response to excitation at $l_N = 38D$ exhibits a slight difference compared to $l_N = 80D$ and $11D$. The maximum response is obtained at $St_D = 0.4$ although no real preference can here be deduced since the variation in x_{pc} between $St_D = 0.2$ and 0.5 amounts to a mere $0.2D$. The absolute values for the decrease in x_{pc} and increase in θ are comparable to those at $l_N = 80D$.

The foundation of the hypothesis made in Sec.4.2 is based on a constant preferred mode Strouhal number - *measured via the jet response to acoustic excitation* - despite changes in the initial conditions. Considering the results presented above one cannot draw a decisive conclusion that neither supports nor disputes that hypothesis. On the one hand, the jet preferred mode does indeed seem to remain constant at $St_D = 0.3$ for $l_N = 80D$ and $11D$. But on the other hand, this would entail that the jet preferred mode is also constant for all nozzle lengths in between. The present results, however, do not allow to conclude that due to the discrepancy of the preferred mode

Strouhal number for $l_N = 38D$. True, the discrepancy is not huge given that the jet response is rather flat for $St_D = 0.2 - 0.5$ and one might hesitate to conclude any local preferred mode at all. The uncertainty of the results as well as the already rather small difference in the vortex passage frequency at the end of the potential core between $l_N = 80D$ and $11D$, however, are further reason to skip any unambiguous conclusion. Ultimately, the present approach of trying to confirm the hypothesis had only little to no success.

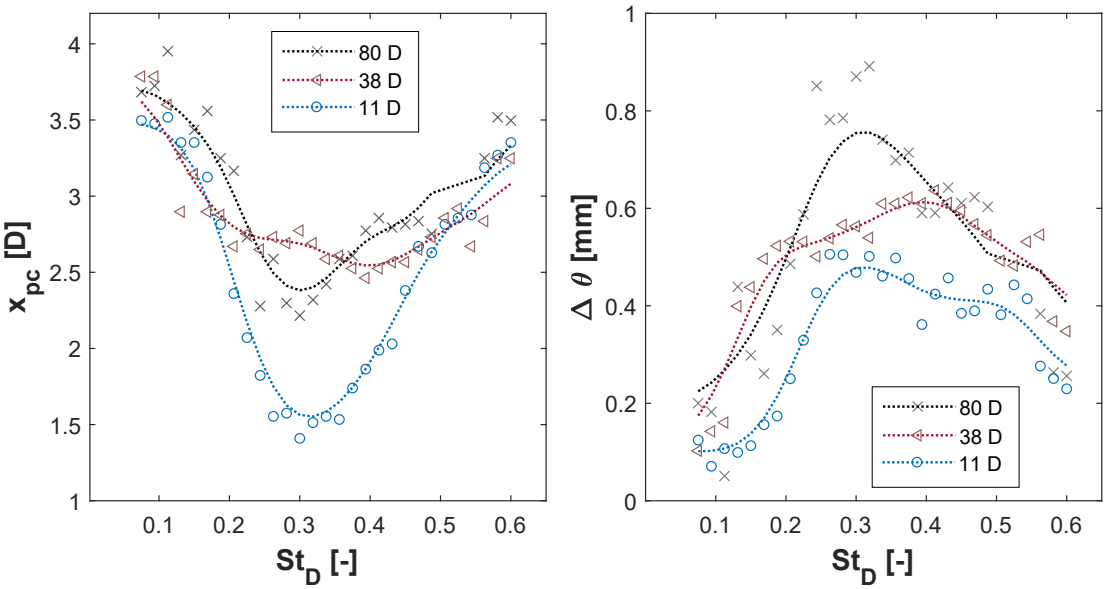

(a) Potential core length

(b) Average increase in θ

Figure 4.10: Jet response to acoustic excitation as a function of excitation frequency and different initial conditions

4.4.3 Discussion

The question whether the jet preferred mode is independent of the shear layer mode or not still remains unanswered. Fig.2.5 which showed that the reported value of the jet preferred mode varies considerably less when actual forcing is applied has first been a striking argument in favour of the new hypothesis. However, the huge scatter of the preferred mode Strouhal number for studies without any means of forcing could also

be based on the location at which the vortex passage frequency is determined [59]. The convection speed clearly decreases at further downstream positions and so would the frequency of fluctuating entities such as streamwise velocity. This, and of course the change in the passage frequency due to different initial conditions, complicates the identification of a potential jet preferred mode. This means that in case the jet preferred mode relates to the shear layer mode, i.e. by pairing of neighbouring vortices, one would probably expect less scattered data if the response of a jet to excitation is measured rather than the passage frequency at the end of the potential core of an unforced jet.

In conclusion and with respect to the working principle of the ultrasonic device, the following statements can be made:

- Initial conditions affect the jet development that is the frequency of the shear layer instability and the spreading of the jet. A smaller momentum thickness increases the initial roll-up frequency an enhances mixing. It further results in vortical structures that develop and pair further upstream. However, the vortex passage frequency at the end of the potential core is lower for a smaller momentum thickness due to more pairing events

- The uncertainty and scatter of the jet response to acoustic excitation makes it impossible to conclude if the jet preferred mode is affected by initial conditions

- The results presented above do neither weaken nor reinforce the hypothesis made in this chapter

- The working principle of the ultrasonic device with splitter is based on the excitation and amplification of the jet preferred mode. This relates to the more accepted point of view that the jet preferred mode is an integer fraction of the shear layer mode. This is then supported by the fact that LES showed that

the preferred excitation frequency corresponded to the first subharmonic of the shear layer mode.

- The working principle of the ultrasonic device without splitter is based on the formation of large vortical structures at the excitation frequency. Its relation to the shear layer mode is unclear.

Chapter 5

Low Frequency Excitation

5.1 Introduction

This chapter serves as a proof of concept study that demonstrates the feasibility of driving a fluidic diverter with sound. The idea of switching a bistable fluidic diverter by means of acoustic excitation stems from previous experimental results of a plasma-fluidic device. Plasma sparks inside the recirculation bubble of a reattached flow were found to switch a jet at medium Reynolds numbers ($Re = 10000$) if the spark is fired at a frequency that coincides with the resonance frequency of the device. This was further confirmed by an increase of the required spark frequency as the gas temperature and hence the speed of sound was increased. The mechanism behind the switching was therefore attributed to the pressure wave caused by the rapid gas heating and the amplification of the same due to resonance. The local increase in temperature and its associated low density region were considered negligible for the switching process since a small deviation of the spark frequency already prevented the jet from switching. As a consequence it was assumed that a direct sound wave could yield similar results while simultaneously reducing the complexity of the actuation mechanism. It was further chosen to scale the new Piezo-fluidic device down to 50% of

its plasma-fluidic counterpart. This was done since the amplitude of the Piezo buzzer was expected to be lower than those caused by the plasma sparks and the dependency of the required amplitude on the kinetic energy of the flow was not known a priori.

It is anticipated at this point that acoustic excitation was found to switch a jet irrespective of the side from which the jet is excited. This means that, at specific flow conditions and signal properties, a jet can be switched by either exciting it from the attached or the unattached side. Experimental results are therefore presented for both 'modes', the attached and the unattached side excitation mode.

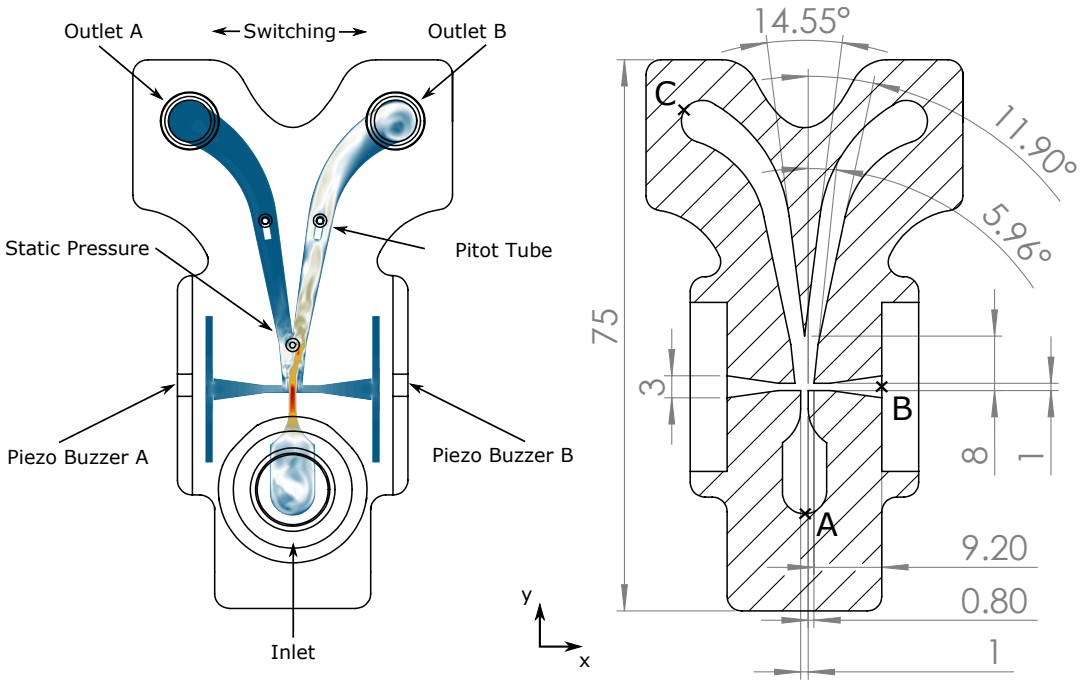

Figure 5.1: Schematic of the device geometry, left: basic device characteristics, right: governing dimensions in $[mm]$

5.2 Device Geometry

Acoustic excitation has not yet been used for actively controlling the attachment of a jet in a fluidic device. This means that neither the influence of the design on the performance nor the feasibility itself was known beforehand. Hence it was chosen to

use a simple and already existing design without any additional features such as vents or a cusped splitter. This led to a design that was studied in the 1970s by Tippetts & Royle [243] and originally used conventional control jets. Only the end wall of the control port chamber was adjusted so that its size matches the opening of the Piezo buzzer. The governing dimensions as well as a schematic of the device are shown in Fig.5.1. The flow enters and exits the device normal to the x-y plane. Nozzle height h and set back distance b amount to $1\,mm$ and $0.8\,mm$, respectively. The aspect ratio is set to $AR = 3$.

A thorough analysis of all key design parameters is further done in the succeeding chapter once the performance and the switching mechanism are elaborated.

5.3 Unattached Side Excitation

5.3.1 Switching Characteristics

To determine the characteristics and deduce the switching mechanism of an acoustically driven FSD it is essential to study the effect of signal properties and flow rate on the switching performance. Here the signal properties comprise the excitation frequency f_{ex} and the sound amplitude $\hat{p}$. The flow rate is represented by the pressure ratio $Pr = \frac{p_{t,in}}{p_{out}}$ across the device. The performance is then described by either the switching time t_s or the minimum required energy E to switch the jet. The later is defined as

$$E = \int_0^{t_{ex}} P(t)dt = \frac{A\hat{p}^2}{\rho c} \cdot cos\phi \cdot t_{ex} \tag{5.1}$$

where P is the acoustic power based on the sound pressure level $\hat{p}$ and ϕ the angle between the direction of sound and the normal to the surface A through which it propagates. The acoustic power is further a function of the acoustic impedance ρc. All variables are further non-dimensionalised where appropriate. The switching

characteristics are then described by a series of experiments at which the excitation frequency is kept constant and the pressure ratio is varied. This was found to be more effective than keeping the flow rate constant and varying the excitation frequency since the pressure amplitude is a function of f_{ex} and thus can hardly be held constant. The switching time is determined by the Pitot probe in the initially unattached channel and defined as the time between the onset of excitation and the point where the signal exceeds 90% of the final mean value. An exemplary pressure signal for a successful switching event is shown in Fig.5.2. The negative gauge pressure at $t < 0$ indicates that flow is entering the device from the unattached outlet. This so-called reverse mass flow depends mainly on the splitter shape and location and will be discussed in more detail in the following chapter. The reverse mass flow makes the attachment more stable and has an adverse effect on the switching. Fig.5.2 also shows that the excitation time t_{ex} is only a fraction of the actual switching time t_s. The excitation time is here defined by the minimum number of excitation cycles that switches the jet 10 out of 10 times ($t_{ex} = \frac{N_{cyc,min}}{f_{ex}}$). Furthermore, each data point presented hereinafter represents the average of 10 successive switching events.

Fig.5.3 shows an example of the switching time T_s over the pressure ratio Pr for which it was possible to switch the jet at $f_{ex} = 1.5\,kHz$ and $\hat{p} = 104\,dB$. Here the switching time is non-dimensionalised by the time it takes a fluid element to travel from the nozzle orifice to the splitter leading edge assuming a constant velocity so that $T_s = \frac{t_s \cdot u_e}{d_s}$. Although the average switching time indicates a preferred switching performance around $Pr = 1.001$ it is obvious that for each pressure ratio the switching time undergoes large variations of up to 30%. This was seen to be especially the case at sound pressure levels that are close to the threshold value that enables the device to switch. Increasing the sound pressure level was found to decrease the standard deviation of switching time as well as the required excitation time t_{ex} but showed only little or no effect on the average switching time T_s.

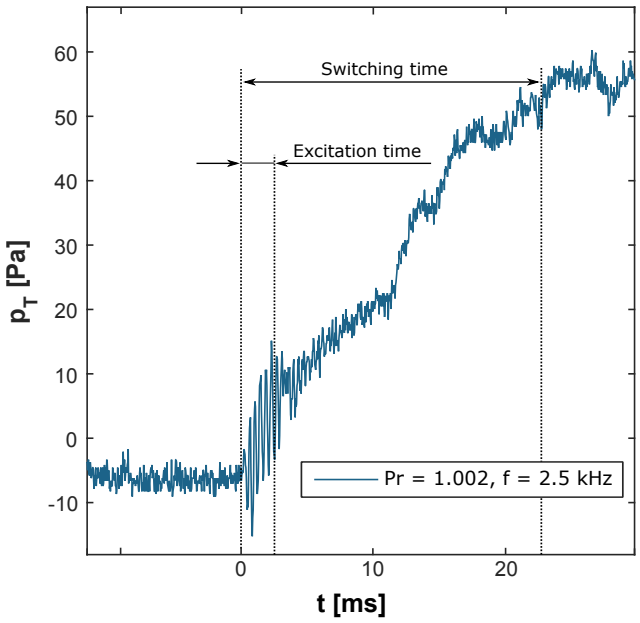

Figure 5.2: Exemplary pressure signal inside the initially unattached channel during switching

The variation of the required energy input as a function of the pressure ratio is shown in Fig.5.4. The required energy E is non-dimensionalised using E_{ref}, the minimum energy required to switch a jet at $f = 3\,kHz$ and its preferred pressure ratio. It is obvious that each excitation frequency features a preferred pressure ratio that enables switching. Besides that, no switching was observed for amplitudes lower than those shown in Fig.5.4. For each excitation frequency we yield a nearly parabolic shape with the required energy shifting to higher pressure ratios as the frequency increases. Given the fact that considerably higher minimum sound pressure levels are required as the frequency and therefore the preferred pressure ratio increases, Fig.5.4 also illustrates that the required energy input increases by more than two orders of magnitude from $f = 1\,kHz$ to $f = 3\,kHz$. It can be concluded that higher excitation frequencies correspond to higher pressure ratios which in turn require higher amplitudes and thus more energy.

The independence of the required energy on $\hat{p}$ above the minimum amplitude required for switching is shown in Fig.5.5 for $f_{ex} = 1.5\,kHz$ and $2.5\,kHz$. The required

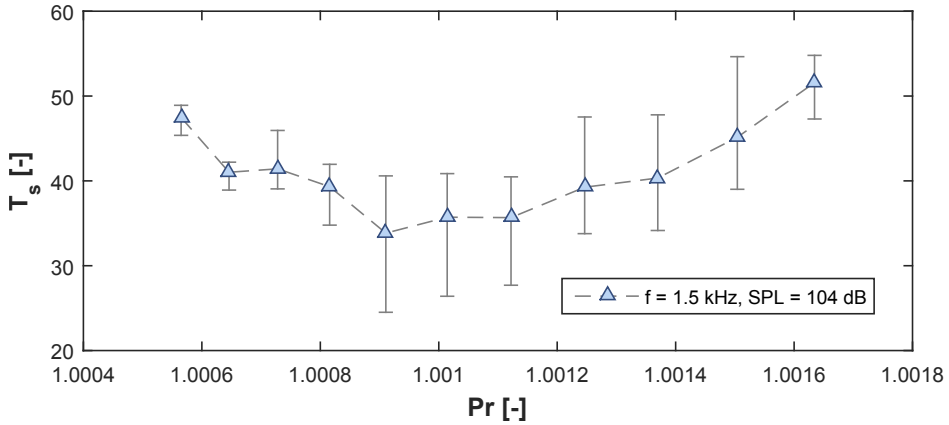

Figure 5.3: The variation in switching time T_s over pressure ratio Pr for $SPL = 104\,dB$ and $f = 1.5\,kHz$

energy exhibits a minimum that is unaffected by changes in $\hat{p}$. This indicates that the preferred pressure ratio is only a function of the excitation frequency. It is further shown that increasing the sound pressure level broadens the range of pressure ratios that allow switching. This means that for a given frequency and pressure ratio there exists a minimum threshold for $\hat{p}$. An increase in $\hat{p}$ beyond that minimum threshold only leads to a decrease in required excitation cycles. As was mentioned previously though this has rather no effect on the switching time.

5.3.2 Global Considerations

Considering that the switching performance exhibits a strong dependency of the excitation frequency on the prevalent flow rate it is appropriate to correlate the switching mechanism to flow instabilities. It is well known that flow instabilities, especially the shear layer instability that leads to the roll-up of vortices, can be influenced by sound. This shear layer mode, often referred to as the most unstable mode, was first shown to depend on the initial shear layer momentum thickness using linear stability theory by Michalke [28, 265] and subsequently quantified to a Strouhal number of $St_\theta = \frac{f \cdot \theta_e}{u_e} = 0.012$ by Zaman and Hussain [39] where θ_e is the momentum thickness of

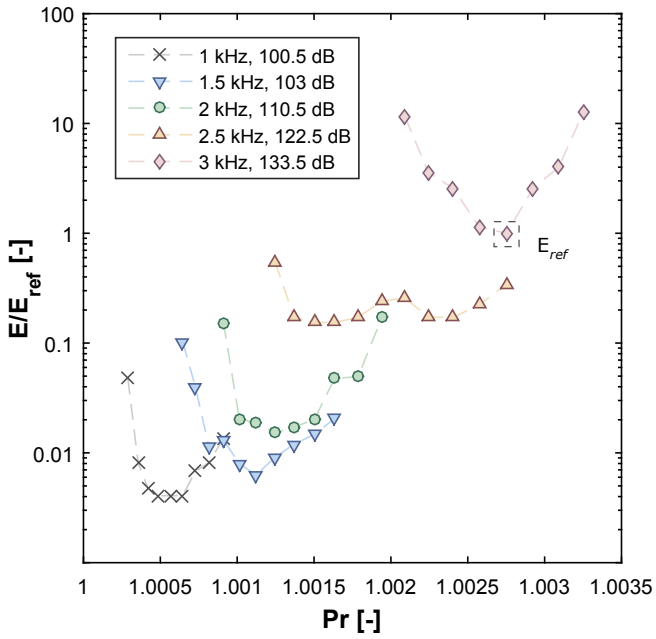

Figure 5.4: Energy input versus pressure ratio for different frequencies and their respective minimum required sound pressure levels

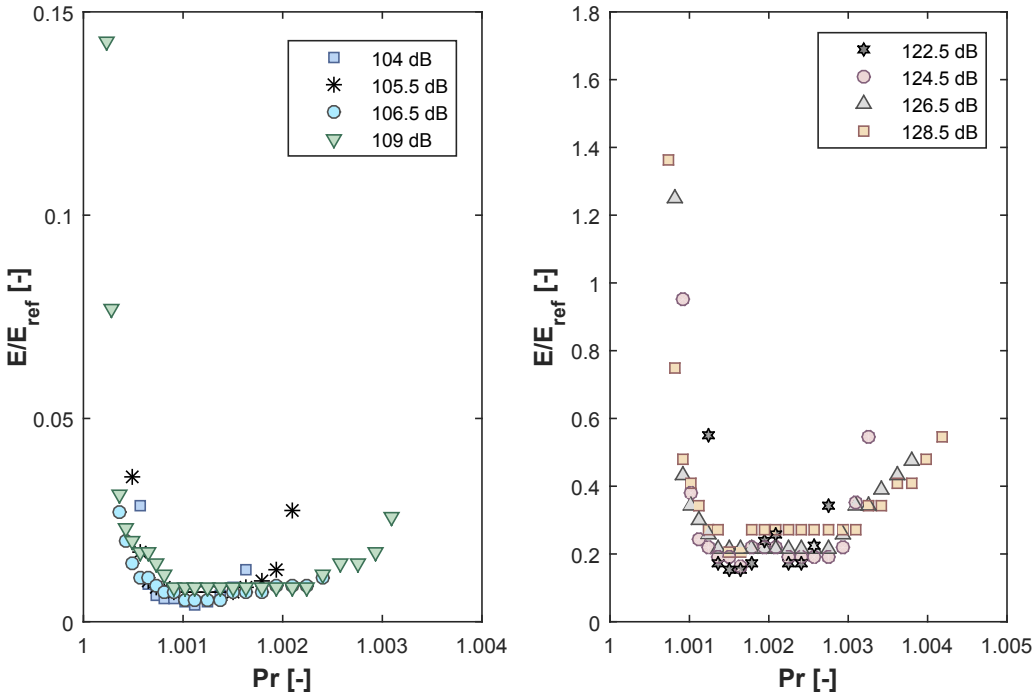

(a) $f_{ex} = 1.5\,kHz$ (b) $f_{ex} = 2.5\,kHz$

Figure 5.5: Required energy input versus pressure ratio for different SPL at constant excitation frequency

the jet. Here the frequency of the most unstable mode corresponding to $St_\theta = 0.012$ is determined by the boundary layer momentum thickness

$$\theta_e = \int_{\pm\frac{h}{2}}^{0} \frac{u}{U_0} \cdot \big(1 - \frac{u}{U_0}\big) dy \tag{5.2}$$

using a laminar velocity profile (2D) according to

$$u(y) = 2 \cdot u_e \big(1 - \frac{y^2}{h^2}\big). \tag{5.3}$$

Comparing the preferred pressure ratios of each excitation frequency obtained in the experiments and the analytically predicted most unstable frequency $f(St_\theta = 0.012)$, gives good agreement (Fig.5.6), suggesting that the preferred frequencies found in the experiments correspond to the shear layer instability that provokes the roll-up of vortices.

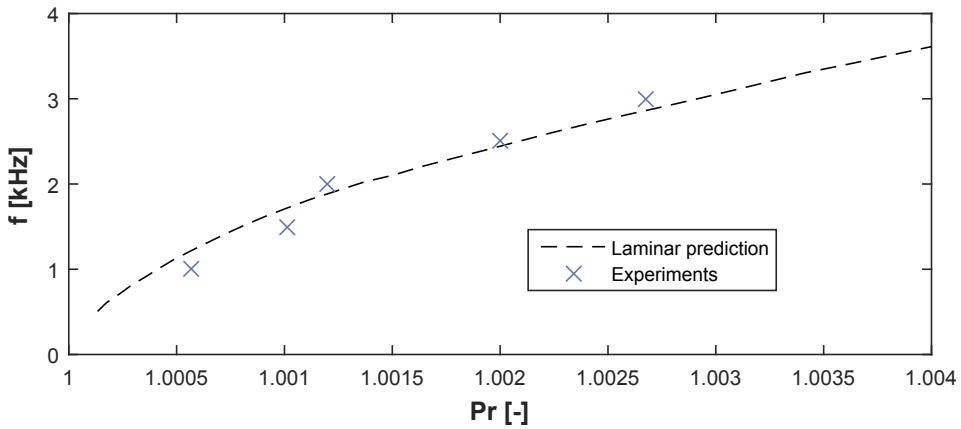

Figure 5.6: Comparison of preferred frequencies found experimentally with the analytical prediction of $f(St_\theta = 0.012)$ using $u_e = \frac{\dot{m}_{exp}}{\rho A}$

Based on the laminar prediction of the vortex shedding frequency given in Fig.5.6, it is now possible to operate the device at any flow rate ($Re < 2500$) while adjusting the excitation frequency to its corresponding preferred value. By simultaneously setting the sound pressure to its maximum value one obtains the minimum switching time

as a function of the pressure ratio Pr (Fig.5.7). It can be seen that the absolute switching time correlates with $\frac{1}{Pr}$ which in turn results in a mostly linear increase of the non-dimensional switching time T_s.

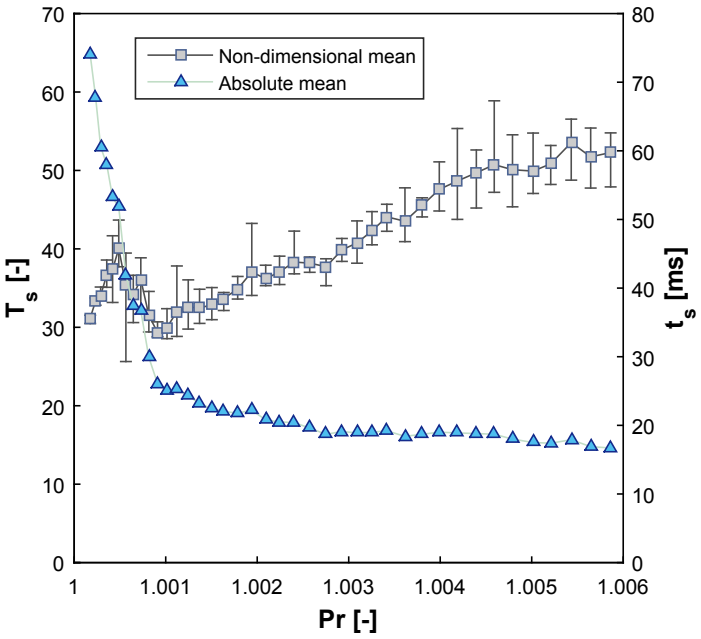

Figure 5.7: Absolute and non-dimensional minimum switching time as a function of Pr. Excitation frequency is adjusted for each pressure ratio according to Fig.5.6.

5.3.2.1 Summary of the Experimental Results

The experiments clearly show the ability to drive a bistable fluidic device solely by means of acoustic excitation. Based on the results presented above we can conclude several general statements regarding the switching characteristic for at least laminar flow conditions:

1.) The switching mechanism can be attributed to instabilities within the free shear layer. This means that a flow can preferably be switched if the excitation frequency matches the natural vortex shedding frequency.

2.) For a given flow rate and excitation frequency there exists a minimum required sound pressure $\hat{p}$ to allow switching.

3.) An increase in amplitude beyond the minimum $\hat{p}$ has no effect on the required energy input but broadens the range of pressure ratios that allow switching.

4.) The absolute minimum switching time correlates with $\frac{1}{Pr}$.

Those key characteristics determine the basics of using acoustic excitation for bistable fluidic devices. Nevertheless, the governing switching mechanism cannot be explained with the present experimental set-up and thus requires a detailed investigation with the help of numerical simulations. In order to fully understand the switching performance the following section aims to highlight both the prevalent flow conditions and the physics of the switching process.

5.3.3 Basic Flow Features

Prior to modelling the switching itself it is interesting to briefly characterize the basic flow features without excitation. For that purpose the reduced size model presented in the previous chapter is used. The attachment point, here defined as the location where the velocity streamlines exhibit an inflection point, coincides with the location of the splitter of the full-scale model ($\frac{x}{h} \approx 8$). The boundary layer shape factor $H = \frac{\theta}{\delta}$ at the nozzle orifice equals to 2.4 since the laminar velocity profile is not yet fully developed due to the short nozzle of the device. Regarding the location and frequency of the natural shear layer roll-up, the pressure fluctuation inside the unattached shear layer is measured downstream of the nozzle orifice at 10 different locations with a spacing of one nozzle height. Pressure isolines shown in Fig.5.8.a.) reveal that the natural shear layer roll-up on the unattached side happens aft of 5 nozzle heights downstream of the orifice. Moreover, the frequency spectra of passing vortices (measured at $\frac{x}{h} = 7$) coincides with the preferred excitation frequency of $f = 3\,kHz$ obtained in the experiments ($f_{LES} = 2.975\,kHz$). This again confirms that the preferred pressure ratios seen in Fig.5.4 correspond to the most unstable

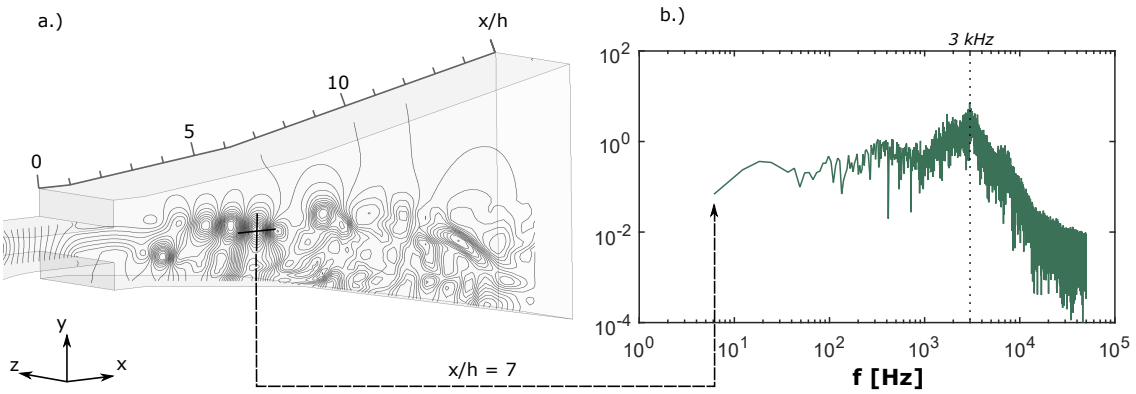

Figure 5.8: a.) Pressure isolines (xy mid-plane, $z = 1.5\,mm$) of the truncated model at $\dot{m} = 2.9\,LPM (Pr = 1.0027)$, b.) Frequency spectra of pressure fluctuation at $\frac{x}{h} = 7$

mode of the unattached shear layer.

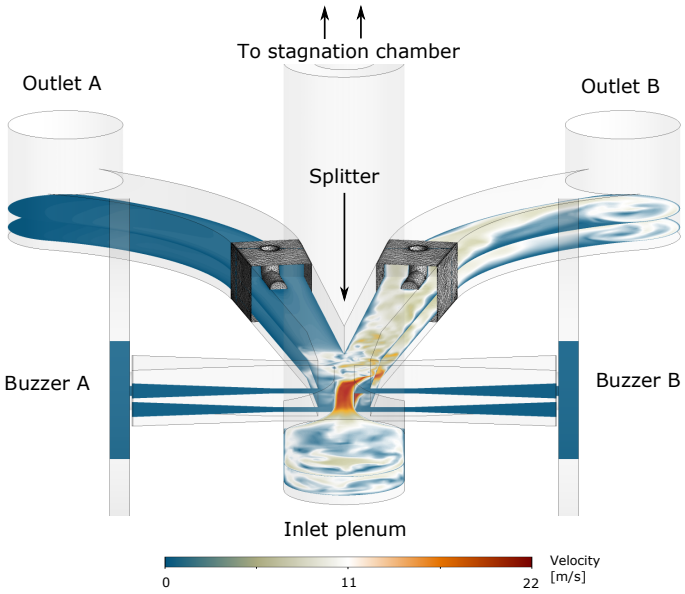

Figure 5.9: Fluid domain with Pitot probes

5.3.4 Full-scale Switching Simulation

A schematic of the fluid domain along with an instantaneous velocity distribution indicating attachment on channel B is displayed in Fig.5.9. Given that the overall dimensions of the device are relatively small both Pitot tubes are included in the

model to account for a possible blockage effect. The maximum membrane displacement Δ is then varied until the experimentally measured sound pressure is matched. At $\Delta = 30\,\mu m$ a reasonable close sound pressure level of $132\,dB$ is achieved. The excitation is turned on at $t = 0\,s$ and is stopped after $5\,ms$. As seen in Fig.5.10 this is sufficient to enable the jet to switch to side A. The switching time is $\approx 11\,ms$ and therefore around $5\,ms$ lower than the average switching time shown in Fig.5.7 but within the uncertainties given by Fig.5.3. With respect to the sound pressure level the difference between CFD and experiments amounts to $1.5\,dB$. But since small changes in flow speed (see Fig.5.4) already require an increase of one or more orders of magnitude in sound energy to enable switching, a difference of around $1.5\,dB$ between CFD and experiments is within reason. However, to understand the qualitative physics of switching process Fig.5.11 shows the velocity vector field at four different time steps T_{1-4} before, during and after the switching (time steps are also highlighted in Fig.5.10 which shows the mass flow at the outlet of both channels. A negative value for $\dot{m}$ represents a mass flow out of the computational domain). The flow field at T_1 reveals a typical recirculation bubble for a Coanda based attachment as well as some reverse mass flow entering through channel A. The fact that the splitter leading edge is located where the shear layer of the natural unforced jet starts to roll up (see Sec.5.3.3) and that the reverse mass flow is causing a highly disturbed free shear layer no discrete vortices can be identified before T_2. At T_2, just after the first acoustic wave ($t = 0.4\,ms$), the flow exhibits a large roll-up of the unattached shear layer. Vortices are then continuously formed at $f = 3\,kHz$ starting already one nozzle width downstream of the nozzle orifice. Despite the fact that there is still more mass flow going through the initial attachment channel at T_3, the excitation can be stopped and we observe that the jet switches to the opposite side (T_4). This can only be explained if the pressure gradient across the jet has already been reversed and therefore counteracts the Coanda based attachment.

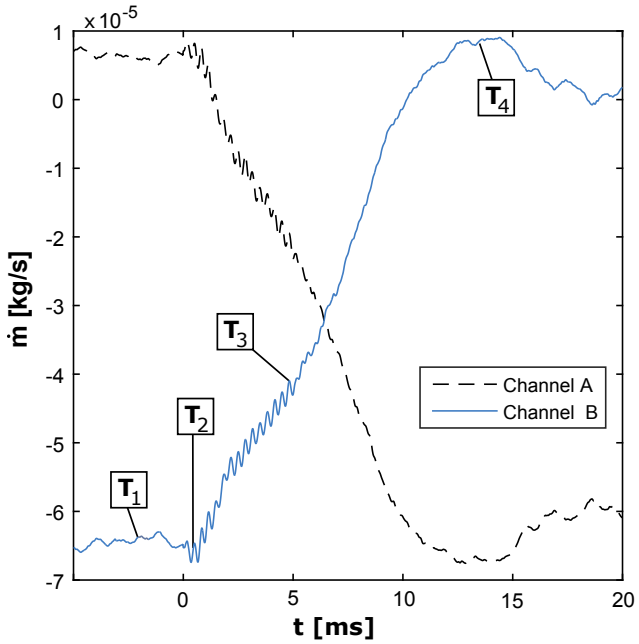

Figure 5.10: Mass flow $\dot{m}$ inside channel A and B during switching

To investigate further that pressure forces can be held responsible for the switching mechanism the average static pressure on the upper and lower yz half-plane UHP and LHP at $x = 2h$ is measured. This is the centre of the recirculation bubble as is shown in Fig.5.11. Before the onset of excitation ($t < 0$), Fig.5.12 illustrates the pressure difference across the jet due to the Coandă induced low pressure region inside the recirculation bubble. During the excitation itself the pressure on the unattached side reveals a stronger decrease than on the initial attachment side. This causes the pressure gradient across the jet to reverse after $t_r \approx 1.8\,ms$. But although the pressure difference has flipped by then the jet needs to be further excited until the difference in pressure reaches the magnitude of the initial (and final) Coandă based pressure difference. This can be seen to be the case at $t = 5\,ms$ where the filtered pressure exhibits its minimum. The reason why the jet doesn't switch as soon as the pressure gradient is reversed might be attributed to the reverse mass flow that counteracts the switching process.

To understand what causes the substantial pressure drop on the unattached side we

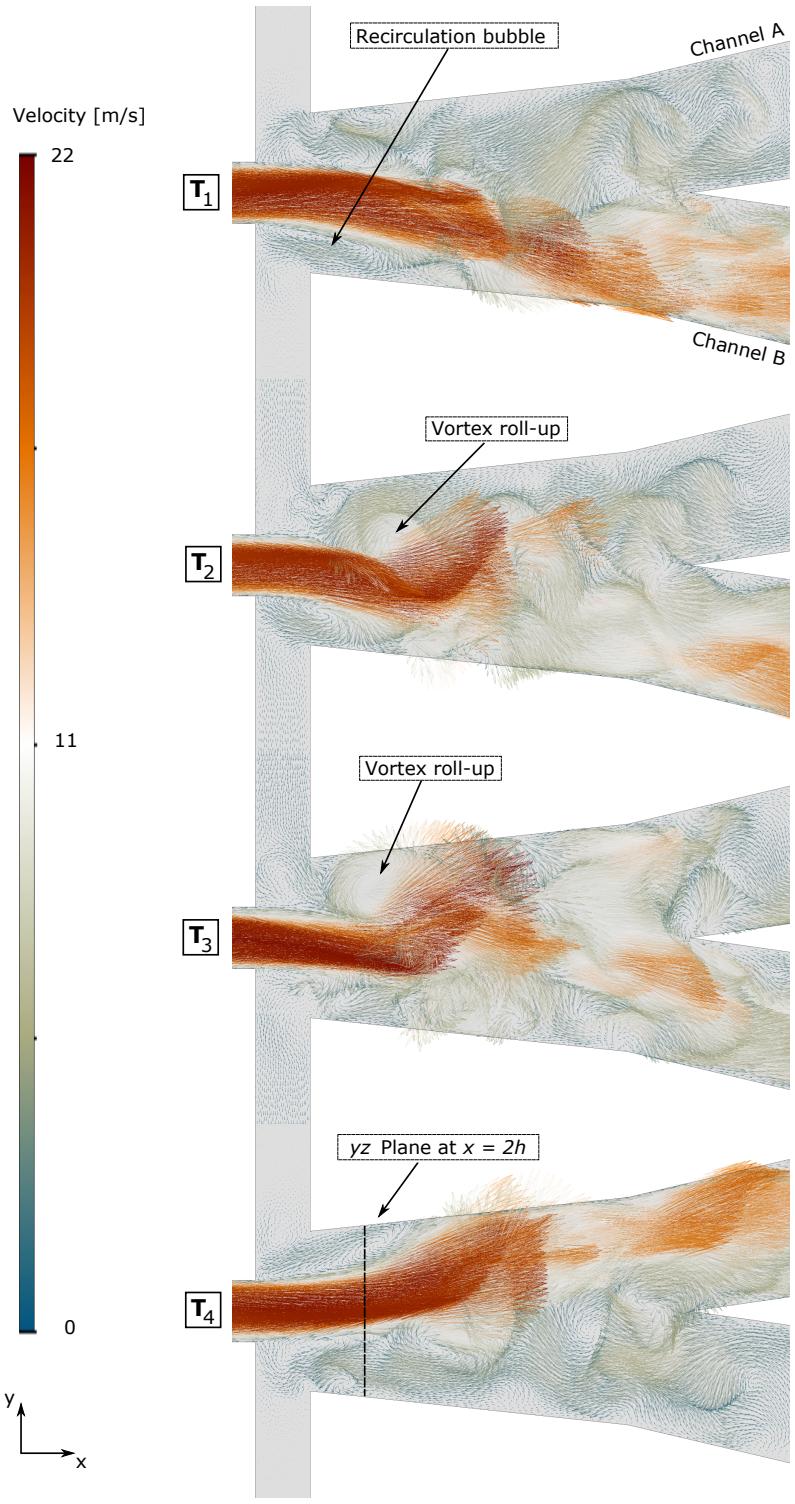

Figure 5.11: Instantaneous velocity vector field at four different time steps T_1,T_2,T_3 and T_4 indicating shear layer roll-up during acoustic excitation

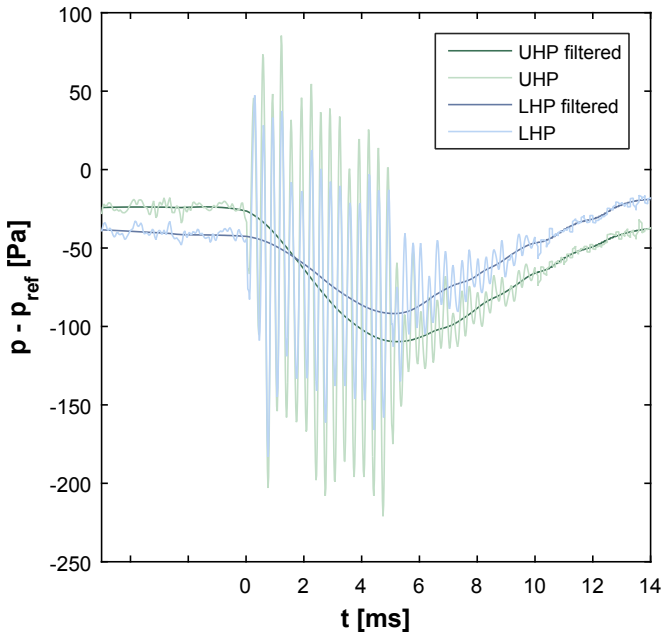

Figure 5.12: Average static pressure on the upper and lower half-plane at $x = 2w$ (filtered using robust local) regression

ought to consider the rate of entrained fluid during the excitation. Entrainment is defined by Wygnanski & Fiedler [266] and Crow & Champagne [3] as the streamwise derivative of the volume flow $Q(x)$ which is defined as the surface integral of the mean streamwise velocity:

$$Q(x) = \int \int_A u_x \, dA \tag{5.4}$$

To calculate the absolute volume of entrained fluid V_e the difference $Q_2 - Q_1$ is integrated over time,

$$V_e(t) = \int \Delta Q_{2-1} \, dt \tag{5.5}$$

where Q_1 and Q_2 are the volume flows inside the nozzle and at $x = 3.5h$, the point where the flow first attaches to the wall, respectively.

As shown in Fig.5.13, the entrained volume features a rather constant and linear increase until the onset of excitation. After $t = 0$ the rate of entrainment is considerably increased, as indicated by a larger gradient of $V_e(t)$. Speaking in relative terms, 3.5 times more volume is being entrained during the course of excitation. Knowing

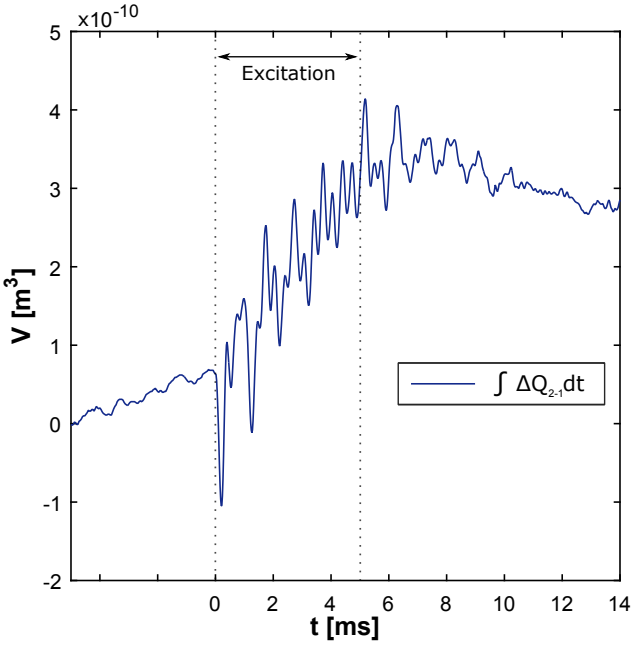

Figure 5.13: Volume of entrained fluid between the nozzle orifice and the point of reattachment as a function of time

that entrainment is primarily caused by streamwise vortical structures [3, 44, 267] it is obvious to correlate the increased entrainment to the enhanced roll-up of the unattached shear layer. To further confirm that vortices are predominantly formed on the unattached side one ought to consider a quantitative vortex identification method.

In general, vortices can be described as circular motion in a fluid. Finding an unambiguous definition in mathematical notation, however, is rather non-trivial. This is because there is no global or absolute criterion that defines the existence of a vortex. This again means that no vortex identification method can include all kinds of vortices. A typical feature of at least most vortices is the existence of a local pressure minimum in the centre of the fluid rotation. The λ_2 vortex method [268], which will be used throughout this thesis, is thus based on an expression that finds regions of local pressure minima in the flow. Consider therefore the Navier-Stokes equation in differential form,

$$\frac{\delta u}{\delta t} + u\nabla u = -\frac{1}{\rho}\nabla p + \mu\nabla^2 u \tag{5.6}$$

where $u = u(x,t)$ is the velocity field, ρ the density of the fluid, and p and μ the pressure and dynamic viscosity, respectively. Taking the spatial gradient of Eq.5.6 we obtain

$$\frac{\delta}{\delta t}A_{ij} + A_{ik}A_{kj} = -\frac{1}{\rho}H_{ij}. \tag{5.7}$$

Here A_{ij} denotes the velocity gradient tensor $\frac{\delta u_i}{\delta x_j}$ while H_{ij} represents the Hessian of the pressure $\frac{\delta^2 p}{\delta x_i \delta x_j}$. Note that the third order term, the gradient of the flow acceleration $u\nabla A_{ij}$, and the viscous forces were neglected. By preventing viscous forces from contributing to the Hessian of the pressure one accounts for the fact that viscous effects can eliminate the pressure minimum in a flow despite the presence of a vortex. This, for instance, is the case for low Reynolds number flows ($Re \ll 1$) in which the pressure gradient is set by the viscous term only ($\mu\nabla^2 u = \nabla p$).

The Hessian of the pressure on the right hand side of Eq.5.7 contains information about local pressure extrema in the flow and hence is the key element of identifying vortices. The λ_2 vortex method then decomposes the velocity gradient tensor into its symmetric and antisymmetric part ($A_{ij} = S_{ij} + \Omega_{ij}$) so that Eq.5.7 reads as

$$\frac{\delta}{\delta t}S_{ij} + S_{ik}S_{kj} + \Omega_{ik}\Omega_{kj} + \frac{\delta}{\delta t}\Omega_{ij} + \Omega_{ik}S_{kj} + S_{ik}\Omega_{kj} = -\frac{1}{\rho}H_{ij} \tag{5.8}$$

Since the second derivative of p is symmetric ($H_{ij} = H_{ji}$) Eq.5.8 reduces to

$$\frac{\delta}{\delta t}S_{ij} + S_{ik}S_{kj} + \Omega_{ik}\Omega_{kj} = -\frac{1}{\rho}H_{ij} \tag{5.9}$$

Here $\frac{\delta}{\delta t}S_{ij}$ describes the unsteady irrotational straining which can cause a pressure minimum despite zero vorticity [268]. Consequently, the λ_2 vortex method determines

the pressure Hessian H_{ij} by $S_{ik}S_{kj} + \Omega_{ik}\Omega_{kj}$ only. A pressure minimum in the flow is then found where H_{ij} is negative. This in turn means that at least two eigenvalues of H_{ij} ought to be negative. Arranging all eigenvalues $\lambda_{1,2,3}$ by their magnitude we obtain the definition that a vortex is present if $\lambda_2 < 0$. Fig.5.14 now shows the time

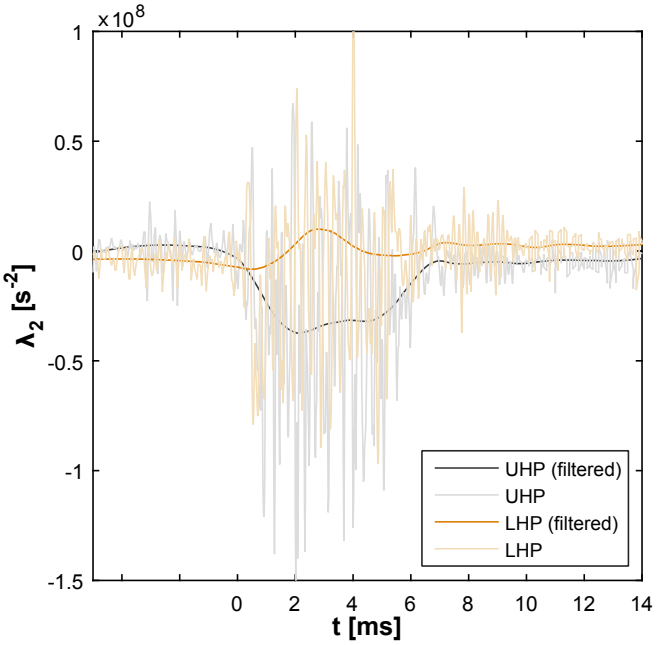

Figure 5.14: Identification of vortices going through the upper and lower half-plane ($x = 2h$) using the λ_2 vortex criterion (filtered using robust local regression)

sequence of λ_2 at the lower and upper half plane before, during and after the switching process. It is evident that vortices dominate on the unattached side as of the onset of excitation ($t > 0$). Furthermore, one can locate a well-developed recirculation bubble (shown as a constant negative λ_2) on either side respectively before and after the excitation.

5.3.5 Discussion

The most unstable mode of a natural shear layer is typically determined by the frequency of shedding vortices ($St_\theta = 0.012$). The discrete roll-up of such vortices depends on the primary unstable velocity fluctuation inside the shear layer. This two-

dimensional fluctuation grows exponentially with downstream distance and triggers the spanwise roll-up when it reaches around 10% of the mean shear layer velocity [28]. At laminar conditions and without artificial forcing this roll-up happens several nozzle heights downstream of the orifice (see Fig.5.8). By acoustically exciting the flow at the most unstable mode the primary fluctuation is amplified so that the roll-up is shifted to further upstream positions ($x \approx 2h$). The excitation and amplification is often described in terms of $\frac{u'_{ex}}{u_e}$, with u'_{ex} being the root-mean-square of the sound induced velocity fluctuation. For the full-scale model of the reference case this amounts to an amplification of the shear layer fluctuation using less than 1% of u_e. However, exciting the flow at the right frequency not only shifts the roll-up closer to the nozzle orifice but also causes more orderly vortical structures. The size of those vortices scale with the excitation amplitude and feature a higher rate of entrainment [3, 33, 121]. Crucial for this study is that the increased entrainment results in a pressure drop that consequently drives the switching process. The correlation between increased entrainment and pressure drop is not intuitive, it is only linked due to the geometry of a Coanda device itself. The vortex formation along with the attachment wall forms a confined space from which fluid is entrained. Since no fluid can re-enter, e.g. the control port, the pressure decreases during the excitation and draws the jet towards the unattached side. With the ideal gas law and a constant Volume V_c (mainly the control port cavity) this pressure drop can be expressed as

$$\Delta p(t) = \frac{\rho R T}{M V_c} \cdot \int \Delta Q_{2-1}\, dt \tag{5.10}$$

Switching can thus be enhanced through a higher rate of entrainment or a smaller control port cavity (V_c) from which fluid is entrained. It is therefore obvious that the switching time decreases as the entrainment increases.

Moreover, the switching time was seen to be independent of the pressure amplitude

provided that the threshold amplitude is exceeded. This means that once the roll-up takes place upstream enough to counteract the Coanda based attachment an increase in amplitude has only little effect on the switching time. This makes insofar sense as the rate of entrainment will be unaffected. The length scale l can't increase arbitrarily and is already limited due to the device geometry whereas the time scale τ and thus u_θ are a function of the main jet velocity. A higher rate of entrainment is therefore only achieved by a higher pressure ratio. However, at relatively high excitation amplitudes it was observed that switching becomes less dependent on the excitation frequency. For a sound pressure level of $135\,dB$ for example, it was irrelevant if the forcing frequency was 1, 2 or $3\,kHz$. Switching was feasible at any given pressure ratio within the range of laminar flow conditions. It is plausible to assume that this is simply due to the fact that at relatively high amplitudes, say $u'_{ex} > 0.01u_e$, the shear layer will adapt the forcing frequency irrespective of being close to the natural instability or not. The switching time was then seen to still follow the same $\frac{1}{Pr}$ relationship which in turn confirms that t_s is a pure function of u_e.

5.4 Attached Side Excitation

5.4.1 Switching Characteristics

The switching mechanism of the unattached side excitation mode was derived after experimental results indicated a clear dependency of the excitation frequency on the preferred pressure ratio. It is here anticipated that such an indication was less obvious for the attached side excitation mode since switching was only feasible for a range of frequencies that was more than an order of magnitude smaller than the range of frequencies that enabled switching for the unattached side excitation mode. The switching mechanism thus remained unclear at first but can be deduced in hindsight and, moreover, by experiments alone.

Similar to the results presented in Sec.5.3.1 the switching performance is characterized by the required energy $\frac{E}{E_{ref}}$ and the switching time t_s (T_s) as a function of the pressure ratio Pr using a constant excitation frequency f_{ex}. In this regard,

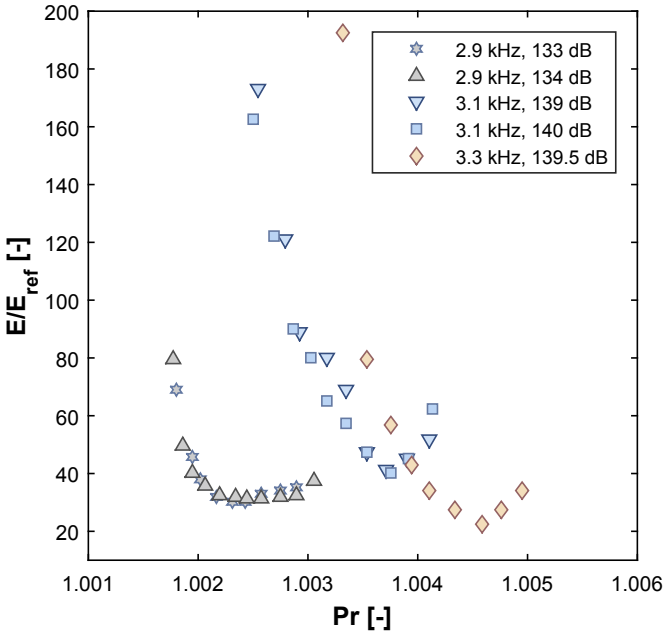

Figure 5.15: Required non-dimensional energy versus pressure ratio for different excitation frequencies

Fig.5.15 shows that, with respect to the unattached side excitation mode (Fig.5.4), the required non-dimensional energy is increased by one or more orders of magnitude. Comparing the preferred pressure ratio of each excitation frequency as was done for the unattached side excitation mode with the laminar prediction of the natural shear layer instability is shown in (Fig.5.16). However, the limited available data points do not allow to draw a decisive conclusion whether the excitation frequencies correspond to the most unstable mode.

The narrow band of frequencies that enables switching ($2.9\,kHz$ to $3.3\,kHz$) corresponds to the most amplified frequencies that achieve the highest sound pressure levels inside the device. This suggests that the threshold amplitude, especially for lower excitation frequencies, is multiple times higher for the attached side excitation

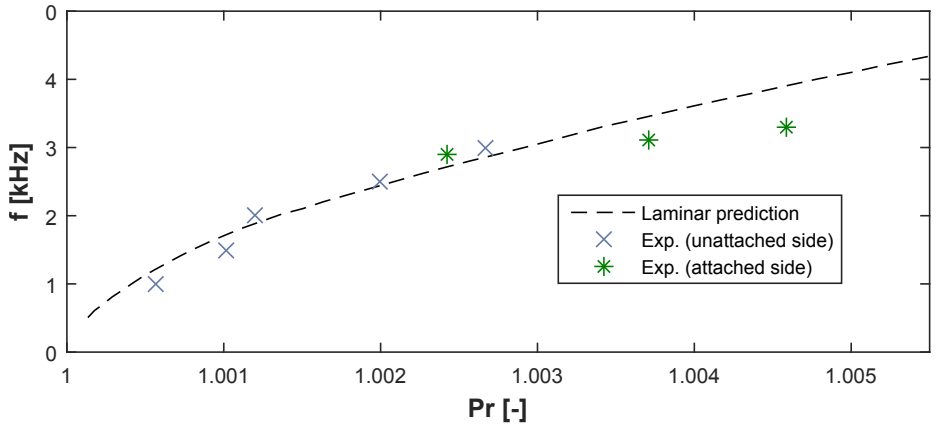

Figure 5.16: Comparison of preferred frequencies found experimentally with the analytical prediction of $f(St_\theta = 0.012)$ using $u_e = \frac{\dot{m}_{exp}}{\rho A}$

mode. Apart from that, it also has to be mentioned that the minimum required energy for each excitation frequency remains rather constant. This is remarkable since the unattached side excitation mode showed a significant increase in $\frac{E}{E_{ref}}$ over Pr. It was initially thought that this is due to the range of frequencies being too small to deduce a clear trend. However, it is more likely due to resonances in the device. This becomes evident if one considers the time period τ of a wave travelling from one end of the device to the other. This time period is defined by twice the distance l between two end walls and the speed of sound c. The time period τ that corresponds to the distance l_{A-C} from the inlet to the outlet (see Fig.5.1) yields a frequency of $2.89\,kHz$ ($f = \frac{1}{\tau} = \frac{l}{c}$). The time period τ that corresponds to the distance l_{B-C} from the control port wall to the outlet yields a frequency of $3.22\,kHz$. This is notably close to the range of frequencies that enable switching ($2.9\,kHz$ to $3.3\,kHz$). In addition, it is in good agreement with the performance of the previously mentioned plasma-fluidic device which was found to switch only at the resonance frequency of the device, too [209]. This suggests that the switching mechanism is identical or at least depends on the same effects despite the fact that two different actuator types are used. Nonetheless, the working principle behind the plasma-fluidic switching still lacks a proper explanation. Hence there is no explanation that can simply be applied

to the attached side excitation mode of the present piezo-fluidic device. To shed some light onto the underlying switching mechanism it is useful to first consider already known mechanisms that can be excluded.

In general, switching a reattached jet in a Coanda-based device requires either reversing the pressure difference across the jet or adding momentum which actively deflects and pushes the jet towards the opposite side. The former was seen to be responsible for the unattached side excitation mode due to a forced asymmetry in entrainment. To investigate whether a pressure driven switching mechanism can be excluded for the attached side excitation mode a new static pressure tap is added in both control port channels. Measuring the static pressure on either side of the jet while constantly exciting it at an amplitude too low to cause switching then reveals if the pressure difference across the jet decreases and thus eventually switches the jet in case $\hat{p}$ would be increased beyond a threshold value.

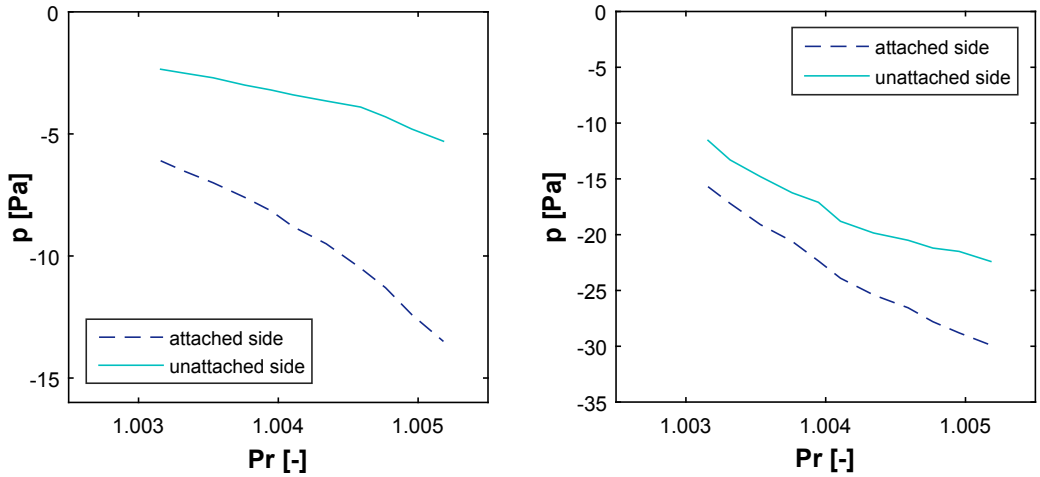

(a) Mean static pressure without excitation (b) Pressure reduction due to excitation

Figure 5.17: Pressure measurements inside the control port channel on either side as a function of Pr

Fig.5.17 a.) shows the static pressure on either side of the jet as a function of the pressure ratio without excitation. The difference between both lines depicts the attachment force that is a function of Δp . The two lines diverge as the pressure ratio

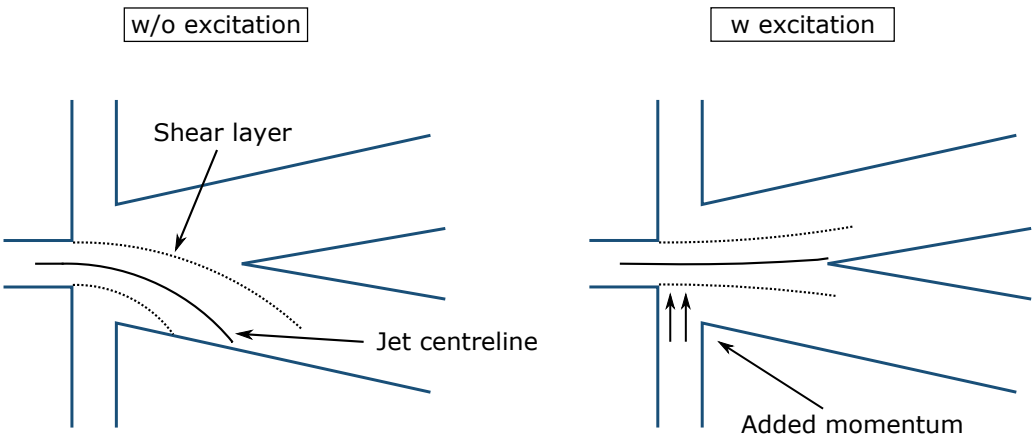

Figure 5.18: Schematic of the jet lift off and switching mechanism of the attached side excitation mode

goes up indicating that the attachment force increases at higher mass flow rates. This is also described by the square relationship $\Delta p \propto u^2$ in the jet curvature equation (Eq.2.3).

Fig.5.17 b.) shows the pressure reduction between the excited and non-excited case at the same two locations. The frequency is set to $f_{ex} = 3\,kHz$ and the amplitude is set to an arbitrary value too small to cause switching. It is apparent that the attached side exhibits a greater pressure reduction then the unattached side indicating that the attachment force Δp increases. This certainly does not favour the jet to switch the jet but demonstrates the asymmetry in entrainment due to the one-sided excitation. A switching mechanism that is based on reversing the pressure difference across the jet can therefore be excluded. Moreover, the results are in good agreement with the experiments of Chung & Sung [269] which show that the reattachment length of an excited flow over a backward facing step decreases for Strouhal numbers ranging from $St_h = 0.1 - 1$ indicating a stronger attachment force Δp. The results therefore suggest that the jet is somehow pushed or deflected towards the opposite side despite an even bigger attachment force.

One possible explanation is that the Piezo buzzer together with the control port

chamber act as a synthetic jet adding net momentum to the jet which ultimately leads to switching (see Fig.5.18). This would be similar to the synthetic jet driven fluidic device studied by Martin et al [208]. The fact that the jet was found to switch only at the highest achievable amplitudes backs up this conclusion. Note that the net momentum of the synthetic jet is a function of the excitation amplitude [208].

For completeness Fig.5.19 shows the absolute and non-dimensional switching time for the attached side excitation mode. The absolute switching time t_s decreases for higher pressure ratios with no indication of an asymptotic behaviour. This is most likely due to the small range of pressure ratios that do not allow an extrapolation. The non-dimensional switching time shown in Fig.5.19 b.) indicates to remain rather constant but doesn't allow an extrapolation either. However, it takes more time to switch the jet when excited from the attached side with respect to the unattached side excitation for all pressure ratios considered. This is even despite multiple times higher sound pressure levels.

The dynamic switching is exemplarily shown in Fig.5.20 for two different output oscillation frequencies. Since the switching time t_s is constant the output signal takes on a square wave at lower frequencies and becomes a more sinusoidal wave as the frequency approaches the limit ($f_{max,out} = \frac{1}{2 \cdot t_{s,min}}$).

5.4.2 Discussion

The switching mechanism was concluded to be due to a net addition of momentum. This ought to say that the Piezo buzzer operates here as a synthetic jet actuator. The main jet is deflected and as soon as its centreline interacts with the splitter leading edge the jet switches to the opposite wall. This type of switching is called splitter switching [270]. The entrainment rate has at most an adverse effect on the switching time which means that no $t_s \propto \frac{1}{\epsilon}$ relationship prevails. Nevertheless, it was still shown that the switching time decreases as the pressure goes up ($t_s \propto \frac{1}{Pr} \propto \frac{1}{u_e}$). It

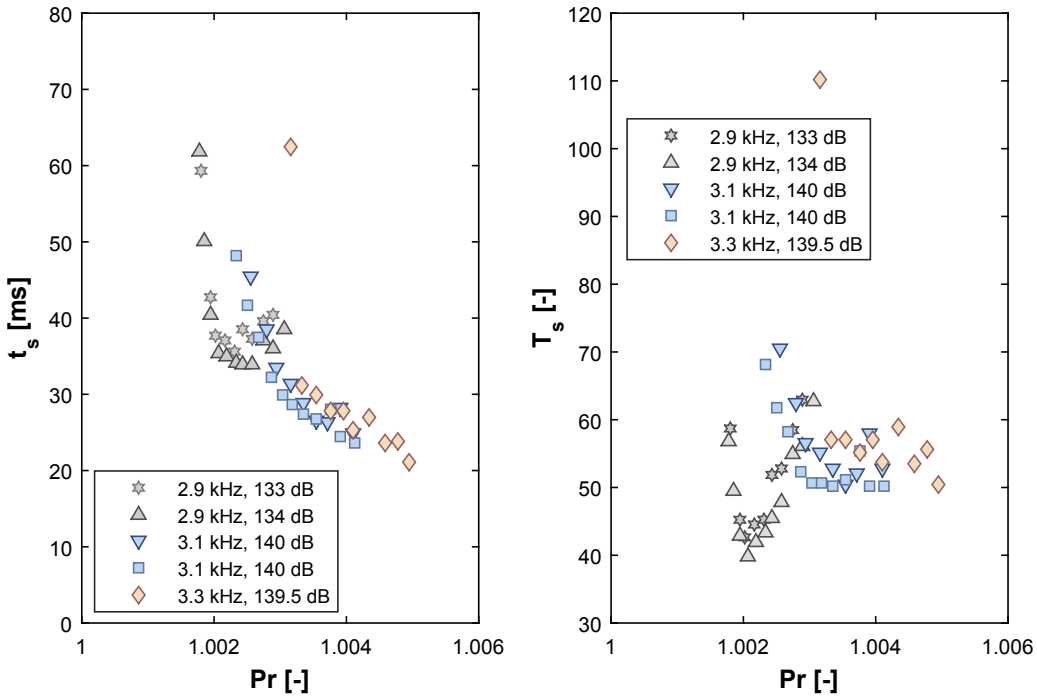

(a) $f_{ex} = 1.5\,kHz$ (b) $f_{ex} = 2.5\,kHz$

Figure 5.19: Required energy input versus pressure ratio for different SPL at constant excitation frequency

also has to be mentioned that it is feasible to switch the jet back and forth with one single Piezo transducer.[1] Each pressure ratio that allows switching with excitation from the attached side therefore allows switching with excitation from the unattached side, too. This could be of interest for future applications that require a second, redundant transducer. However, although no splitter is necessary for the unattached side excitation it is a key requirement for the attached side excitation mode.

5.5 Conclusion

In this chapter it was shown that sound alone is able to actively drive a bistable fluidic device. Moreover, two distinct excitation modes that enable the jet to switch sides were found and explained in detail. The flow physics and switching mechanism of

[1]Only at certain pressure ratios that allow switching using both attached and unattached side excitation mode

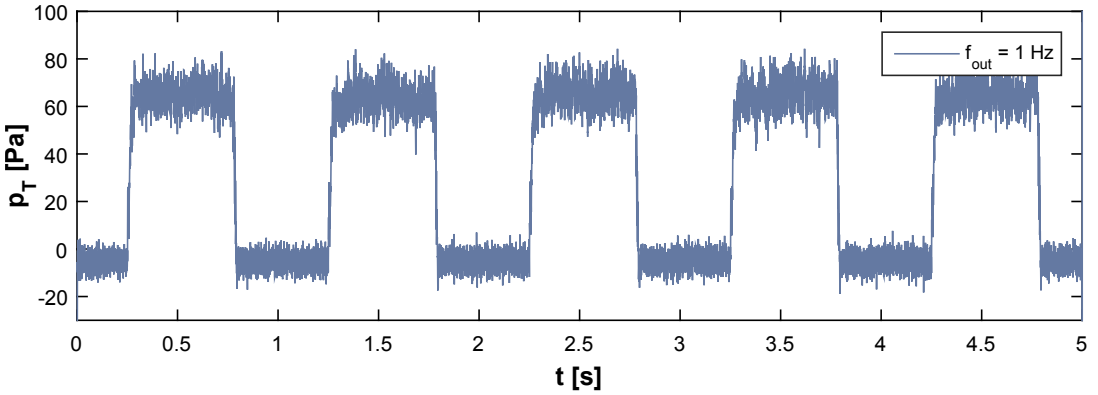

(a) $f_{out} = 1\,Hz$

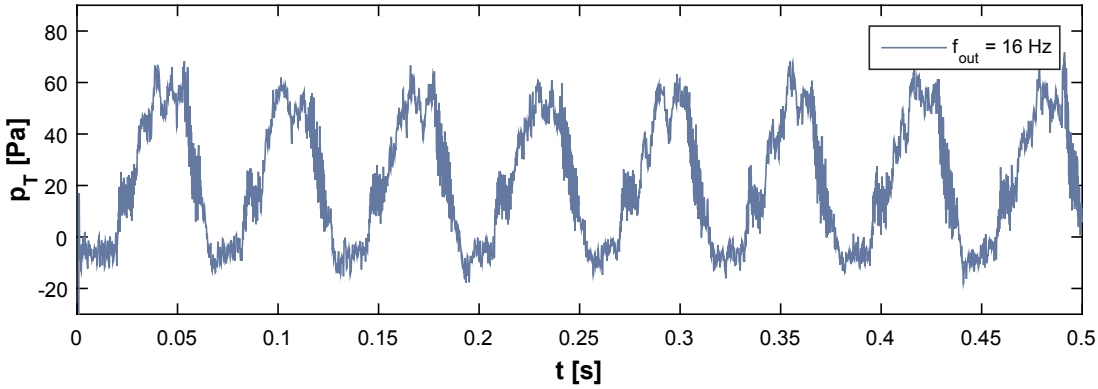

(b) $f_{out} = 16\,Hz$

Figure 5.20: Dynamic switching at two different output oscillation frequencies at $Pr = 1.0025$ and $f_{ex} = 3.1\,kHz$

the unattached side excitation mode were studied by a combination of experimental and numerical methods. For the investigation and characterisation of the attached side excitation mode it was sufficient to perform experiments only. The switching mechanism could be deduced and explained by the information gained from the results of the unattached side excitation mode and by excluding conventional switching mechanisms.

The attached side excitation mode requires more energy and higher threshold amplitudes and is, moreover, characterized by a lower switching time and a smaller range of pressure ratios that allow switching. Yet the results indicated that the non-dimensional switching time for the attached side excitation mode remains rather constant. This means that switching might become much faster at higher pressure

ratios. However, at least for the flow conditions considered in this chapter the performance of the unattached side excitation mode exceeds that of the attached side excitation mode.

Chapter 6

Ultrasonic Excitation

6.1 Introduction

Based on the results gained in the previous chapter it was decided to follow up the possibility of driving a Piezo-fluidic diverter at higher excitation frequencies so to extend the bandwidth of the device to more engine realistic conditions. As the unattached side excitation mode features a substantial advantage in terms of required power/energy over the attached side excitation mode it was further decided to focus on studies on this mode only.[1]

It was also shown that the required energy for the unattached side excitation mode increases exponentially as the pressure ratio across the device goes up. This poses a dilemma since high amplitude, high frequency and high bandwidth actuation are opposing requirements. This issue will therefore be addressed separately in Sec.6.4. A brief discussion of the target operating conditions as well as the key design param-

[1]That is not to say that no attempt has been made to switch a jet at higher pressure ratios with sound emitted from the initial attachment side. However, for all conditions tested and presented subsequently it was not feasible to switch the jet with the attached side excitation mode. This is most likely due to the higher threshold amplitudes and the fact that the resonant frequency (end wall to end wall) of the following device does not match the excitation frequency. The latter would otherwise require a device geometry as small as the size of the transducer itself. This again is rather unfavourable on account of manufacturing tolerances and the use of measurement probes such as Pitot tubes or microphones.

eters and their effect on the switching performance is done prior to that. This will simultaneously be used to derive the basic geometry of the new device. A set of non-dimensional parameters describing the overall system is further derived to provide a framework for the subsequent characterisation of the switching performance. The chapter is then divided into two main parts that correspond to two different device configurations. The first one considers a splitter-less design that allows non-intrusive optical measurements. Switching characteristics and flow properties will then be elaborated using both experimental and numerical methods. The second design separates the two outlets with a conventional splitter. No flow visualisation studies are here required for the interpretation of the experimental results.

6.2 Target Operating Conditions

Prior to the actual design of the device it is indispensable to first determine the target operating pressure ratio Pr. This sets the jet speed u_e and therefore the shear layer instability St_θ for a given nozzle height h. This in turn limits the choice of the excitation frequency f_{ex}. Pressure ratio, nozzle height and excitation frequency are therefore key parameters that do not allow an independent consideration.

The desired range of pressure ratios at which the new device ought to operate is broadly set to $Pr = 1.1 - 1.5$. Once the pressure ratio is set one can estimate the shear layer instability $f = \frac{St_\theta \cdot \theta}{u_e}$ using

$$\theta = \int_{\pm\frac{h}{2}}^{0} \frac{u}{U_0} \cdot \big(1 - \frac{u}{U_0}\big) dy \tag{6.1}$$

where u, the velocity profile at the nozzle orifice, is determined by the one seventh power law ($n = 7$)

$$u = u_e \cdot \frac{(n+1) \cdot (2n+1)}{2n^2} \cdot \Big(1 - \frac{y}{0.5h}\Big)^{\frac{1}{n}} \tag{6.2}$$

The jet speed u_e is further found by means of the isentropic flow equations

$$\frac{p}{p_t} = \left(1 + \frac{\gamma - 1}{2} \cdot Mn^2\right)^{\frac{-\gamma}{\gamma-1}}, \tag{6.3}$$

$$\frac{T}{T_t} = \left(1 + \frac{\gamma - 1}{2} \cdot Mn^2\right)^{-1} \tag{6.4}$$

and

$$u_e = \sqrt{\gamma RT} \cdot Mn \tag{6.5}$$

under the assumption that pressure losses across the device are negligible. Note that the nozzle height h was assumed to be known a priori. This is because two parameters out of Pr, $f_{ex} = g(St_\theta)$ and h need to be predefined so to determine the value of the remaining third. If, for example, the excitation frequency instead of the nozzle height is fixed (which is the case if a specific transducer needs to be used), the nozzle height can be adjusted so that the shear layer instability satisfies the dependency $f_{ex} = g(St_\theta)$. This in turn might pose a problem since the mass flow $\dot{m}$ through the device can be restricted as well. This, however, can be resolved by changing the aspect ratio AR.

The dependency of the excitation frequency on the shear layer instability is kept quite general ($f_{ex} = g(St_\theta)$) since there is the possibility that specific flow conditions or device configurations require the excitation of different instability modes. This becomes more obvious if the switching mechanism for a laminar jet discussed in the previous chapter is considered. The working principle was partially explained by the amplification of modes corresponding to $St_\theta = 0.012$ and a consequent shift of the shear layer roll-up to further upstream positions. The location of the shear layer roll-up, however, approaches the nozzle orifice as the Reynolds number goes up. It is therefore suggested that the excitation of the fundamental wave ($St_\theta = 0.012$) might not result in sufficient entrainment if the flow is turbulent. Given that turbulent jets

are also characterized by pairing events of neighbouring vortices, the main contribution to entrainment [33], it might be more appropriate to amplify the subharmonic, the driving force that leads to pairing. The estimated required excitation frequency for switching is therefore $f_{ex} = \frac{1}{2}\frac{St_\theta u_e}{\theta}$.

With the above equations and $Pr = 1.1 - 1.5$ this leads to shear layer instabilities ranging from $31 - 63\,kHz$ and subharmonics from $15.5 - 31.5\,kHz$. An excitation frequency of $f_{ex} = 25\,kHz$ was therefore found to be a good candidate, and is kept constant through out this chapter. This is due to the use of one particular transducer that features a resonant frequency at $25\,kHz$ with a relatively small bandwidth. Nonetheless, as is shown later, it is not simply the subharmonic alone that triggers the switching process at higher Re.

6.3 Design Aspects

The geometry of any fluidic device is, in general, crucial for its performance. This seems obvious considering that the fluid mechanic foundation of such devices, the Coanda attachment, is nothing but an effect that depends entirely on geometry. The design aspects are therefore of great importance and require a careful evaluation prior to the design process itself. Fig.6.1 shows a schematic of a typical bistable fluidic diverter with its most relevant geometric parameters. Those are:

1.) Setback distance b

2.) Splitter distance d_s

3.) Wall attachment angle β

4.) Nozzle width w

5.) Presence and location of vents d_v

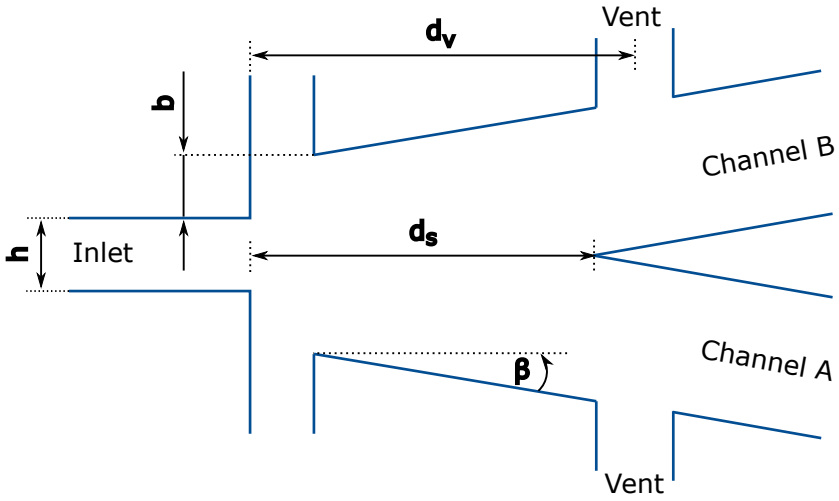

Figure 6.1: Schematic of a bistable fluidic device with its key geometric features

6.) Nozzle height h

Each parameter affects the device performance subject to the switching mechanism. Hence the design aspects are discussed with respect to acoustic excitation and its mechanism outlined in the previous chapter. The effect on the switching performance is further discussed assuming a constant pressure ratio across the jet. Parameters are non-dimensionalised with the nozzle height h where appropriate.

Setback distance b

The setback distance b is the most relevant dimension since it determines enables the switching in the first place. That is to say that a too large setback would prevent the rolled-up vortical structures from forming a confined space with the attachment wall and would therefore allow that the enhanced entrainment is supplied by an infinite reservoir, e.g. reverse mass flow. Hence the pressure would not drop and switching not occur. It is therefore obvious to correlate the setback distance to the size of the expected vortical structures. This means that the setback should not be larger than the nozzle height itself. The present FSD features a setback of $0.8h$ as it was used in chapter 4. Setbacks smaller than that have only limited effect on the pressure drop

of the unattached side since the volume from which fluid is entrained depends mainly on the size of the control port chamber.

Splitter distance d_S

Typical bistable devices have two independent outlet channels that are separated by a splitter. The distance between the splitter and the nozzle orifice d_s is usually crucial to the performance of the device and was already outlined in Chapter 2.

While some switching mechanisms require the presence of a splitter, such as the plasma switched vortex valve in [209], acoustic excitation is suggested to work just as fine without. The enhanced entrainment and subsequent pressure drop on the unattached side due to excitation is independent of a splitter being present or not. However, as will be shown later, the absence of a splitter enables the initial recirculation bubble to increase in size and therefore keep the initial attachment maintained which can delay the switching process. Experimental results in this chapter are shown for two different configurations, with and without a splitter. The reason for the splitter-less device is twofold. First, it enables non-intrusive laser optical measurements which will be discussed in Sec.6.6.2 and second, it demonstrates the ability to operate the device as a frequency controlled sweeping jet. The configuration with splitter features a splitter distance $\frac{d_s}{h} = 7$.

Wall attachment angle β

The wall attachment angle β is inversely proportional to the curvature of the jet centreline R and therefore affects the strength of the attachment force. This is because in steady state condition ($\frac{dR}{dt} = 0$) a smaller radius R increases the pressure difference Δp across the jet. This is evident when looked at the jet-curvature equation (Eq.2.3). To keep the attachment force small and hence decrease the required time to entrain sufficient fluid to reverse the pressure difference across the jet, the present

FSD features a straight attachment wall for the first two nozzle heights downstream of the orifice. A subsequent increase to 42° with respect to the streamwise direction allows the two outlets to be far enough apart enabling a big enough window for an incoming laser. In addition, 42° is also large enough to assure that the spreading of the unattached shear layer will not result in a portion of the jet leaving through the opposite outlet given that maximum reported values of the jet half-angle go up to 20° [271].

Even though the radius of the jet centreline is close to its smallest possible limit it was found that the steady state attachment of the splitter-less configuration is remarkably stable and even maintained if the attached side outlet is completely blocked.

Nozzle width w

The nozzle width w and thus the aspect ratio AR have no effect on the switching mechanism but can affect the switching performance. That is to say that all active means to switch a bistable fluidic device do not rely on a switching mechanism that is based on three dimensional effects. Hence it is theoretically possible to arbitrarily increase the aspect ratio if the actuation mechanism in question can be extruded as well. However, a downside in performance due to a higher aspect ratio is still possible if the power per unit nozzle width decreases. In other words, the control authority goes down as the aspect ratio increases if the absolute input power remains the same. This is also true since the width of the device has no effect on the attachment force (steady state form of Eq.2.3). The aspect ratio is therefore mainly dependent on the type of actuation used. For a plasma-fluidic device, for example, the electrodes that cause the spark discharge cannot be too far apart unless additional trigger electrodes are located along the way. With respect to Piezo-fluidic devices this means that an increase in AR will eventually require a second acoustic source but otherwise not change the switching process. All fluidic devices considered subsequently feature an

aspect ratio of 3.

Presence and location of vents d_v

The switching mechanism of most bistable fluidic devices is based on the supply of fluid to the recirculation bubble so to increase local pressure and/or shift the attachment point further downstream and thereby causing the jet to interact with the splitter. A vent downstream of the steady state attachment point can therefore be used as a high pressure reservoir to inflate the recirculation bubble once the attachment point has passed d_v. Such vents can then be used to enhance the switching performance by reducing the required energy or speeding up the switching. This can be relevant for Piezo-fluidic devices, especially if no splitter is present. This is because the jet centreline radius is inversely proportional to the pressure difference across the jet and the continuous decrease of the attachment force as of the onset of excitation causes the attachment point to shift to further downstream locations. A vent might therefore speed up the switching for Piezo-fluidic devices even though the switching mechanism does not rely on the supply of fluid to the initial recirculation bubble. For the 'splitterless' configuration results are presented with and without vents ($d_v = 14h$).

Nozzle height h

A change in nozzle height h as a significant effect on the device performance, especially if the absolute dimensions of other geometric parameters remain the same. As mentioned previously, it is the setback and splitter distance in particular that need to be commensurate with the nozzle height so to not adversely affect the roll-up of vortical structures or cause too much spillage leading to an unstable attachment. But irrespective of other device dimensions the nozzle height also affects the Reynolds number Re, the momentum thickness θ as well as the attachment force Δp. A higher

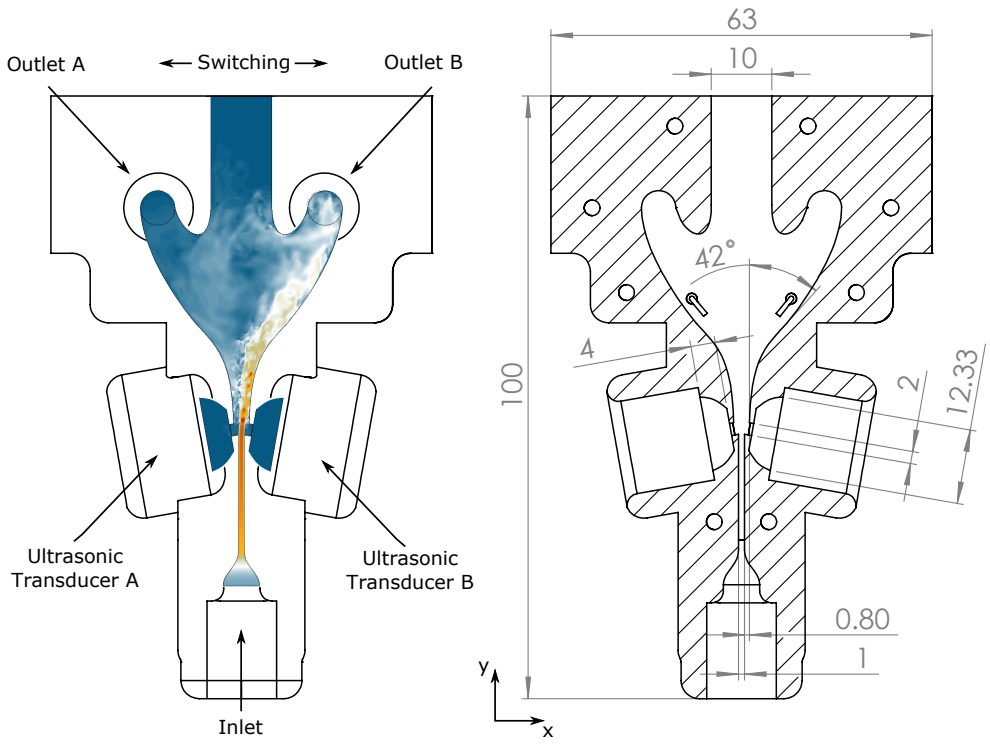

Figure 6.2: Schematic of the device geometry, left: basic device characteristics and instantaneous velocity field, right: governing dimensions in $[mm]$

Reynolds number due to a bigger nozzle height increases the momentum thickness leading to a lower frequency of the natural shear layer instability ($St_\theta = \frac{f\theta}{u_e} = const$). At a given pressure ratio the nozzle height is therefore a key parameter for the excitation frequency. The preliminary design of any Piezo-fluidic device should therefore always be derived from the reciprocal effect of pressure ratio, nozzle height and excitation frequency as mentioned in Sec.6.2. In addition, the attachment force is linearly proportional to the nozzle height (see Eq.2.3). This in turn means that the nozzle height is directly proportional to the energy required to switch the jet and, as a consequence, to the number of excitation cycles (t_{ex}). This is evident from the fact that the pressure difference across the jet needs to be reversed during the time of excitation. A stronger attachment thus requires a longer excitation period if the sound power remains the same. The nozzle height of the fluidic devices presented subsequently is $h = 1\,mm$. Nozzle heights larger than that result in overall larger devices and

hence might hamper a possible integration in future real world applications. Nozzle heights smaller than $1\,mm$ adversely affect the manufacturing as well as the bias of the device. Hence, $h = 1\,mm$ is a compromise between manufacturing capabilities, overall device size, target operating pressure ratio as well as the preferred excitation frequency.

A schematic of the resulting geometry (splitter-less configuration) is shown in Fig.6.2.

6.4 Acoustic Considerations

The results in Chapter 4 give rise to the assumption that a considerable higher sound pressure level is required if the pressure ratio across the device increases and the preferred excitation frequency becomes ultrasonic. This poses a problem for two reasons. First, the ultrasonic transducers used in this study feature an only marginally larger sound pressure level than the low frequency buzzers used in Chapter 4. At reference conditions ($10\,cm$ & $10\,V_{rms}$) the difference in SPL amounts to a mere $4\,dB$. This will most likely not meet the requirements of switching high subsonic flows since the threshold amplitude, as shown subsequently, increases with the square of the flow velocity. Second, high frequency actuators feature a lower bandwidth (higher Q-factor) than low frequency actuators. The Q-factor of the ultrasonic and low frequency transducers amount to ≈ 16 and ≈ 1, respectively. The relatively flat frequency response of the low frequency buzzers therefore enables different excitation frequencies without having to compromise on the sound pressure level. This in turn has a positive effect on the range of pressure ratios that allow switching. The inherent limitations of ultrasonic transducers with respect to flow control applications might therefore be a reason why the perturbation of free shear layers with ultrasound has not been studied in the open literature yet. However, those limitations can potentially

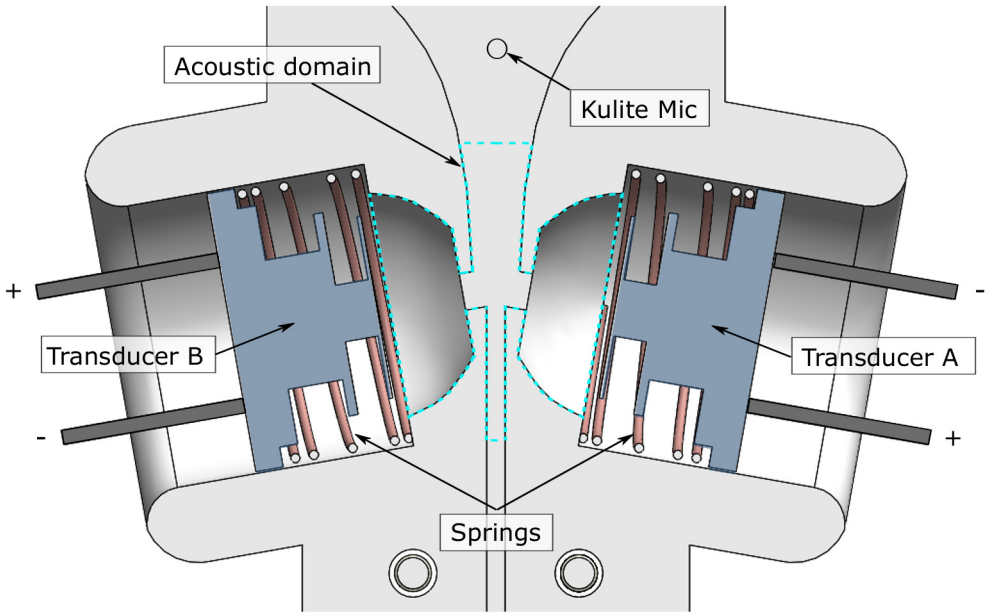

Figure 6.3: Cutaway model of the nozzle and interaction region and display of the acoustic domain

be overcome if the device itself is used to amplify the signal amplitude. In this regard, a big advantage of ultrasonic frequencies is that the wavelength of the acoustic signal becomes comparable to the smallest dimensions of the device ($\lambda_{25kHz} \approx 10h$). This means that the control port chamber can be used to amplify the sound pressure level by matching one of its eigenmodes to the transducer resonance frequency. Such eigenmodes can be found by means of the Helmholtz equation, a time-independent form of the wave equation as described in Chapter 3. Solving the wave equation in the frequency domain then yields the frequency response at any given point for a given geometry.

With regard to the present FSD this means that the control port chamber should have a geometry that satisfies the requirements of sufficient amplification of the input signal so to enable switching. Such a geometry can be found by iteratively solving the time-independent wave equation along with an optimisation algorithm. Here a simple gradient based algorithm that uses the so called interior-point method is used [272]. Such an algorithm searches for a minimum of a constrained nonlinear multivariable

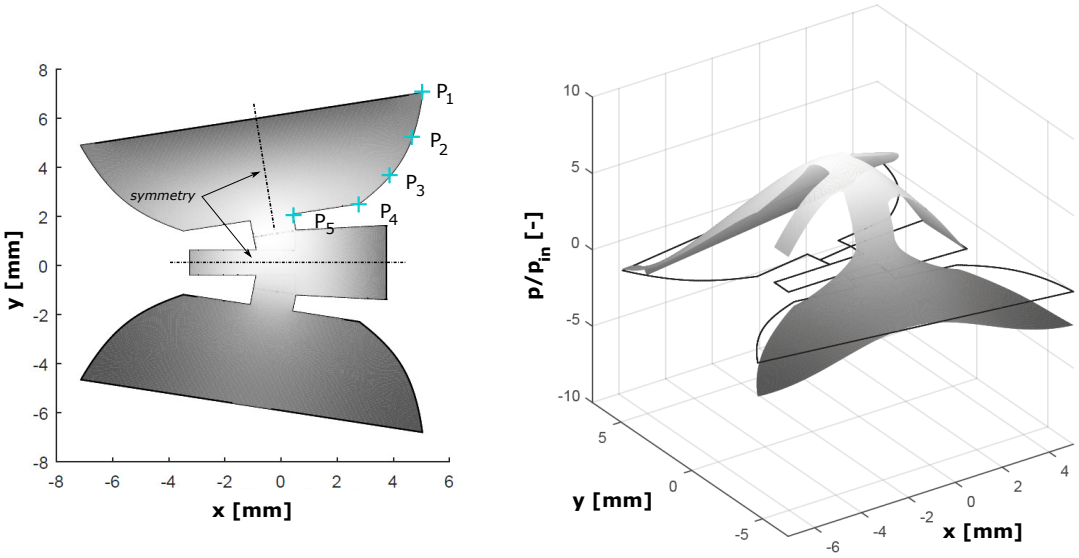

(a) Left: Acoustic domain with 5 Bézier points and symmetry lines, right: input pressure amplification of the optimized design across the domain

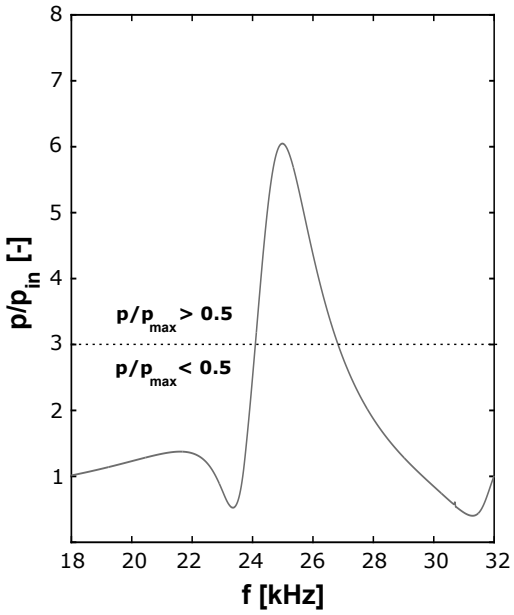

(b) Amplification of input pressure vs. frequency with full width at half maximum

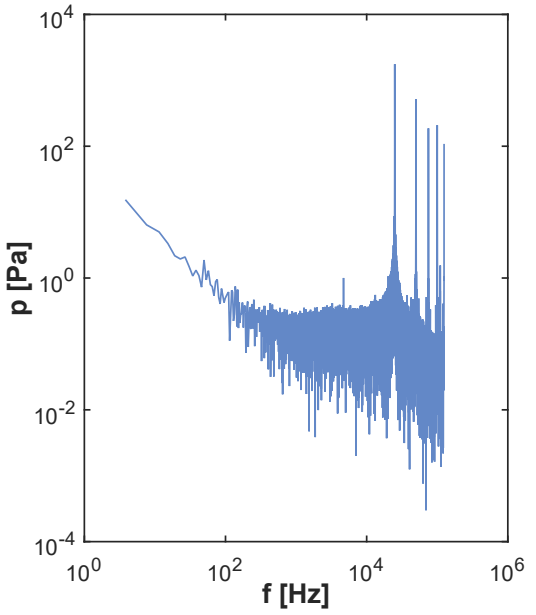

(c) Frequency response measured by Kulite microphone at $f_{ex} = 25\,kHz$ and maximum input voltage

Figure 6.4: Acoustic optimisation of the control port chamber

function. It is multivariable because the control port chamber consists of more than one x or y coordinates which in addition are geometrically constrained. The objectives for the design are

1 Keep chamber resonant frequency close to transducer resonant frequency

2 Maximise sound pressure level SPL at resonant frequency

3 Design for Q so that bandwidth is $2\,kHz$

Note that the latter objective takes into account inevitable manufacturing tolerances. The objectives can be summarized mathematically as

$$f(x) = min \begin{cases} |f_T - f^*| \\ \frac{1}{SPL^*} \\ |\frac{f_T}{2\,kHz} - Q| \end{cases} \tag{6.6}$$

f_T is the transducer resonance frequency and f^* the frequency at the highest sound pressure level SPL^*. The location where SPL^* is computed is a separate measurement domain between the control port throat and the nozzle orifice, the point where the acoustic wave interacts with the shear layer. For each iteration the sum of all objectives ($|f_T - f^*| + \frac{1}{SPL^*} + |\frac{f_T}{2\,kHz} - Q|$) is returned as the value to be minimized. The variables to be optimized are then the x and y coordinates of 5 Bézier points that form each side wall of the symmetrical control port chambers. The acoustic domain in which the wave equation is solved for frequencies between $18 - 32\,kHz$ is further highlighted in Fig.6.3 and Fig.6.4 a.). Given that the optimisation requires more than 100 iterations it is further opted for a 2D eigenmode calculation to keep computational costs within reasonable bounds.[2] The optimised geometry, as shown in Fig.6.3, features a sextuple amplification of the input pressure (Fig.6.4 b.)). In absolute numbers this amounts to a maximum sound pressure level of $158.8\,dB$ for the splitterless configuration (Fig.6.4 d.)). Further information regarding the optimisation is given in appendix A.

Furthermore, Tam [273] derived a measure of the relative sensitivity of the shear layer to sound induced instability as a function of the angle of incidence. For the range of Mach numbers expected in this study ($Mn \approx 0.3$) the angle that generates

[2]Results for a 3D acoustic simulation are compared to 2D results in the Appendix A

instability waves with the largest amplitudes was found to be 10°. The control port chambers are thus rotated by 10° with respect to the cross-stream y-direction. Fig.6.3 further shows that springs are used to place the ultrasonic transducers inside the chambers. This was found to ensure that the membrane is at the correct location so to obtain the amplification set by the optimisation. The final geometry of the device is now fully described.

6.5 Non-dimensional Parameters

The concept of similarity, also called the principle of dimensional homogeneity, constitutes the basis of research in engineering science. It implies that the results of different experiments of a given system at different absolute quantities but identical non-dimensional parameters are equivalent. Such non-dimensional parameters are therefore substantial to study the physics of a system since they allow different sized experimental set-ups without compromising on the validity of the results. They can be found by means of the Buckingham-π theorem which states:

Any relation of the form $\Phi(R_1, R_2, \ldots R_n) = 0$ *where* R_i *are the relevant physical variables of the system having* m *primary dimensions, is equivalent to a relation of the form* $\Psi(\Pi_1, \ldots, \Pi_{n-m}) = 0$ *in which the* Π*'s are all independent non-dimensional products that can be constructed from* $R_i^j \cdot R_k^l$ *where the exponents* j *and* l *are rational numbers and* R_k *the so called repeating variables. The* m *repeating variables can further be chosen at random but must include all primary dimensions.*

With respect to the switching mechanism of an acoustically driven FSD, the most relevant variables that describe the system are:

- Pressure amplitude $\hat{p}$
- Excitation frequency f_{ex}

- Required energy E
- Fluid density ρ
- Jet speed u_e
- Nozzle height h
- Momentum thickness θ
- Switching time t_s
- Pressure ratio $\frac{p_{t,in}}{p_{out}}$
- Splitter distance d_s

Fluid density ρ, nozzle height h and jet speed u_e are chosen as the repeating variables R_k. With $m = 3$ (s, kg, m) and $n = 10$ this amounts to the following $n - m = 7$ non-dimensional parameters:

$$0 = \Psi(\frac{t_s u_e}{d_s}, \frac{\hat{p}}{\rho u_e^2}, \frac{f_{ex} h}{u_e}, \frac{E}{u_e^2 \rho h^3}, \frac{p_{t,in}}{p_{out}}, \frac{d_s}{h}, \frac{h}{\theta}) \tag{6.7}$$

The non-dimensional switching time can then be written as a function of all the remaining parameters such that:

$$T_s = \Psi(Am, St_h, \bar{E}, Pr, \frac{d_s}{h}, \frac{h}{\theta}). \tag{6.8}$$

The switching time is non-dimensionalised by the transport time $\frac{d_s}{u_e}$, the time it takes a fluid particle to travel form the nozzle orifice to the splitter leading edge assuming a constant velocity u_e. For the splitter-less configuration considered subsequently the splitter distance d_s is replaced by the distance between the nozzle and the Pitot probe.

The first parameter on the right side of Eq.6.8 is the non-dimensional amplitude which will be called the Amplitude Flow Factor (Am). It indicates that the sound power required for switching depends on the kinetic energy of the flow. The second parameter, the Strouhal number St, can either be based on the nozzle height h or the momentum thickness θ. It will become evident what is more appropriate for the current study. The non-dimensional energy $\bar{E}$ is a pure function of the excitation time if signal properties and flow conditions remain the same. Together with the pressure ratio Pr and the switching time T_s, those three parameters form the foundation of all subsequent performance characteristics.

The two remaining parameters $\frac{d_s}{h}$ and $\frac{h}{\theta}$ are independent of the excitation properties but nonetheless affect the switching process. The effect of the non-dimensional splitter distance was already discussed and hence will not be reviewed. The ratio of nozzle height to momentum thickness, equivalent to $\frac{Re_h}{Re_\theta}$, is an important parameter with significant contribution to the downstream development of vortices. It is in fact a measure for the turbulence level at the nozzle exit and hence has a strong effect on the initial jet growth, i.e. spreading rate [274]. For a laminar exit velocity profile, $\frac{h}{\theta}$ is small and results in a low spreading rate with a location of the initial shear layer roll-up relatively close to the end of the potential core. As the Reynolds number increases and the velocity profile becomes fully turbulent $\frac{h}{\theta}$ approaches an asymptotic value. The location of the initial shear layer roll-up is then shifted to further upstream positions and eventually reaches its limit close to the nozzle orifice due to the asymptotic behaviour of $\frac{h}{\theta}$. Apart from that, it is well established that the position of the vortex roll-up coincides with the nonlinear saturation of the initial instability which in turn leads to multiple harmonic modes [275]. The subharmonic then provokes the downstream pairing of neighbouring vortices before the end of the potential core. Such pairing events were further found to be responsible for the shear layer spreading and hence its entrainment. With respect to an acoustically driven

FSD, this means that a sufficient increase in entrainment (which counteracts the attachment force) is unlikely to be accomplished by fundamental forcing if Re exceeds a certain threshold. In other words, the excitation and amplification of the primary instability ($St_\theta = 0.012$) will not achieve the necessary increase in entrainment if $\frac{h}{\theta}$ is high since the shear layer characteristics become less dependent on the initial roll-up of vortical structures. This suggests, as already assumed at the beginning of this chapter, that different instability modes need to be addressed if Re exceeds a certain threshold. Clearly, this threshold corresponds to the location of the shear layer roll-up and hence to $\frac{h}{\theta}$. The ratio of nozzle height to momentum thickness can therefore be used as a measure for which instability has to be excited and, what will be shown later, which length scale the non-dimensional frequency St should be based on.

Note that the above parameters were derived from a limited set of variables. Other device dimensions or, for instance, the flow rate through the device were not included so to not unnecessarily complicate the description of the system.

6.6 Splitter-less Configuration

6.6.1 Performance Characteristic

6.6.1.1 Switching Characteristics

Fig.6.5 shows an example for 10 successive switching events at $Pr = 1.07$ ($Mn \approx 0.3$) measured via the Pitot probe on the initially unattached side. The average switching time amounts to $t_s = 5.5\,ms$ with a maximum deviation of 9%. The negative total gauge pressure measured on the unattached side illustrates the reverse mass flow that supplies the entrainment of the unforced jet. The graph further reveals that the excitation time is only a fraction of the time needed to switch the jet, that

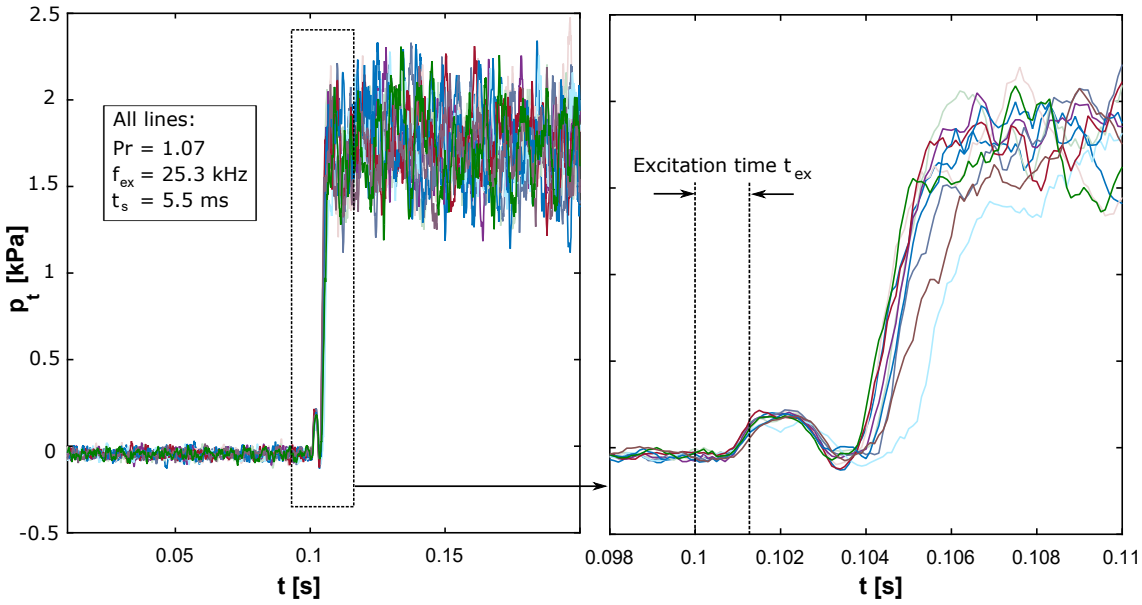

Figure 6.5: Ten successive switching events measured via the Pitot probe and close-up view for the comparison of different time scales

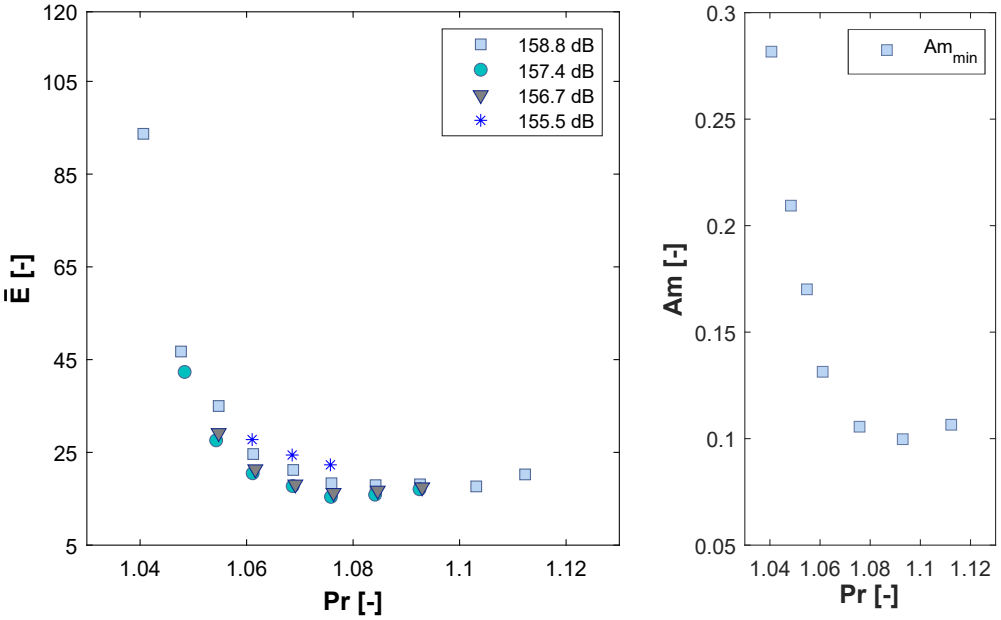

(a) Minimum required energy

(b) Minimum required Amplitude Flow factor

Figure 6.6: Non-dimensional switching parameters as a function of Pr

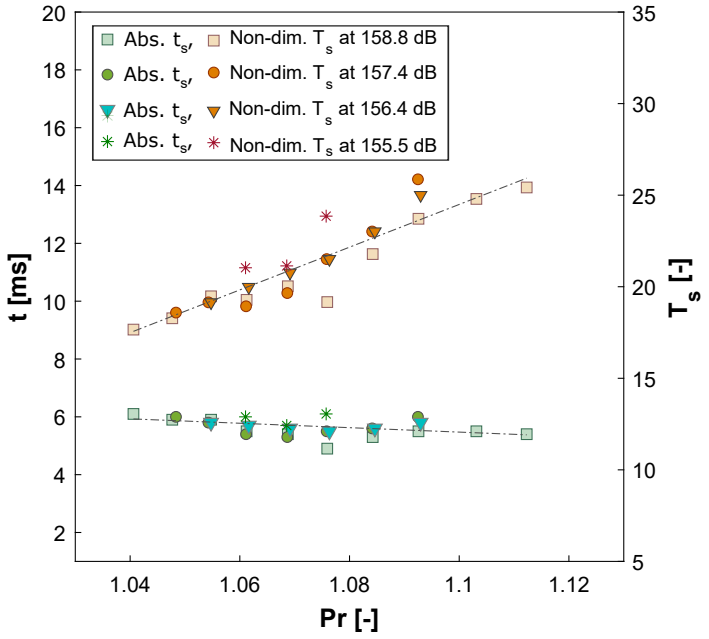

Figure 6.7: Non-dimensional and absolute switching time vs. Strouhal number and pressure ratio for different sound pressure levels

all lines show a similar hump prior to the switching and that the actual switching seems somehow delayed. Note that the delay is an order of magnitude larger than the transport time and is therefore not caused by the downstream location of the Pitot probe. The short excitation time indicates that the driving force, caused by the pressure drop on the unattached side, is reached long before the jet has fully responded to the new steady state condition. This indicates that the jet has already attached to the opposite side after the excitation has stopped but the recirculation bubble on the initial attachment side persists, increases in size and elongates downstream (see Fig.6.8. This 'double attached' flow stalls the detachment from the initial side and causes the delay in switching. This again is simply due to the absence of a splitter that would otherwise put a stop to the elongation of the recirculation bubble. It is interesting to note that the condition of the 'double attachment' persists for several flow-through times. However, it is reasonable to assume that the switching time can be decreased by either using a splitter or introducing vents downstream of the

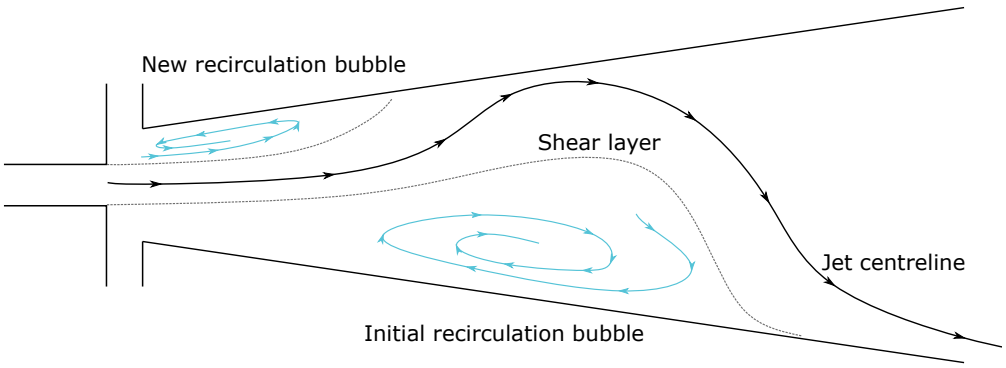

Figure 6.8: Schematic of a 'double attached' flow

reattachment point.

The hump, which is consistent for every single switching event, shows that the shear layer responds instantly with an increased spreading rate as of the onset of excitation. The deflected shear layer travels downstream along the attachment wall and is measured as an increase in total pressure. This is verified by the fact that the hump starts off one flow-through time between the nozzle and the Pitot probe after the onset of excitation and that the flat peak of the hump lasts exactly for t_{ex}.

6.6.1.2 Non-dimensional Energy and Switching Time

It was found in the previous chapter that the minimum required energy to switch the jet serves as an appropriate criterion to find the preferred pressure ratio and/or Strouhal number for a fixed excitation frequency. In that respect Fig.6.6 a.) shows the non-dimensional minimum energy for four different sound pressure levels as a function of Pr. An increase in sound pressure level simply increases the range of pressure ratios that enable switching similar to the results at laminar flow conditions and low frequency excitation presented in Chapter 4. At the lowest sound pressure level switching is only feasible between $Pr = 1.06$ and $Pr = 1.075$, or rather $St_{D_{eq}} = 0.47$ and $St_{D_{eq}} = 0.43$. The preferred pressure ratio ($Pr \approx 1.07$) thus seems to be at $St_{D_{eq}} \approx 0.45$ suggesting that the excitation of the jet preferred mode is responsible

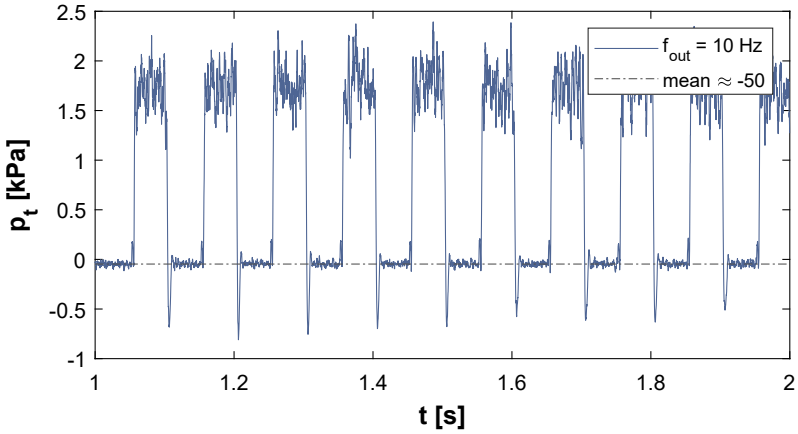

(a) $f_{out} = 10\,Hz$

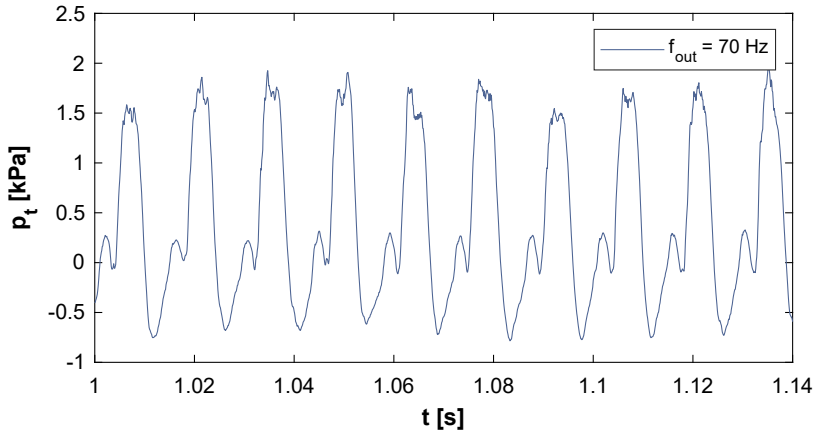

(b) $f_{out} = 70\,Hz$

Figure 6.9: Dynamic switching at two different oscillation frequencies

for switching [65]. The non-dimensional energy exhibits an exponential increase as the pressure ratio approaches the lower end ($Pr = 1.04$) at which only the highest tested amplitude ($\hat{p} = 158.8\,dB$) can switch the jet. At higher pressure ratios, in contrast, only a moderate linear increase in $\bar{E}$ is required for switching. The global minimum in energy ($\bar{E}$) is found around $Pr = 1.075$ which corresponds to $St_{D_{eq}} = 0.43$ and is marginally shifted to higher pressure ratios with respect to the preferred mode. In absolute terms the energy E follows a symmetrical parabolic curve with its minimum at $St_{D_{eq}} = 0.45$ ($Pr = 1.07$). The shift towards higher pressure ratios when looked at the non-dimensional numbers is also shown in Fig.6.6. Here the minimum required non-dimensional amplitude Am corresponds to $Pr \approx 1.09$. It is clear that

the minimum amplitude that allows switching increases exponentially as the pressure ratio moves away from the preferred mode. This can be observed especially at lower pressure ratios since $Am \propto \frac{1}{u_e^2}$. The minimum required amplitude flow factor around the jet preferred mode amounts to ≈ 0.1.

The non-dimensional switching time, shown in Fig.6.7, exhibits a linear increase over Pr that results in a minor decrease when put to absolute terms. No preferred mode in terms of t_s can thus be derived. This indicates that, once $\bar{E}$ (or rather Am) and $St_{D_{eq}}$ are within the feasible range that triggers the switching process, the switching time is a mere function of the jet speed. The average switching time at $Pr = 1.07$ amounts to $5.5\,ms$.

6.6.1.3 Dynamic Switching

Fig.6.9 a.) shows a forced oscillating jet at $f_{out} = 10\,Hz$ measured with the Pitot probe on side B. For each switching away from the measurement probe a significant undershoot is observed before the new steady state is reached. It is suggested that this is caused by the previously mentioned recirculation bubble that increases in size and elongates in the downstream direction. The undershoot is, in fact, a measure of the low pressure region inside the recirculation bubble that extends across the location of the Pitot probe. This is further supported by calculating the pressure difference across a reattached jet using the steady state form of the jet curvature equation (Eq.2.3) and a jet centreline radius R equal to the attachment wall radius, so that

$$\Delta p = -\frac{\dot{m}^2}{\rho h^3 A R^2} \cdot \frac{1}{R} = -535\,Pa. \tag{6.9}$$

In general, the FSD can output any desired frequency pattern and is only limited by the minimum switching time t_s. Given the standard deviation of t_s of $\sigma = 9\%$ and that we defined the switching time as the time span between the onset of excitation

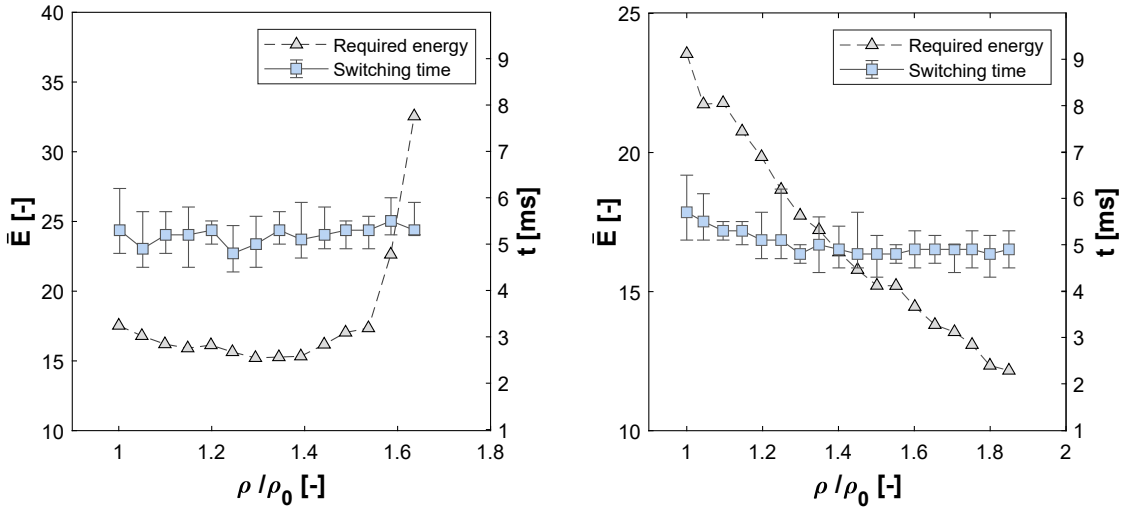

(a) $\hat{p} = const.$ (b) $Am = const.$

Figure 6.10: Non-dimensional energy and absolute switching time vs. changes in density

and the point where 90% of the final mean value is reached, we can determine the maximum output oscillation frequency by:

$$f_{out}^{max} \leq \frac{0.9}{2 \cdot 1.09 \cdot t_{s,min}} = 75\,Hz \tag{6.10}$$

Unfortunately, sometimes the switching process takes longer than $(1+\sigma)t_{s,min}$ and so in practice the maximum reliable switching frequency was found to be $70\,Hz$ which corresponds to a 2σ deviation

$$f_{out}^{max} \leq \frac{0.9}{2 \cdot (1 + 2 \cdot \sigma) \cdot t_{s,min}} = 70\,Hz \tag{6.11}$$

Dynamic switching at $70\,Hz$ is displayed in Fig.6.9 b.).

It should also be mentioned at this point that the dynamic operation of a fluidic device has, in general, the potential for hysteresis. In [276], for instance, it has been reported that the swithcing mechanism (of a passive oscillator) depends on two different modes which again depend on the flow velocity. More over, it was shown

that there is a jump to higher oscillation frequencies when the switching mechanism changes form one mode (momentum mode) to the other (acoustic mode). If the flow velocity is again decreased after it has jumped to higher oscillation frequencies, the second mode still prevails and the switching mechanism transitions back to the first mode only at lower jet velocities than is has transitioned from the momentum mode to the acoustic mode. For the present device, however, no such hysteresis effect has been observed and neither was it reported for other active fluidic devices in the open literature.

6.6.1.4 Effect of Changes in Density

Temperature and absolute pressure in aerospace components differ from the conditions of typical bench test experiments. This is to say, the effect of changes in density on the demeanour of fluidic devices is crucial for the implementation in real world applications. Here the effect of changes in density is examined by increasing the mass flow rate while simultaneously adjusting the back pressure so as to maintain a constant volume flow rate. The pressure ratio across the device is therefore kept constant while the density increases. Fig.6.10 a.) shows the absolute switching time along with the required non-dimensional energy as a function of $\frac{\rho}{\rho_0}$ at a constant pressure amplitude $\hat{p}$. The pressure amplitude is kept constant by decreasing the input voltage since $\hat{p}$ increases in compliance with the acoustic impedance ρc. The volume flow rate tested corresponds to a pressure ratio of $Pr = 1.07$ at $\frac{\rho}{\rho_0} = 1$. It can be seen that the required energy, in absolute and non-dimensional terms, increases exponentially as the density goes up. Since $\hat{p} = const$ and the increase in density is linear, it is the excitation time that has to be increased exponentially. However, at density ratios $\frac{\rho}{\rho_0} > 1.65$ an increase in excitation time is not able to cancel out the decrease in Am any more and switching becomes out of reach. The switching time t_s is somehow independent and is maintained around $5.5\,ms$. With a constant Amplitude Flow Fac-

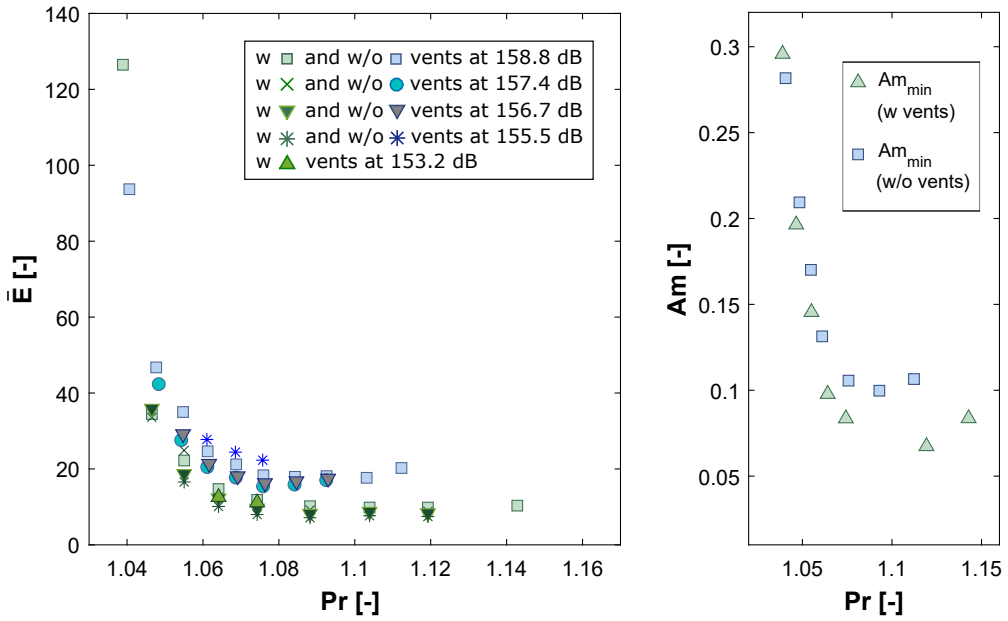

(a) Minimum required energy

(b) Minimum required Amplitude Flow factor

Figure 6.11: Comparison of non-dimensional switching parameters between vents and no vents

tor Am Fig.6.10 b.) shows that the non-dimensional energy decreases linearly as the density goes up. This corresponds to a constant energy when put to absolute numbers ($\frac{Ap^2 t_{ex}}{\rho c} = const$). The switching time is again not affected. It is therefore concluded that the switching performance is independent of changes in density, and thus mass flow rate, if the Strouhal number $St_{D_{eq}}$ and the Amplitude Flow Factor Am remain constant. Hence there is no downside in performance when used at engine realistic conditions, i.e. high temperatures and high absolute pressures.

6.6.1.5 Effect of Vents

The switching mechanism of most bistable fluidic devices is based on the supply of fluid to the recirculation bubble so as to increase local pressure and/or shift the attachment point further downstream and thereby causing the jet to interact with a potential splitter. A vent downstream of the steady state attachment point can

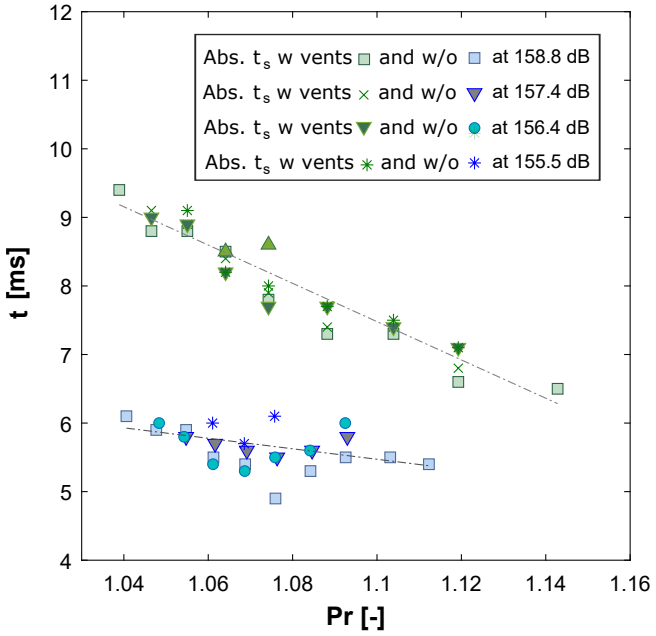

Figure 6.12: Absolute switching time t_s versus pressure ratio Pr

therefore be used as a high pressure reservoir to inflate the recirculation bubble so to speed up the switching or reduce the required energy. This seems highly relevant for the present device since the recirculation bubble on the initial attachment side was found to hamper and delay the switching. Circular vents with a radius of $1.5h$ are, on that account, placed at a location $d_v = 14h$ downstream of the nozzle orifice. Fig.6.11 a.) depicts the non-dimensional energy as a function of Pr for both cases with and without vents. It can be seen that the range of pressure ratios that allow switching increases towards higher pressure ratios ($Pr > 1.14$) and that the lowest pressure amplitude enables switching around $St_{D_{eq}} = 0.45$ only. Moreover, less energy is required to switch the jet. At $Pr = 1.07$ the difference amounts to $\approx 50\%$ but is shown to increase even further as the pressure ratio goes up. This is also backed up by Fig.6.11 b.) which shows the minimum required amplitude Am_{min} as a function of Pr. The minimum is again shifted towards higher pressure ratios (lower Strouhal numbers) with respect to the preferred mode and the difference between both cases

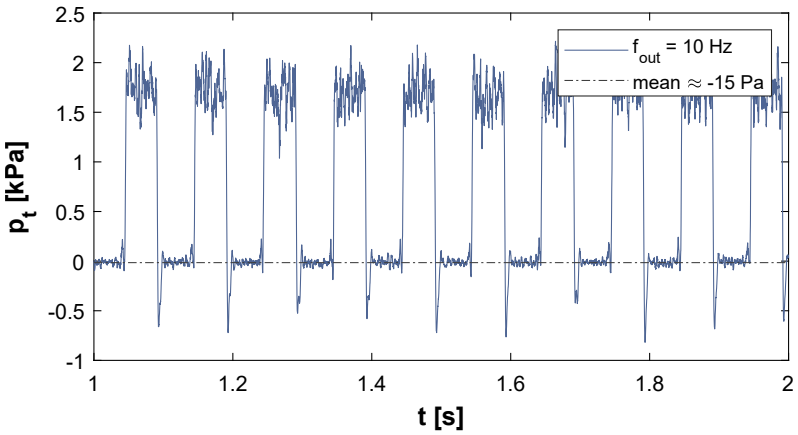

Figure 6.13: Absolute switching time t_s versus pressure ratio Pr

increases as the pressure ratio goes up.

The effect of vents on the switching time t_s is quite the opposite of what was expected. Fig.6.12 shows that the switching time is considerably increased by up to 70%. The vent on the initial attachment side thus fails to inflate the recirculation bubble and therefore cannot eliminate the 'double attached' flow. This is also confirmed by Fig.6.13 which shows the same undershoot at the end of every switching away from the Pitot probe. This, however, cannot explain why switching is even more delayed when using vents. It must therefore have to do with flow entering the device through the opposite vent. Fig.6.13 shows that the mean value measured on the unattached side ($-15\,Pa$) is closer to zero than for the case without vents (Fig.6.9 a.)). This implies that a portion of the flow entrained by the free shear layer is now supplied by the vent. It is obvious that the incoming flow momentum counteracts the switching and acts as a new source of delay. This is further supported by Fig.6.14. The hump that was attributed to the shear layer spreading on the unattached side appears to be suppressed for the device with vents.

In addition, it is striking that the decrease of $t_{s,vents}$ at higher pressure ratios exhibits a steeper gradient than t_s. A possible reason could be that the momentum of the main jet increases faster than the momentum of the flow through the vent as the

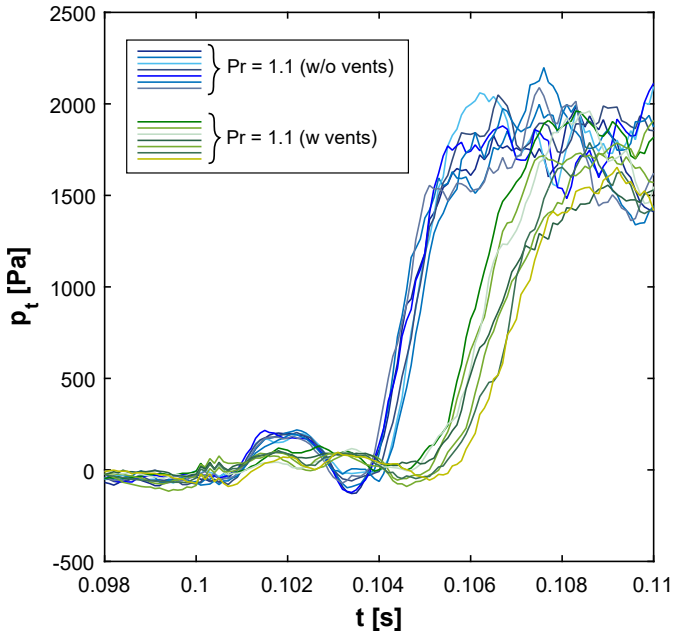

Figure 6.14: Single switching events with and without vents at $Pr = 1.1$

mass flow rate goes up. This would ease the counter-effect and delay in switching and, as a consequence, explain the difference in $\frac{dt_s}{dPr}$. This also suggests that $t_{s,vents}$ will eventually approach t_s at higher Pr.

To summarize, the use of vents lowers the required energy for switching and therefore increases the range of pressure ratios. However, vents were also shown to simultaneously delay the switching process resulting in a lower bandwidth of the device.

6.6.2 Flow Visualisation Studies

A more detailed investigation of the splitter-less device requires the visualisation of the prevalent flow conditions in steady state as well as during the switching itself. Both numerical (LES) and experimental (PIV) flow visualisation methods are therefore presented subsequently. Basic flow features and the development of shear layer instabilities at different mass flow rates are discussed first. This is followed by a detailed analysis of a single switching event at the preferred mode found in the preceding

section.

6.6.2.1 Basic Flow Features and Shear Layer Instabilities

The results presented in Sec.6.6.1 gave rise to the assumption that the switching process is triggered by the excitation of the jet preferred mode ($St_{D_{eq}} = 0.45$). This contrasts the findings gained in the preceding chapter. There it was concluded that, at least for laminar flow conditions, the switching is triggered by the excitation and amplification of the shear layer mode ($St_\theta = 0.012$). This is interesting as it supports the assumption in Sec.6.2 that a different mode than the shear layer mode has to be triggered to switch a jet at higher Pr. It seems obvious to correlate the shift of the required excitation mode to a change in the shear layer characteristics as the Reynolds number increases. This calls for an in-depth analysis of the development and dynamics of the natural shear layer roll-up without excitation. Time series of vorticity along the free shear layer as well as snapshots and mean values (transient average) of the velocity field, both LES and PIV, are thus studied in the following. However, since a truncated model is used (model IV in Chapter 3) there is no reason to use the experimentally measured pressure ratios (across the full device) as boundary conditions for the numerical model. Inlet total pressures were thus chosen rather arbitrarily but, at the same time, adjusted so as to match the mass flow rates $\dot{m}_{exp}$ to within 4%. All mass flow rates $\dot{m}_{1-10}$ obtained from both LES and experiments are summarized in Tab.6.1. The preferred mode found in the experiments corresponds to $\dot{m}_5$.

	1	**2**	**3**	**4**	**5**	**6**	**7**	**8**	**9**	**10**
Pr (Exp.)[−]	1.041	1.048	1.055	1.061	1.068	1.076	1.084	1.093	1.103	1.112
ṁ (Exp.)[**g/s**]	0.298	0.319	0.340	0.361	0.383	0.404	0.425	0.446	0.468	0.489
ṁ (LES)[**g/s**]	0.303	0.326	0.350	0.374	0.395	0.418	0.440	0.460	0.487	0.508
Δṁ [%]	1.89	2.10	2.83	3.26	3.12	3.42	3.32	2.99	3.93	3.85

Table 6.1: Mass flow rates through the truncated model ($\dot{m}\,(LES)$) and the full-scale device ($\dot{m}\,(Exp.)$) as set during the experiments in Sec.6.6.1

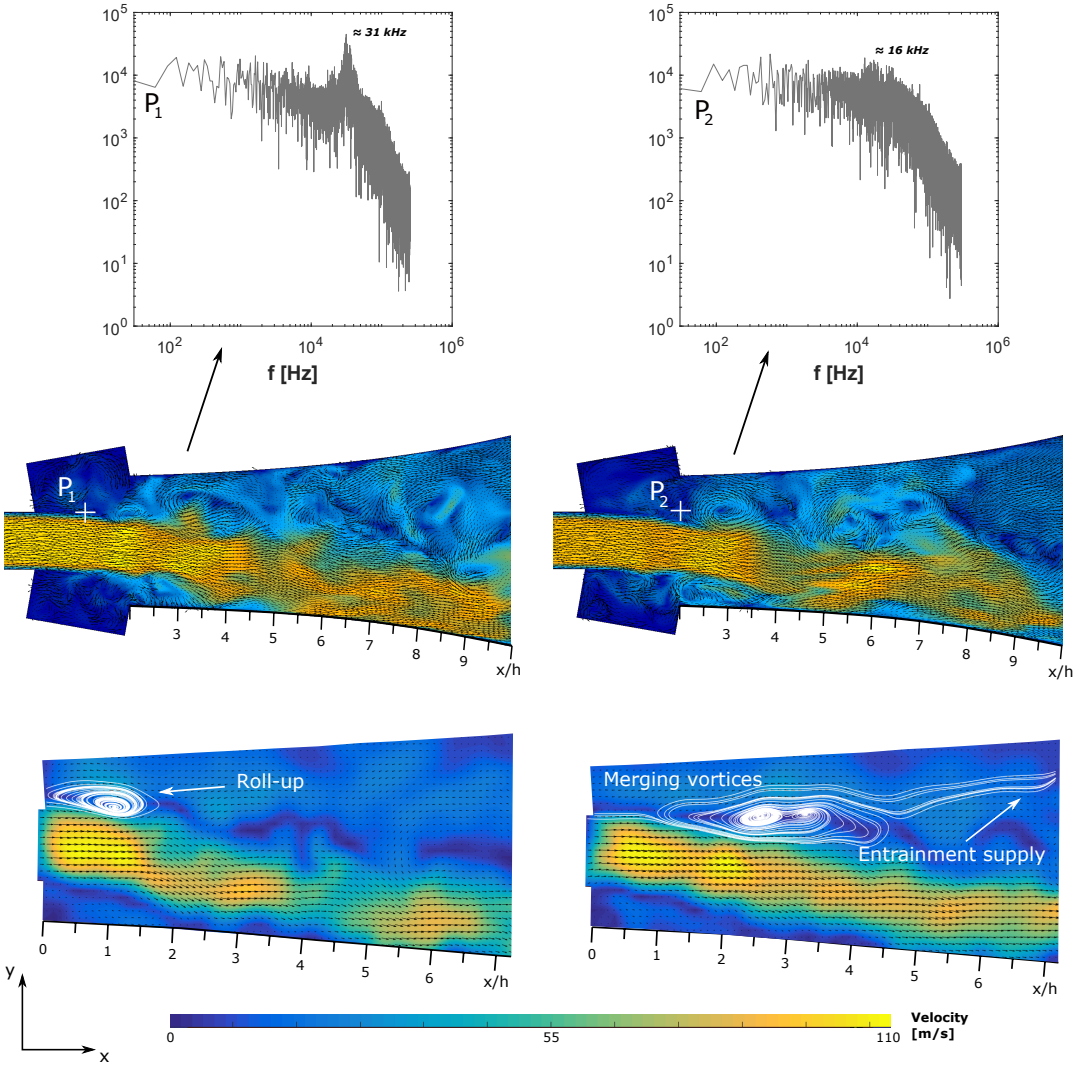

Figure 6.15: Bottom: Instantaneous velocity vector field (PIV) with streamlines showing shear layer roll-up, middle: Instantaneous velocity vector field (LES) with monitor points P_1 $(x = 1\,h)$ and P_2 $(x = 2\,h)$, top: frequency spectra of vorticity at P_1 and P_2 for $\dot{m}_5$

Fig.6.15 shows the velocity vector field at two arbitrary time steps for $\dot{m}_5$ ($Re_h = 9500$). The shear layer is observed to roll-up at around $1\,h$ downstream of the nozzle. This is considerably closer to the nozzle orifice than for a jet with an initially laminar velocity profile as discussed in Chapter 4. The frequency of the shear layer roll-up is further quantified by the peak in the frequency spectra of vorticity at P_1 $(x = 1h)$ and amounts to $\approx 31\,kHz$ (see Fig.6.15). Merged vortices are observed sporadically and

only downstream of $x = 1.5\,h$. The spatial and temporal randomness of neighbouring vortices merging together is also expressed by a very minor peak in the frequency spectra at $\approx 16kHz$ and $x = 2h$. It further reveals that the flow breaks down to a turbulent flow regime and no coherent structures dominate further downstream. This is also supported by frequency spectra of vorticity, pressure and streamwise velocity downstream of $x = 4h$ that do not exhibit any peak at all. Coherent structures, pairing events and turbulent flow with random and complex vortex topologies are further shown in Fig.6.16 by means of the λ_2 vortex method. Isosurfaces of λ_2 demonstrate the chaotic three-dimensional flow pattern by different-sized vortex tubes that are aligned in all directions. A more qualitative representation of the governing flow structures is given by the λ_2 contour plot on the right of Fig.6.16.

It is reasonable to correlate the difference of the shear layer roll-up location between the reference case in Chapter 4 and the current study to a change in the turbulence level of the shear layer, hence the boundary layer at the nozzle orifice. A measure for that turbulence level is $\frac{Re_h}{Re_\theta}$ and therefore the ratio of nozzle height to momentum thickness $\frac{h}{\theta}$, one of the non-dimensional parameters derived in Sec.6.5. For a laminar exit velocity profile, $\frac{h}{\theta}$ is small and was shown to result in a location of the initial shear layer roll-up relatively close to the end of the potential core. As the Reynolds number increases and the velocity profile becomes turbulent the boundary layer momentum thickness decreases which in turn causes the ratio $\frac{h}{\theta}$ to increase. Now, given that the location of the shear layer roll-up can be attributed to the turbulence level of the initial shear layer thickness, it can be said that the location of the shear layer roll-up moves upstream with an increase in $\frac{h}{\theta}$ and eventually reaches its limit close to the nozzle orifice. The change of the required excitation mode from $St_\theta = 0.012$ to $St_{D_{eq}} = 0.45$ is therefore related to the value of $\frac{h}{\theta}$. The length scale with which the frequency is made non-dimensional (St_θ or $St_{D_{eq}}$) thus depends on $\frac{h}{\theta}$.

Values for $\frac{h}{\theta}$ are shown in Fig.6.17 b.) using the transient average velocity profiles

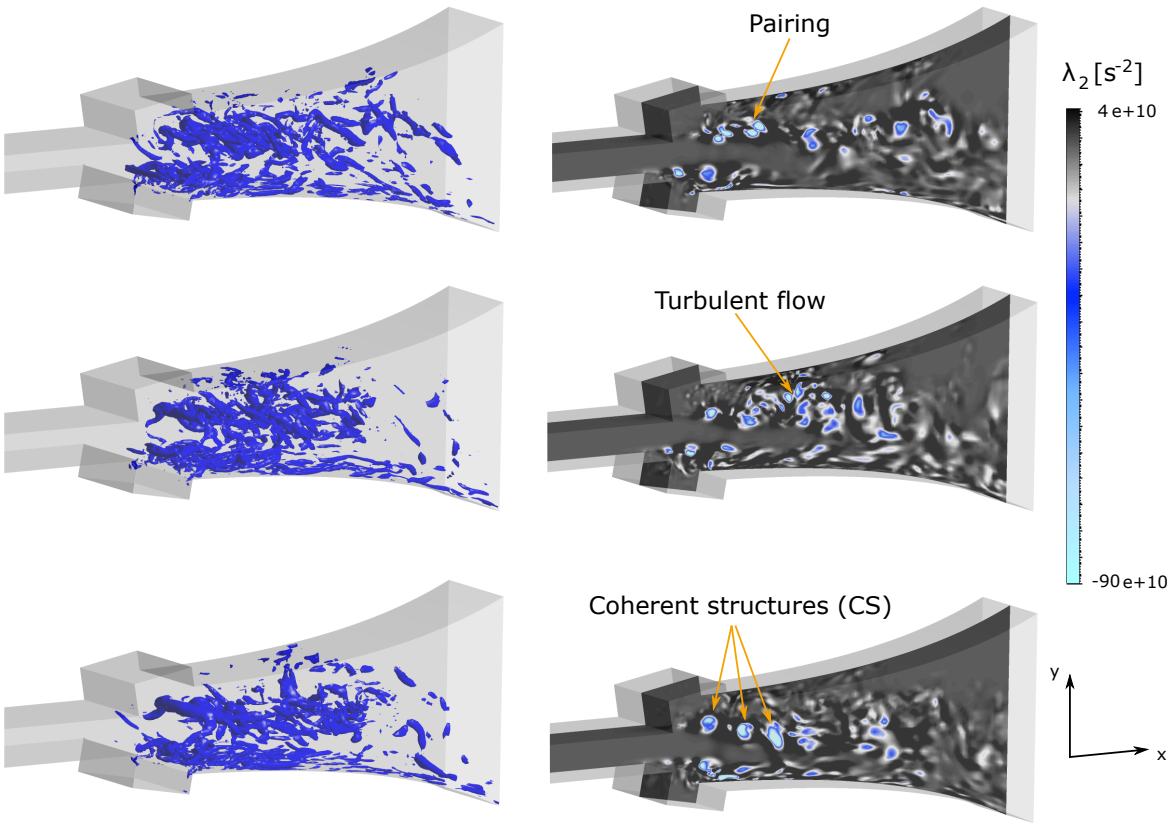

Figure 6.16: Snapshots of λ_2 at $\dot{m}_5$, left: isosurfaces at $\lambda_2 = -3 \cdot 10^{10}$, right: mid plane ($z = 1.5h$)

of all mass flow rates $\dot{m}_{1-10}$ shown in Fig.6.17 a.). Values taken from Chapter 4 are included as well so to demonstrate the difference at higher Re_h. Note that the asymmetry of the velocity profiles is due to the non-zero jet curvature downstream of the nozzle orifice. The frequency spectra at $x = 1h$ for $\dot{m}_{2,4,6,8,10}$ is further shown in Fig.6.17 c.). The peak frequency of all mass flow rates is then displayed in Fig.6.17 d.) together with the predicted shear layer instability based on $f = \frac{St_\theta u_e}{\theta}$ and $St_\theta = 0.012$. The shear layer roll-up frequency increases linearly from $25\,kHz$ at $\dot{m}_1$ to $43\,kHz$ at $\dot{m}_{10}$. The good agreement between the frequency of vorticity fluctiation ω' and the frequency determined by St_θ shows that the most unstable mode of the shear layer scales with the initial momentum thickness θ. The excitation frequency $f_{ex} = 25\,kHz$ matches the subharmonic of the shear layer mode at $\dot{m} > \dot{m}_{10}$ and thus shows that the

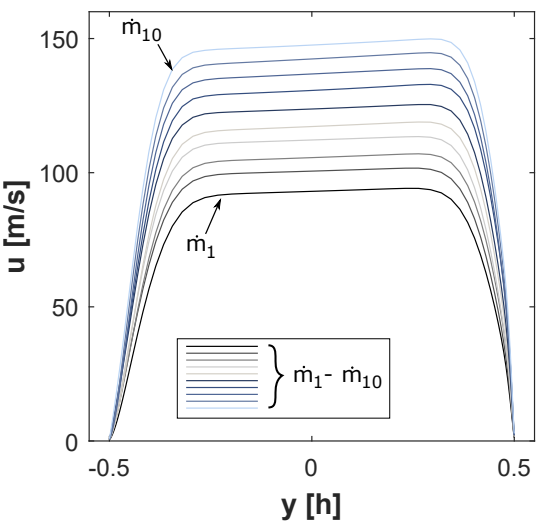

(a) Transient average velocity profile for all $\dot{m}$

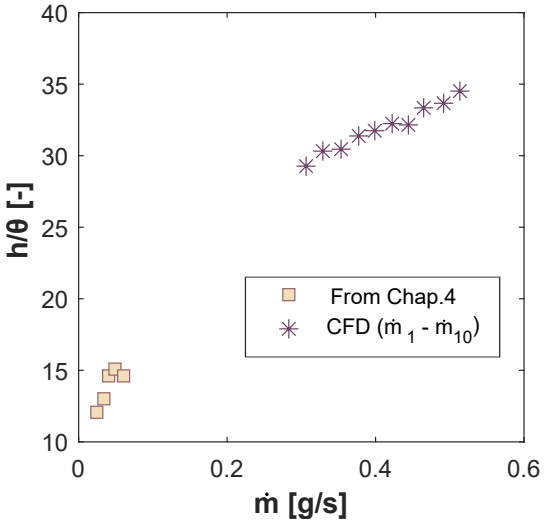

(b) Turbulence level at the nozzle orifice

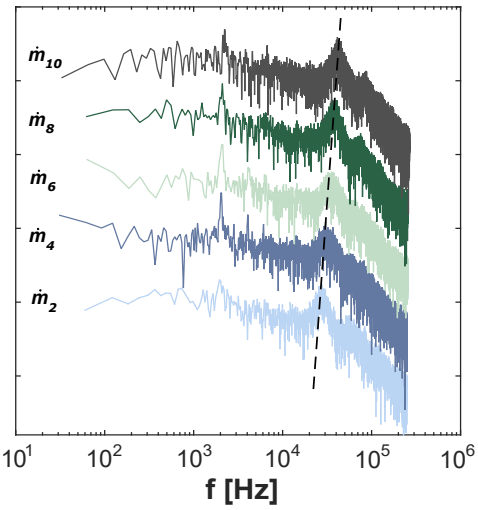

(c) Frequency spectra of vorticity at $x = 1\,h$

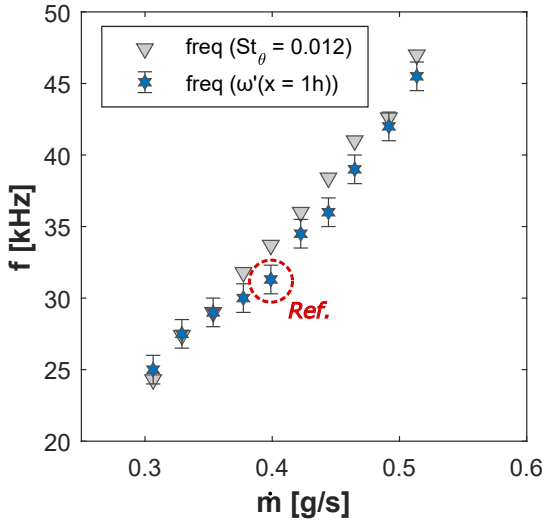

(d) Shear layer instability frequency

Figure 6.17: Flow characteristics obtained by Large Eddy Simulations of the reduced size model

initial assumption that was made in Sec.6.2 is only partially confirmed. The required excitation mode is indeed different to the shear layer mode but does not correspond to the subharmonic of it. The pressure ratios that allow switching (Sec.6.6.1) are therefore lower than those expected. The middle of that range of pressure ratios is chosen to be the reference case. It is also interesting to mention that the subharmonic of the shear layer mode for all mass flow rates correspond to $St_{D_{eq}} \approx 0.3$. This is often

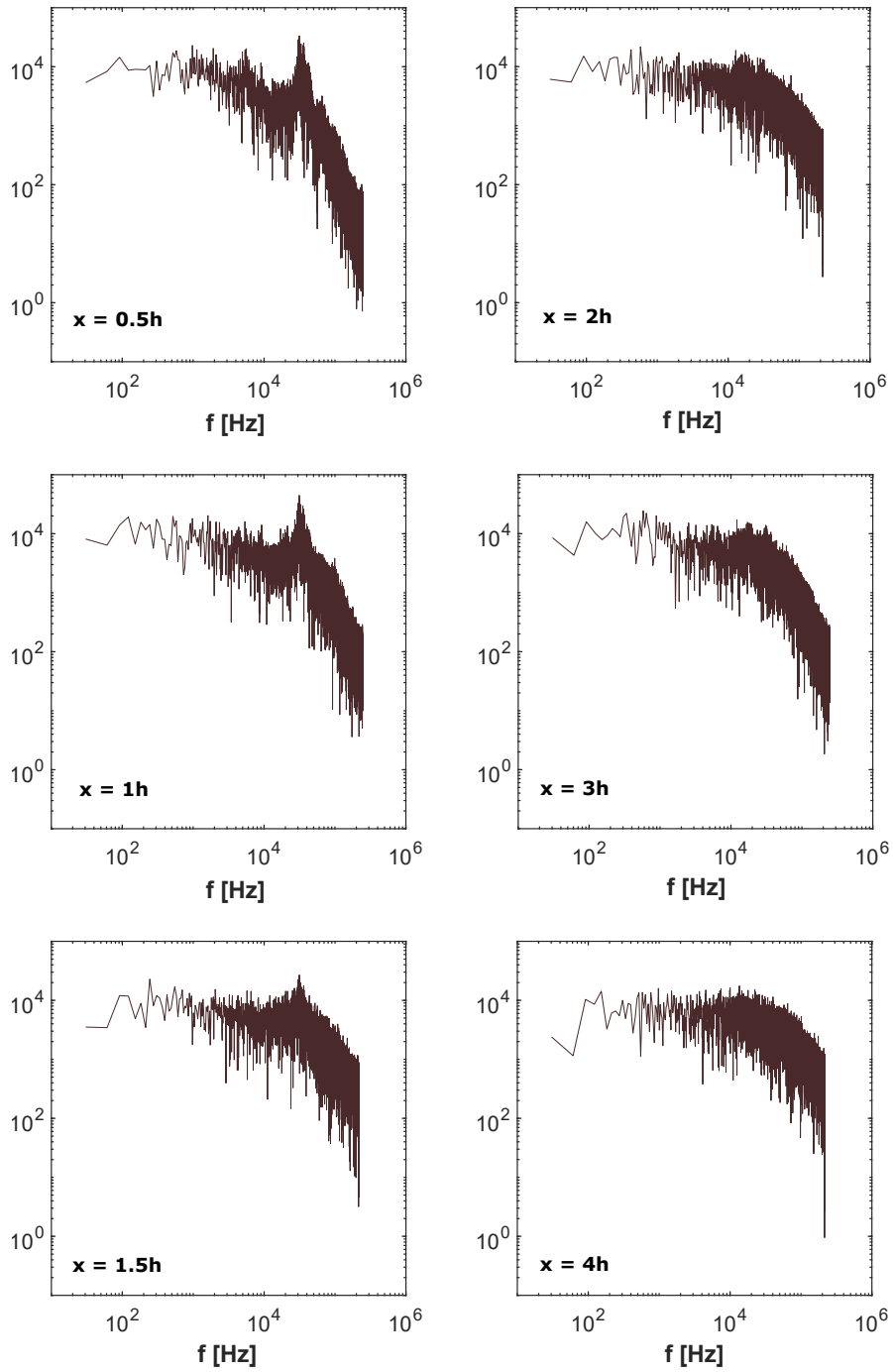

Figure 6.18: Frequency spectra of vorticity at different downstream distances

referred to be the passage frequency at the end of the potential core. This suggests that there are no further pairing events (e.g. three vortices merging together) as it was also seen in the frequency spectra at further downstream positions (Fig.6.18).

A rough estimation of the shear layer roll-up frequency at $\dot{m}_5$ can also be obtained through PIV. Even though images are recorded at a sampling frequency vastly lower than the shear layer mode one can quantify the shear layer instability by means of the average distance between consecutive vortices and the convection speed u_c. The location of the initial shear layer roll-up as well as the mean spacing between two rolled-up vortices before pairing amounts to $1h$. The vortex convection speed can then be estimated by the velocity difference between two points P_2 and P_3 on the outer radius of the vortex using the mean velocity field of 100 images (see Fig.6.19). The distance Δy between the two points represents the size of individual vortices at $x = 1h$. For the smallest and biggest vortices that were observed the convection speed u_c amounts to $27.5\frac{m}{s}$ and $34\frac{m}{s}$, respectively. The frequency of the shear layer instability can then be specified to be within $f = \frac{u_c}{\Delta x} = 27.5\,kHz - 34\,kHz$. This is a rather wide range of frequencies but is within $\pm 15\%$ of the LES prediction.

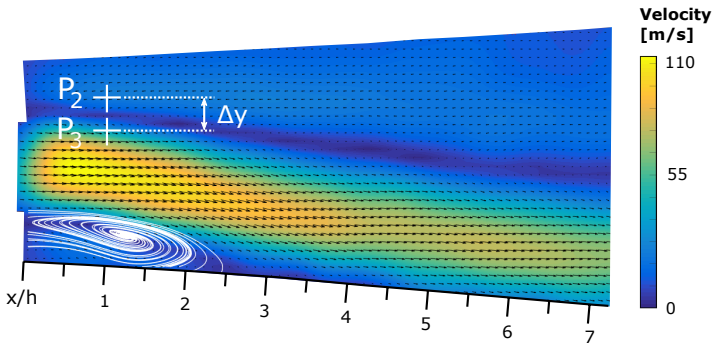

Figure 6.19: Time averaged flow field of a steady state attached jet

Given that the shear layer characteristics and its downstream development are now known it is possible to better understand why the excitation mode that triggers the switching process changes from $St_\theta = 0.012$ to $St_{D_{eq}} = 0.45$ as $\frac{h}{\theta}$ increases. For a shear layer with a low turbulence level at the nozzle orifice and hence low $\frac{h}{\theta}$ the roll-up location is relatively close to the end of the potential core and therefore downstream of the reattachment point. The pressure difference that maintains the attachment exercises its force only upstream of that. To trigger the switching the

shear layer roll-up needs to be shifted further upstream so to increase the entrainment where a subsequent pressure drop can counteract the attachment force. Since the roll-up location depends on the fluctuation amplitude of the shear layer instability it is therefore sufficient to amplify the most unstable mode ($St_\theta = 0.012$). The saturation amplitude is then attained closer to the nozzle orifice and the jet eventually switches to the opposite wall. At higher Re_h and hence larger $\frac{h}{\theta}$ the natural roll-up location approaches the nozzle orifice and ultimately reaches a limit at $x \leq 1h$. As a consequence, an amplification of the shear layer mode will not achieve the required increase in entrainment so to counteract the attachment. It thus becomes obvious that, at least for the current splitter-less configuration, forcing of the fundamental shear layer instability is not appropriate to trigger the switching process. This in turn indicates that the jet preferred mode ($St_{D_{eq}} = 0.45$) causes the strongest growth in entrainment and hence corresponds to the required excitation mode that enables switching.

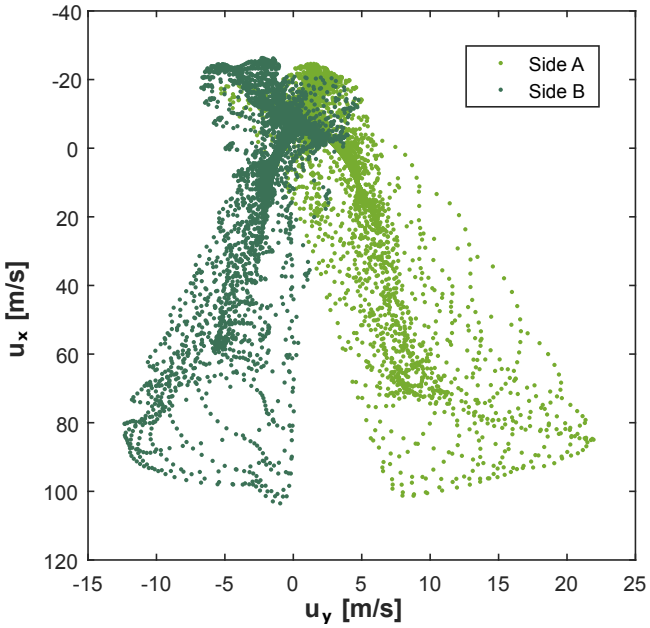

Figure 6.20: x and y components of velocity for a steady state attached jet on both sides A and B

6.6.2.2 Sensitivity to Geometrical Imperfections

Another interesting feature of most fluidic devices is shown in Fig.6.20. The scatter plot of the velocity components u_x and u_y obtained by the mean velocity fields for both attachment sides reveals an inherent problem of bistable devices. Even if manufacturing tolerances are kept at a minimum the device is still likely to exhibit a bias towards one side. This is because the Coanda effect relies on the smallest disturbances in entrainment between both sides of the jet and the smallest geometric discrepancy already causes the jet to favour one side over the other. This is shown in Fig.6.20 by a higher velocity component u_y for an attachment on side A. Higher velocity components normal to the streamwise direction indicate a smaller radius of the jet centreline and hence a stronger attachment force. In practice, this means that less energy is required to switch the jet towards its preferred side. For this study the difference in required energy amounts to less than 10% and is easily overcome by increasing the necessary number of excitation cycles. The difference in required energy has no measurable effect on the switching time t_s.

6.6.2.3 Full-scale Switching

A single switching event at $\dot{m}_5$ is now studied in more detail using both PIV and LES. The membrane displacement Δ in Eq.6.12 (introduced in Chapter 3)

$$\delta(r,t) = \frac{\Delta}{2} \cdot \left[1 - \frac{r^2}{r_M^2} + \frac{2r^2}{r_M^2} \cdot ln\Big(\frac{r}{r_M}\Big)\right] \cdot sin(2 \cdot \pi \cdot f \cdot t) \tag{6.12}$$

is initially set so to match the lowest experimentally measured SPL that enables the jet to switch ($SPL = 155.5\,dB$). However, for sound pressure levels lower than $156.7\,dB$ it was not feasible to achieve a full switch. An increased entrainment on the unattached side lowered the attachment force and increased the radius of the jet centreline but the pressure drop on the unattached side was not sufficient to reverse

the pressure gradient across the jet. At 156.7 dB the jet eventually switches after 25 excitation cycles. Fig.6.21 shows the acoustic wave for both LES and experiments at ambient conditions without any flow present. Despite the overall higher amplitude for the LES it can further be seen that the real transducer features a relatively long response time before reaching its final amplitude. Nonetheless, the mesh displacement model shows good agreement with the experimentally measured sound wave. Furthermore, the damping of the pressure oscillation following the end of excitation is well matched by the numerical model.

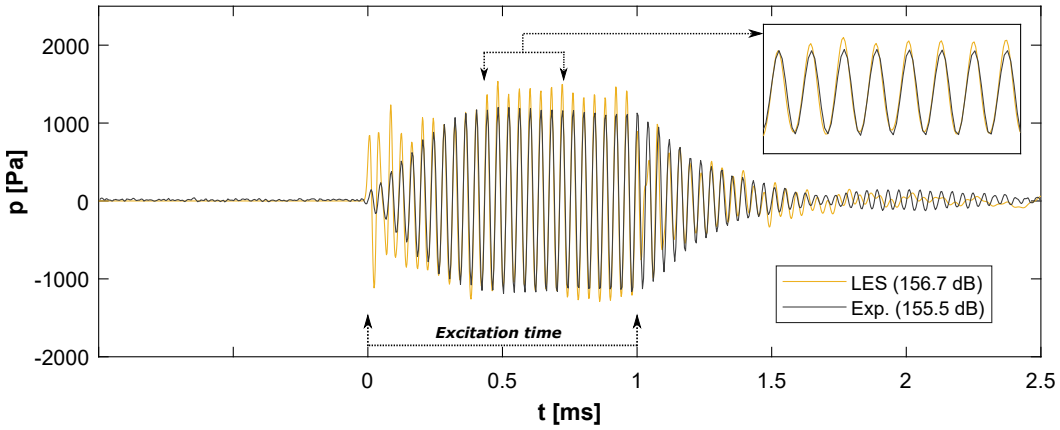

Figure 6.21: Comparison of the measured sound pressure level inside the interaction region between LES and experiments

Fig.6.22 shows a series of instantaneous velocity vector fields during a full switch. The first snapshot shows an unforced jet attached to one side. Streamlines indicate the location and size of individual vortices as well as the spacing Δx between them. The three snapshots that follow exhibit the flow dynamics while the jet is excited. The last one is taken after the excitation has stopped and the jet has attached to the opposite side. It is evident for both PIV and LES that rolled-up vortices are significantly larger whilst the jet is excited. Moreover, the spacing Δx between two vortices increases by a factor of two and higher. Given that the vortices emerge at a frequency equal to the excitation frequency this leads to a vortex convection speed

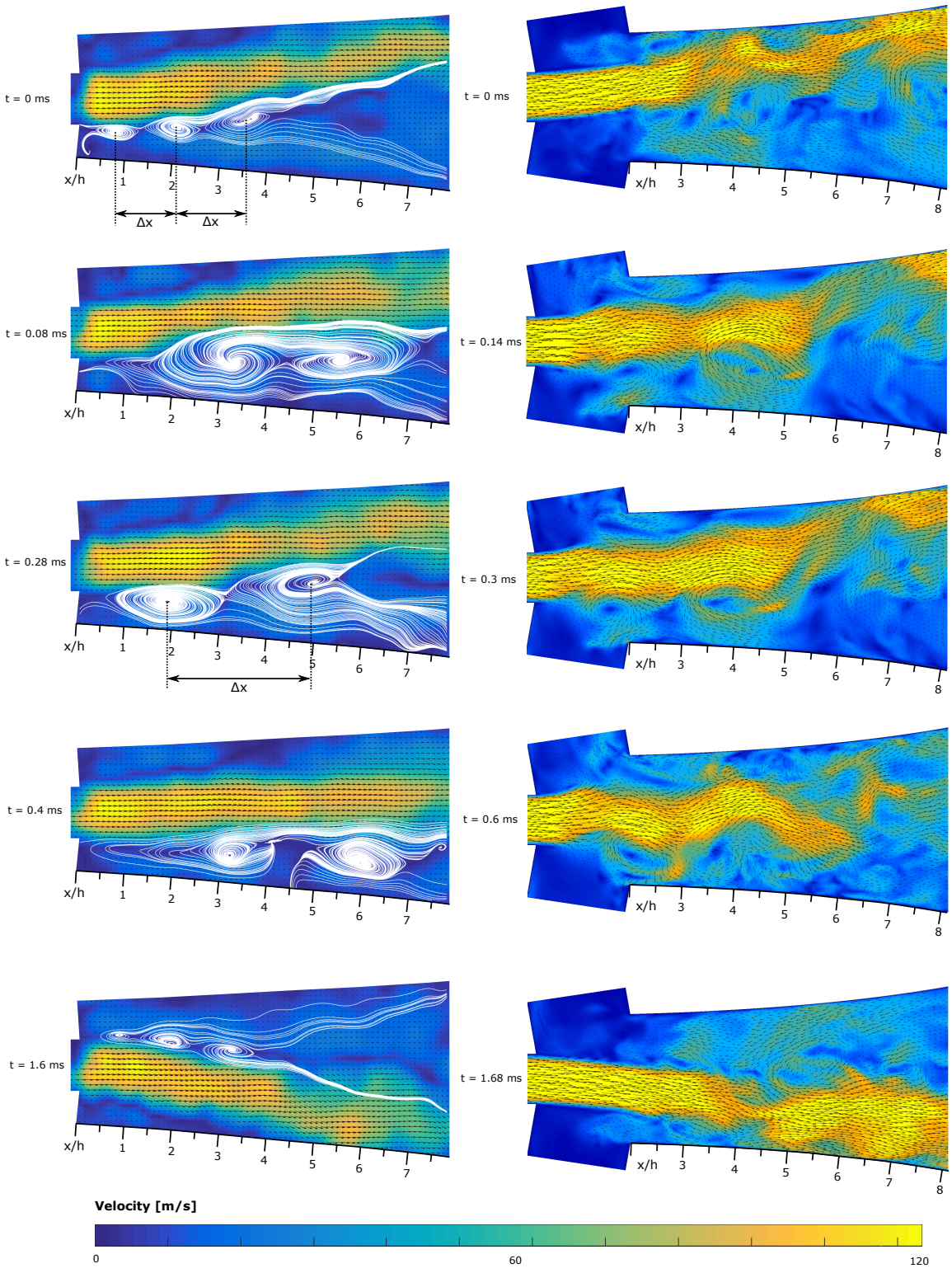

Figure 6.22: Instantaneous velocity vector field during switching, left: PIV, right: LES

of $u_c = \Delta x \cdot f_{ex} \approx 0.65 u_0$ and therefore considerable higher than for the unforced jet. This is also in perfect agreement with the results of Kuo et al [62] who obtained a vortex convection speed of $0.67 u_0$ for an excited high spped jet. This increase in u_c seems further reasonable since large scale structures convect at speeds significantly higher than small scale structures [277, 278]. Vortices are further observed to decay after $x = 7h$ without any prior pairing event. This is quite different when compared to the unforced jet. Vortices of a plain jet at $\dot{m}_5$ and no excitation were found to merge at around $x = 2h$. No large scale structures were further found beyond $x = 4h$. Excitation at $St_{D_{eq}} = 0.45$ thus generates stable wave packets with a high saturation amplitude and without any apparent subharmonic growth. The higher saturation amplitude also explains why the roll-up location of the excited jet appears to be further downstream (no vortices are observed upstream of $x = 2h$ during excitation). To put that in more general terms, the shear layer of an unforced jet rolls up where the saturation amplitude, say $\frac{u'}{u_e} = 0.1$ [39], is reached. If controlled excitation leads to a higher saturation level the roll-up will then take place further downstream where, for instance, $\frac{u'}{u_e} = 0.15$ is reached.

It further appears that the shear layer mode is completely suppressed since vortices roll-up at $25\,kHz$ and dominate along the entire jet potential core starting at $x = 2h$. This is most likely because the excitation amplitude and its downstream growth exceeds any fluctuation at $St_\theta = 0.012$. Similar results are reported by Hussain & Zaman [73] who state that the large scale structures lock onto the frequency of the jet preferred mode without the tendency to undergo pairing. Exciting a jet at the preferred mode is further known to require higher excitation amplitudes [59]. For the minimum sound pressure level that is required to switch the jet ($155.5\,dB$) the ratio of $\frac{u'_{ex}}{u_e}$, with u'_{ex} being the root-mean-square of the sound induced velocity fluctuation, amounts to 0.023. This is more than two times the required amplitude that was needed to switch an initially laminar jet at $St_\theta = 0.012$. This makes insofar sense

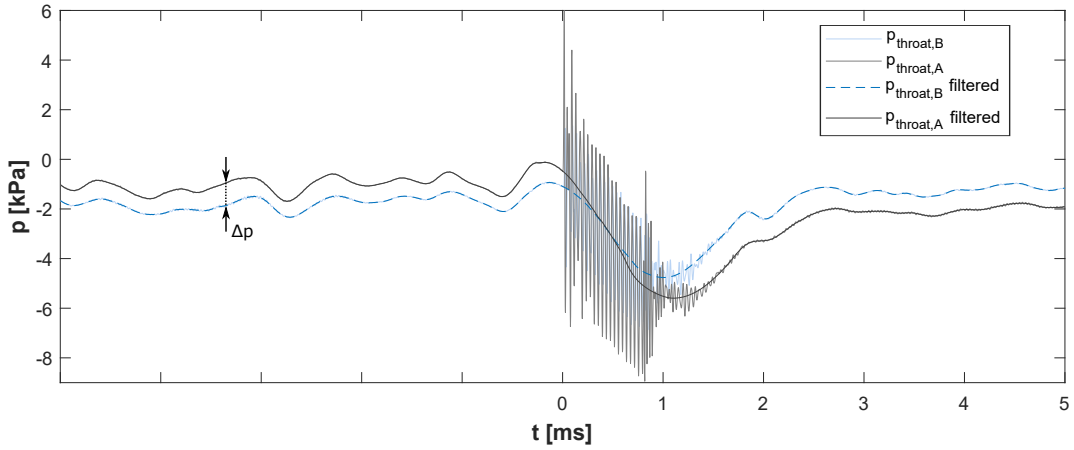

(a) Static pressure inside both control port throats

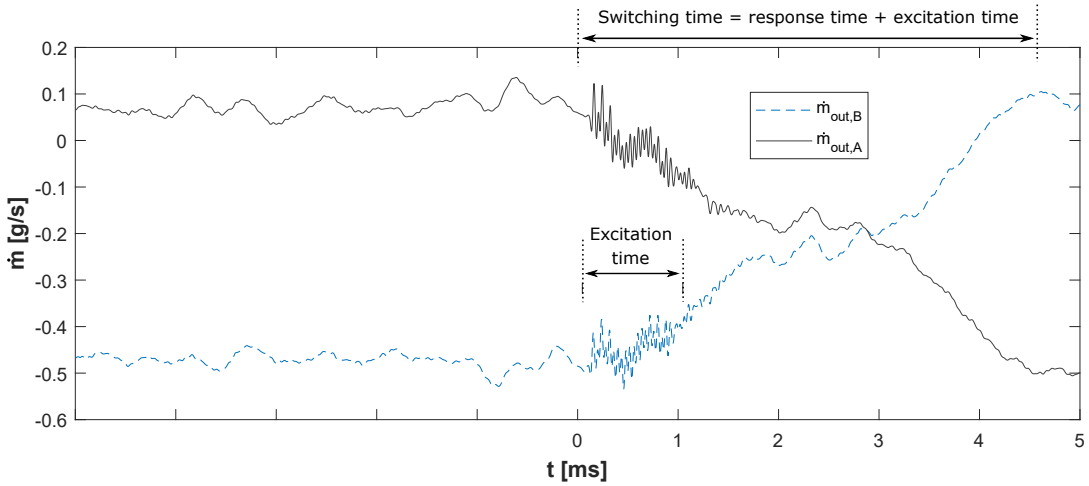

(b) Mass flow $\dot{m}$ through outlet A and B

Figure 6.23: LES results before, during and after excitation with $f_{ex} = 25\,kHz$ and $t_{ex} = 1\,ms$. Filtered graphs were obtained using a 2nd order Butterworth filter with a cut-off frequency of $5\,kHz$

since the jet preferred mode does not amplify any existing shear layer fluctuation but nonetheless has to achieve high enough amplitudes for the shear layer to roll up. Given that the jet preferred mode generates large, coherent and stable vortices that exhibit no apparent subharmonic growth one might then hesitate to call $St_{D_{eq}} = 0.45$ an instability. Conversely, it seems to be the most stable mode of the jet.

It is further obvious that the large coherent structures increase the entrainment on the initially unattached side. Fig.6.23 shows that the resulting asymmetry in entrainment causes the pressure difference Δp across the jet to reverse. The attachment

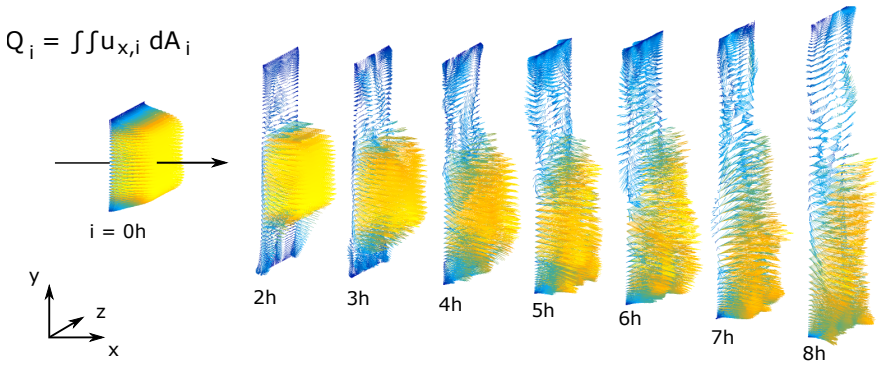

Figure 6.24: Velocity vector field through yz-planes at different x for the calculation of Q_i

force is zero at around $\frac{t_{ex}}{2}$. The same amount of energy ($P \cdot \frac{t_{ex}}{2}$) is then needed to establish the required pressure difference for the attachment on the opposite side. The pressure drop on either side can further be considered mostly linear. The new steady state is reached after the pressure has recovered and is back in equilibrium ($\approx 2.5\,ms$). The mass flow through both outlets, shown in Fig.6.23 b.), further indicates that the time it takes the jet to switch amounts to approximately $4\,ms$. This is somewhat lower than the average value measured in the experiments but still in good agreement given the deviation in t_s and the complexity of the numerical model.

The increased entrainment which is responsible for the pressure drop can further be quantified by the downstream growth of the volume flow Q, which is defined as the surface integral of the mean streamwise velocity

$$Q(x) = \int \int_A u_x \, dA \tag{6.13}$$

The locations at which Q is plotted is shown in Fig.6.24. All planes are normal to x and separated by $\Delta x = h$. The first plane ($i = 0$) is located at the nozzle exit and hence represents the incoming volume flow Q_0. Only positive values of the streamwise velocity component that are normal to the yz-plane are taken to determine Q. Recirculating fluid is therefore not considered. The steady state entrainment of the

unexcited jet is then obtained by averaging the volume flow through each plane during the first $5\,ms$ before the onset of excitation ($t < t_0$). The enhanced entrainment due to the excitation is likewise obtained by averaging Q between $t_0 = 0\,ms$ and $t_{ex} = 1\,ms$. The ratios $\frac{Q_i}{Q_0}$ are shown in Fig.6.25. The entrainment rate of the natural (unforced) jet can be considered constant. Hence the volume flow increases linearly. At $x = 8h$ the jet has entrained $\approx 20\%$ of its initial volume flow. This is less than half of what is typically reported for both free circular and rectangular jets [106]. This, however, is not surprising since less than half of the jet perimeter allows entrainment at all, as a result of the reattachment. No further comparison with other rectangular reattached jets can be made since, to the author's best knowledge, no such study exists in the open literature.

The entrainment rate $\frac{Q_i}{Q_0}$ of the excited jet features an interesting slope. After a substantial increase for the first two nozzle heights the flow seems to loose rather than entrain fluid. This suggests that, during the course of excitation, the upstream jet supplies itself with fluid from further downstream. Although unexpected at first, this seems obvious after a careful consideration of the prevalent flow field. That is to say that the highly disturbed jet fills out the entire interaction region during the switching process so that no reverse mass flow that enters through the unattached side outlet could be used as entrainment supply. The forced increase in entrainment around $x = 2h$ can therefore only be satisfied if a portion of the jet itself travels back upstream. To confirm that the fluid is also entrained from inside the control port, Fig.6.26 shows the mass of fluid in each control port before, during and after the switching. It is evident that the initially unattached side port (port B) looses more fluid during the excitation. This loss causes the pressure drop displayed in Fig.6.23 a.).

However, what still lacks is an explanation of the difference between the switching time t_s and the excitation time t_{ex} (see Fig.6.23 b.)). This difference ($\approx 4\,ms$) cannot

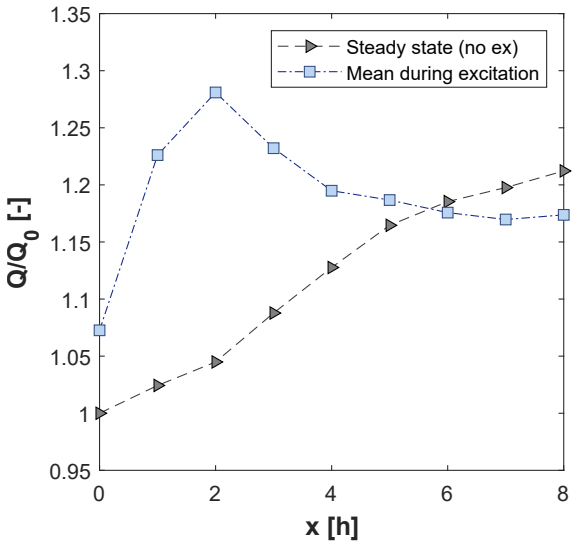

Figure 6.25: Non-dimensional volume flow rate as a function of streamwise distance for an excited and unexcited jet

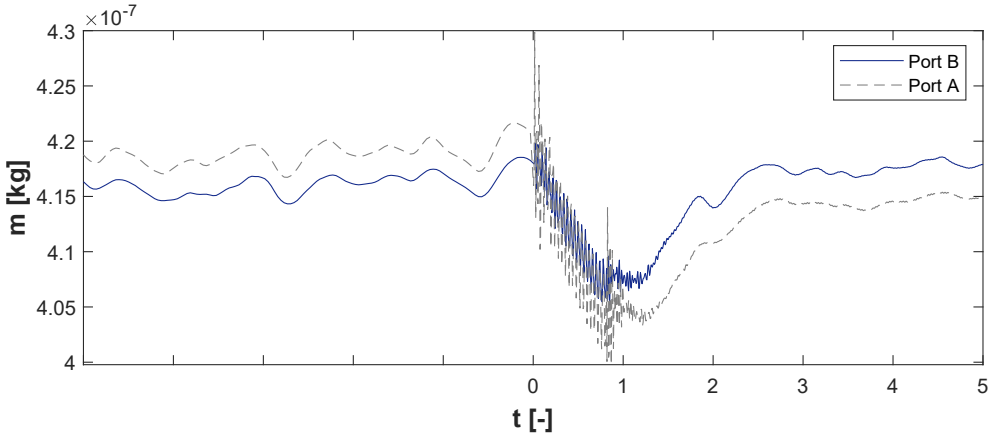

Figure 6.26: Mass inside the control port channels as a function of time indicating an higher entrainment on the initially unattached side

be attributed to the transport time alone ($t_{transport} \approx 1\,ms$). The reason for the delay in switching is twofold. One, there is an offset between the time at which the pressure difference across the jet is fully reversed (t_{ex}) and the time at which the jet curvature has responded to it. Fig.6.27 shows the velocity vector field as well as the streamlines originating at the inlet at $t = 1\,ms$. Clearly the jet curvature is straight for the first nozzle heights downstream of the orifice despite a fully reversed pressure difference

Δp. It takes another $\approx 0.8\,ms$ until the jet has fully attached to the opposite side. At this point ($t = 1.8\,ms$) the second reason for the delay becomes apparent. It is

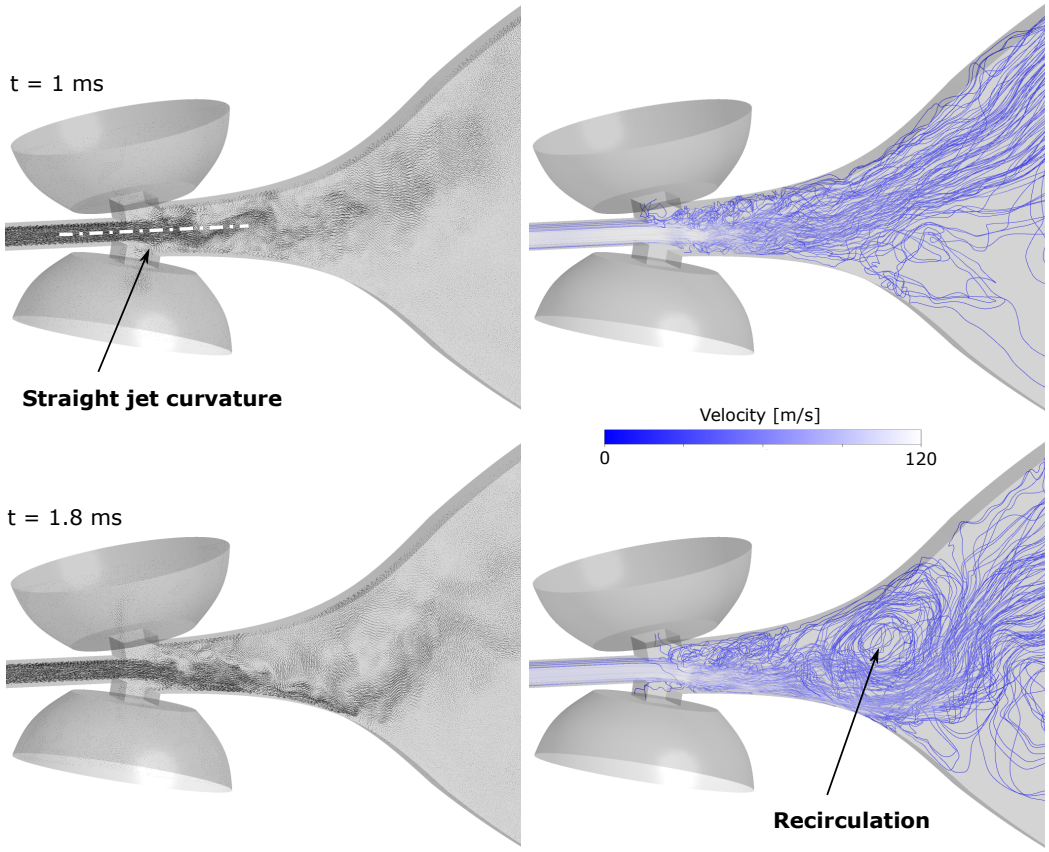

Figure 6.27: Velocity vector field (left) and velocity streamlines (right) indicating a straight jet curvature at $t = 1\,ms$ and a 'double attached' flow at $t = 1.8\,ms$

observed that the initial recirculation bubble persists on side B, travels downstream during the switching process and leads to a 'double attached' flow that delays the switching. As the recirculation bubble moves downstream it increases in size and prevents the jet from following the new attachment side. Fig.6.27 shows how the flow is still bent towards the initial attachment side and mainly exiting through the initial outlet channel $0.8\,ms$ after the excitation has stopped. This was already assumed in Sec.6.6.1 since the Pitot probe on the initial attachment side indicated a low pressure region just before the new steady state is reached. This highlights that the switching time might be decreased by placing a splitter between the two attachment walls, the

subject of what will be discussed later on.

6.6.3 Discussion

The excitation mode that triggers the switching process is defined as the non-dimensional frequency that corresponds to the pressure ratio at which the device shows a preference to switch. This is further defined as the centre of the bandwidth, or in other words, the pressure ratio at which the lowest sound pressure level still enables switching. Without prior reason but all the more confidence, the excitation mode of the splitter-less device was said to correspond to the so-called jet preferred mode. This, however, requires a more thorough discussion and literature review as the topic surrounding the jet preferred mode is a more complex one.

Despite the vast amount of published articles regarding the evolution of vortical structures and its effect on entrainment, there is still an astonishing lack in agreement between the results of theoretical [48, 279], numerical [65] and experimental studies [280]. The most striking discrepancy concerns the occurrence of the so-called jet preferred mode, the excitation frequency that *attains the highest possible amplitude under the combined effects of linear amplification and non-linear saturation* [3]. This definition, it seems, is the only common ground all scientists share. Opinions start to diverge with the attempt to quantify the non-dimensional frequency. Reported values for the jet preferred Strouhal number St_D range from 0.2 to 0.6 [33, 26, 61]. Here St_D is based on the diameter D of a circular jet and the jet centreline velocity u_0. However, most studies acknowledge the huge scatter in the open literature but consider $St_D = 0.3$ the actual preferred mode.

Irrespective of the disparities concerning the actual value of the preferred mode Strouhal number, it is well established that the excitation of the jet preferred mode causes distinct and unique flow characteristics. These include the roll-up of robust and large coherent structures at $\approx 1.5\,D$ and the absence of any downstream pairing

events [3, 59, 62, 73, 80]. The structures grow in size until the saturation amplitude is reached at $\approx 4D$. The spectrum is free of any subharmonic peak, anywhere in the downstream direction, and the coherent structures dominate the flow even downstream of the end of the potential core. Furthermore, the structure spacing Δx as well as the vortex convection speed u_c increases with respect to the unforced jet. The latter was found to be around $0.62u_0$ and $0.65u_0$, in [39, 281] and [62] respectively. Beyond that, the excitation of the jet preferred mode moves the end of the potential core upstream and causes the maximum increase in entrainment [3, 26, 59, 80].

It is obvious that the previously presented PIV and LES results for the splitter-less device are in perfect agreement with the characteristics of the jet preferred mode. However, the results also contradict the common point of view that the jet preferred mode corresponds to the passage frequency of vortices at the end of the potential core, formed in the absence of artificial forcing [34]. Technically, this implies that the jet preferred mode should be considered a local shear layer instability. Petersen & Samet [78] and Petersen & Clough [282] go even further and claim that there is no such thing as a single preferred mode and that the most amplified wave depends on the downstream location and the shear layer thickness. This is perplexing since they do not measure entrainment, potential core length or fluctuation amplitude which would indicate the preferred mode Strouhal number and probably distinguish it from possible subharmonics of $St_\theta = 0.012$. However, a more restrained position is taken on by Samimy et al [59] who state that even if the preferred mode depends on the shear layer, "*it is not clear from the literature how to get from the most amplified mode to the jet preferred mode*". In contrast to Petersen & Samet, Zaman & Hussain [73] argue that the jet preferred mode is independent of the shear layer instability which is supported by the fact that the preferred mode Strouhal number was found to be the same regardless of the exit boundary layer being laminar or turbulent. They nonetheless agree that in the case of no excitation and little background disturbance,

the jet would form large-scale structures predominantly at the preferred mode frequency. Some studies have also shown that the preferred mode scales with the shear layer mode at low $\frac{D}{\theta}$ but locks on to $St_D \approx 0.45$ as $\frac{D}{\theta}$ exceeds a certain threshold [33]. This again contradicts the findings of Zaman & Hussain [73] who claim that the value of the jet preferred mode increases somewhat at lower Re. The huge scatter regarding the reported values for the preferred mode Strouhal number might therefore also be due to different Reynolds numbers used in different studies. Hence, there might not even be a globally valid jet preferred mode. Or, different excitation frequencies might have been mistaken for the jet preferred mode since the flow responds to more or less all frequencies in the vicinity of the shear layer mode and its subharmonics. In this regard, Zaman & Hussain [39] showed that the excitation of the shear layer mode can produce stable vortex pairing resulting in a centreline fluctuation intensity that exceeds that of the jet preferred mode. It was further shown in [283] and [284] that simultaneous excitation at two frequencies, i.e. fundamental and subharmonic, can easily provoke pairing depending on the phase difference between the two waves. Furthermore, the subharmonic component of the most unstable mode in a natural (unforced) shear layer is a precondition to vortex pairing rather than just a by-product of it [30, 284]. It thus seems obvious that subharmonic excitation provokes stable vortex pairing. This is also shown for a two-dimensional free shear layer studied by Ho and Huang [30]. They found that the number n of vortices merging together correlates with the excitation of the nth subharmonic of the most unstable mode. However, if subharmonic excitation encourages the pairing of vortices it seems somehow strange that the excitation of the jet preferred mode, which is meant to be an integer fraction of the shear layer mode, discourages the merging of vortices completely. It thus seems reasonable to raise some doubt that the jet preferred mode is a subharmonic of the shear layer mode. This would also support the assumption that the jet preferred mode was held responsible for the switching mechanism of

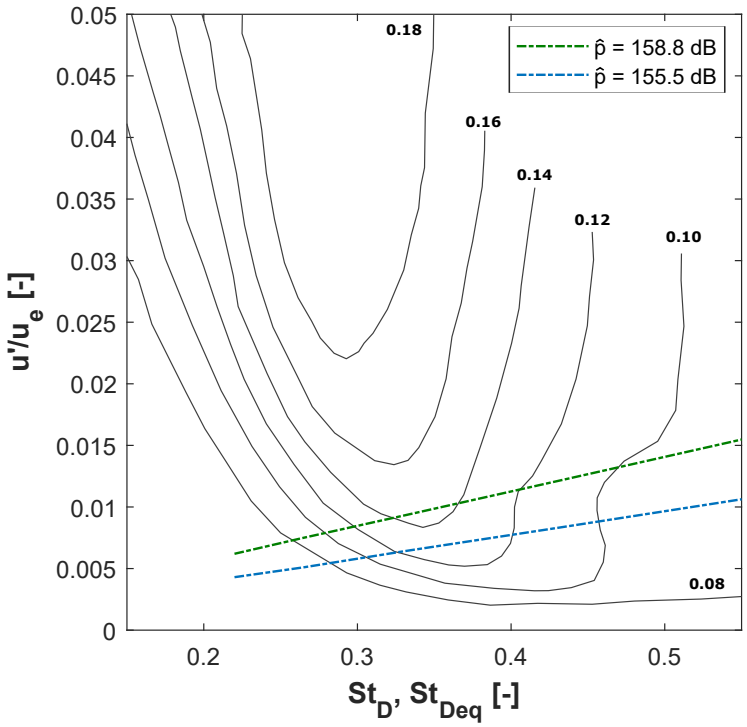

Figure 6.28: Contour map of the total response at $x = 4D$ on the centreline, as a function of Strouhal number and amplitude of forcing. The contours are labelled with the turbulence intensity. Graph is taken from Crow & Champagne's experimental study of a forced jet [3].

the splitter-less device although the excitation frequency does not match the vortex passage frequency at the end of the potential core.

Another, for now, more reasonable explanation for the frequency mismatch, is based on the amplitude dependency of the jet preferred mode Strouhal number. This dependency is depicted in Fig.6.28. The contour lines represent lines of equal jet response to an excitation with amplitude $\frac{u'}{u_0}$ and frequency St_D. The jet response is here defined as the turbulence intensity on the jet centreline at $x = 4D$. The data of the amplitude response surface is taken from Crow & Champagne [3]. It can be seen that the maximum jet response shifts towards higher Strouhal numbers as the forcing amplitude $\frac{u'}{u_0}$ decreases. In other words, the actual jet preferred mode ($St_D = 0.3$) can only be identified at sufficiently high excitation amplitudes. The two straight lines in Fig.6.28 represent the forcing amplitudes $\frac{u'}{u_0}$ for the lowest and highest sound pressure

levels used in this study. Note that no quantitative comparison can here be made since both Reynolds number and nozzle geometry are different when compared to the set-up of Crow & Champagne. However, it suggests that the excitation amplitudes used for the splitter-less device in Sec.6.6.1 do not achieve the necessary level to identify the actual jet preferred mode. What was called the preferred Strouhal number in Sec.6.6.1 ($St_D \approx 0.45$) might rather just be a Strouhal number preference for the given excitation amplitudes.

It has probably been noticed by now that the above discussion comprised the results of circular jets only. Shear layer mode, vortex merging or jet preferred mode, however, exist likewise for non-circular jets and also rely on the same mechanism. In general, a rectangular jet might indeed add more complexity due to its three-dimensional flow field but otherwise feature similar qualitative flow characteristics. Besides, Shih et al [114] show that a rectangular jet with $AR = 3$ can be considered two-dimensional along most of its span and even downstream up to $14h$.

The reason for having focused on circular jets only is simply due to the fact that round jets have been studied considerable more extensively in the past. What's more, studies regarding the excitation of rectangular jets do seldom examine the fundamental flow physics but focus rather on specific applications. Studies regarding the excitation of the free shear layer of a rectangular reattached jet are, to the author's best knowledge, even non-existent. Nevertheless, qualitative and also quantitative results gained from circular jets are, in most cases, applicable to rectangular jets as well. But besides the already huge scatter of the preferred mode Strouhal number there is an additional inconsistency regarding the length scale with which the Strouhal number is made non-dimensional. Both the nozzle height h as well as the equivalent diameter D_{eq} are equally often found in the literature [106, 114]. This makes it more problematic to compare the results of different studies. However, in [285], for instance, the preferred Strouhal number St_h of a jet with $AR = 3$ is found to be at 0.22. This corresponds to

0.44 when based on D_{eq} and is therefore in good agreement with the preferred mode found in this study ($St_{D_{eq}} = 0.45$). The definition of the preferred mode in [285] is identical to circular jets (the excitation frequency that obtains the most intense large scale structures resulting in the strongest entrainment). They further found that the frequency spectra of the unforced jet exhibits a dominant peak at $St_h = 0.22$ between $x = 3h$ and $6h$. This was not observed in the present study. It is also noteworthy that neither the preferred mode nor the passage frequency at the end of the potential core change as the aspect ratio is increased from 2 to 5 [285]. For higher aspect ratio jets, however, the long side of the nozzle was found to impose an additional length scale affecting the dominant passage frequency [286]. A clear second peak in the frequency spectra arises as AR is increased to 15. This is also supported by Deo et al [287] who found that the jet preferred mode of a rectangular jet with $AR = 60$ changes from $St_h = 0.36$ to 0.22 by just removing the sidewall. In the present study it is therefore assumed that the aspect ratio affects the shear layer development only if the momentum thickness θ_s at the short side of the nozzle differs substantially from θ_l at the long side. For the reference case of the splitter-less device the difference in θ amounts to $\approx 6\%$. For better comparability between different studies it is therefore recommended to use $St_{D_{eq}}$ if $AR \gg 1$ and St_h if $AR < 6$. Therefore, the Strouhal number preference of the reference case as well as its passage frequency of vortices at the end of the potential core are henceforth based on the nozzle height h. They amount to $St_h = 0.25$ and $St_h = 0.15$, respectively.

In conclusion, there is a twofold interpretation and explanation for the excitation mode of the splitter-less device. The first suggests that the excitation mode refers to a Strouhal number preference for the given amplitudes rather than to the actual jet preferred mode. This would explain why the excitation frequency does not match the first subharmonic and hence the passage frequency at the end of the potential core. The second interpretation suggests that the excitation mode corresponds to

the actual jet preferred mode which would then be independent of the shear layer roll-up frequency and therefore independent of the passage frequency at the end of the potential core. This would explain the huge scatter regarding the reported values of the Strouhal number since the frequency at the end of the potential core is linked to the boundary layer development inside the nozzle. This ought to say that most experimental studies do not use the required entrance length so to obtain a fully developed velocity profile. The shear layer roll-up, however, depends on the momentum thickness θ and hence on the velocity profile. The nozzle diameter D or D_{eq} is constant but θ can vary due to different nozzle lengths. A less fully developed velocity profile features a smaller momentum thickness and hence a higher shear layer roll-up frequency. The value for St_θ might remain constant at 0.012 for different nozzle lengths but if the jet preferred mode is based on D and simply measured by, say a hot wire at the end of the potential core and no excitation, the value of St_D can differ substantially.

Whether the first or second explanation is more plausible shall be transpired, among other things, in the remaining course of this thesis.

6.7 Splitter Configuration

The splitter-less configuration is now extended by a sharp splitter with $d_s = 7h$ as shown in Fig.6.29.

Similar to the experimental investigation in the preceding part of this chapter the performance characteristic of the splitter-device is described in terms of the key non-dimensional parameters. Those include the switching time t_s, the amplitude flow factor Am, the minimum required energy $\bar{E}$ and the pressure ratio Pr. The effect of potential vents on the performance of the splitter-device is not investigated. Simulations of the full-scale device are not performed either since both the flow conditions

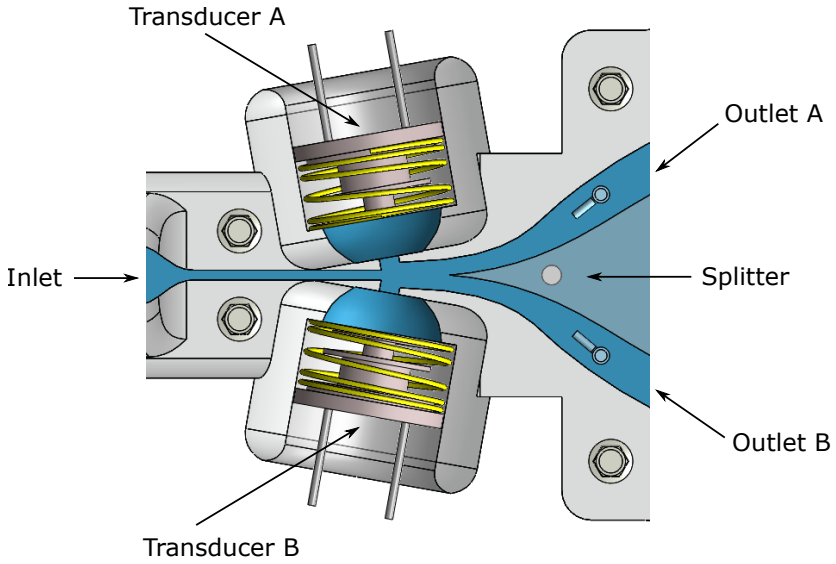

Figure 6.29: Schematic of the splitter configuration

and the switching mechanism can be derived from the results obtained from the splitter-less configuration.

6.7.1 Performance Characteristic

6.7.1.1 Non-Dimensional Energy and Switching Time

The non-dimensional energy $\bar{E}$ necessary to switch the jet is shown in Fig.6.30 a.),b.) and c.) for three different sound pressure levels. The difference to the splitter-less device is immediately evident. The operation ranges from low subsonic velocities ($Mn = 0.2$, $Pr = 1.05$) up to sonic conditions ($Mn = 1$, $Pr = 1.9$). The graph in Fig.6.30 a.) further reveals a series of already known features. First, a lower sound pressure level shortens the range of pressure ratios that allow switching on both the lower and upper end. Second, the required energy $\bar{E}$ increases exponentially at lower Pr but shows only a minor, almost indistinguishable, linear increase at higher Pr. It is also not surprising that the required energy appears to be independent of the sound pressure level once a threshold value is exceeded. The pressure ratio at

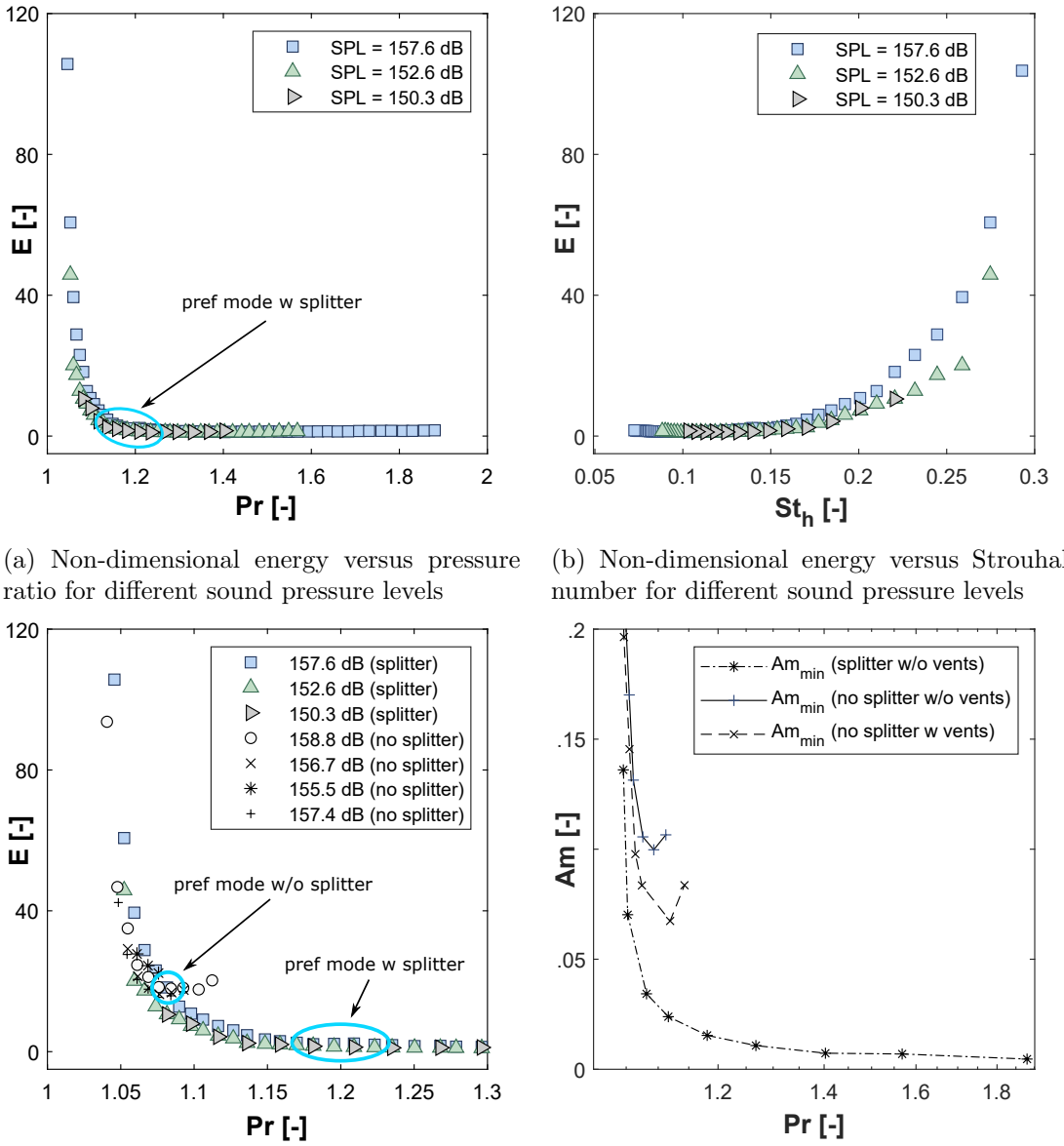

(a) Non-dimensional energy versus pressure ratio for different sound pressure levels

(b) Non-dimensional energy versus Strouhal number for different sound pressure levels

(c) Required energy for both splitter and splitter-less configuration versus pressure ratio

(d) Minimum amplitude flow factor versus pressure ratio for both configurations (including vents)

Figure 6.30: Switching performance of the splitter configuration - Comparison with the splitter-less device.

which the device exhibits its preference to switch amounts to ≈ 1.2.[3] The range of pressure ratios that allow switching is further seen to extend more towards higher pressure ratios as the sound pressure level is increased. It is also obvious that, in

[3]Pressure ratio at which the lowest possible SPL would still cause switching. This corresponds to the centre of the range of pressure ratios that allow switching.

terms of the required energy, Strouhal numbers lower than the preference value are more favourable for switching (Fig.6.30 b.)). It can be seen in Fig.6.30 c.) that the range of pressure ratios that allow switching is considerably increased for the device that uses a splitter. Furthermore, the preferred mode of switching is further shifted from $Pr = 1.07$ ($St_h = 0.25$) to $Pr = 1.2$ ($St_h = 0.15$) Fig.6.30 d.) indicates that the minimum amplitude flow factor decreases as the preference to switch shifts to higher pressure ratios. Given that the excitation properties are the same for all device configurations, it seems that the splitter-less device did somehow not achieve to get to the actual preferred mode. Either way, the minimum amplitude flow factor and required energy for the present device at $St_h = 0.15$ amount to 0.015 and 1.6, respectively.

Similar to the required energy, the absolute switching time, shown in Fig.6.31, appears to be rather independent of the sound pressure level.[4] The variation of and from the mean value is as large as 100%. Values between 4 and 15 ms are obtained within the given range of pressure ratios. Furthermore, no clear trend or dependency on the pressure ratio is apparent. If made non-dimensional, however, the dependency of the switching time on Pr becomes more apparent and $T_s = \frac{t_s u_e}{d_s}$ seems to have a linear relationship with Pr (Fig.6.32).

The large variation in switching time was found to be caused by setting the excitation time to its minimum required value $t_{ex,min}$. Recall that the required energy is found through the lowest number of excitation cycles that switch the jet 10 out of 10 times. This was numerically shown to correspond to the time it takes to reverse the pressure gradient across the jet. It was further shown that the jet does not respond instantly to a change in Δp. The flow field thus lags behind the pressure field. That is to say that if excited at the minimum required energy, the end of excitation ($t = t_{ex,min}$) coincides with the point where the jet curvature approaches a straight line and hence

[4]This is supported by the fact that such a behaviour was seen for all device configuration and excitation conditions presented in this thesis.

interacts with the splitter leading edge. The latter now poses a physical barrier that hampers the jet to switch to the other side. The jet first smoothly detaches from the initial attachment wall due to the steady decrease in Δp but is 'pushed back' once it hits the splitter leading edge. But since the pressure gradient across the jet has been reversed already, the jet eventually switches to the other side nonetheless. This 'pushing back' is shown on the left of Fig.6.33 for a $Mn = 0.75$ jet. A series of single switching events, all triggered at $t = 0.1\,s$ and measured via the Pitot probe on the initially unattached side, reveal that the jet "hesitates" to switch to the opposing wall right after the excitation has stopped (the time where $R \to \infty$).

To eliminate the adverse effect of the splitter the number of excitation cycles is increased beyond its required minimum. Hence, the asymmetry in entrainment is maintained further on which decreases the pressure on the unattached side even more. This is synonymous to increasing the switching/attachment force Δp. The result is shown

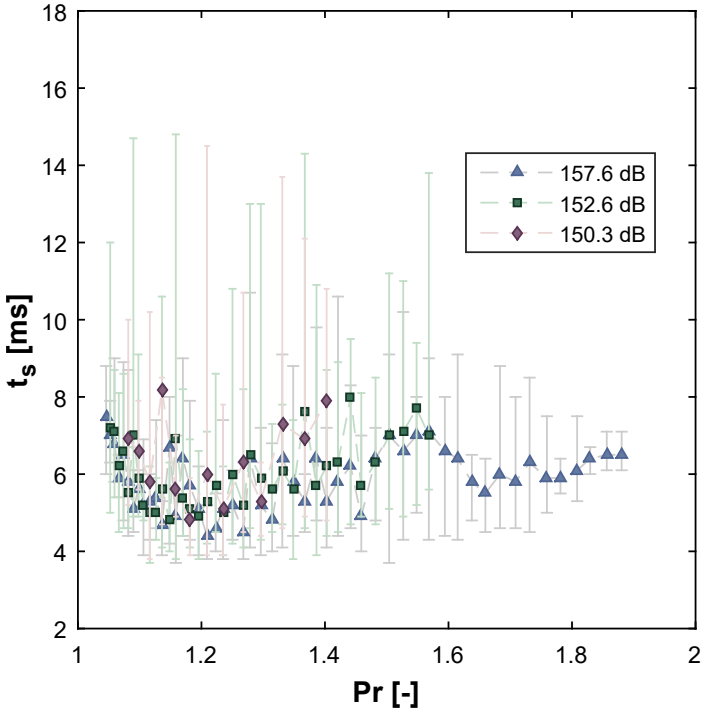

Figure 6.31: Switching time over pressure ratio

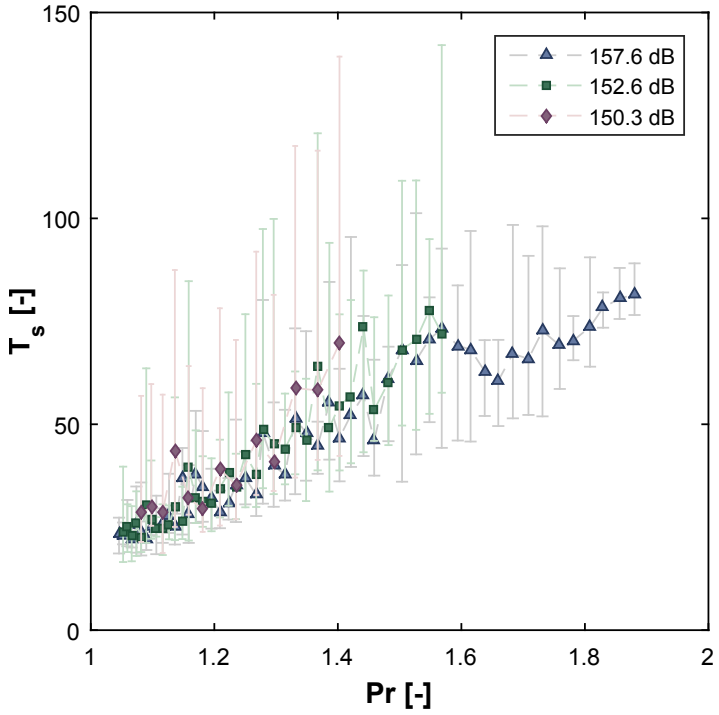

Figure 6.32: Non-dimensional switching time over pressure ratio

on the right of Fig.6.33. Not only does the hump shown on the left of Fig.6.33 disappear for $t_{ex} = 2 \cdot t_{ex,min}$ but it also decreases the huge variation in switching time presented in Fig.6.3. This is highlighted in Fig.6.34 where twice as many excitation cycles are used then actually required. The trend of t_s is now clearly visible. The switching time decreases exponentially up to $Pr \approx 1.2$ but appears to increase linearly thereafter. The global minimum is found at $Pr = 1.19$ and amounts to $4.3\,ms$. This is the lowest value achieved in this study.

The fact that the lowest switching time is found at the preferred mode, the centre of the bandwidth in Fig.6.30, is somewhat intuitive but nonetheless calls for a separate explanation. This is because the switching time was hitherto shown to decrease continuously as the jet velocity u_e increases. To shed some light into what causes such behaviour the following section aims to investigate the switching time from a more theoretical perspective.

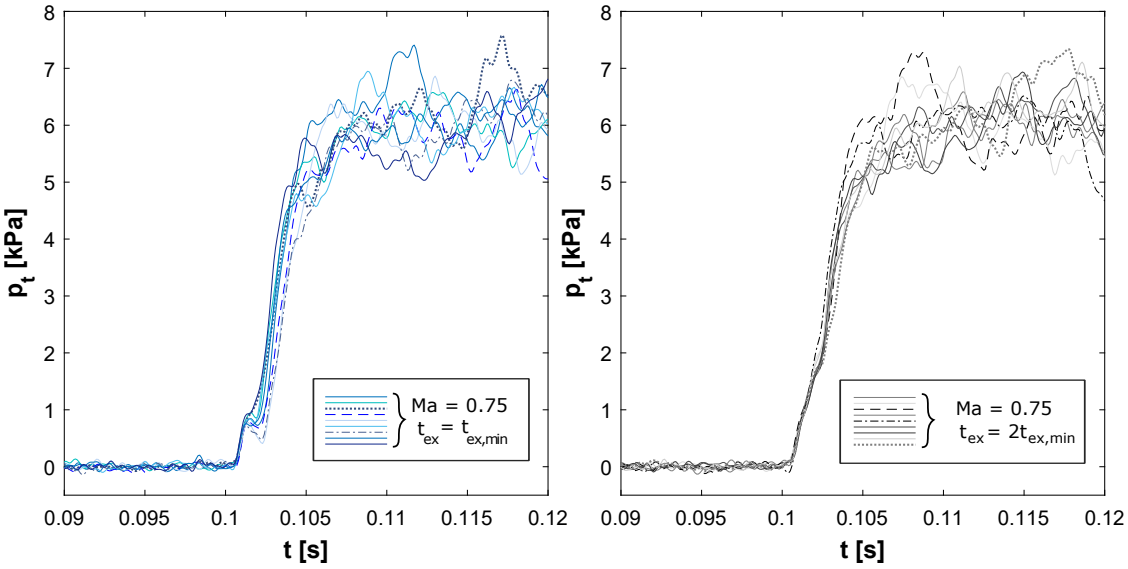

Figure 6.33: Single switching events of a $Mn = 0.75$ jet with $t_{ex} = t_{ex,min}$ (left) and $t_{ex} = 2t_{ex,min}$ (right)

6.7.1.2 Jet Response Time

The switching time is a function of the entrainment rate, the attachment force and the jet response to a change in pressure. The rate of entrainment ϵ determines the time it takes to lower the pressure on the unattached side and hence the time to reverse the attachment force Δp. It is then the jet response time to the reversed pressure difference that determines the time it takes the jet to be fully attached to the opposing wall.

It was shown previously that the pressure difference across the jet is reversed at the end of excitation ($t = t_{ex}$). It was further shown that this coincides with the point at which the radius of the jet centreline approaches a straight line ($R \to \infty$). The switching time is thus the sum of the minimum required excitation time and the time it takes the jet to bend from R^{∞} to R^{*} under the driving force Δp^{*}. Here * denotes the steady state conditions of the attached jet.[5] To estimate the switching time t_s

[5]The excitation time is further given by the number of excitation cycles that enable switching. Note that the number of excitation cycles N_{cyc} depends on the sound pressure level $\hat{p}$. A higher sound pressure means that less excitation cycles are required. This is because the size of the rolled-up vortices and hence the entrainment rate depend on $\hat{p}$, too.

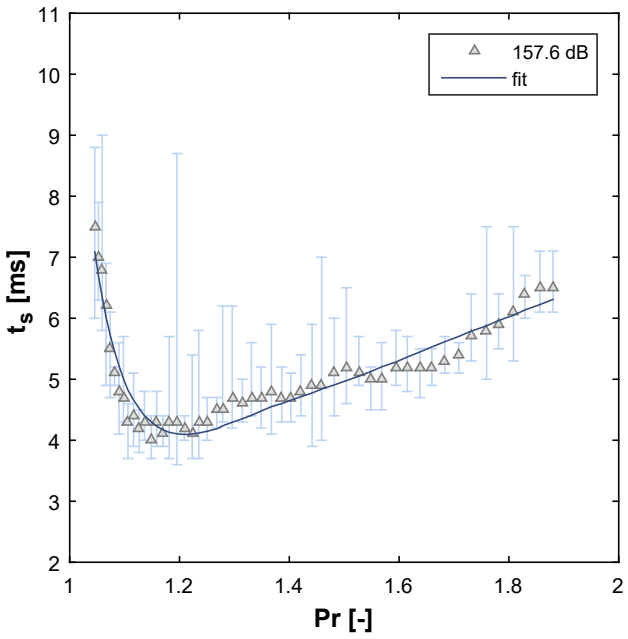

Figure 6.34: Switching time over pressure ratio with $t_{ex} = 2t_{ex,min}$

it is nonetheless reasonable to use the jet response time t_R based on $R^{\infty} \rightarrow R^{*}$ and Δp^{*}, since the excitation time is a small fraction of t_s ($< 10\%$).

The response time is then derived from the jet curvature equation (Eq.2.3) using a constant jet spreading of 31.5 as determined by Epstein [270]. The angle θ can be related to the wall attachment angle β and the jet centreline radius R so that

$$R = \frac{h(1.3 - tan(\beta))}{1 - cos(\theta) - tan(\beta)sin(\theta)} \tag{6.14}$$

To ease the further notation of the subsequent equations the following constants are introduced:

$$k_1 = h(1.3 - tan(\beta)) \tag{6.15}$$

$$k_2 = tan(\beta) \tag{6.16}$$

$$k_3 = \dot{m}\sqrt{\frac{3}{\sigma h^3 A R^2}} \tag{6.17}$$

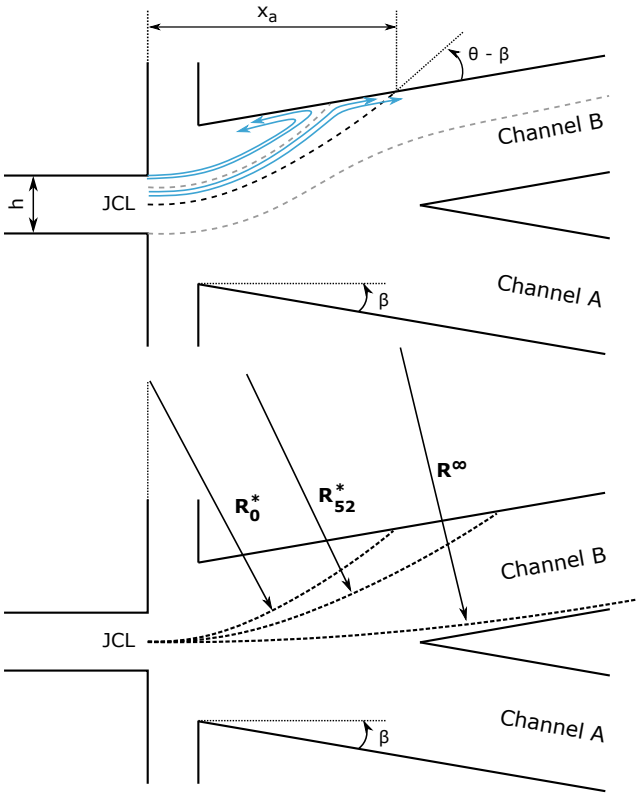

Figure 6.35: Schematic of the device and its relevant dimensions for the jet curvature equation

$$k_4 = \frac{\dot{m}^2}{\rho h^3 A R^2} \tag{6.18}$$

The jet curvature equation now reads as

$$\frac{k_3}{\sqrt{\theta R}} \frac{dR}{dt} - \frac{k_4}{R} = \Delta p \tag{6.19}$$

The first term on the left governs the dynamic response of the jet to a change in Δp.

The second term relates $\dot{m}$ and R to the attachment force Δp in steady state.

Using chain rule, Eq.6.19 leads to

$$\frac{k_3}{\sqrt{\theta R}} \frac{dR}{d\theta} \frac{d\theta}{dR} - \frac{k_4}{R} = \Delta p \tag{6.20}$$

and hence

$$\frac{k_3}{\sqrt{\theta R}}\frac{d\theta}{dt} - \frac{k_4}{R}\frac{d\theta}{dR} = \Delta p \frac{d\theta}{dR} \tag{6.21}$$

From Eq.6.14 it follows that

$$dR = \frac{h(1.3 - tan(\beta))}{(1 - cos(\theta) - tan(\beta)sin(\theta)} \cdot (sin(\theta) - tan(\beta)cos(\theta))d\theta \tag{6.22}$$

and so

$$\frac{k_3}{\sqrt{\theta R}(\frac{k_4}{R} + \Delta p)} \frac{k_1(k_2 cos(\theta) - sin(\theta))}{(-k_2 sin(\theta) - cos(\theta) + 1)^2}\frac{d\theta}{dt} = 1 \tag{6.23}$$

Finally, an expression for the jet response time is given by

$$t_R = \int_{\theta_\infty}^{\theta_0} \frac{k_3}{\sqrt{\theta R}} \frac{1}{\Delta p^* + \frac{k_4}{R}} \frac{k_1(k_2 cos(\theta) - sin(\theta))}{(-k_2 sin(\theta) - cos(\theta) + 1)^2} d\theta \tag{6.24}$$

The steady state attachment force Δp^* - which already prevails after t_{ex} - is obtained by

$$\frac{\dot{m}^2}{\rho h^3 A R^2}\frac{1}{R^*} = \Delta p^* \tag{6.25}$$

The steady state radii R_i^* for all $\dot{m}_i$ are further found by linear interpolation between R_0^* and R_{52}^*, the centreline radii of the lowest and highest mass flow rate, respectively. The linear dependency of R^* on $\dot{m}$ was found by Epstein [270]. The radii R_0^* and R_{52}^* are furthermore determined by the reattachment length x_a (see Fig.6.35) obtained from CFD (see Appendix B). The upper and lower limit of the integral in Eq.6.24, θ_∞ and θ_0, are finally determined by solving Eq.6.14. R^∞ is here defined as the centreline radius at $0.01 \cdot \Delta p^*$. This is reasonably close to a straight curvature upstream of the splitter leading edge.

The time it takes the jet to go from R^∞ to R^* under the driving force Δp^* as a function of Pr is shown in Fig.6.36. Note that the curve is rather qualitative than quantitative since $t_R \to \infty$ for $\Delta p \to 0$. A value of 1% of Δp^* to determine R^∞,

however, yields good agreement with experimental data. Despite any quantitative comparison to t_s or t_{ex}, it is most interesting that the response time decreases exponentially up to $Pr = 1.2$ but increases linearly thereafter. This was not expected since it was assumed that the switching time and hence the response time decrease at higher jet velocities. Nevertheless, this explains the linear increase in t_s found in the experiments.

The excitation time shown in Fig.6.36 a.) corresponds to the minimum required number of excitation cycles at a sound pressure level $\hat{p} = 157.6\,dB$. The good agreement between the semi-theoretical and experimentally measured switching time shown in Fig.6.36 b.) allows a rough prediction of the output oscillation frequency f_{out} for different flow conditions or device configurations. The increase in t_R, or t_s, with an increase in Pr was found to be due to an increase in R^* as the mass flow rate goes up. This, however, is believed to be due to the almost straight attachment walls of the current design. Note that the wall attachment angle is 0° for the first two nozzle heights downstream of the orifice. Other device geometries, such as that examined by Nicholls and Bacic [288], exhibit a decreasing attachment radius R as the flow rate goes up. Based on Eq.6.24 this leads to a steady decrease of the switching time t_s for higher pressure ratios. This suggests that there is an optimal device geometry.

6.7.1.3 Dynamic Switching

The dynamic operation of the device is constrained by the switching time t_s. Given that the switching time was defined as the time between the onset of excitation and the point where 90% of the final mean value is reached the maximum output frequency can be obtained by $f_{out,max} = \frac{0.9}{2 \cdot t_s}$. At the preferred pressure ratio that yields $f_{out,max} = 112\,Hz$. But as we can see in Fig.6.37 a.) single switching events start to fail at $f_{out} = 100\,Hz$ given that there is still some scatter in t_s. At $Mn = 1$ ($Pr = 1.9$) the maximum output frequency would be $f_{out,max} = 70\,Hz$. But without having

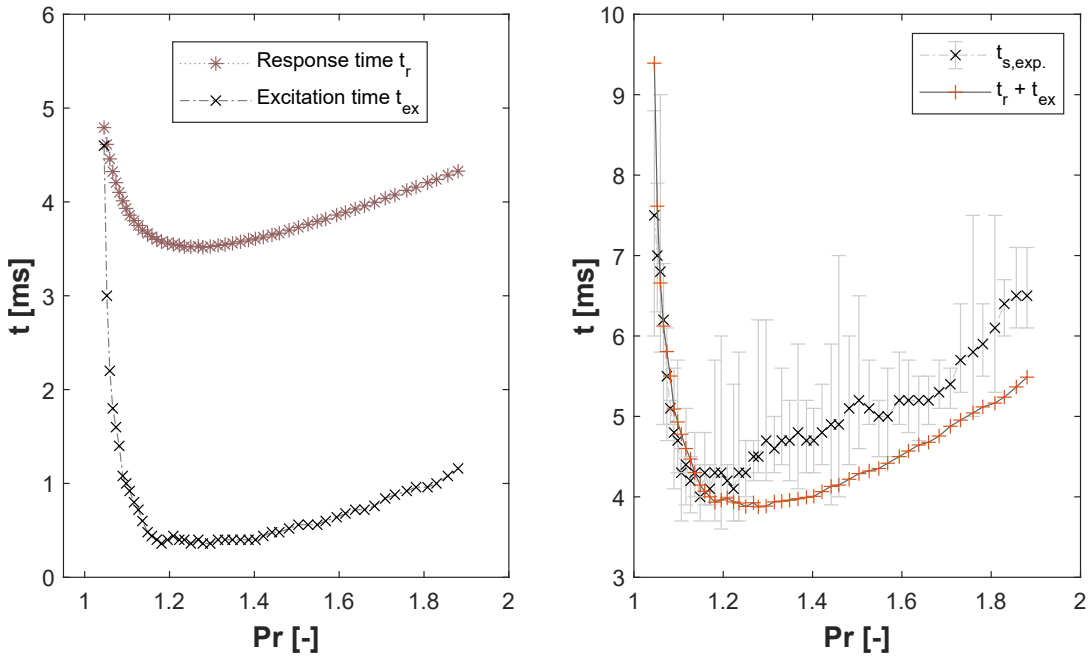

(a) Excitation and theoretical response time

(b) Experimental and theoretical switching time

Figure 6.36: Different time scales of the jet performance versus pressure ratio

to compromise on randomly failing switching events the actual output frequency amounts to $f_{out} = 60\,Hz$ and is shown in Fig.6.37 b.).

6.7.2 Discussion

It was already assumed in the introduction that the excitation mode that triggers the switching process will shift to lower frequencies as the Reynolds number across the device increases. It was, however, not anticipated or expected that the excitation mode of both device configurations differ from one another. The preferred Strouhal number has now shifted from $St_h = 0.25$ to $St_h = 0.15$ by just inserting a splitter into the device. Interestingly this corresponded to the vortex passage frequency at the end of the potential core for the flow rates considered for the splitter-less device. In order to allow a more accurate extrapolation of the shear layer frequency to higher flow rates, especially at which the splitter device showed its preference to switch, two

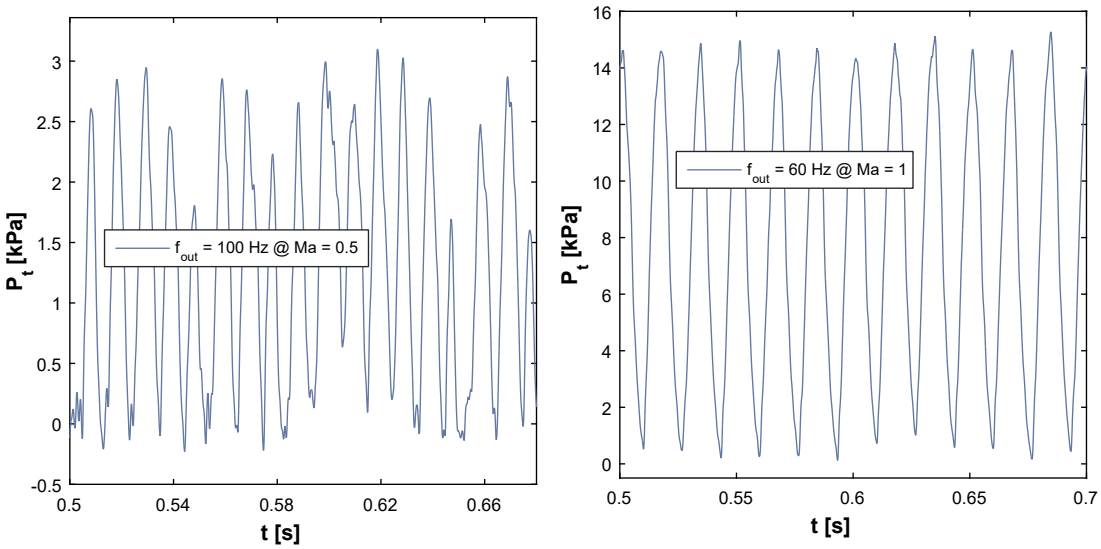

(a) $Mn = 0.5$ and $f_{out} = 100\,Hz$ (b) $Mn = 1$ and $f_{out} = 60\,Hz$

Figure 6.37: Total gauge pressure inside channel A during switching

additional simulations of the reduced size model at $\dot{m}_{11}$ and $\dot{m}_{12}$ were performed. The two flow rates are represented by the last two points in Fig.6.38 and correspond to the flow rates at which the pressure ratio across the device was $Pr = 1.16$ and $Pr = 1.19$, respectively. The graph indicates that the frequency of $St_h = 0.15$ still matches well the first subharmonic of the shear layer roll-up at higher flow rates. Subharmonic excitation is therefore responsible for the switching of the splitter device. The question now arises which of the two excitation modes ($St_h = 0.15$ for the splitter- and $St_h = 0.25$ for the splitter-less) represent the actual jet preferred mode and why it differs in the first place. Two possible explanations are again plausible. The switching mechanism of the splitter device relies on the jet preferred mode whereas the splitter-less device shows only a Strouhal number preference at $St_h = 0.25$ given that the sound pressure level is not high enough. This would support the common point of view that the jet preferred mode corresponds to the passage frequency of vortices at the end of the potential core. This, however, is not supported by the amplitude measurements for either devices. The minimum required sound pressure

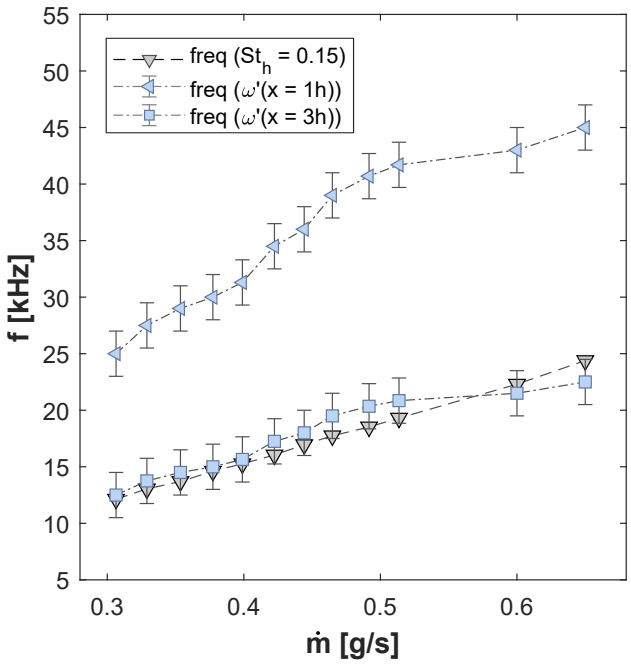

Figure 6.38: Natural roll-up frequency and its subharmonic along with the frequency corresponding to $St_h = 0.15$

level of the splitter device is even lower than that for the splitter-less device. And even if the measurements exhibit an extreme uncertainty the splitter device would show a shift of the preferred mode Strouhal number as the amplitude is decreased. This is not the case. It is therefore unclear what causes the different excitation frequencies if the excitation mode of the splitter device corresponds to the jet preferred mode. The second interpretation is that the currently accepted perception of the jet preferred mode being a subharmonic of $St_\theta = 0.012$ is not necessarily true, as was already suggested in the discussion of the splitter-less device. This would mean that switching of the splitter device is simply caused by subharmonic excitation which most likely encourages the pairing of neighbouring vortices. This interpretation and explanation is furthermore supported by the fact that subharmonic excitation requires (and saturates at) lower amplitudes than the jet preferred mode [26]. Note that the minimum threshold required for switching is more than $5\,dB$ lower for the splitter device. This is then assumed to be because the subharmonic component is already

inherent in the shear layer and thus only needs to be amplified. The higher threshold amplitude for the jet preferred mode (and hence the splitter-less device) is then an indication that the preferred mode frequency is not part of any already existing instability - hence doesn't correspond to the passage frequency at the of the potential core. It would nonetheless be unclear why the excitation mode switches between the two devices. The only possible explanation the author can come up with is that the reverse flow of the splitter configuration or the interaction of the free shear layer with the splitter leading edge has sufficient influence on the flow field so to prevent or encourage one of the two modes. However, jet preferred mode as well as subharmonic excitation result in an increased and asymmetric rate of entrainment that causes the jet to switch to the opposite side.

6.8 Conclusion

The knowledge gained from the previous chapter was used to develop a new device that is capable of switching a jet over a large range of pressure ratios from low subsonic ($Pr = 1.04$) to sonic conditions ($Pr = 1.9$). The active control mechanism allows any arbitrary output oscillation pattern subject to the minimum switching time $t_{s,min}$ which was shown to be limited mainly by the jet response time to a change in pressure. Such a device has not existed so far and thus might have a considerable impact on the advancement of flow control applications.

The chapter first examined the desired operating conditions so to narrow down the choice of the excitation frequency. The discussion of key design parameters as well as the acoustic optimisation then completed the design of the new device. Two device configurations, with and without splitter, were subsequently examined by means of non-dimensional parameters. The splitter-less device allowed the visualisation of the flow field using non-intrinsic optical measurements (PIV) and revealed that large vor-

tical structures at the excitation frequency cause a sufficient increase and asymmetry in entrainment leading to jet detachment. This was further supported by Large Eddy Simulations of both a truncated and full-scale model of the device. The effects of vents and changes in absolute pressure were investigated as well. The latter showed no downside of the performance at higher densities and pressures which is important for future real world applications. The second device configuration, with splitter, extended the bandwidth of the device considerably. Experiments further showed that the switching time has a minimum at $Pr \approx 1.2$. This was explained analytically using the jet curvature equation. The excitation mode that triggers the switching process was further found to change by simply inserting a splitter. A thorough discussion of that occurrence revealed that the jet preferred mode might not depend on the shear layer instability.

Chapter 7

Conclusion and Future Work

A novel methodology to drive a fluidic switching device has been developed within the scope of this thesis. At low flow velocities and low-frequency excitation it was found that an acoustic signal can provide sufficient control authority to enable switching. The switching mechanism was further found to rely solely on the interaction of a pure tone acoustic wave with the free shear layer of a Coandă reattached jet. Switching was then shown to depend on the flow velocity u_e (pressure ratio Pr), the excitation frequency f_{ex} (Strouhal number St) and the sound pressure level $\hat{p}$ (amplitude flow factor Am). More precisely, a preferred mode of switching was found if the excitation Strouhal number matches the natural shear layer instability of the reattached flow. The required sound pressure level that enables switching was further found to increase as the Strouhal number moves away from the preferred mode. It was also shown that switching can be achieved irrespective of the side from which the flow is excited. However, the excitation from the unattached side of the flow was found to be several times more effective. Hence, the focus was put on the unattached side excitation mode only. Large Eddy Simulations were then performed to investigate the flow physics of a single switching event in more detail. The results revealed that the excitation and amplification of the shear layer instability enhances the roll-up charac-

teristics of the free shear layer. A resulting asymmetry in entrainment then leads to a pressure drop on the unattached side sufficient to counteract the attachment force. The results gained from the low-frequency device were then used to design a new device that is capable of switching high-speed jets up to $Mn = 1$ using ultrasonic excitation frequencies. The performance of the ultrasonic device was investigated for a range of different conditions including higher overall densities. The latter showed no downside in performance which is crucial when used at engine engine realistic conditions. The geometry of the control port chambers were optimized so that a 2D eigenmode matches the resonance frequency of the ultrasonic transducer. This was necessary so to increase the sound pressure level required for switching. Particle Image Velocimetry and Large Eddy Simulation revealed that the preferred mode Strouhal number of the ultrasonic device is different to the Strouhal number preference of the low-frequency device. This was then attributed to a shift of the natural roll-up location of the free shear layer to further upstream positions as the Reynolds number increases. The Strouhal number preference was also shown to be different whether a splitter is used or not. In the case of no splitter, the results indicated that the jet preferred mode, the excitation frequency that attains the maximum amplification, is responsible for switching. If a splitter is used, however, the results suggested that the merging of two neighbouring vortices trigger the switching process. This shift of the preferred excitation mode could not be explained satisfactorily. However, the results gave rise to the assumption that the jet preferred mode might not be a shear layer instability and, in fact, independent of the natural shear layer roll-up. This was believed to explain the huge scatter in the literature regarding the jet preferred mode Strouhal number. Hence, a separate, more fundamental, investigation of the shear layer characteristics of an excited round jet subject to different initial conditions was conducted. A literature review regarding the variation of the jet preferred mode Strouhal number supported the initial assumption but experimental results were not

able to come to a decisive conclusion. To be more precise, two out of three test cases suggest that the preferred mode of excitation remains constant irrespective of the initial conditions. The third test case, however, shows a rather broad range of the preferred mode Strouhal number and therefore doesn't allow to conclude a clear statement.

With respect to the objectives set in chapter 2 it can be said that the present fluidic device overcomes most of the inherent drawbacks of conventional actuator technologies and, in addition, outperforms the current state of the art fluidic devices. This is because of its output frequency not being a function of the mass flow rate, its active switching mechanism, its ability to operate under higher densities with no downside in performance as well as its low cost and weight. Moreover, no device has yet been developed that can switch jet velocities ranging from low subsonic up to sonic conditions in an active manner, including the ability to be used in closed-loop control. What's more is that no moving parts are involved. Thus, the device holds great potential to be used in future AFC applications.

With respect to possible future work, there is room for numerous follow-up studies. The analytical model describing the response time of a jet derived in chapter 6, for example, could be used to identify specific geometric parameters that might improve the switching performance. Here it would be of high interest how a change in the attachment radius R affects the increase or decrease in t_R at higher pressure ratios. The influence of different geometric parameters should also be investigated both experimentally and numerically. Especially the change in R for different device configurations including the use of high back pressures [1] is, in this context, of high interest. Geometric parameters could further be investigated by means of an optimisation procedure similar to that performed for the control port chamber in chapter 6. This ought to say that parameters such as setback distance, wall attachment angle

[1] A higher back pressure causes the attachment to stall which moves the point of reattachment further downstream, hence increasing R.

and splitter distance or shape[2], all defined by multiple Bézier points, could be optimised with respect to various objectives, e.g. a minimum attachment force Δp or a maximum reattachment length x_a.

The investigation of the device performance at super-sonic conditions is also worth considering. Many applications require high momentum outputs at the device outlet with pressure ratios in excess of $Pr = 2$. Here it is especially interesting how a sound wave can affect the shear layer characteristics if the vortex convection speed exceeds the speed of sound.

Another possibility for a follow-up study involves the use of ultrasonic transducers with frequencies above $25\,kHz$. Recall that the switching time as well as the required energy depend on the time it takes to reverse the pressure gradient across the jet. This is equivalent to the minimum required excitation time t_{ex}. Recall as well that the required excitation time relies mainly on the volume of the control port chamber since this is the reservoir from which fluid is entrained. The size of the control port chamber and hence its volume would decrease if the frequency of the 2D eigenmode increases. A smaller control port chamber would then lead to a faster reverse of the pressure difference across the jet and thus to an overall reduction in switching time.

In addition, the author of this thesis would also like to mention a finding that has not yet been discussed but is nonetheless interesting for future studies. During the experiments of the ultrasonic device with splitter it was found that an increase in back pressure eventually leads to an unstable flapping of the flow around the splitter leading edge. It was then found that simultaneous excitation using both transducers with slightly varying frequencies $f_{trans.I}$ and $f_{trans.II}$ well above the resonance frequency results in an output oscillation frequency at the beat frequency $f_{output} = |f_{trans.II} - f_{trans.I}|$. The mechanism behind that operation mode and its benefits are discussed separately in the appendix. A further investigation regarding the unstable operation

[2]The possibility of having different splitter shapes has not been discussed in this thesis. Various different geometries such as a cusped splitter can, however, be found in the open literature.

mode is highly encouraged.

Last but not least, although chapter 4 has failed to come to a decisive conclusion it has raised some doubts about validity of the current point of view regarding the relation of the natural shear layer instability and the jet preferred mode. Both the literature review as well as the experimental results can be interpreted so that the stated hypotheses hold their ground. However, this topic requires a further, more detailed, analysis with a more sophisticated test rig that allows for a wider nozzle exit diameter so to reduce the scatter of the results. The author of this thesis is looking forward to possibly working on this topic in the future.

Appendix A

Acoustic Optimisation

The optimised geometry is found by solving the time-independent wave equation for a variety of control port chamber geometries that are given to the numerical solver through an optimisation algorithm. Given that the initial design was found to have a 2D eigenmode that is already near the target frequency of $25\,kHz$ (see Fig.A.1), it was opted for a computationally less expensive gradient-based (*fmincon*[1]) algorithm rather than an evolutionary algorithm. This is also because the initial design was found to be a relatively good initial guess for the final optimised geometry. The five Bézier points forming the control port chamber together with their lower and upper bounds are shown in Fig.A.2. In order to satisfy the objective function and minimize the value of

$$|f_T - f^*| + \frac{1}{SPL^*} + |\frac{f_T}{2\,kHz} - Q| \tag{A.1}$$

less than 100 iterations were required.

It was further chosen to perform the optimisation in 2D only since a 3D model showed no significant difference. As can be seen in Fig.A.1, the resonance frequency of $22.5\,kHz$ of the initial design is effectively the same for both 2D and 3D models.

[1]A built-in optimisation tool in Matlab

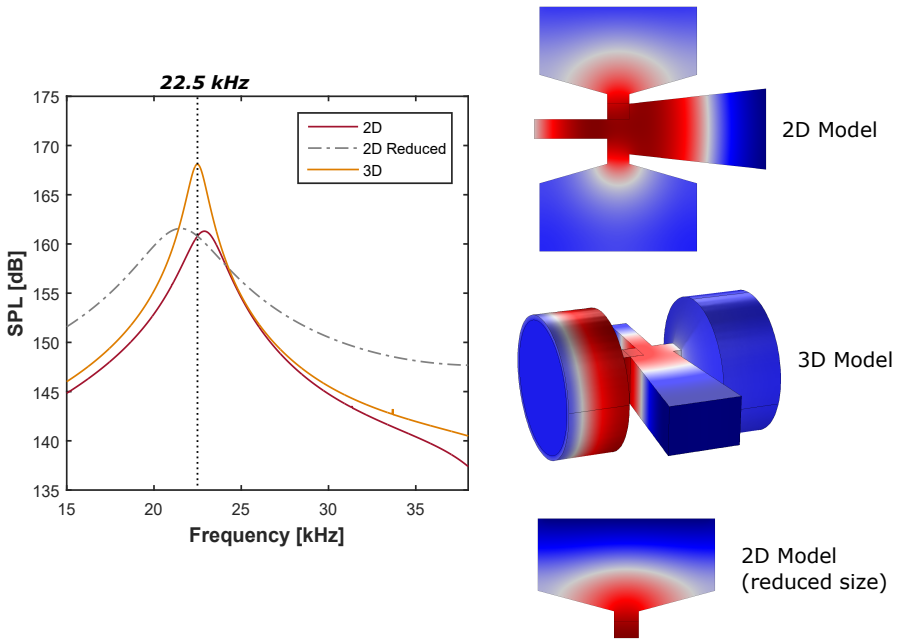

Figure A.1: Example and schematic of the lower and upper bounds of the 5 Bezier points.

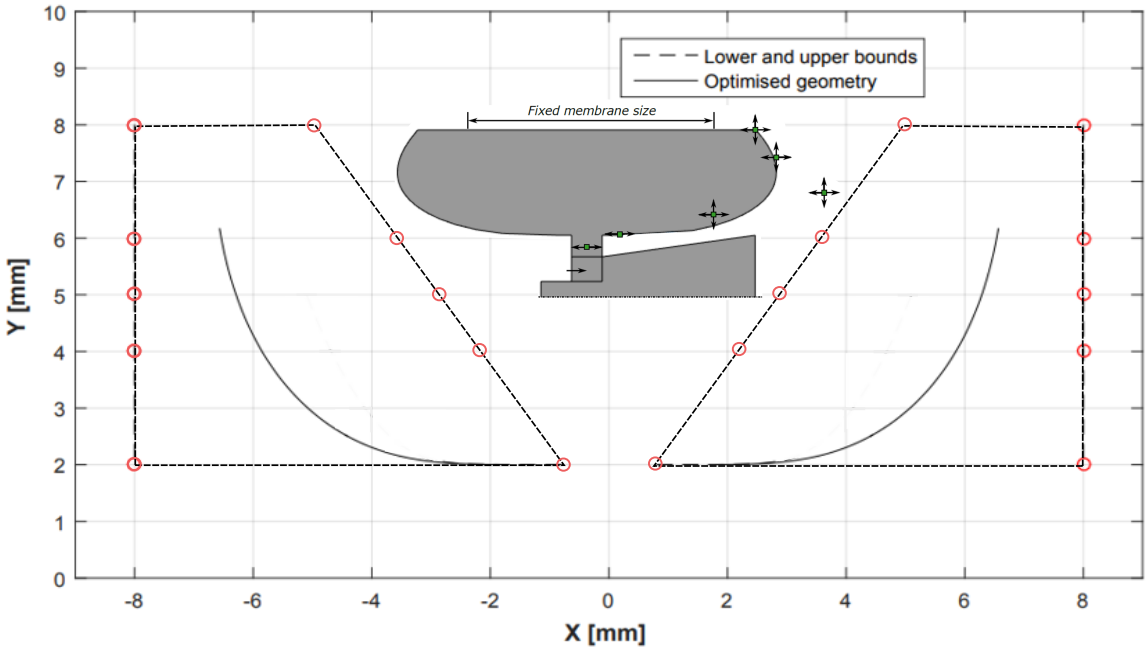

Figure A.2: Difference in the frequency response of the 2D, 2D reduced and 3D acoustic model

Appendix B

Jet Curvature Radius

The analytical model for the response time of a jet to a change in pressure requires the radius of the jet curvature of the attached flow in steady state. This radius is determined by the reattachment point (x_r, y_r) obtained from RANS simulations. The reattachment point is further defined as the point of maximum pressure on the attachment wall. The radius is then given by

$$R = \frac{x_r^2 + y_r^2}{2 \cdot y_r} \tag{B.1}$$

Note that only the radii for the lowest and highest flow rates ($\dot{m}_1$ and $\dot{m}_{52}$) are computed whereas the values in between are interpolated.

The reduced size model was here used to obtain steady state results of the reattached jet. Surface pressure and isolines shown for both flow rates are depicted in Fig.B.1. The jet curvature radius amounts to $4h$ and $6.5h$, for $\dot{m}_1$ and $\dot{m}_{52}$ respectively.

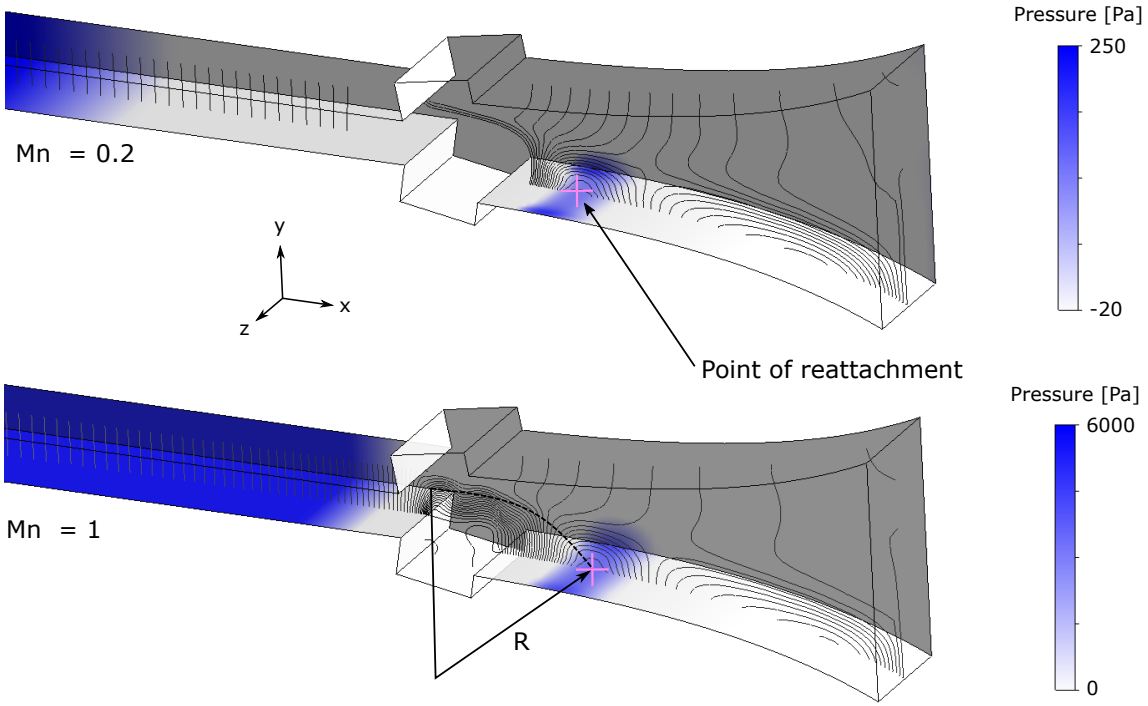

Figure B.1: Surface pressure on the wall and pressure isolines at the x-y plane ($z = 1.5\,mm$) for the lowest and highest flow rates, respectively, indicating a shift of the attachment point to further downstream positions at higher Mn.

Appendix C

Unstable Operation Mode

Both outlets of the ultrasonic device with splitter were connected to a ball valve so to increase back-pressure and hence simulate a flow restriction of a potential application. It was noticed that the jet becomes unstable as the back pressure exceeds a certain threshold. This is due to the blockage effect of the restricted outlets. Once the flow exits through the nozzle it starts to favour one of the two attachment walls by means of the Coandă effect. The flow travels down one of the two outlet channels and fills its volume with fluid. The blockage effect of the ball valve causes the pressure to rise inside the channel as the jet starts to attach to the wall. With sufficient blockage the back-pressure increases until the flow cannot follow the attachment wall anymore causing the attachment to stall. The jet is pushed towards the opposite attachment wall and the same cycle begins anew. This causes the jet to flap around the splitter leading edge without being fully attached do either sides. This highly unsteady flow field is similar to that of a fluidic oscillator, though without any feedback paths.
It was then found that a constant acoustic excitation at $\approx 42kHz$ stabilizes the jet and causes it to attach to the side of excitation. This is obviously a result of enhanced entrainment. What's more is that simultaneous excitation from both transducers with frequencies $f_{trans.I} = 42\,kHz$ and $f_{trans.II} = f_{trans.I} + f_B$ with $f_B = 1 - 200\,Hz$ results

in an output oscillation frequency at the beat frequency f_B. The acoustic signal of the superimposed wave seen by the jet is exemplarily shown in Fig.C.2 with $f_B = 100\,Hz$.

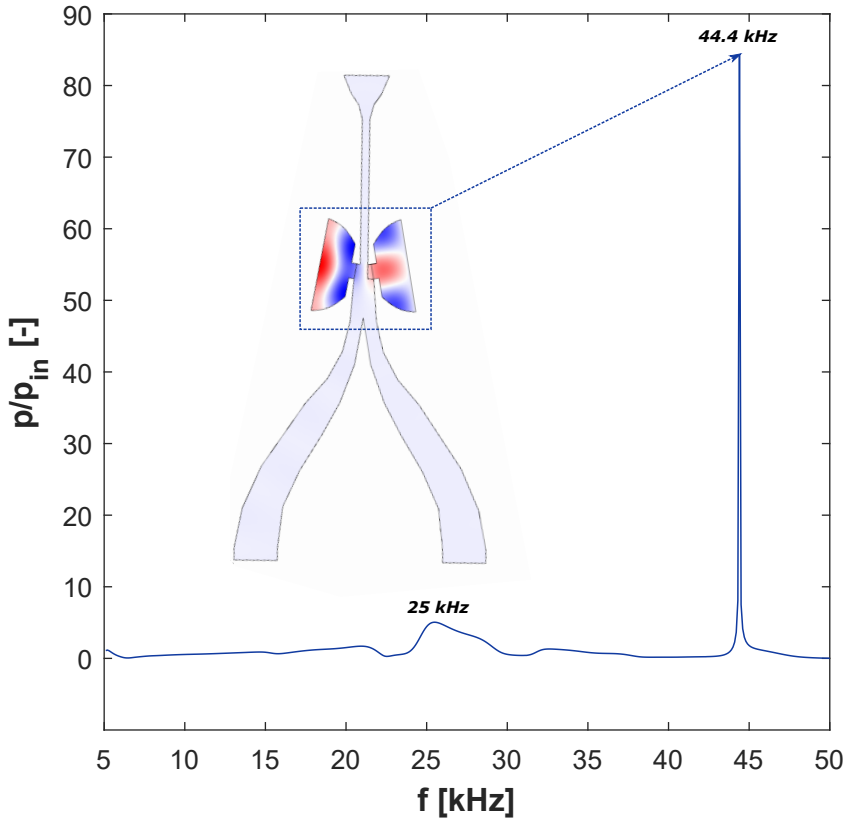

Figure C.1: Frequency response of the full-scale device and 2D surface acoustic pressure at the eigenfrequency $f = 44.392\,kHz$

However, it still remained unclear at first why an excitation frequency of $\approx 42\,kHz$ is required to achieve such a behaviour. Note that the frequency response of the transducer has a very low Q-factor and the sound pressure level (under reference conditions) amounts to less than $90\,dB$ at $\approx 42\,kHz$. An acoustic simulation in the frequency domain together with an eigenfrequency analysis then revealed that maximum amplification inside the interaction region happens at an incoming pressure wave with $f = 44392\,Hz$. The frequency response of a 2D simulation of the full-scale device is shown in Fig.C.1. The surface acoustic pressure at the eigenfrequency is

exemplarily shown as well. This indicates that the maximum amplification is due to an acoustic coupling of the two control port chambers and the interaction region. Note the difference in amplification $\frac{p}{p_{in}}$ between the transducer resonance frequency at $25\,kHz$ and the eigenfrequency at $44.392\,kHz$.

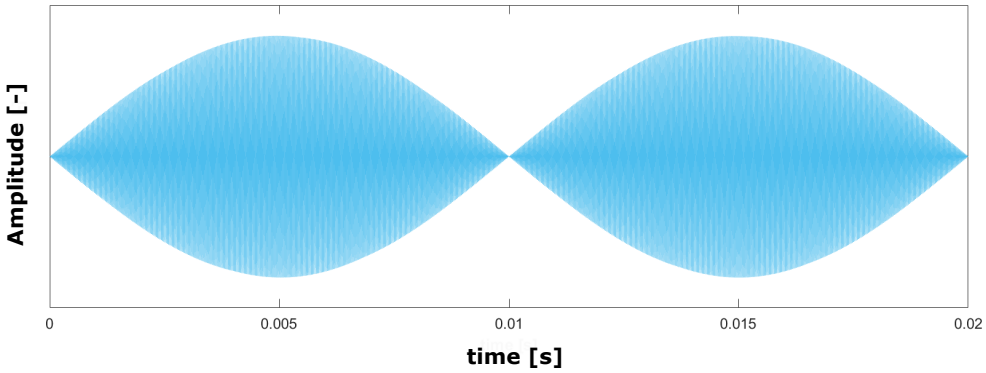

Figure C.2: Superposition of two acoustic signals f_1 and f_2 with $f_2 = f_1 + 100\,Hz$ and $f_1 = 44400\,Hz$

Bibliography

[1] Dearing, S. S., Morrison, J. F., and Iannucci, L., 2010. "Electro-active polymer (eap)"dimple" actuators for flow control: Design and characterisation.". *Sensors and Actuators A: Physical,* **157**(2), pp. 210–218.

[2] Cattafesta III, L. N., and Sheplak, M., 2011. "Actuators for active flow control". *Annual Review of Fluid Mechanics,* **43**, pp. 247–272.

[3] Crow, S. C., and Champagne, F., 1971. "Orderly structure in jet turbulence". *Journal of Fluid Mechanics,* **48**(3), pp. 547–591.

[4] Ploetner, K. O., Rothfeld, R., Urban, M., Hornung, M., Tay, G., and Oguntona, O., 2017. "Technological and operational scenarios on aircraft fleet-level towards atag and iata 2050 emission targets". In 17th AIAA Aviation Technology, Integration, and Operations Conference, p. 3771.

[5] Szodruch, J., Grimme, W., Blumrich, F., and Schmid, R., 2011. "Next generation single-aisle aircraft–requirements and technological solutions". *Journal of air transport management,* **17**(1), pp. 33–39.

[6] Zhang, W., and Samtaney, R., 2015. "A direct numerical simulation investigation of the synthetic jet frequency effects on separation control of low-re flow past an airfoil". *Physics of Fluids,* **27**(5), p. 055101.

[7] Rathay, N. W., Boucher, M. J., Amitay, M., and Whalen, E., 2014. "Performance enhancement of a vertical tail using synthetic jet actuators". *AIAA Journal,* **52**(4), pp. 810–820.

[8] Shmilovich, A., and Yadlin, Y., 2008. "Flow control for the systematic buildup of high-lift systems". *Journal of Aircraft,* **45**(5), pp. 1680–1688.

[9] You, D., and Moin, P., 2008. "Active control of flow separation over an airfoil using synthetic jets". *Journal of Fluids and Structures,* **24**(8), pp. 1349–1357.

[10] Ross, M. H., Cameron, J. D., Morris, S. C., Chen, H., and Shi, K., 2017. "Axial compressor stall, circumferential groove casing treatment, and the tip-clearance momentum flux". *Journal of Propulsion and Power,* **34**(1), pp. 146–152.

[11] Van Paridon, A., 2016. "Thermal modelling and control of high pressure turbine subsystems". PhD thesis, University of Oxford.

[12] Wang, L., Luo, Z., Xia, Z., Liu, B., and Deng, X., 2012. "Review of actuators for high speed active flow control". *Science China Technological Sciences,* **55**(8), pp. 2225–2240.

[13] Bons, J. P., Sondergaard, R., and Rivir, R. B., 2000. "Turbine separation control using pulsed vortex generator jets". In ASME Turbo Expo 2000: Power for Land, Sea, and Air, American Society of Mechanical Engineers, pp. V003T01A067–V003T01A067.

[14] Seifert, A., and Pack, L., 1999. "Oscillatory control of separation at high reynolds numbers". *AIAA journal,* **37**(9), pp. 1062–1071.

[15] Greenblatt, D., and Wygnanski, I. J., 2000. "The control of flow separation by periodic excitation". *Progress in aerospace Sciences,* **36**(7), pp. 487–545.

[16] Griffin, W. S., 1966. "Design of a fluid jet amplifier with reduced receiver-interaction-region coupling".

[17] Gregory, J., and Tomac, M. N., 2013. "A review of fluidic oscillator development". In 43rd AIAA Fluid Dynamics Conference, p. 2474.

[18] Bobusch, B. C., Woszidlo, R., Bergada, J., Nayeri, C. N., and Paschereit, C. O., 2013. "Experimental study of the internal flow structures inside a fluidic oscillator". *Experiments in fluids,* **54**(6), p. 1559.

[19] Sieber, M., Ostermann, F., Woszidlo, R., Oberleithner, K., and Paschereit, C. O., 2016. "Lagrangian coherent structures in the flow field of a fluidic oscillator". *Physical review fluids,* **1**(5), p. 050509.

[20] Woszidlo, R., Ostermann, F., Nayeri, C. N., and Paschereit, C. O., 2015. "The time-resolved natural flow field of a fluidic oscillator". *Experiments in fluids,* **56**(6), p. 125.

[21] Ostermann, F., Woszidlo, R., Nayeri, C. N., and Paschereit, C. O., 2015. "Phase-averaging methods for the natural flowfield of a fluidic oscillator". *AIAA Journal,* **53**(8), pp. 2359–2368.

[22] Tesař, V., Trávníček, Z., Kordík, J., and Randa, Z., 2007. "Experimental investigation of a fluidic actuator generating hybrid-synthetic jets". *Sensors and Actuators A: Physical,* **138**(1), pp. 213–220.

[23] Gregory, J. W., Gnanamanickam, E. P., Sullivan, J. P., and Raghu, S., 2009. "Variable-frequency fluidic oscillator driven by a piezoelectric bender". *AIAA Journal,* **47**(11), pp. 2717–2725.

[24] Gad-el Hak, M., 2006. *Flow control: passive, active, and reactive flow management.* Cambridge university press.

[25] Robinson, S. K., 1991. "Coherent motions in the turbulent boundary layer". *Annual Review of Fluid Mechanics,* **23**(1), pp. 601–639.

[26] Samimy, M., Webb, N., and Crawley, M., 2018. "Excitation of free shear-layer instabilities for high-speed flow control". *AIAA Journal,* **56**(5), pp. 1770–1791.

[27] PIJUSH K. KUNDU, IRA M. COHEN, D. R. D., 2012. *Fluid Mechanics 5th.* Elsevier.

[28] Michalke, A., 1965. "On spatially growing disturbances in an inviscid shear layer". *Journal of Fluid Mechanics,* **23**(3), pp. 521–544.

[29] Holmes, P., Lumley, J. L., Berkooz, G., and Rowley, C. W., 2012. *Turbulence, coherent structures, dynamical systems and symmetry.* Cambridge university press.

[30] Ho, C.-M., and Huang, L.-S., 1982. "Subharmonics and vortex merging in mixing layers". *Journal of Fluid Mechanics,* **119**, pp. 443–473.

[31] Browand, F. K., 1966. "An experimental investigation of the instability of an incompressible, separated shear layer". *Journal of Fluid Mechanics,* **26**(2), pp. 281–307.

[32] Sato, H., 1960. "The stability and transition of a two-dimensional jet". *Journal of Fluid Mechanics,* **7**(1), pp. 53–80.

[33] Ho, C.-M., and Huerre, P., 1984. "Perturbed free shear layers". *Annual Review of Fluid Mechanics,* **16**(1), pp. 365–422.

[34] Kibens, V., 1980. "Discrete noise spectrum generated by acoustically excited jet". *AIAA Journal,* **18**(4), pp. 434–441.

[35] Wille, R., 1963. *Beiträge zur Phänomenologie der Freistrahlen.*

[36] Freymuth, P., 1966. "On transition in a separated laminar boundary layer". *Journal of Fluid Mechanics,* **25**(4), pp. 683–704.

[37] Winant, C. D., and Browand, F. K., 1974. "Vortex pairing: the mechanism of turbulent mixing-layer growth at moderate reynolds number". *Journal of Fluid Mechanics,* **63**(2), pp. 237–255.

[38] Pope, S. B., 2001. Turbulent flows.

[39] Zaman, K., and Hussain, A., 1980. "Vortex pairing in a circular jet under controlled excitation. part 1. general jet response". *Journal of Fluid Mechanics,* **101**(3), pp. 449–491.

[40] Nickels, T., and Marusic, I., 2001. "On the different contributions of coherent structures to the spectra of a turbulent round jet and a turbulent boundary layer". *Journal of Fluid Mechanics,* **448**, pp. 367–385.

[41] Gudmundsson, K., and Colonius, T., 2011. "Instability wave models for the near-field fluctuations of turbulent jets". *Journal of Fluid Mechanics,* **689**, pp. 97–128.

[42] Liepmann, H. W., 1952. "Aspects of the turbulence problem". *Zeitschrift für angewandte Mathematik und Physik ZAMP,* **3**(6), pp. 407–426.

[43] Townsend, A., 1980. *The structure of turbulent shear flow.* Cambridge university press.

[44] Brown, G. L., and Roshko, A., 1974. "On density effects and large structure in turbulent mixing layers". *Journal of Fluid Mechanics,* **64**(4), pp. 775–816.

[45] Hussain, A. F., 1986. "Coherent structures and turbulence". *Journal of Fluid Mechanics,* **173**, pp. 303–356.

[46] Michalke, A., 1972. "The instability of free shear layers". *Progress in Aerospace Sciences,* **12**, pp. 213–216.

[47] Monkewitz, P. A., and Huerre, P., 1982. "Influence of the velocity ratio on the spatial instability of mixing layers". *The Physics of Fluids,* **25**(7), pp. 1137–1143.

[48] Michalke, A., 1964. "On the inviscid instability of the hyperbolictangent velocity profile". *Journal of Fluid Mechanics,* **19**(4), pp. 543–556.

[49] Michalke, A., 1965. "Vortex formation in a free boundary layer according to stability theory". *Journal of Fluid Mechanics,* **22**(2), pp. 371–383.

[50] Miksad, R. W., 1972. "Experiments on the nonlinear stages of free-shear-layer transition". *Journal of Fluid Mechanics,* **56**(4), pp. 695–719.

[51] Landers, B. D., 2016. "Mixing characteristics of turbulent twin impinging axisymmetric jets at various impingement angles". PhD thesis, University of Cincinnati.

[52] Zaman, K., and Hussain, A., 1981. "Turbulence suppression in free shear flows by controlled excitation". *Journal of Fluid Mechanics,* **103**, pp. 133–159.

[53] Rajagopalan, S., and Ko, N., 1996. "Velocity and spanwise vorticity measurements in an excited mixing layer of a plane jet". *Experiments in fluids,* **20**(5), pp. 346–357.

[54] PFIZENMAIER, E., 1973. "On the instability of a sound-influenced free jet[ph. d. thesis- tech. univ. berlin]".

[55] Betchov, R., and Szewczyk, A., 1963. "Stability of a shear layer between parallel streams". *The physics of fluids,* **6**(10), pp. 1391–1396.

[56] Husain, Z., and Hussain, A., 1979. "Axisymmetric mixing layer: influence of the initial and boundary conditions". *AIAA Journal,* **17**(1), pp. 48–55.

[57] Cheung, L. C., and Lele, S. K., 2009. "Linear and nonlinear processes in two-dimensional mixing layer dynamics and sound radiation". *Journal of Fluid Mechanics,* **625**, pp. 321–351.

[58] Gaitonde, D., and Samimy, M., 2011. "Coherent structures in plasma-actuator controlled supersonic jets: Axisymmetric and mixed azimuthal modes". *Physics of Fluids,* **23**(9), p. 095104.

[59] Samimy, M., Kim, J.-H., Kastner, J., Adamovich, I., and Utkin, Y., 2007. "Active control of high-speed and high-reynolds-number jets using plasma actuators". *Journal of Fluid Mechanics,* **578**, pp. 305–330.

[60] Samimy, M., Kim, J.-H., Kastner, J., Adamovich, I., and Utkin, Y., 2007. "Active control of a mach 0.9 jet for noise mitigation using plasma actuators". *AIAA Journal,* **45**(4), pp. 890–901.

[61] Gutmark, E., and Ho, C.-M., 1983. "Preferred modes and the spreading rates of jets". *The Physics of fluids,* **26**(10), pp. 2932–2938.

[62] Kuo, C.-W., Cluts, J., and Samimy, M., 2017. "Effects of excitation around jet preferred mode strouhal number in high-speed jets". *Experiments in Fluids,* **58**(4), p. 35.

[63] Gaitonde, D., and Samimy, M., 2010. "Effect of plasma-based azimuthal mode excitation on supersonic jet flow". In 5th Flow Control Conference, p. 4416.

[64] Sasaki, K., Cavalieri, A. V., Jordan, P., Schmidt, O. T., Colonius, T., and Brès, G. A., 2017. "High-frequency wavepackets in turbulent jets". *Journal of Fluid Mechanics,* **830**.

[65] Garnaud, X., Lesshafft, L., Schmid, P., and Huerre, P., 2013. "The preferred mode of incompressible jets: linear frequency response analysis". *Journal of Fluid Mechanics,* **716**, pp. 189–202.

[66] Ray, P. K., Cheung, L. C., and Lele, S. K., 2009. "On the growth and propagation of linear instability waves in compressible turbulent jets". *Physics of Fluids,* **21**(5), p. 054106.

[67] Schmid, P. J., 2010. "Dynamic mode decomposition of numerical and experimental data". *Journal of fluid mechanics,* **656**, pp. 5–28.

[68] Cohen, J., and Wygnanski, I., 1987. "The evolution of instabilities in the axisymmetric jet. part 1. the linear growth of disturbances near the nozzle". *Journal of Fluid Mechanics,* **176**, pp. 191–219.

[69] Jung, D., Gamard, S., and George, W. K., 2004. "Downstream evolution of the most energetic modes in a turbulent axisymmetric jet at high reynolds number. part 1. the near-field region". *Journal of Fluid Mechanics,* **514**, pp. 173–204.

[70] Gamard, S., Jung, D., and George, W. K., 2004. "Downstream evolution of the most energetic modes in a turbulent axisymmetric jet at high reynolds number. part 2. the far-field region". *Journal of Fluid Mechanics,* **514**, pp. 205–230.

[71] Tinney, C., Glauser, M. N., and Ukeiley, L., 2008. "Low-dimensional characteristics of a transonic jet. part 1. proper orthogonal decomposition". *Journal of Fluid Mechanics,* **612**, pp. 107–141.

[72] Taira, K., Brunton, S. L., Dawson, S. T., Rowley, C. W., Colonius, T., McKeon, B. J., Schmidt, O. T., Gordeyev, S., Theofilis, V., and Ukeiley, L. S., 2017. "Modal analysis of fluid flows: An overview". *Aiaa Journal*, pp. 4013–4041.

[73] Hussain, A. F., and Zaman, K., 1981. "The 'preferred mode'of the axisymmetric jet". *Journal of fluid mechanics,* **110**, pp. 39–71.

[74] Samimy, M., Adamovich, I., Webb, B., Kastner, J., Hileman, J., Keshav, S., and Palm, P., 2004. "Development and characterization of plasma actuators for high-speed jet control". *Experiments in Fluids,* **37**(4), pp. 577–588.

[75] Samimy, M., Kim, J.-H., Kearney-Fischer, M., and Sinha, A., 2010. "Acoustic and flow fields of an excited high reynolds number axisymmetric supersonic jet". *Journal of Fluid Mechanics,* **656**, pp. 507–529.

[76] Goparaju, K., and Gaitonde, D. V., 2016. "Large-eddy simulation of plasma-based active control on imperfectly expanded jets". *Journal of Fluids Engineering,* **138**(7), p. 071101.

[77] Gohil, T. B., Saha, A. K., and Muralidhar, K., 2013. "Direct numerical simulation of forced circular jets: effect of varicose perturbation". *International Journal of Heat and Fluid Flow,* **44**, pp. 524–541.

[78] Petersen, R., and Samet, M., 1988. "On the preferred mode of jet instability". *Journal of Fluid Mechanics,* **194**, pp. 153–173.

[79] Hussain, A., and Zaman, K., 1980. "Vortex pairing in a circular jet under controlled excitation. part 2. coherent structure dynamics". *Journal of fluid mechanics,* **101**(3), pp. 493–544.

[80] Kastner, J., Kim, J.-H., and Samimy, M., 2007. "Correlation of large-scale structure dynamics and far-field radiated noise in a mach 0.9 jet". In 45th AIAA Aerospace Sciences Meeting and Exhibit, p. 830.

[81] Chan, Y.-Y., 1974. "Spatial waves in turbulent jets". *The Physics of Fluids,* **17**(1), pp. 46–53.

[82] Kim, J.-H., Kastner, J., and Samimy, M., 2009. "Active control of a high reynolds number mach 0.9 axisymmetric jet". *AIAA Journal,* **47**(1), pp. 116–128.

[83] Hussain, A., and Zaman, K., 1978. "Controlled perturbation of circular jets". In *Structure and Mechanisms of Turbulence I.* Springer, pp. 31–42.

[84] Ko, N., and Davies, P., 1971. "The near field within the potential cone of subsonic cold jets". *Journal of Fluid Mechanics,* **50**(1), pp. 49–78.

[85] Fuchs, H. V., 1972. "Measurement of pressure fluctuations within subsonic turbulent jets". *Journal of Sound and Vibration,* **22**(3), pp. 361–378.

[86] Petersen, R., 1978. "Influence of wave dispersion on vortex pairing in a jet". *Journal of Fluid Mechanics,* **89**(3), pp. 469–495.

[87] Yule, A., 1978. "Large-scale structure in the mixing layer of a round jet". *Journal of Fluid Mechanics,* **89**(3), pp. 413–432.

[88] Drubka, R. E., 1981. "Instabilities in near field of turbulent jets and their dependence on initial conditions and reynolds number.". PhD thesis, Illnois Institue of Technology, Chicago.

[89] Kim, J., and Choi, H., 2009. "Large eddy simulation of a circular jet: effect of inflow conditions on the near field". *Journal of Fluid Mechanics,* **620**, pp. 383–411.

[90] Bi, W., Sugii, Y., Okamoto, K., and Madarame, H., 2003. "Time-resolved proper orthogonal decomposition of the near-field flow of a round jet measured by dynamic particle image velocimetry". *Measurement Science and Technology,* **14**(8), p. L1.

[91] Raman, G., Rice, E., and Reshotko, E., 1994. "Mode spectra of natural disturbances in a circular jet and the effect of acoustic forcing". *Experiments in fluids,* **17**(6), pp. 415–426.

[92] Bechert, D., and Pfizenmaier, E., 1975. "On the amplification of broad band jet noise by a pure tone excitation". *Journal of Sound and Vibration,* **43**(3), pp. 581–587.

[93] Cavalieri, A., Jordan, P., Gervais, Y., Wei, M., and Freund, J., 2010. "Intermittent sound generation in a free-shear flow". In 16th AIAA/CEAS Aeroacoustics Conference, p. 3963.

[94] Bridges, J., and Hussain, A., 1987. "Roles of initial condition and vortex pairing in jet noise". *Journal of Sound and Vibration,* **117**(2), pp. 289–311.

[95] Zaman, K., 1985. "Far-field noise of a subsonic jet under controlled excitation". *Journal of Fluid Mechanics,* **152**, pp. 83–111.

[96] Parekh, D., Reynolds, W., and Mungal, M., 1987. "Bifurcation of round air jets by dual-mode acoustic excitation". In 25th AIAA Aerospace Sciences Meeting, p. 164.

[97] Reynolds, W., Parekh, D., Juvet, P., and Lee, M., 2003. "Bifurcating and blooming jets". *Annual review of fluid mechanics,* **35**(1), pp. 295–315.

[98] Gohil, T. B., Saha, A. K., and Muralidhar, K., 2015. "Simulation of the blooming phenomenon in forced circular jets". *Journal of Fluid Mechanics,* **783**, pp. 567–604.

[99] Wu, X., and Huerre, P., 2009. "Low-frequency sound radiated by a nonlinearly modulated wavepacket of helical modes on a subsonic circular jet". *Journal of Fluid Mechanics,* **637**, pp. 173–211.

[100] Davitian, J., Getsinger, D., Hendrickson, C., and Karagozian, A., 2010. "Transition to global instability in transverse-jet shear layers". *Journal of Fluid Mechanics,* **661**, pp. 294–315.

[101] Han, B., and Goldstein, R. J., 2003. "Instantaneous energy separation in a free jet. part i. flow measurement and visualization". *International Journal of Heat and Mass Transfer,* **46**(21), pp. 3975–3981.

[102] Narayanan, S., Barooah, P., and Cohen, J., 2003. "Dynamics and control of an isolated jet in crossflow". *AIAA journal,* **41**(12), pp. 2316–2330.

[103] Gohil, T. B., Saha, A. K., and Muralidhar, K., 2012. "Numerical study of instability mechanisms in a circular jet at low reynolds numbers". *Computers & Fluids,* **64**, pp. 1–18.

[104] Hilgers, A., 2000. "Control and optimization of turbulent jet mixing". *Center for Turbulence Research. Annual Research Brief*, pp. 45–54.

[105] Sfeir, A., 1979. "Investigation of three-dimensional turbulent rectangular jets". *AIAA journal,* **17**(10), pp. 1055–1060.

[106] Grinstein, F. F., 2001. "Vortex dynamics and entrainment in rectangular free jets". *Journal of Fluid Mechanics,* **437**, pp. 69–101.

[107] Gutmark, E., and Grinstein, F., 1999. "Flow control with noncircular jets". *Annual review of fluid mechanics,* **31**(1), pp. 239–272.

[108] Mi, J., and Nathan, G., 2010. "Statistical properties of turbulent free jets issuing from nine differently-shaped nozzles". *Flow, turbulence and combustion,* **84**(4), pp. 583–606.

[109] Ho, C.-M., and Gutmark, E., 1987. "Vortex induction and mass entrainment in a small-aspect-ratio elliptic jet". *Journal of Fluid mechanics,* **179**, pp. 383–405.

[110] Gohil, T. B., Saha, A. K., and Muralidhar, K., 2015. "Direct numerical simulation of free and forced square jets". *International Journal of Heat and Fluid Flow,* **52**, pp. 169–184.

[111] Rembold, B., Adams, N. A., and Kleiser, L., 2002. "Direct numerical simulation of a transitional rectangular jet". *International Journal of Heat and Fluid Flow,* **23**(5), pp. 547–553.

[112] Tam, C. K., and Thies, A. T., 1993. "Instability of rectangular jets". *Journal of Fluid Mechanics,* **248**, pp. 425–448.

[113] Miller, R., Madnia, C., and Givi, P., 1995. "Numerical simulation of non-circular jets". *Computers & fluids,* **24**(1), pp. 1–25.

[114] Shih, C., Krothapalli, A., and Gogineni, S., 1992. "Experimental observations of instability modes in a rectangular jet". *AIAA journal,* **30**(10), pp. 2388–2394.

[115] Hussain, F., and Husain, H. S., 1989. "Elliptic jets. part 1. characteristics of unexcited and excited jets". *Journal of Fluid Mechanics,* **208**, pp. 257–320.

[116] Bradshaw, P., 1987. "Turbulent secondary flows". *Annual review of fluid mechanics,* **19**(1), pp. 53–74.

[117] Shabaka, I., and Bradshaw, P., 1981. "Turbulent flow measurements in an idealized wing/body junction". *AIAA journal,* **19**(2), pp. 131–132.

[118] Cattafesta, L., and Sheplak, M., 2009. "Actuators and sensors". *Fundamentals and Applications of Modern Flow Control*, pp. 1–20.

[119] Seifert, A., Eliahu, S., Greenblatt, D., and Wygnanski, I., 1998. "Use of piezoelectric actuators for airfoil separation control". *AIAA journal,* **36**(8), pp. 1535–1537.

[120] Jeon, W.-P., and Blackwelder, R. F., 2000. "Perturbations in the wall region using flush mounted piezoceramic actuators". *Experiments in Fluids,* **28**(6), pp. 485–496.

[121] Wiltse, J. M., and Glezer, A., 1993. "Manipulation of free shear flows using piezoelectric actuators". *Journal of Fluid Mechanics,* **249**, pp. 261–285.

[122] Arthur, G., McKeon, B., Dearing, S., Morrison, J., and Cui, Z., 2006. "Manufacture of micro-sensors and actuators for flow control". *Microelectronic Engineering,* **83**(4-9), pp. 1205–1208.

[123] Dearing, S., Lambert, S., and Morrison, J., 2007. "Flow control with active dimples". *The Aeronautical Journal,* **111**(1125), pp. 705–714.

[124] Morrison, J., 2013. "Mems devices for active drag reduction in aerospace applications". In *MEMS for Automotive and Aerospace Applications*. Elsevier, pp. 153–176.

[125] Gallas, Q., Holman, R., Nishida, T., Carroll, B., Sheplak, M., and Cattafesta, L., 2003. "Lumped element modeling of piezoelectric-driven synthetic jet actuators". *AIAA journal,* **41**(2), pp. 240–247.

[126] Glezer, A., and Amitay, M., 2002. "Synthetic jets". *Annual review of fluid mechanics,* **34**(1), pp. 503–529.

[127] Amitay, M., Smith, D. R., Kibens, V., Parekh, D. E., and Glezer, A., 2001. "Aerodynamic flow control over an unconventional airfoil using synthetic jet actuators". *AIAA journal,* **39**(3), pp. 361–370.

[128] Lee, C., Hong, G., Ha, Q., and Mallinson, S., 2003. "A piezoelectrically actuated micro synthetic jet for active flow control". *Sensors and Actuators A: Physical,* **108**(1-3), pp. 168–174.

[129] Gorton, S., Jenkins, L., and Anders, S., 2002. "Flow control device evaluation for an internal flow with an adverse pressure gradient". In 40th AIAA Aerospace Sciences Meeting & Exhibit, p. 266.

[130] Shuster, J. M., and Smith, D. R., 2007. "Experimental study of the formation and scaling of a round synthetic jet". *Physics of fluids,* **19**(4), p. 045109.

[131] Mallinson, S., Reizes, J., and Hong, G., 2001. "An experimental and numerical study of synthetic jet flow". *The Aeronautical Journal,* **105**(1043), pp. 41–49.

[132] Mallinson, S., Kwok, C., and Reizes, J., 2003. "Numerical simulation of micro-fabricated zero mass-flux jet actuators". *Sensors and Actuators A: Physical,* **105**(3), pp. 229–236.

[133] Jain, M., Puranik, B., and Agrawal, A., 2011. "A numerical investigation of effects of cavity and orifice parameters on the characteristics of a synthetic jet flow". *Sensors and actuators A: Physical,* **165**(2), pp. 351–366.

[134] Murugan, T., Deyashi, M., Dey, S., Rana, S. C., and Chatterjee, P., 2016. "Recent developments on synthetic jets". *Defence Science Journal,* **66**(5), pp. 489–498.

[135] Pack, L. G., and Seifert, A., 2001. "Periodic excitation for jet vectoring and enhanced spreading". *Journal of Aircraft,* **38**(3), pp. 486–495.

[136] Chandratilleke, T., Jagannatha, D., and Narayanaswamy, R., 2010. "Heat transfer enhancement in microchannels with cross-flow synthetic jets". *International journal of thermal sciences,* **49**(3), pp. 504–513.

[137] Smith, D., Amitay, M., Kibens, V., Parekh, D., and Glezer, A., 1998. "Modification of lifting body aerodynamics using synthetic jet actuators". In 36th AIAA Aerospace Sciences Meeting and Exhibit, p. 209.

[138] Belanger, R., Boom, P. D., Hanson, R. E., Lavoie, P., and Zingg, D. W., 2017. "Skin friction drag reduction on a flat plate turbulent boundary layer using synthetic jets". In APS Meeting Abstracts.

[139] Qin, Y., Song, Y., Wang, R., Liu, H., and Chen, F., 2018. "Flow separation control on a highly loaded compressor cascade using endwall synthetic jets". *Proceedings of the Institution of Mechanical Engineers, Part G: Journal of Aerospace Engineering,* **232**(11), pp. 2059–2075.

[140] Tang, Z., Sheng, J., Zhang, G., and Periaux, J., 2018. "Large-scale separation flow control on airfoil with synthetic jet". *International Journal of Computational Fluid Dynamics,* **32**(2-3), pp. 104–120.

[141] Sawant, S. G., George, B., Ukeiley, L. S., and Arnold, D. P., 2017. "Microfabricated electrodynamic synthetic jet actuators". *Journal of Microelectromechanical Systems,* **27**(1), pp. 95–105.

[142] Bons, J. P., Sondergaard, R., and Rivir, R. B., 2001. "The fluid dynamics of lpt blade separation control using pulsed jets". In ASME Turbo Expo 2001: Power for Land, Sea, and Air, American Society of Mechanical Engineers, pp. V003T01A064–V003T01A064.

[143] McManus, K., and Magill, J., 1996. "Separation control in incompressible and compressible flows using pulsed jets". In Fluid Dynamics Conference, p. 1948.

[144] Garnier, E., 2015. "Flow control by pulsed jet in a curved s-duct: a spectral analysis". *AIAA Journal,* **53**(10), pp. 2813–2827.

[145] Sarpotdar, S., Raman, G., and Cain, A. B., 2005. "Powered resonance tubes: resonance characteristics and actuation signal directivity". *Experiments in Fluids,* **39**(6), pp. 1084–1095.

[146] Kastner, J., and Samimy, M., 2002. "Development and characterization of hartmann tube fluidic actuators for high-speed flow control". *AIAA journal,* **40**(10), pp. 1926–1934.

[147] Raman, G., and Srinivasan, K., 2009. "The powered resonance tube: From hartmann's discovery to current active flow control applications". *Progress in Aerospace Sciences,* **45**(4-5), pp. 97–123.

[148] Raman, G., Mills, A., Othman, S., and Kibens, V., 2003. "Development of powered resonance tube actuators for active flow control". In 2001 ASME Fluids Engineering Division Summer Meeting, pp. 533–546.

[149] Khanafseh, S., Raman, G., and Cain, A., 2001. "Development of a high bandwidth hartmann–whistle type actuator". *The Journal of the Acoustical Society of America,* **109**(5), pp. 2403–2403.

[150] Brzozowski, D. P., K. Woo, G. T., Culp, J. R., and Glezer, A., 2010. "Transient separation control using pulse-combustion actuation". *AIAA journal,* **48**(11), pp. 2482–2490.

[151] Crittenden, T., Glezer, A., Funk, R., and Parekh, D., 2001. "Combustion-driven jet actuators for flow control". In 15th AIAA Computational Fluid Dynamics Conference, p. 2768.

[152] Woszidlo, R., Stumper, T., Nayeri, C., and Paschereit, C. O., 2014. "Experimental study on bluff body drag reduction with fluidic oscillators". In 52nd Aerospace Sciences Meeting, p. 0403.

[153] Corke, T. C., Enloe, C. L., and Wilkinson, S. P., 2010. "Dielectric barrier discharge plasma actuators for flow control". *Annual review of fluid mechanics,* **42**, pp. 505–529.

[154] Franck, J. A., Cooney, J., and Fine, N., 2018. "Simulations of plasma flow control strategies for trailing edge separation". In 2018 Flow Control Conference, p. 3524.

[155] Likhanskii, A., Shneider, M., Opaits, D., Macheret, S., and Miles, R., 2010. "Limitations of the dbd effects on the external flow". In 48th AIAA Aerospace Sciences Meeting Including the New Horizons Forum and Aerospace Exposition, p. 470.

[156] Thomas, F., Kozlov, A., and Corke, T., 2006. "Plasma actuators for bluff body flow control". In 3rd AIAA Flow Control Conference, p. 2845.

[157] Corke, T., and Post, M., 2005. "Overview of plasma flow control: concepts, optimization, and applications". In 43rd AIAA Aerospace Sciences Meeting and Exhibit, p. 563.

[158] Göksel, B., Rechenberg, I., and Bannasch, R., 2004. "Active separation flow control experiments in weakly ionized air". In Advances in Turbulence X, Proceedings of the 10th Euromech European Turbulence Conference, CIMNE, Barcelona.

[159] Wall, J., Boxx, I., Rivir, R., and Franke, M., 2007. Effects of pulsed-dc discharge plasma actuators in a separated low pressure turbine boundary layer (postprint). Tech. rep., AIR FORCE INST OF TECH WRIGHT-PATTERSON AFB OH.

[160] Utkin, Y. G., Keshav, S., Kim, J.-H., Kastner, J., Adamovich, I. V., and Samimy, M., 2006. "Development and use of localized arc filament plasma actuators for high-speed flow control". *Journal of Physics D: Applied Physics,* **40**(3), p. 685.

[161] Kleinman, R., Bodony, D., and Freund, J., 2010. "Shear-flow excitation mechanisms of recessed localized arc-filament plasma actuators". *Physics of Fluids,* **22**(11), p. 116103.

[162] Narayanaswamy, V., Raja, L. L., and Clemens, N. T., 2010. "Characterization of a high-frequency pulsed-plasma jet actuator for supersonic flow control". *AIAA journal,* **48**(2), pp. 297–305.

[163] Zong, H.-h., Wu, Y., Li, Y.-h., Song, H.-m., Zhang, Z.-b., and Jia, M., 2015. "Analytic model and frequency characteristics of plasma synthetic jet actuator". *Physics of fluids,* **27**(2), p. 027105.

[164] Popkin, S. H., Taylor, T. M., and Cybyk, B. Z., 2013. "Development and application of the sparkjet actuator for high-speed flow control". *Johns Hopkins APL technical digest,* **32**(1), pp. 404–18.

[165] Cattafesta, L. N., Garg, S., and Shukla, D., 2001. "Development of piezoelectric actuators for active flow control". *AIAA journal,* **39**(8), pp. 1562–1568.

[166] Tesař, V., Hung, C.-H., and Zimmerman, W. B., 2006. "No-moving-part hybrid-synthetic jet actuator". *Sensors and Actuators A: Physical,* **125**(2), pp. 159–169.

[167] Tesař, V., and Trávníček, Z., 2005. "Pulsating and synthetic impinging jets". *Journal of Visualization,* **8**(3), pp. 201–208.

[168] Cutler, A., Beck, B., Wilkes, J., Drummond, J., Alderfer, D., and Danehy, P., 2005. "Development of a pulsed combustion actuator for high-speed flow control". In 43rd AIAA Aerospace Sciences Meeting and Exhibit, p. 1084.

[169] Turrner, J., 2019. "Private communication". *Postdoctoral Research Assistant, Oxford Thermofluids Institute.*

[170] Evans, R., 1965. Applied fluids technology. Tech. rep., SAE Technical Paper.

[171] Cheng, R., and Foster, K. t., 1972. "Systematic method of designing fluidic–pneumatic control circuits". *Proceedings of the Institution of Mechanical Engineers,* **186**(1), pp. 401–408.

[172] Joyce, J. W., 1983. Fluidics: basic components and applications. Tech. rep., Harry Doamond Labs.

[173] Reba, I., 1966. "Applications of the coanda effect". *Scientific American,* **214**(6), pp. 84–93.

[174] Foster, K., and Parker, G. A., 1970. *Fluidics: components and circuits.* John Wiley & Sons.

[175] Bourque, C., and Newman, B., 1960. "Reattachment of a two-dimensional, incompressible jet to an adjacent flat plate". *The Aeronautical Quarterly,* **11**(3), pp. 201–232.

[176] Savkar, S. D., 1966. "An experimental study of switching in a bistable fluid amplifier".

[177] Ozgu, M., and Stenning, A., 1972. "Switching dynamics of bistable fluidic amplifiers with low setbacks". *Journal of Dynamic Systems, Measurement, and Control,* **94**(1), pp. 21–29.

[178] Ries, J. P., 1972. Dynamic modeling of the bistable fluid amplifier. Tech. rep., Lehigh University.

[179] Healey, A., 1968. "Vent effects on the response of a proportional fluid amplifier". *Journal of Basic Engineering,* **90**(1), pp. 90–96.

[180] Tesař, V., 2010. "No-moving-part valve for automatic flow switching". *Chemical Engineering Journal,* **162**(1), pp. 278–295.

[181] Roger, R., and Chan, S., 2003. "Numerical study of fluidic bistable amplifiers". In 33rd AIAA fluid dynamics conference and exhibit, p. 3459.

[182] Sarpkaya, T., and Kirshner, J. M., 1968. "The comparative performance characteristics of vented and unvented, cusped, and straight and curved-walled bistable amplifiers". In Proceedings of the Third Cranfield Fluidics Conference, pp. 3–37.

[183] Ozaki, M. H. S., and Hara, Y., 1968. "Output characteristics of wall attachment elements". In 3rd Cranfield Fluidics Conference, May.

[184] Lush, P., 1967. "Investigation of the switching mechanism in a large scale model of a turbulent reattachment amplifier(switching time of turbulent reattachment fluid amplifier in large scale model and in theory)". In CRANFIELD FLUIDICS CONFERENCE, 2 ND, CAMBRIDGE, ENGLAND, Vol. 3.

[185] Hogland, G. H., 1972. "Studies of bistable fluid devices for particle flow control".

[186] Cerretelli, C., Wuerz, W., and Gharaibah, E., 2010. "Unsteady separation control on wind turbine blades using fluidic oscillators". *AIAA journal,* **48**(7), pp. 1302–1311.

[187] Cerretelli, C., and Kirtley, K., 2009. "Boundary layer separation control with fluidic oscillators". *Journal of Turbomachinery,* **131**(4), p. 041001.

[188] Gokoglu, S., Kuczmarski, M., Culley, D., and Raghu, S., 2009. "Numerical studies of a fluidic diverter for flow control". In 39th AIAA Fluid Dynamics Conference, p. 4012.

[189] Gokoglu, S., Kuczmarski, M., Culley, D., and Raghu, S., 2011. "Numerical studies of an array of fluidic diverter actuators for flow control". In 41st AIAA Fluid Dynamics Conference and Exhibit, p. 3100.

[190] Gokoglu, S., Kuczmarski, M., Culley, D., and Raghu, S., 2010. "Numerical studies of a supersonic fluidic diverter actuator for flow control". In 5th Flow control conference, p. 4415.

[191] Bettrich, V., and Niehuis, R., 2018. "Experimental investigation of geometric design parameters of a high frequency fluidic oscillator at turbomachinery relevant conditions". In 2018 Flow Control Conference, p. 3059.

[192] Wang, S., Baldas, L., Colin, S., Orieux, S., Kourta, A., and Mazellier, N., 2016. "Experimental and numerical study of the frequency response of a fluidic oscillator for active flow control". In 8th AIAA Flow Control Conference, p. 4234.

[193] Tomac, M. N., and Gregory, J. W., 2018. "Phase-synchronized fluidic oscillator pair". *AIAA Journal,* **57**(2), pp. 670–681.

[194] Spyropoulos, C. E., 1964. "A sonic oscillator(operational principles and characteristics of sonic oscillator- pneumatic clock pulse generator)". *1964.*, pp. 27–52.

[195] Viets, H., 1975. "Flip-flop jet nozzle". *AIAA journal,* **13**(10), pp. 1375–1379.

[196] Arwatz, G., Fono, I., and Seifert, A., 2008. "Suction and oscillatory blowing actuator modeling and validation". *AIAA journal,* **46**(5), pp. 1107–1117.

[197] Kim, J., Moin, P., and Seifert, A., 2017. "Large-eddy simulation-based characterization of suction and oscillatory blowing fluidic actuator". *AIAA journal*, pp. 2566–2579.

[198] Tomac, M. N., and Gregory, J. W., 2014. "Internal jet interactions in a fluidic oscillator at low flow rate". *Experiments in Fluids,* **55**(5), p. 1730.

[199] Raghu, S., 2001. Feedback-free fluidic oscillator and method, July 3. US Patent 6,253,782.

[200] Gregory, J. W., Sullivan, J. P., and Raghu, S., 2005. "Visualization of jet mixing in a fluidic oscillator". *Journal of Visualization,* **8**(2), pp. 169–176.

[201] Zhang, Y., Fu, Q., Mo, C., and Yang, L., 2017. "Molecular dynamics simulation of a nanoscale feedback-free fluidic oscillator". *AIP Advances,* **7**(11), p. 115311.

[202] Tomac, M. N., and Gregory, J. W., 2018. "Oscillation characteristics of mutually impinging dual jets in a mixing chamber". *Physics of Fluids,* **30**(11), p. 117102.

[203] Reichenzer, F., Schneider, M., and Dörr, S., 2018. "Influence of geometry on a feedback-free fluidic oscillator with nonoutlet facing jets". *AIAA Journal,* **56**(12), pp. 4768–4774.

[204] Culley, D., 2006. "Variable frequency diverter actuation for flow control". In 3rd AIAA Flow Control Conference, p. 3034.

[205] Sun, F., Lin, R.-S., Haas, M., and Brogan, T., 2002. "Air flow control by fluidic diverter for low nox jet engine combustion". In 1st Flow Control Conference, p. 2945.

[206] Gregory, J., Ruotolo, J., Byerley, A., and McLaughlin, T., 2007. "Switching behavior of a plasma-fluidic actuator". In 45th AIAA Aerospace Sciences Meeting and Exhibit, p. 785.

[207] Tesař, V., and Šonskỳ, J., 2015. "No-moving-part electro/fluidic transducer based on plasma discharge effect". *Sensors and Actuators A: Physical,* **232**, pp. 20–29.

[208] Martin, N. D., Bottomley, M., and Packwood, A., 2014. "Switching of a bistable diverter valve with synthetic jet actuators". *AIAA Journal,* **52**(7), pp. 1563–1568.

[209] Chen, L.-W., Turner, J., Bacic, M., and Ireland, P., 2016. "Exeprimental and numerical studies of a plasma fluidic device for active flow control". In 8th AIAA Flow Control Conference, p. 4235.

[210] Raghu, S., 2013. "Fluidic oscillators for flow control". *Experiments in Fluids,* **54**(2), p. 1455.

[211] Margalit, S., Greenblatt, D., Seifert, A., and Wygnanski, I., 2005. "Delta wing stall and roll control using segmented piezoelectric fluidic actuators". *Journal of Aircraft,* **42**(3), pp. 698–709.

[212] Molton, P., Dandois, J., Lepage, A., Brunet, V., and Bur, R., 2013. "Control of buffet phenomenon on a transonic swept wing". *AIAA journal,* **51**(4), pp. 761–772.

[213] Amitay, M., Pitt, D., and Glezer, A., 2002. "Separation control in duct flows". *Journal of Aircraft,* **39**(4), pp. 616–620.

[214] Culley, D. E., Bright, M. M., Prahst, P. S., and Strazisar, A. J., 2004. "Active flow separation control of a stator vane using embedded injection in a multistage compressor experiment". *Journal of Turbomachinery,* **126**(1), pp. 24–34.

[215] Guyot, D., Bobusch, B., Paschereit, C. O., and Raghu, S., 2008. "Active combustion control using a fluidic oscillator for asymmetric fuel flow modulation". In 44th AIAA/ASME/SAE/ASEE Joint Propulsion Conference & Exhibit, p. 4956.

[216] Huang, J., Corke, T. C., and Thomas, F. O., 2006. "Plasma actuators for separation control of low-pressure turbine blades". *AIAA journal,* **44**(1), pp. 51–57.

[217] Raman, G., Packiarajan, S., Papadopoulos, G., Weissman, C., and Raghu, S., 2005. "Jet thrust vectoring using a miniature fluidic oscillator". *The Aeronautical Journal,* **109**(1093), pp. 129–138.

[218] Glezer, A., Amitay, M., and Honohan, A. M., 2005. "Aspects of low-and high-frequency actuation for aerodynamic flow control". *AIAA journal,* **43**(7), pp. 1501–1511.

[219] Kumar, V., and Alvi, F. S., 2009. "Toward understanding and optimizing separation control using microjets". *AIAA journal,* **47**(11), pp. 2544–2557.

[220] Amitay, M., and Glezer, A., 2002. "Role of actuation frequency in controlled flow reattachment over a stalled airfoil". *AIAA journal,* **40**(2), pp. 209–216.

[221] Seele, R., Graff, E., Lin, J., and Wygnanski, I., 2013. "Performance enhancement of a vertical tail model with sweeping jet actuators". In 51st AIAA Aerospace Sciences Meeting including the New Horizons Forum and Aerospace Exposition, p. 411.

[222] MacMartin, D. G., Murray, R., Verma, A., and Paduano, J. D., 2001. "Active control of integrated inlet/compression systems: initial results". *ASME Fluid Engng. FEDSM,* **18275**.

[223] Kumar, V., and Alvi, F. S., 2006. "Use of high-speed microjets for active separation control in diffusers". *AIAA journal,* **44**(2), pp. 273–281.

[224] Braunscheidel, E., Culley, D., and Zaman, K., 2008. "Application of synthetic jets to reduce stator flow separation in a low speed axial compressor". In 46th AIAA Aerospace Sciences Meeting and Exhibit, p. 602.

[225] De Jager, B., 1995. "Rotating stall and surge control: A survey". In Proceedings of 1995 34th IEEE Conference on Decision and Control, Vol. 2, IEEE, pp. 1857–1862.

[226] D'Andrea, R., Behnken, R. L., and Murray, R. M., 1996. "Active control of an axial flow compressor via pulsed air injection".

[227] Staats, M., Nitsche, W., Steinberg, S., and King, R., 2017. "Closed-loop active flow control of a non-steady flow field in a highly-loaded compressor cascade". *CEAS Aeronautical Journal,* **8**(1), pp. 197–208.

[228] Saiki, Y., Tanaka, S., Hattori, S., Nakura, K., and Ishino, Y., 2016. "Manipulation of large-scale vortical structures and mixing in a coaxial jet with miniature jet actuators toward active combustion control". *Flow, Turbulence and Combustion,* **97**(4), pp. 1127–1145.

[229] Meier, E., Casiano, M. J., Anderson, W. E., and Heister, S. D., 2015. "Investigation of combustion control in a dump combustor using the feedback free fluidic oscillator". In 51st AIAA/SAE/ASEE Joint Propulsion Conference, p. 4209.

[230] Sondergaard, R., Rivir, R. B., and Bons, J. P., 2002. "Control of low-pressure turbine separation using vortex-generator jets". *Journal of propulsion and power,* **18**(4), pp. 889–895.

[231] Kurz, J., Hoeger, M., and Niehuis, R., 2018. "Active boundary layer control on a highly loaded turbine exit case profile". *International Journal of Turbomachinery, Propulsion and Power,* **3**(1), p. 8.

[232] Bettrich, V., Bitter, M., and Niehuis, R., 2018. "Interaction phenomena of high frequency pulsed blowing in lp turbine-like boundary layers at high speed test conditions". In ASME Turbo Expo 2018: Turbomachinery Tech-

nical Conference and Exposition, American Society of Mechanical Engineers, pp. V02BT41A007–V02BT41A007.

[233] Rizzetta, D. P., and Visbal, M. R., 2007. "Numerical investigation of plasma-based flow control for transitional highly-loaded low-pressure turbine". *AIAA journal,* **45**(10), pp. 2554–2564.

[234] Volino, R. J., and Ibrahim, M. B., 2012. "Separation control on high lift low-pressure turbine airfoils using pulsed vortex generator jets". *Applied Thermal Engineering,* **49**, pp. 31–40.

[235] Sondergaard, R., Bons, J. P., Sucher, M., and Rivir, R. B., 2002. "Reducing low-pressure turbine stage blade count using vortex generator jet separation control". In ASME Turbo Expo 2002: Power for Land, Sea, and Air, American Society of Mechanical Engineers, pp. 1055–1061.

[236] Rizzetta, D. P., and Visbal, M. R., 2006. "Numerical study of active flow control for a transitional highly loaded low-pressure turbine". *Journal of fluids engineering,* **128**(5), pp. 956–967.

[237] Burns, A., 2015. "Turbine tip clearance control using fluidic oscillators". PhD thesis, University of Kansas.

[238] Jeong, H.-S., and Kim, K.-Y., 2018. "Shape optimization of a feedback-channel fluidic oscillator". *Engineering Applications of Computational Fluid Mechanics,* **12**(1), pp. 169–181.

[239] Stone, M., Shyam, V., Poinsatte, P. E., Thurman, D. R., and Raghu, S., 2018. "Fluidic actuation for aeropropulsive acoustic improvements".

[240] Páscoa, J. C., Dumas, A., Trancossi, M., Stewart, P., and Vucinic, D., 2013. "A review of thrust-vectoring in support of a v/stol non-moving mechanical

propulsion system". *Central European Journal of Engineering,* **3**(3), pp. 374–388.

[241] Kowal, H., 2002. "Advances in thrust vectoring and the application of flow-control technology". *Canadian aeronautics and space journal,* **48**(2), pp. 145–151.

[242] Deere, K., 2003. "Summary of fluidic thrust vectoring research at nasa langley research center". In 21st AIAA applied aerodynamics conference, p. 3800.

[243] Tippetts, J., and Royle, J., 1971. "Design of flow control circuits involving unvented bistable amplifiers (flow control circuits design based on unvented bistable fluid amplifiers)". *Fluidics Quarterly,* **3**, pp. 1–15.

[244] Versteeg, H. K., and Malalasekera, W., 2007. *An introduction to computational fluid dynamics: the finite volume method.* Pearson education.

[245] Koli, B. R., 2015. "Cfd investigation of a switched vortex valve for cooling air flow modulation in aeroengine". PhD thesis, © Bharat Ramesh Koli.

[246] Jamshed, S., 2015. *Using HPC for Computational Fluid Dynamics: A Guide to High Performance Computing for CFD Engineers.* Academic Press.

[247] Fröhle, P. *Lecture notes: Environmental Hydraulic Simulation.* TU Hamburg.

[248] Pitsch, H., 2006. "Large-eddy simulation of turbulent combustion". *Annu. Rev. Fluid Mech.,* **38**, pp. 453–482.

[249] Sagaut, P., 2006. *Large eddy simulation for incompressible flows: an introduction.* Springer Science & Business Media.

[250] Ferziger, J., 1997. "Large eddy simulation: an introduction and perspective". In *New tools in turbulence modelling.* Springer, pp. 29–47.

[251] Menter, F., 1993. "Zonal two equation kw turbulence models for aerodynamic flows". In 23rd fluid dynamics, plasmadynamics, and lasers conference, p. 2906.

[252] Nicoud, F., and Ducros, F., 1999. "Subgrid-scale stress modelling based on the square of the velocity gradient tensor". *Flow, Turbulence and Combustion,* **62**(3), pp. 183–200.

[253] De Moura, C. A., and Kubrusly, C. S., 2013. "The courant-friedrichs-lewy (cfl) condition". *AMC,* **10**, p. 12.

[254] Kolmogorov, A. N., 1941. "Dissipation of energy in locally isotropic turbulence". In Dokl. Akad. Nauk SSSR, Vol. 32, pp. 16–18.

[255] Urzay, J., Bassenne, M., Park, G., and Moin, P., 2014. "Characteristic regimes of subgrid-scale coupling in les of particle-laden turbulent flows". *Proceedings of Summer Program, Center for Turbulence Research, Stanford University*, pp. 3–13.

[256] Timoshenko, S. P., and Woinowsky-Krieger, S., 1959. *Theory of plates and shells*. McGraw-hill.

[257] *The Acoustics Module User's Guide, Version 5.4, Comsol Mutliphysics.*

[258] Russ, S., and Strykowski, P., 1993. "Turbulent structure and entrainment in heated jets: The effect of initial conditions". *Physics of Fluids A: Fluid Dynamics,* **5**(12), pp. 3216–3225.

[259] Xu, G., and Antonia, R., 2002. "Effect of different initial conditions on a turbulent round free jet". *Experiments in Fluids,* **33**(5), pp. 677–683.

[260] Hussain, A., and Zedan, M., 1978. "Effects of the initial condition on the axisymmetric free shear layer: Effects of the initial momentum thickness". *The Physics of Fluids,* **21**(7), pp. 1100–1112.

[261] Hussain, A., and Zedan, M., 1978. "Effects of the initial condition on the axisymmetric free shear layer: Effect of the initial fluctuation level". *The Physics of Fluids,* **21**(9), pp. 1475–1481.

[262] George, W. K., 1989. "The self-preservation of turbulent flows and its relation to initial conditions and coherent structures". *Advances in turbulence,* **3973**.

[263] Grandchamp, X., and Van Hirtum, A., 2013. "Near field round jet flow downstream from an abrupt contraction nozzle with tube extension". *Flow, turbulence and combustion,* **90**(1), pp. 95–119.

[264] Antonia, R., and Zhao, Q., 2001. "Effect of initial conditions on a circular jet". *Experiments in fluids,* **31**(3), pp. 319–323.

[265] Michalke, A., 1977. "Instability of a compressible circular free jet with consideration of the influence of the jet boundary layer thickness".

[266] Wygnanski, I., and Fiedler, H., 1969. "Some measurements in the self-preserving jet". *Journal of Fluid Mechanics,* **38**(3), pp. 577–612.

[267] Balarac, G., Métais, O., and Lesieur, M., 2007. "Mixing enhancement in coaxial jets through inflow forcing: A numerical study". *Physics of Fluids,* **19**(7), p. 075102.

[268] Jeong, J., and Hussain, F., 1995. "On the identification of a vortex". *Journal of Fluid Mechanics,* **285**, pp. 69–94.

[269] Chun, K.-B., and Sung, H. J., 1996. "Control of turbulent separated flow over a backward-facing step by local forcing". *Experiments in fluids,* **21**(6), pp. 417–426.

[270] Epstein, M., 1971. "Theoretical investigation of the switching mechanism in a bistable wall attachment fluid amplifier". *Journal of Basic Engineering,* **93**(1), pp. 55–62.

[271] Horn, G., and Thring, M., 1956. "Angle of spread of free jets". *Nature,* **178**(4526), p. 205.

[272] *Optimization Toolbox User's Guide, Matlab R2019a.*

[273] Tam, C. K., 1978. "Excitation of instability waves in a two-dimensional shear layer by sound". *Journal of Fluid Mechanics,* **89**(2), pp. 357–371.

[274] Goldschmidt, V., and Bradshaw, P., 1981. "Effects of nozzle exit turbulence on the spreading/or widening/ rate of plane free jets". In American Society of Mechanical Engineers and American Society of Civil Engineers, Joint Applied Mechanics, Fluids Engineering, and Bioengineering Conference, University of Colorado, Boulder, CO.

[275] Gordeyev, S., and Thomas, F., 1999. "Temporal subharmonic amplitude and phase behaviour in a jet shear layer: wavelet analysis and hamiltonian formulation". *Journal of Fluid Mechanics,* **394**, pp. 205–240.

[276] Nicholls, C., Tang, B., Turner, J., and Bacic, M., 2019. "Experimental and numerical studies of physical mechanisms in fluidic oscillators". In AIAA Aviation 2019 Forum, p. 3394.

[277] Buxton, O., and Ganapathisubramani, B., 2011. "Piv measurements of convection velocities in a turbulent mixing layer". In Journal of Physics: Conference Series, Vol. 318, IOP Publishing, p. 052038.

[278] Krogstad, P.-Å., Kaspersen, J., and Rimestad, S., 1998. "Convection velocities in a turbulent boundary layer". *Physics of Fluids,* **10**(4), pp. 949–957.

[279] Crighton, D., and Gaster, M., 1976. "Stability of slowly diverging jet flow". *Journal of Fluid Mechanics,* **77**(2), pp. 397–413.

[280] Drubka, R. E., and Nagib, H. M., 1981. Instabilities in near field of turbulent jets and their dependence on initial conditions and reynolds number. Tech. rep., ILLINOIS INST OF TECH CHICAGO DEPT OF MECHANICAL ENGINEERING.

[281] Hussain, A., and Clark, A., 1981. "On the coherent structure of the axisymmetric mixing layer: a flow-visualization study". *Journal of Fluid Mechanics,* **104**, pp. 263–294.

[282] Petersen, R., and Clough, R., 1992. "The influence of higher harmonics on vortex pairing in an axisymmetric mixing layer". *Journal of Fluid Mechanics,* **239**, pp. 81–98.

[283] Raman, G., and Rice, E. J., 1991. "Axisymmetric jet forced by fundamental and subharmonic tones". *AIAA journal,* **29**(7), pp. 1114–1122.

[284] Cho, S., Yoo, J., and Choi, H., 1998. "Vortex pairing in an axisymmetric jet using two-frequency acoustic forcing at low to moderate strouhal numbers". *Experiments in Fluids,* **25**(4), pp. 305–315.

[285] Jiang, P., Guo, Y., Chan, C., and Lin, W., 2007. "Frequency characteristics of coherent structures and their excitations in small aspect-ratio rectangular jets using large eddy simulation". *Computers & fluids,* **36**(3), pp. 611–621.

[286] Alnahhal, M., and Panidis, T., 2009. "The effect of sidewalls on rectangular jets". *Experimental Thermal and Fluid Science,* **33**(5), pp. 838–851.

[287] Deo, R. C., Nathan, G. J., and Mi, J., 2007. "Comparison of turbulent jets issuing from rectangular nozzles with and without sidewalls". *Experimental Thermal and Fluid Science,* **32**(2), pp. 596–606.

[288] Nicholls, C., and Bacic, M., 2018. "Closed-loop control of a piezo-fluidic amplifier". In 2018 Flow Control Conference, p. 3695.